Irradiation of cometary surfaces, application to the origin of the organic matter in ultra-carbonaceous micrometeorites

Julien Rojas Arispe

THESE DE DOCTORAT

NNT : 2022UPASP011

Irradiation of cometary surfaces, application to the origin of the organic matter in ultra-carbonaceous micrometeorites

Irradiation de surfaces cométaires, application à l'origine de la matière organique des micrométéorites Ultra-Carbonées

Thèse de doctorat de l'université Paris-Saclay

École doctorale n° 576, particules, hadrons, énergie et noyau : instrumentation, imagerie, cosmos et simulation (PHENIICS)
Spécialité de doctorat : Astrophysique nucléaire et nucléosynthèse
Graduate School : Physique. Référent : Faculté des sciences d'Orsay

Thèse préparée à **IJCLab (Université Paris-Saclay, CNRS)**, sous la direction de **Jean DUPRAT**, directeur de recherche, la co-direction de **Emmanuel DARTOIS**, directeur de recherche

Thèse soutenue à Paris-Saclay, le 26 Janvier 2022, par

Julien ROJAS ARISPE

Composition du Jury

Elias KHAN Professeur, Université Paris-Saclay, IJCLab	Président du Jury
Karine DEMYK Directrice de recherche, Université Fédérale Toulouse Midi-Pyrénées, IRAP	Rapporteur & Examinatrice
Kevin MCKEEGAN Professeur émérite, University of California	Rapporteur & Examinateur
Marc CHAUSSIDON Directeur de recherche, Université de Paris, IPGP	Examinateur
Laurette PIANI Chargée de recherche, Université de Lorraine, CRPG	Examinatrice
Jean DUPRAT Directeur de recherche, Université Paris-Saclay, IMPMC/SU/MNHN	Directeur de thèse

université PARIS-SACLAY
ÉCOLE DOCTORALE
Particules, hadrons, énergie et noyau: instrumentation, imagerie, cosmos et simulation (PHENIICS)

Titre : Irradiation de surfaces cométaires, application à l'origine de la matière organique des micrométéorites Ultra-Carbonées

Mots clés : micrométéorites, matière organique, disque protoplanétaire, comètes, irradiation, spectrométrie de masse

Résumé : Les micrométéorites sont des particules extraterrestres submillimétriques qui représentent la majeure source de matière interplanétaire accrétée par la Terre chaque année. L'analyse des micrométéorites permet d'étudier la diversité des petits corps du système solaire (astéroïdes et comètes). Cette thèse porte sur l'étude de micrométéorites provenant de la collection Concordia, constituée depuis 20 ans grâce à un programme réalisé auprès de la station de Dôme C (Antarctique). La première partie du travail présenté porte sur une étude quantitative sur le flux de matière interplanétaire arrivant sur Terre. L'étude basée sur plus de 2000 micrométéorites de la collection Concordia montre que le flux de micrométéorites est de ~10 µg/m^2/an, qui correspond à un flux global annuel de 5200 ± 1500 tonnes sur l'ensemble de notre planète. Les résultats obtenus permettent de mieux contraindre les distributions en masse des particules dans le domaine en taille inférieure à 300 µm et leur comparaison avec les prévisions théoriques indiquent que la majorité des particules ont très probablement une origine cométaire.

La seconde partie du travail présenté porte sur l'étude d'un type rare de micrométéorites, riches en matière organique : les micrométéorites antarctiques ultra-carbonées (UCAMM - Ultra-Carbonaceous Antarctic MicroMeteorites). L'analyse isotopique par spectrométrie de masse des ions secondaires à résolution nanométrique (NanoSIMS) révèle des hétérogénéités isotopiques en H, N et C de la matière organique des UCAMMs à l'échelle de plusieurs microns.

La troisième partie présente des expériences d'irradiations de glaces par des ions lourds, menées à l'aide du dispositif IGLIAS durant trois sessions expérimentales auprès du Grand Accélérateur National d'Ions Lourds (GANIL). Ces expériences ont permis de simuler l'interaction du rayonnement cosmique Galactique sur des mélanges de glaces azotées et carbonées à basse température (10K). Un résidu organique solide est obtenu après sublimation des espèces volatiles à la fin de l'irradiation du film de glace. Les résultats obtenus montrent qu'il est possible de transmettre au résidu organique produit des hétérogénéités isotopiques présentes dans des couches initialement adjacentes de glaces irradiées. L'analyse par imagerie ionique NanoSIMS des résidus organiques montre la formation d'hétérogénéités isotopiques dans le résidu organique, qui sont comparables à celles observées dans les UCAMMs. Ces hétérogénéités isotopiques dépendent de la nature chimique du mélange de glaces irradiées.

L'ensemble des résultats obtenus sur les UCAMMs et les expériences d'irradiation menées à GANIL sont mis en perspective et comparés aux données sur d'autres matériaux interplanétaires d'origine astéroïdale et cométaire. Les travaux menés confirment que ces particules interplanétaires exceptionnelles proviennent très probablement de la surface de corps glacés, riches en azote, ayant évolués dans les zones externes du système solaire. Ils confirment que les signatures isotopiques en éléments légers (H, N et C) des UCAMMs peuvent, en partie, être héritées de réservoirs parents gazeux présents dans le disque protoplanétaire. Je présenterai enfin de futures études possibles sur les UCAMMs permettant de mieux contraindre la composition de la surface des corps glacés présents à de grandes distances héliocentriques.

Title: Irradiation of cometary surfaces, application to the origin of the organic matter in ultra-carbonaceous micrometeorites

Keywords: micrometeorites, organic matter, protoplanetary disk, irradiation, mass spectrometry

Abstract: Micrometeorites are submillimeter extraterrestrial particles that represent the major source of interplanetary material accreted by the Earth each year. The analysis of micrometeorites allows to study the diversity of small bodies of the solar system (asteroids and comets). This thesis is about the study of micrometeorites from the Concordia collection, developed over the last 20 years thanks to a program carried out at the Dome C station (Antarctica). The first part of the work presented concerns a quantitative study of the flow of interplanetary matter arriving on Earth. The study based on more than 2000 micrometeorites from the Concordia collection shows that the flux of micrometeorites is ~10 μg/m²/year, which corresponds to a global annual flux of 5200 ± 1500 tons on our planet. The obtained results allow to better constrain the mass distributions of the particles in the size range below 300 μm and their comparison with the theoretical predictions indicate that the majority of the particles have most probably a cometary origin.

The second part of the presented work concerns the study of a rare type of micrometeorites, rich in organic matter: the Ultra-Carbonaceous Antarctic MicroMeteorites (UCAMM). Isotopic analysis of UCAMMs by nanoscale secondary ion mass spectrometry (NanoSIMS) reveals isotopic heterogeneities in H, N and C of the organic matter of UCAMMs at the scale of several microns. The third part presents experiments of ice irradiations by heavy ions, carried out with the IGLIAS device during three experimental sessions at the Large Heavy Ion National Accelerator (GANIL).

These experiments have simulated the interaction of the Galactic cosmic rays on mixtures of nitrogen- and carbon-rich ices at low temperature (10K). A solid organic residue is obtained after sublimation of the volatile species at the end of the irradiation of the ice film. The results obtained show that isotopic heterogeneities present in initially adjacent layers of irradiated ice can be transmitted to the organic residue produced. NanoSIMS ion imaging analysis of the organic residue shows the formation of isotopic heterogeneities in the organic residue, which are comparable to those observed in UCAMMs. These isotopic heterogeneities depend on the chemical nature of the irradiated ice mixture.

All the results obtained on UCAMMs and the irradiation experiments carried out at GANIL are put in perspective and compared to data on other interplanetary materials of asteroidal and cometary origin. The work carried out confirms that these exceptional interplanetary particles most probably come from the surface of icy bodies, rich in nitrogen, having evolved in the outer regions of the solar system. They confirm that the isotopic signatures in light elements (H, N and C) of UCAMMs can, in part, be inherited from gaseous parent reservoirs present in the protoplanetary disk. Finally, I will present possible future studies on UCAMMs to better constrain the surface composition of icy bodies present at large heliocentric distances.

Remerciements/Acknowledgments

I start with a few words in English to thank the members of the Jury Karine Demyk, Marc Chaussidon, Elias Khan, Kevin McKeegan and Laurette Piani for having accepted to review the thesis. Their suggestions and comments helped a lot to improve the final version of the manuscript. I want to specially thank Karine Demyk and Kevin McKeegan that accepted to read and review the manuscript during the Christmas holidays.

I am really grateful to Larry Nittler and Rhonda Stroud that kindly received me at Washington D.C. during the first year of my Ph.D. for my first NanoSIMS session, that was quite something.

Et maintenant, quelques mots en français…

Tout d'abord je voudrais remercier Jean Duprat et Emmanuel Dartois pour avoir accepté de m'encadrer au cours de cette thèse. Les nombreux moments passés à échanger ont toujours été très riches scientifiquement et humainement et leur implication m'a permis de découvrir des pans de recherche passionnants : les micrométéorites qui m'ont été présentées par Jean et les expériences de laboratoires présentées par Emmanuel. Apprendre à marcher avec un pied dans chaque monde a pris un certain temps mais le jeu en valait la chandelle, surtout en si bonne compagnie. En démarrant la thèse, je n'imaginais pas que la recherche sur les micrométéorites pouvait conduire à martyriser des petits films de glace avec des ions lourds et je ne pouvais envisager qu'un jour je me retrouverais dans un état d'excitation extrême après avoir observé une petite tâche organique informe au microscope… Tout commença sans doute un an avant le début de la thèse, lorsque Jean me présenta la collection de micrométéorites collectées en Antarctique, promesse d'un double dépaysement, extraterrestre et géographique. Après plus de trois années de thèse, je n'ai finalement pas posé le pied en Antarctique mais j'ai été amené à découvrir bien d'autres endroits insolites, du motel de la banlieue de Houston, aux immenses hangars du GANIL encerclés par les lapins, en passant par les chalets des Houches, les quartiers résidentiels de Washington, les immenses hangars de GSI encerclés par bien peu de monde (pandémie oblige), les sous-sols d'IJCLab, les combles de l'IMPMC et j'en oublie. Des endroits peuplés d'êtres humains diverses, très souvent intéressants, où je ne serais jamais allé si ça n'avait pas été pour la recherche. Toutes ces découvertes ne se seraient pas faites sans la thèse et sans Jean et Emmanuel, merci à eux donc.

Il me faut aussi remercier ici Georges Slodzian qui m'a introduit dans le monde complexe et multipolaire de l'optique ionique et de la spectrométrie de masse des ions secondaires. Travailler avec Georges a été très enrichissant et je lui suis extrêmement reconnaissant de sa confiance et du temps qu'il a pris pour nos échanges et ma bonne compréhension du NanoSIMS. Au même titre que je ne m'imaginais pas à quoi pouvait conduire la recherche sur les micrométéorites, je ne m'imaginais pas tous les mystères que pouvait renfermer un hexapole.

Maintenant que la mèche est allumée, il me faut remercier tous ceux, rencontrés ici ou là-bas, avant ou pendant, qui m'ont aidé/apporté/encouragé/aucun des trois mais qui ont eu le mérite d'être là, ce qui est déjà beaucoup.

En commençant par le laboratoire IJCLab/ex-CSNSM j'aimerais remercier Cécile qui a été très présente tout au long de la thèse et qui a veillé à bien des points de vue à son bon déroulement au sein du laboratoire (merci pour la soutenance !) et au milieu des micrométéorites. Un grand merci à Lucie, pour tout, les quelques mots ici ne refléterons que très peu tout ce que m'a apporté sa présence pendant ces années. Nos discussions qui entrecoupaient les journées au laboratoire étaient toujours

(et le seront encore pour longtemps j'espère) de très bons et très nécessaires moments d'évasion. Il en va de même pour Baptiste avec qui nous avons partagé le bureau des poignards volants pendant les trois années de nos thèses respectives, merci à lui. Il était rassurant de s'aventurer à deux dans ce chemin pavé d'UCAMMs. Bon courage à Laure (!) qui nous succède et à qui je lègue un écran et ma collection de gobelets, mon objectif était d'arriver à une tour à la fin de la thèse, deux thèses seront peut-être assez. Merci à Marie pour sa disponibilité et sa bonne humeur, je garde précieusement la copie de TP de M1 que tu avais pris soin de conserver dans tes archives, je ne pensais pas la revoir un jour… Je terminerai ce paragraphe en remerciant toutes les personnes que j'ai eu le plaisir de côtoyer au laboratoire et/ou avec lesquelles j'ai travaillé : Vincent, mes voisins de bureau Anne et Corentin et toute l'équipe d'Astrophysique et Cosmochimie avec une pensée pour Adrien, bon courage pour la fin ! Sans oublier Marin aux conseils précieux pour survivre une semaine dans un accélérateur et trouver des châtaignes, Silvin et Harald riverains du couloir du 104, Florian collègue de maté, Claire toujours disponible pour discuter à des heures tardives et Réjane qui me guida lors de mes premiers pas balbutiant au CSNSM.

Je continuerai par remercier Ting-Di, monument de force tranquille, avec qui j'ai eu beaucoup de plaisir à travailler tout au long de ma thèse. Les séances estivales de NanoSIMS étaient toujours très agréables et ponctuées de riches discussions sur des sujets divers, autour d'un thé et des nougats, à tel point qu'on en arrivait à oublier qu'à l'extérieur rayonnait un très beau soleil.

Par-delà les rives septentrionales de l'Yvette, il me faut saluer la très accueillante équipe de l'ICP, Jérémie, Ariane et Alexandre. C'était toujours un plaisir de se rendre dans ce temple de machines de pointe. Merci à Jérémie pour son aide et ses très intéressantes considérations sur le chocolat dans le bœuf bourguignon. Ce fut une très bonne surprise de travailler et surtout d'enseigner avec Ariane, 5 ans après avoir suivi benoitement ses TP, je peux maintenant m'amuser à recoriger mes copies de l'époque.

Toujours à Orsay, je voudrais particulièrement remercier Khuon Viet Pham, Jean Bénit et plus généralement le département de physique pour m'avoir permis d'enseigner pendant la thèse. En plus d'être agréable à donner, les cours-TD et les TP étaient de bons moyens de prendre du recul sur les recherches. Merci à Valérie Hortaut pour son incroyable implication et efficacité et à Romain pour nos échanges. Merci également à David Verney et à l'école doctorale PHENIICS pour leur suivi et leur gestion administrative de la thèse.

En m'éloignant d'Orsay et en rejoignant la côte normande, je remercierai l'équipe du CIMAP, Philippe, Hermann et Alicja pour leur accueil et leur implication dans les séjours à GANIL et ce malgré les contraintes sanitaires. Il est toujours rassurant de savoir qu'on peut appeler quelqu'un en urgence lorsqu'on est seul devant la manip une nuit d'un week-end du premier Mai et il est toujours réconfortant de manger une araignée de mer ouverte au marteau lorsqu'on n'est pas sorti de l'enceinte du labo depuis plusieurs jours. C'est d'ailleurs entre les grillages du GANIL que j'ai découvert que les lapins pouvaient se cogner très fort la tête sur un plot, en bon francilien j'avais toujours cru qu'ils ne pouvaient que se coincer les doigts dans les portes. Il convient ici de remercier Basile qui m'initia au concept des expériences d'irradiation de glace, bien que nous nous soyons d'abord rencontrés au CSNSM. Premier co-bureau de ces années de thèse, il me montra très vite les bonnes pratiques telles que bien nettoyer son bureau, ne pas éteindre intempestivement les multiprises et faire bien attention aux destinataires des mails. Etant donné que le présent manuscrit s'inscrit dans la lignée de son manuscrit de thèse, je lui ferai l'honneur de la première citation, lumière dans la manière d'organiser son travail : figure 0 dans B. Augé (2015). Covid et postdoc obligent, nous devînmes co-bureaux virtuels aux côtés de Alice. Il s'impose de remercier Alice pour nous avoir patiemment toléré et parfois agi comme une juge de paix, merci à elle.

De retour à Paris, j'adresserai un grand merci aux membres de l'IMPMC. Merci à Mathieu Roskosz et Matthieu Gounelle pour m'avoir accueilli au laboratoire et au sein de l'équipe COSMO. Merci à Laurent, Sylvain et Sylvain pour des discussions intéressantes scientifiquement mais pas que, merci à Emmanuel Jacquet pour le mail d'annonce de la soutenance qui m'a fait bien plaisir, merci à Brigitte pour ses encouragements et merci à Jean-Jacques pour son aide lors de mon installation. Encore des mercis pour les non-permanents (ou presque) qui m'ont très bien reçu, la bonne ambiance du labo était un vrai moteur et j'ai maintenant plein de souvenirs pour me rappeler encore plus de vous (pallasite 4ever) : merci à Boris peintre en herbe bassecourophile, Chloé aux recommandations musicales très avisées et bien plus, Isis pourfendeuse de Nairfol (il finira par être dernier), J-C fier défenseur des argiles, Lauranne aux couteaux bien affutés, Marceau et sa science du placement stratégique, Marine toujours très attentionnée (merci pour les gâteaux !), Maximilien qui n'a plus tout à fait sa place dans cette catégorie, Samantha très claire en 180 secondes, Tommy l'ami des plantes et du fromage et Virgile aux très belles chaussettes.

Enfin, je terminerai ces remerciements avec quelques mots plus personnels. Etant donné que, par sa nature, le travail de thèse déborde souvent sur la vie personnelle, je tente ici de rééquilibrer la balance en laissant déborder un peu de mon monde personnel sur mon travail de thèse. Je voudrais remercier ma mère, mon père et mon frère, havre de paix en tout temps et toute circonstance. Quand quelque chose cloche, je sais où trouver la sérénité, merci à vous. Je voudrais également remercier ma grand-mère qui, sans aucun doute, m'a transmis l'envie de faire des sciences et avec qui j'aurais aimé discuter de mon travail, elle l'aurait sans doute compris. Beaucoup de choses ont changé mais l'envie est restée. Même s'ils ne liront très probablement jamais ces lignes, je remercie les 7 fantastiques qui sont autant de points de repère dans les brumes de l'avenir et ceci depuis maintenant bien des années. Merci également à mes chères amies et chers amis qui étaient présents pendant ces années, qui l'étaient avant et le seront longtemps après, j'espère. Encore une fois, ces quelques lignes ne reflètent que très peu tout le bien que m'a apporté leur présence, quotidienne ou occasionnelle, et il m'aurait été impossible d'avancer sans eux. Merci à Nat et Clémence, Raph et Jordan (pas plus d'une fois par an, sauf quelques fois), Fabrice, Antoine, Rémy, Ludo, Loïc, Kevin, Daniel, Darius, à tous les membres de l'AFA et des petits cueilleurs d'étoiles et aux sportifs dominicaux de Maraichers. Le manuscrit qui suit ne reflète, malheureusement, absolument pas toute l'humanité qui a surgit des dernières années et qui restera pour moi la principale chose à retenir.

Introduction

This Ph.D. thesis is focused on the study of micrometeorites, that are sub-millimeter particles recovered at the Earth surface. These particles are originating from solar system small bodies, asteroids and comets, that have kept the memory of the birth of the solar system.

The solar system formed 4,6 billion years ago from the collapse of a molecular cloud into a dense core, triggered by gravitational instabilities. In the first hundreds of thousands years, the temperature and pressure increase in the center of the dense core gave rise to the proto-sun where fusion reactions started. In the meantime, under the effect of its own angular momentum, the stellar envelope formed a circumstellar disk around the proto-sun. The Sun entered the main sequence phase and within about one to tens of millions year, the material remaining within the circumstellar disk concentrated into the protoplanetary disk. Large objects (such as planets, dwarf planets and small bodies) formed at this stage by accreting debris in the protoplanetary disk. Planetary formation led to the loss of the initial composition of the protoplanetary disk through differentiation, resulting in the impossibility to probe the early phases of the solar system with planetary matter. Smaller non-differentiated bodies such as asteroids and comets are likely to have preserved pristine matter from that period.

Asteroids are principally located in the main belt, orbiting between Mars and Jupiter. They consist in rocky bodies with sizes ranging from several meters to hundreds of kilometers, from one asteroid to another. Although, the larger asteroids are likely to have undergone differentiation, most of them have escaped to it, thus preserving some of the pristine materials (for those escaping subsequent alteration by metamorphism and/or space weathering, impacts). Comets are icy objects with mixed organics and rocks, originating from further regions, beyond the Neptune orbit: the Kuiper belt and, even further, the Oort cloud. When injected in the inner regions of the solar system, the increasing temperature of their surface triggers the sublimation of the ice, leading to the ejection of cometary materials in the interplanetary medium.

The cometary and asteroidal fragments that encounter the Earth give rise to the meteorite and micrometeorite populations. While most of the meteorites sample the asteroids belt, more external regions are sampled by a part of the sub-millimeter particles such as the interplanetary dust particles (IDPs) and the micrometeorites. The study of micrometeorites provides information on the assemblage of minerals and organics present at the surface of icy bodies originating from the most remote regions of the solar system.

This Ph.D. thesis is based on the study of micrometeorites from the Concordia collection that were collected in Antarctica over the last twenty years. In the first chapter, the Concordia collection is described to introduce a comprehensive study that aimed at determining the extraterrestrial sub-millimeter flux falling on Earth. The mass fluxes and size distributions of unmelted micrometeorites and cosmic spherules are reported in the 30-350 µm diameter range. By combining our results with previous work, we inferred the global flux of unmleted micrometeorites and cosmic spherules over their entire size range and extrapolated their global annual flux on Earth. Taking into account the carbon abundances in the different types of micrometeorites form the Concordia collection, lower and upper limits of the carbon input on Earth are derived.

In chapter 2, we report H, N and C isotopic data on ultra-carbonaceous micrometeorites (UCAMMs). UCAMMs are rare carbon-rich micrometeorites that most probably formed in outer regions of the solar system. The isotopic composition of the organic matter of UCAMMs provides clues to better understand their origin. Within the course of this thesis, 5 fragments of 3 UCAMMs were analyzed by

NanoSIMS at the Earth and Planets Laboratory (Carnegie, Washington DC) in collaboration with Dr. Nittler. A new analysis of C isotopic data acquired on an UCAMM studied by NanoSIMS at MNHN and at Institut Curie prior this thesis is presented.

In chapter 3, we present experiments that aimed at synthetizing organic residues from the ion-irradiation of isotopically heterogeneous ice films. Nine refractory organic residues were produced, with a dedicated set-up (IGLIAS, developed at CIMAP), during three experimental sessions in 2019, 2020 and 2021 at the Large Collider for Heavy Ions (GANIL, France). Various ices mixtures were irradiated to simulate the Galactic Cosmic Ray interaction with the ice mantles at the surface of small bodies in the cold regions of the protoplanetary disk. The ice mixtures were isotopically heterogeneous in order to study the transmission of these heterogeneities to the irradiation-induced residue. The H, N and C isotopic compositions of the organic residues were analyzed by NanoSIMS at Institut Curie (Orsay, France). The results of these experiments are discussed within the scope of the astrophysical conditions expected in the formation regions of UCAMMs.

The last chapter is a discussion putting into perspective the results obtained in Chapter 2 and 3 aiming at proposing hypotheses on the formation of UCAMMs. The diversity of the isotopic compositions of UCAMMs is summarized and compared with other solar system objects. The formation scenario of UCAMM's organic matter is exposed. Different types of organic matter, induced by irradiation of different types of ices, are considered. Based on theoretical models from the literature, a scenario is proposed considering the condensation and irradiation of different volatile molecular reservoirs expected to be present in the protoplanetary disk. Finally, perspectives are proposed to further characterize and deepen the understanding of UCAMMs.

1 Chapter 1: The micrometeorite flux measured with the Concordia collection

1.1 The extraterrestrial matter input on Earth

The extraterrestrial (ET) matter in the interplanetary medium is composed of asteroids, comets and sub-millimeter-diameter dust. These objects are likely to fall on Earth when encountering the planet along its orbit. The frequency of the falls depends on the size of the objects, it varies over orders of magnitudes from about one large impactor of 5 km diameter each 10^7 years to about 10^7 sub-millimeter particles per day (Flynn, 2002; Plane, 2012). Over geologic time scale (> 10^6-10^7 yrs), the contribution to the ET input on Earth of rare large impactor becomes comparable to the daily input of sub-millimeter size particles (Murad and Williams, 2002; Plane, 2012). However, while the fall of a large impactor on Earth liberates huge amounts of energy, strongly altering its matter, an important fraction of sub-millimeter size particles reaches the surface with moderate alteration. Meteorites (*i.e.* centimeter to meter size objects) represent a lower contribution of the global ET input on Earth. Measuring the flux of sub-millimeter size particles thus means estimating the global amount of ET matter on Earth on short time scales (< 10^6 yrs). It specifically addresses the quantification of the exogenous material (including carbon-rich matter) input on Earth on a daily basis.

1.1.1. The extraterrestrial flux before and after atmospheric entry

Previous works have intended to measure the ET mass input on Earth driven by objects in the 10^{-9}-10^1 m diameter range (Cziczo et al., 2001; Hughes, 1992; Mathews et al., 2001; Plane, 2012; Taylor et al., 1998), leading to estimations varying sometimes by orders of magnitude (Plane, 2012). Such discrepancies are partly due to the fact that these techniques are not sampling exactly the same components of the ET flux. During atmospheric entry, an important fraction of the particles suffers severe heating due to friction forces, resulting in their complete or partial ablation. This fraction feeds the atmospheric medium in exogenous quasi-atomic elements that eventually reach the Earth' surface. Their contribution to the ET mass input is evaluated by meteor radar detection (Mathews et al., 2001), LIDAR measurements of atmospheric metal layers (Gardner et al., 2014), elemental abundances and isotope records in deep seas (Peucker-Ehrenbrink, 2001). The size distribution of ablated dust $\mathbf{D_{Abl}}$ (see *Figure 1-1*) is by definition not directly measurable. Conversely, atmospheric IDP collections, ground-based meteorite and micrometeorite collections and deep-sea sediment collections sample the size distribution $\mathbf{D_{dust}}$ (see *Figure 1-1*) of the ET flux that survived the atmospheric entry and reached the Earth's surface. Combining $\mathbf{D_{dust}}$ and $\mathbf{D_{Abl}}$ leads to $\mathbf{D_{ZC}}$ (see *Figure 1-1*), the size distribution of the Zodiacal cloud (ZC) dust at 1 A.U, before atmospheric entry. The Zodiacal cloud is made of grains formed by collisions and destructions of comets and asteroids which derive towards the Sun (e.g. Carrillo-Sánchez et al. (2016); Nesvorný et al. (2011)). A direct sampling of $\mathbf{D_{ZC}}$, outside the Earth atmosphere, is in practice not achievable in the current state of the art due to the very high relative speeds of the particles encountering Earth orbiting facilities (Carrillo-Sánchez et al., 2016; Cremonese et al., 2012; Love and Brownlee, 1993). Although Love and Brownlee (1993) estimated $\mathbf{D_{ZC}}$ by counting and measuring the particles impact craters on the Long Duration Exposure Facility (LDEF) solar panels, Cremonese et al. (2012) indicates that these results are highly sensitive to the speed and density assumptions, leading to large uncertainties (up to a factor 10 in the dust mass estimation).

Several scientific communities are interested in the determination of the size/mass distributions $\mathbf{D_{dust}}$, $\mathbf{D_{Abl}}$ and $\mathbf{D_{ZC}}$. For instance, the amount of ET carbon matter (altered and unaltered) falling on Earth is of interest for cosmochemistry and exobiology; atmospheric physicists need to constrain the exogenous elements playing a role in the atmospheric dynamics and studies on the ZC needs accurate dust distribution at 1 A.U. Stating the complexity of direct determination of $\mathbf{D_{Abl}}$ and $\mathbf{D_{ZC}}$, measurements of $\mathbf{D_{dust}}$ is a starting point to address the question of the ET matter distribution, before and after atmospheric entry.

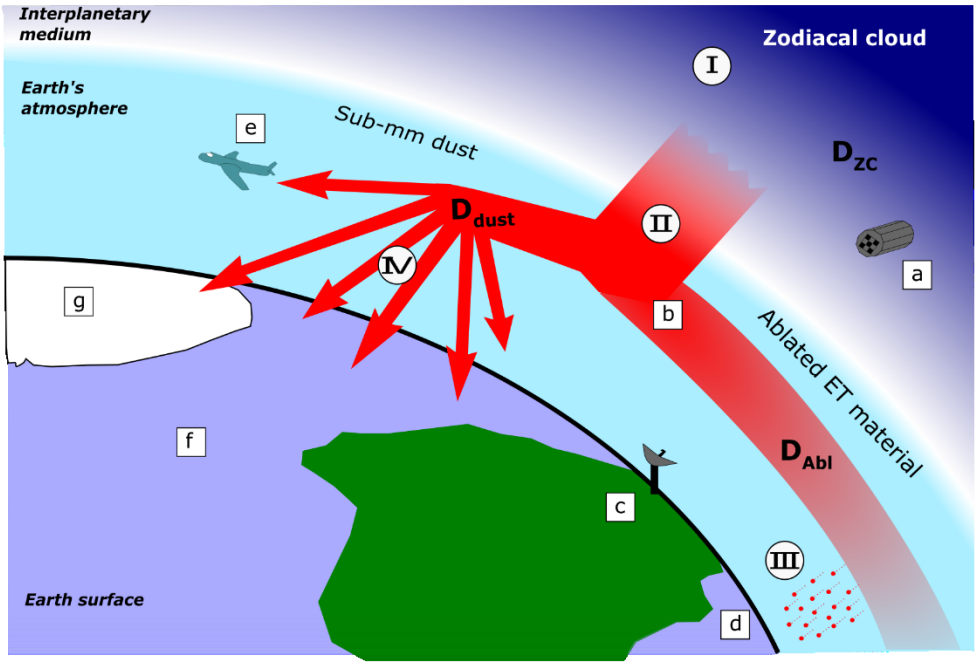

ET matter input on Earth

I The interplanetary medium is fed by dust from the cometary and asteroidal reservoirs, forming the Zodiacal cloud (ZC). Earth accretes the matter of the ZC at 1 A.U.

II When entering the Earth's atmosphere, a fraction of the interplanetary dust is ablated and remains under a quasi-atomic form in suspension in the atmosphere. The other fraction survives the atmospheric entry as sub-mm dust and falls on the Earth' surface following a free-falling motion.

III Quasi-atoms deposit at the surface and in the oceans.

IV ET sub-mm dust deposits at the Earth'surface and in the deep-seas.

ET matter distributions

D_{ZC} Mass distribution of the Zodiacal cloud (ZC) dust. Poorly constrained by the actual measuring techniques.

D_{Abl} Mass distribution of the ET matter undergoing ablation during the atmospheric entry. Not directly measurable. The total mass of the ablated population may be assessed by measuring the quantity of ET matter in quasi-atomic form in the atmosphere.

D_{dust} Mass distribution of sub-mm ET dust surviving the atmospheric entry and reaching the Earth' surface. This population is divided between thermally unaltered and altered dust.

Measuring the ET input on Earth

ZC distribution

a Hypervelocity craters on the LDEF panels (Love and Brwonlee, 1993)

Ablated dust

b Visual meteors detection

c Atmospheric metal ion layers detection (LIDAR, RADAR, satellite)

d Elemental and isotopic measurements in ice-core and deep-sea sediments

Sub-mm dust

e IDP collection by stratospheric plane.

f Spherule collection in deep-sea sediments.

g Micrometeorites and spherules collection in Antarctic ices and snows.

Figure 1-1: Schematic view of the accretion of ET matter on Earth. The atmospheric entry divides the incoming ET flux in ablated dust and sub-millimeter dust. A direct measurement of the interplanetary dust size/mass distribution D_{ZC} is model-dependent and subject to important uncertainties. The size/mass distribution D_{dust} is the one that can be directly measured.

1.1.2. Extraterrestrial dust collections

Murray and Renard (1891) reported the first collection of sub-millimeter ET particles collected in deep-sea sediments during the expedition of the *H.M.S. Challenger* ship between 1872 and 1876. The scientific team onboard the ship performed several drills of the oceanic sedimentary deposits and identified, trapped within them, a family of ET sub-millimeter spherical grains called cosmic spherules (CS). Cosmic spherule' shape is characteristic of melting occurring during the atmospheric entry. A part of the particle is ablated while the remaining mass rapidly cools down, solidifies and eventually deposits on land or on the seabed. The hardness of CSs favors their preservation from destruction and erosion at the Earth surface. Murrell et al. (1980) extracted 22 mg of CSs from 411 kg of deep-see clays from the Pacific Ocean. They estimated a CS mass flux of 90 tons.yr^{-1}, but modern works showed that this value was largely underestimated, probably due to the destruction of particles in the sediments. Taylor et al. (1998) recovered and identified several hundreds of CSs trapped into the South Pole water well (SPWW) at the Scott-Amundsen base, Antarctica. The visual aspect and the relative resistance of the CSs helped their detection. They estimated a flux of CS in the 50-700 µm diameter range of 1600 ± 300 tons.yr^{-1}.

Hints of the existence of an unmelted ET dust population were reported by Landsberg (1947), and theoretically described 3 years later by Whipple (1950). To differentiate them from CSs, they are referred as unmelted micrometeorites (uMMs). The uMMs are more fragile and can be destroyed during the deposition processes or during the collection procedure itself. As a result, that population of dust, that has experienced less alteration at the atmospheric entry, is often under-sampled by collections where ET grains are subjected to high mechanical stress (due to the environment or to the collection itself). Due to these experimental constraints, the uMM population was first reported almost a century after the identification of CSs (Maurette et al., 1989; Maurette et al., 1987; Sandford and Walker, 1985). Since the uMM visual aspect is less characteristic than that of CSs, their identification implies a more comprehensive investigation of the particles to assert their ET origin. It results in a more meticulous work of characterization for which it is mandatory to reduce the amount of terrestrial contamination that can be misled with the genuine ET particles. Therefore, uMM collections are performed in regions where the terrestrial contamination is as low as possible. Yada et al. (2004), Maurette et al. (1987), Suttle and Folco (2020) performed sub-millimeter ET dust collections in several regions of Antarctica and reported the presence of uMMs. They estimated global mass fluxes of sub-millimeter ET particles, including CSs and uMMs, exhibiting a wide range of variation from about 1,500 tons.yr^{-1} (Suttle and Folco, 2020) up to 16,000 tons.yr^{-1} (Yada et al., 2004). The origin of these discrepancies may be related to the evaluation of the corresponding accumulation time of the particles in their host matrix (see sections 1.4.1 and 1.5.1).

Interplanetary dust particles (IDPs), collected at 25 km altitude by NASA' stratospheric aircraft (Bradley, 2003) are part of the unmelted cosmic dust population available in laboratories. Their typical diameter is below 15 µm. The study of unmelted IDPs is of great interest, unfortunately their collection protocol does not allow to derive a mass flux. In addition, their small size makes them unlikely to contribute significantly to the ET sub-millimeter mass flux (see the discussion on the cut-off at low sizes in section 1.4.4)

The work presented in this chapter is based on an Antarctic collection of sub-millimeter ET particles trapped in ultra-clean snow. It aims at providing better constraints on the ET flux in the 30-350 µm diameter range for both uMMs and CSs thanks to a well-controlled collection of ET particles in this size range. The reliability of the flux measurement stands on the control of the extraction procedure and the preservation of the smaller and most fragile ET particles as detailed in sections 1.2 and 1.3.

1.2 Collection of micrometeorites in the central regions of Antarctica

The micrometeorites (MM) presented in this work were collected in the vicinity of the French-Italian CONCORDIA station at Dome C (hereafter DC), 1100 km inland on the high Antarctic plateau (75° 06'S 123° 20'E). This specific location offers unique preservation conditions for micrometeorites against aqueous alteration, and anthropic and terrestrial contaminations. The human activities in the region started in the 1990s ensuring that the layers of snow in the subsurface have remained pristine.

1.2.1. The collection protocol at Dome C

Micrometeorites falling in Antarctica are trapped within the snow that accumulates at the surface. Temperatures in the station area are ranging from -20°C to -40°C in summer and drop below -60°C in winter. These regions are among the only places where the temperature stays far below 0°C all along the year, preventing the transformation of snow into water that can alter the micrometeorites.

Figure 1-2: Dome C station in Antarctica. The base is located 1100 km inland on the Antarctic plateau.

In order to access ultraclean snow samples, 5 to 9 meters' deep trenches were dig by a Kassbohrer snow groomer. Ultraclean snow was extracted from the walls of the trenches and transported to the station in 60 liters' high-density polyethylene closed barrels. The snow was melted using a dedicated stainless-steel melter (*Figure 1-2*) combined with a 35 kW propane gas boiler that warmed the stainless-steel tank via an external water bath.

The melted snow water was sieved with a 30 µm mesh nylon filter for the 2002 (DC02) and 2006 (DC06) campaigns, and a 20 µm mesh filter for the 2016 (DC16) campaign (

Table 1-1). The filtering was made using gravity without water pumping to avoid mechanical stress on micrometeorites. The melter is a closed system and the total weight of melted snow was obtained by measuring the volume of filtered water. The total weight of each melt was ranging from 200 to 1100 kg, which represent between 2 and 7 round trips to the trench. The duration of the full operation was about 1-2 days, exceptionally 3 days in the rare cases of melts above 1000 kg. The residence time of the particles in liquid water inside the melter was ranging from a few hours up to about a day, as the water was regularly sieved to allow additional snow in. However, once trapped in the filter, the particles were still in contact with water droplets but their maximum exposure time was always less than 3 days. Most of the time the final temperature of water was between 0 and a few degrees Celsius, exceptionally above 10°C. Each melt was sieved on a single filter and extensive rinsing of the melter walls was performed to ensure maximum recovery of the particles. In some melts, the rinsing was performed directly on the same filter as the melt itself while on others the rinsing was performed on a dedicated filter. Immediately after the melting procedure, the filters were examined under a binocular microscope. For the 3 last campaigns (2019, 2016, 2014) the filters were dried under primary vacuum and kept under vacuum or N_2 inert atmosphere prior shipping back to France. All filters were

subsequently analyzed in a dedicated clean room (ISO 7) under a clean hood at CSNSM (Centre de Sciences Nucléaires et de Sciences de la Matière, now IJCLab).

Figure 1-3: Blocks of snow are extracted from a trench with clean shovels and barrels (left). The extracted snow is subsequently melted in a clean closed-system (center). The melted snow is sieved by 30 µm mesh filters (right).

1.2.2. The field campaigns at Dome C

Since the beginning of the program at Dome C, six expeditions have been performed.

Table 1-1 summarizes these field campaigns. In this work, we used the data from MMs collected during the three austral summers 2001-2002, 2005-2006 and 2015-2016 (respectively referred as DC02, DC06 and DC16).

Year	Name	Participant	Number filters	Total weight of snow (kg)	Period of stay	Trench depth (m)	Trench location
2000	DC00	J. Duprat G. Immel	-	3900	Winter 2000	0m	-
2002	DC02	J. Duprat C. Engrand	12	3620	17/01/2002 – 04/02/2002	3 - 4	(75°06’25.5’’S 123°20'39.66’’E)
2006	DC06	J. Duprat M. Gounelle	12	7636	05/01/2006 – 03/02/2006	3.3-4.3	(75°06’35.46’’S 123°20’39.66’’E)
2014	DC14	J. Duprat M. Godard L. Delauche	5	2400	14/01/2014 – 28/01/2014	5-6 m	(75°07’44’’S 123°22’6.74’’E)
2016	DC16	E. Dartois M. Godard L. Delauche	17	16598	18/12/2015 – 30/01/2016	6 - 9	(75°07'29.1’’S 123°21'42.6’’E)
2019	DC19	E. Dartois F. Fortuna S. Hervé	10	21000	13/12/2018 – 30/01/2019	7-8	(75° 07' 23.5''S 123° 21' 23.4''E)

Table 1-1: List of the expeditions at Dome C in the course of the micrometeorite @ DC program.

Figure 1-4 shows the locations of the DC extraction sites around the Concordia station. The DC02 site was located 600 m to the south of the station at GPS coordinates (75°06’25.5’’S 123°20'39.66’’E). Twelve melts were performed with snow extracted at 3-4 m depths in the trench. The DC06 extraction

site was in the same zone as DC02 but 300 m further to the south (75°06'35.46''S 123°20'39.66''E). Thirteen melts were achieved with snow samples extracted between 3.3-4.3 m deep in the trench. The trace of the trench has been captured on a satellite image, the January 25th, 2006 (Google Earth, *Figure 1-4*). In 2014, 2016 and 2019, the trenches were done in another zone, at about 3 km from the station, at the South West of the plane landing runway. The snow of the 14 melts of DC16 were extracted 2500 m to the south of the station (75°07'29.1''S 123°21'42.6''E) at depths ranging from 6 to 9 meters.

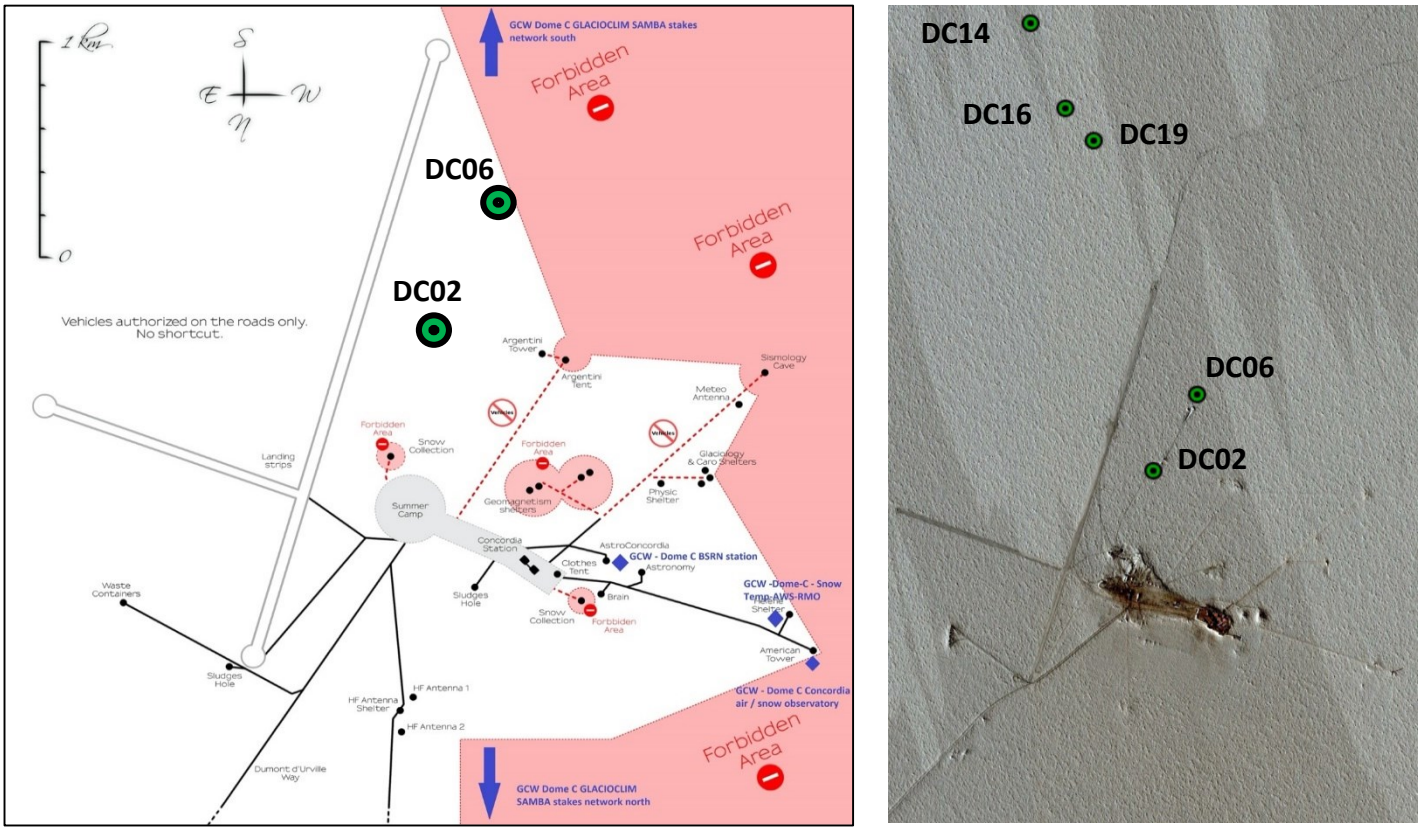

Figure 1-4: Map (left) and satellite image (right) of the Dome C station surroundings. Black and green dots indicate the sampling location of the DC field campaigns. The satellite image (right) was captured the 13th of January, 2006, the DC06 trench is visible but not DC14, DC16 and DC19 that performed later.

Among all melts, most were not suitable to perform flux measurements due to issues during the collect itself, the particle extraction protocol or, in most cases, to incomplete sorting. We first selected a set of 23 melts available to perform a first flux estimation, we then further restricted that set (see section 1.4.3).

1.3 The CONCORDIA collection

For more than a decade, the filters were examined under a binocular microscope, in the clean room at CSNSM/IJCLab, Orsay, France. Particles were manually extracted using dedicated fine brushes. The main contaminants observed in the filters were fibers from polar clothes and gloves, plastic chips from the barrels and from the tools used to extract and transport the snow. These contaminants were easily identified and removed during the filter sorting procedure.

1.3.1. The different types of micrometeorites

Optical images of all extracted particles were taken and both their longest (a) and shortest (b) dimensions were documented. From these values, we derived, for each particle, an equivalent diameter, D_{eq}, and an asymmetry factor, As, to quantify the geometry of the extraterrestrial particles. They are defined as:

$$D_{eq} = (a \times b \times b)^{\frac{1}{3}}$$

$$As = \frac{b}{a}$$

D_{eq} accounts for the mean diameter of a particle whereas As is a proxy of its spherical shape. Spherical particles have As = 1 and D_{eq} is their effective diameter. Non-spherical particles are characterized by As < 1. The mesh size of the filters was 30 µm for DC02 and DC06, and 20 µm for DC16, however some particles with D_{eq} slightly smaller than these mesh sizes were retrieved due to their non-spherical geometry and/or trapping within the textile fibers present in the filters.

After extraction from the filters, all the extraterrestrial particles were classified into two main categories: unmelted micrometeorites (uMMs) and cosmic spherules (CSs). uMMs were subsequently fragmented with a needle or a thin scalpel blade and a fragment was deposited on a conductive carbon tape mounted on a one-inch aluminum stub for analytical scanning electron microscopy (SEM-EDX). Cosmic spherules (CSs) were mounted on carbon tape without fragmentation. All CS and uMM fragments were analyzed with a SEM equipped with secondary (SE) and back-scattered electron (BSE) detectors and an Energy Dispersive X-ray spectrometer (EDX) to determine their major elemental composition patterns and assess their terrestrial or extraterrestrial origins. The types of uMM differ by their chemical and textural compositions. Examples of the various kinds of micrometeorites are displayed in *Figure 1-5*.

The uMMs were then subdivided into 5 types:

- Fine grain compact (FgC).
- Fine grain fluffy (FgF).
- Crystalline (Xtal).
- Scoriaceous (Sc).
- Ultra carbonaceous micrometeorites (UCAMM).

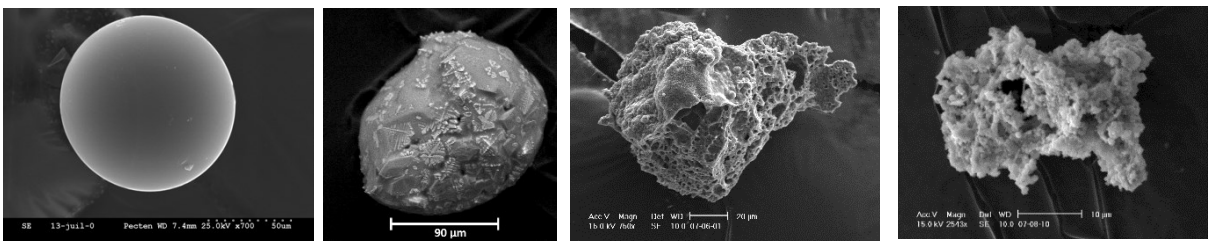

Figure 1-5: Cosmic spherules and unmelted micrometeorites from CONCORDIA collection (SEM images). From left to right: glassy cosmic spherule, stony cosmic spherule, partially melted (scoriaceous) micrometeorite, unmelted fine-grained micrometeorite.

1.3.2. Mass densities

MMs consist in an aggregation of phases with different densities: organic matter, silicates, oxides, … Their individual densities can substantially vary between values ranging from <1 to 3-4 depending on the various proportion of these phases and the porosity of the particle.

Weighing individual grains with size lower than about 100 µm requires a dedicated experimental apparatus and implies a substantial risk of losing samples. These measurements were unfortunately out of our capabilities. As weighting each individual grain could not be performed, this work relied on D_{eq} measurements and consider an average mass density for the grains. We considered the melted (CS) and unmelted (uMMs) particles separately, taking for each subset an average density inferred from previous studies.

The individual CS masses were estimated assuming an average density of 3.0 g.cm^{-3} (Murrell et al., 1980). Although, Yada et al. (2004) differentiated S- and G-type spherules (3.0 g.cm^{-3}) from I-type spherules (5.0 g.cm^{-3}), I-type spherules represent a minor proportion of the CS population and do not account significantly in the total mass estimation.

Different average densities have been reported for unmelted extraterrestrial particles originating from space-borne, stratospheric and Antarctic collections (*Figure 1-6*). In their detailed study of Antarctic micrometeorites (AMMs), Yada et al. (2004) reported an average density of 1.0 g.cm^{-3} for unmelted particles from the mass and the apparent volume of 2 groups of 15 and 30 AMMs, measured with a microbalance and SEM images. The GIADA instrument onboard Rosetta measured the mass and the cross section of cometary dust ejected from the comet 67P-Churyumov-Gerasimenko thanks to the combination of a microbalances system and a laser (Fulle et al., 2016). From the data collected, and by taking into account different shapes of the grains, they estimated an average cometary dust mass density of about 0.8 g.cm^{-3}. Individual interplanetary dust particles collected in the stratosphere by NASA (IDPs) exhibit densities ranging from 0.6 up to 4.2 g.cm^{-3} depending on their compact or fluffy nature (Joswiak et al., 2007). The technique used to derive these values is detailled in Love et al. (1994): EDX spectra were used to quantify the relative elemental abundances within a grain. Subsequently, a numerical model asserted the weigh percentage of major elements. The absolute mass of Fe was measured using the Fe Kα X-rays and led to the absolute mass of the grain. Grains' volume were estimated from SEM images. The authors indicates that such a technique was likely to underestimate the weight of grains made of light elements as EDX spectra fail to detect them.

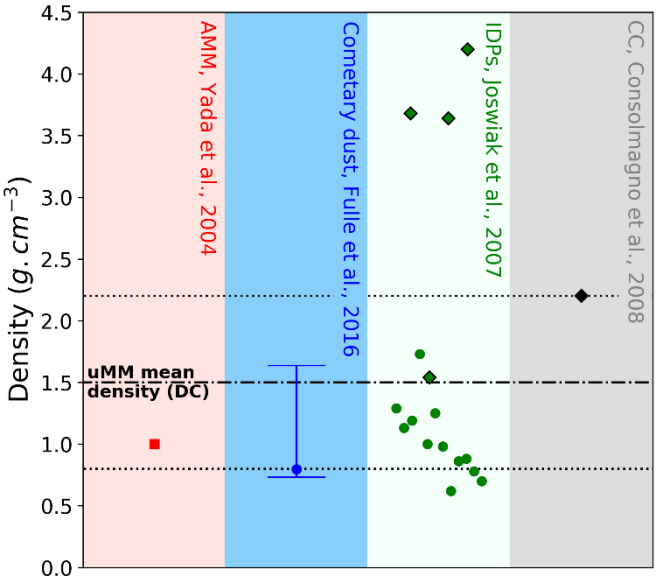

Figure 1-6: densities reported in previous works for unmelted cometary and asteroidal grains including AMM (Yada et al., 2004, in red), cometary dust from 67P Churyumov-Gerasimenko (Fulle et al., 2016, in blue), stratospheric IDPs (Joswiak et al., 2007, in green) and carbonaceous chondrites (CC, Consolmagno et al., 2008, in grey). The uMM mean density adopted for this work is indicated by the black dash-dotted line. Upper and lower dotted lines represent the extreme densities expected in the case of a chondritic composition and a cometary composition respectively.

The range of densities reported in genuine interplaneray material provides clues for identifying their asteroidal or cometary origin (Consolmagno et al., 2008). Unmelted particles originating from the cometary reservoir most probably have higher porosity, *i.e.* densities around 0.8-1.0 g.cm^{-3}, while those originating from the asteroidal reservoir have lower porosity and an average densitity close to that reported for cabonaceous chondrites, i.e. 2.2 g.cm^{-3} (Consolmagno et al., 2008; Flynn and Sutton, 1991; Joswiak et al., 2007; Love et al., 1994).

In the following, we considered an average density of 1.5 g.cm^{-3} for uMMs, intermediate between these two end-members. This average density is slightly higher than that used by Yada et al. (2004), in agreement with the fact that we include partially melted grains in the set of uMMs particles. The uncertainties related to the range of possible densities will be included in the discussion on the flux of uMM in section 1.5.1.

1.4 Measurement of the micrometeorite influx

1.4.1. The exposure parameter *S*

To estimate a micrometeorite flux at the Earth surface, one has to determine the time during which the particles accumulated on a given surface. When extraterrestrial particles are trapped in a host matrix (sediments, snow,…), it is mandatory to control the quantity of the host matrix and its growth rate at the age of the fall in order to infer the corresponding exposure parameter *S*, expressed in m².yr. *S* is an area-time product representing the accumulated quantity of host matrix trapping the particles (Peucker-Ehrenbrink et al., 2016). The number of micrometeorites per m^2.yr is intrinsically low, and subject to alteration and rapid dilution into terrestrial counterparts. Most collections involve rather small surface exposed for rather long periods of time (see *Table 1-2*) for which it is not trivial to precisely determine the total exposure parameter and/or to accurately control its related uncertainties.

In the case of micrometeorites collected in deep-sea sediments, the low growth rate of the host matrix implies that a small volume of sediments might represent a high *S*. For instance, Prasad et al. (2013) extracted two volumes of deep sea sediments $V_{1,sed}$ = 50×50×15 cm^3 and $V_{2,sed}$ = 250×250×15 cm^3 and assumed a growth rate of $3 \cdot 10^{-6}$ *m.yr^{-1}*, resulting in two exposure parameters $S_{1,sed}$ = 12,500 *m^2.yr* and $S_{2,sed}$ = 312,500 *m^2.yr*. In such conditions, the micrometeorites trapped in the sediments have accumulated over a 50,000 years' period. Particles that remain exposed to the deep sea environment for a long period of time undergo alteration and destruction (for the most fragile) involving a bias in the flux estimation (Genge et al., 2020). As a consequence, a high exposure parameter based on a large period of time have to be considered carefully since it might come with an under-sampling of the particles. By contrast, a high exposure parameter based on a short period of time and a large sampled surface is more relevant for a flux measurement.

Micrometeorite collections in ancient marine limestone (Martin et al., 2018; Schmitz et al., 2019) are subject to the same constraints as deep-sea collections. Extraterrestrial particles trapped in the limestone have accumulated over 10^4 to 10^5 years' period of time with typical sedimentation rates of about 10^{-6} to 10^{-7} *m.yr^{-1}* (Schmitz et al., 2019). Although a loss of a significant part of the flux may occur as proposed by the authors, the remaining ET material allows studying the flux variations over large periods of time as well as relative abundance of ET grain families contributing to the flux.

Antarctic sediment traps are also reported in the literature as micrometeorites' accumulation sites where the particles are focused under the action of winds. The traps in the Transantarctic Mountains (Rochette et al., 2008; Suavet et al., 2009; Suttle and Folco, 2020) and in the Sør Rondane Mountains

(Goderis et al., 2020) consist in relatively small areas (0.5 m² in Suttle and Folco (2020)) in which terrestrial and extraterrestrial dust have piled up over extended period of time, ranging from 0.8 to 3 Myr. The weak constraints on the accumulation times of the sediments lead to important uncertainties on the exposure parameter, which eventually affect the flux estimation. For instance, Suttle and Folco (2020) mentioned an *S* ranging from $0.4 \cdot 10^6$ to $1.15 \cdot 10^6$ m².yr that introduce a factor 3 error on the flux measurement.

Collections of magnetic ET dust in urban environment (Genge et al., 2017) presumably fall under the same considerations with gutters playing the role of the sediment trap (Genge et al., 2020). Although the processes of accumulation of dust is similar, the time periods of deposition differ greatly, being estimated to less than 6 years for the urban collections (Genge et al., 2017). Nevertheless, the exposure parameter is again not straightforward to derive. To date, no absolute micrometeorite fluxes have been derived from urban micrometeorite collections.

Yada et al. (2004) and Maurette et al. (1991) extracted cosmic spherules and unmelted micrometeorites from volumes of blue ice fields, in Antarctica. The blue ice fields are formed from the encounter of a drifting glacier and geological obstacles as mountains. In such areas, the ice of the glacier shows on the surface where it is exposed to erosion and sublimation (Yada et al., 2004). Sublimation of the ice layers reveals the extraterrestrial particles trapped across the years. Yada et al. (2004) estimate that the age of the ice from which they collected micrometeorites ranges from 33 to 27 kyrs, also mentioning the existence of a delay of about 2000-6000 years between the fall of the snow and its transformation in ice. Such extended time periods introduce uncertainties on the exposure parameter associated with blue ice field collections of micrometeorites. Measurements of the oxygen isotopes in air bubbles of ice cores allow at most a 6 kyr precision on the actual age of the ice, leaving unaddressed the determination of the snow accumulation rate at the time of the micrometeorites fall (Yada et al., 2004). Although blue ice fields collections shed light on the ancient micrometeorite input on Earth, the processes of the ice evolution and the lack of information on the accumulation rate of the snow at the age of the fall make the exposure parameters very hard to determine precisely.

The collections of ET particles in Antarctic snows intrinsically allow more precise constraints on both the accumulation rate of the host matrix and the exposure parameter due to the young age of the snow by comparison with the ice and the sediments. By its less compressed structure, snow enables an accurate dating of the age of fall of the micrometeorites. Taylor et al. (1998) estimate that the CSs of the SPWW collection fell on Earth between 1000 and 1600 AD. The complexity of the South Pole water well's geometry and the water flows prevent to unambiguously assert the exact surface of collection and the related exposure parameter can thus be subjected to uncertainties.

In this work, uMMs and CSs collected near Dome C were trapped in snows from 3-9 m depths. The spatial configuration of the collection area (*i.e.* a flat area) prevent confusion in the original location of the falls. The snow accumulation rate R_{snow} in the region of the collect is a mandatory parameter in order to estimate the age of fall of the micrometeorites. Previous articles on the micrometeorite flux at Dome C (Duprat et al., 2006; Duprat et al., 2001; Engrand et al., 2017; Rojas et al., 2019) have considered an average R_{snow} of 3.5 g.cm^{-2} reported by Petit et al. (1982). This value was measured at (74°39'S, 124°10'E), 55 km away in the North-East direction from the actual Dome C station, using rather limited methods (see Petit et al. (1982)). More recent studies based on the analyses of ice cores sampled at Dome C (Frezzotti et al., 2005; Le Meur et al., 2018) indicate values ranging from 2.6 to 2.8 g.cm^{-2}.yr^{-1} over the last century.

In the present work, we considered an average value of R_{snow} = (2.7±0.1) g.cm^{-2}.yr^{-1} to convert the masses of snow into exposure parameters, in order to compute the micrometeorite flux. In addition, by considering a snow density equal to ρ_{snow} = 300 kg.m^{-3}, we derived a snow level growth rate of:

$$f_{snow} = \frac{R_{snow}}{\rho_{snow}} = 0.09\ m.yr^{-1}$$

f_{snow} allows to estimate the ages of fall of the extracted snow samples, thus, that of the micrometeorites therein. All of CSs and uMMs are thought to have fallen between 1920 and 1980. *Table 1-3* summarizes the exposure parameter *S* for each melt. They are derived from the mass of snow in a melt M_{melt} (g) and the accumulation rate R_{snow} (g.m^{-2}.yr^{-1}) by :

$$S = \frac{M_{melt}}{R_{snow}}$$

The small uncertainties on the weighed masses of snow, the good constraints on the snow accumulation rate at Dome C and the limited time (i.e. depth) extension of the collection sampling leads to an unprecedented control on the exposure parameter. Such result can be achieved thanks to the existence of a young host matrix. In section 1.6, we discuss the impact of the exposure parameter on an extraterrestrial flux measurement.

Table 1-2: Summary of the characteristics of micrometeorite flux measurements reported in the literature adapted from Suttle and Folco (2020). The result from this work are presented in the last column (Rojas et al., 2021). The flux derived from the Concordia collection do not take into account the extrapolation made for CSs with the SPWW data (see section 1.5.1).

References	Prasad et al. (2013)	Schmitz et al. (2019)	Suttle and Folco (2020)	(Genge et al., 2017)	Yada et al. (2004)	Taylor et al. (1998)	Rojas et al. (2021)
Collection type	Deep sea sediments	Ancient marine limestone	Sediment trap	Urban trap	Blue ice fields	Snow of the South Pole water well	Subsurface Antarctic snow
Exposure parameter ($m^2.yr$)	12,500 – 312,500	-	$0.4 \cdot 10^6$ - $1.15 \cdot 10^6$	$1.8 \cdot 10^5$ -$1.5 \cdot 10^6$	13 - 93	6500 - 8200	89 - 132
Host matrix growth rate ($m.yr^{-1}$)	$3 \cdot 10^{-6}$	10^{-6} – 10^{-7}	-	-	0.15 *(at the time of the fall)*	_	0.09
Estimated duration of the accumulation (yr)	50,000	10^4 - 10^5	10^6	6 - 50	6000	450	60
Flux ($tons.yr^{-1}$)	160 ± 70	-	1550 ± 750	_	15,000 ± 10,000	1,600 ± 300	4,400 ± 1,300 *(DC data only)*
Time period sampled	50,000 B.C. - present	Various	3,000,000 – 800,000 B.C.	1960 A.D. - Present	33,000 – 27,000 B.C.	1000 – 1500 A.D.	1920 – 1980 A.D.

1.4.2. Collection efficiency *Q*

We defined *Q*, the efficiency of collecting the particles within a filter during a melt. *Q* was monitored by introducing in the inner tank, before the snow-melting, a given number of colored terrestrial sand and glass particles of two size ranges: 50-100 µm and 100-400 µm. The colors were different from one melt to another and between the two size ranges in order to identify possible size dependence in the collection efficiency as well as possible mixing between consecutive melts in the case of incomplete rinsing. These colored particles were recovered and counted during the extraction procedure in the clean room, in France. The inferred average *Q* for these two size ranges was found to be *Q* = (90±10) % with no significant variations from one melt to another or between the two size ranges. This high *Q* was obtained by virtue of the design and polishing of the melter walls, and the extensive and careful rinsing of the overall apparatus after each melt. We systematically divided the number of micrometeorites recovered per melt by *Q* in order to infer the actual number of particles in the melt.

1.4.3. Melts selection

In order to achieve the extraterrestrial flux estimation, we selected a subset of melts appropriated for the study. Let us consider the number and mass of reference of extraterrestrial particles per liter of snow, n_{ref} and m_{ref}.

The 23 melts listed in the *Table 1-3* were ranked according to the 3 following parameters (*Figure 1-7*):

- The exposure parameter.
  A low exposure parameter (S < 20 $m^2.yr$) implies a small amount of extraterrestrial particles (typically < 0.05 kg^{-1}) collected and so a large statistical error on both the number and total mass of particles from the melt (see section 1.6.1).
- The numbers of extraterrestrial particles per kilograms of snow *n*.
  It has to be compared to the exposure parameter. Melts with similar exposure parameters (greater than 20 $m^2.yr$) are expected have *n* values clustering around an average value with a dispersion related to statistical variations. However, some melts can have substantially lower *n* value due to an incomplete sorting of the filter.
- The mass of extraterrestrial particles per kilograms of snow *m*.
  This parameter is the mass influx we want to measure. We expect that melts with increasing exposure parameters will converge on the m_{ref} value.

For unbiased melts with S > 20 $m^2.yr$, *m* and *n* are not expected to be greater than m_{ref} and n_{ref}. However, the two proxies are not equivalent as *n* depends on the size cut-off at low size during the searching procedure. The examination of one filter takes weeks and is often performed sequentially by different persons. Therefore, all filters were not examined with strictly the same efficiency. The important point is to maximize the number of particles recovered in the size range that is contributing the most to the mass flux.

The smaller the particle, the harder to identify and extract. We thus expect that the relative number of particles per kg in the smallest size range (i.e. < 40 µm) may exhibit substantial variation as some filters may have been better checked than others. However, these potential large variations in *n*, may not affect significantly the mass per kg as long as the contribution of these tiny grains remains low. In the following we show how we manage these potential issues. We treated CSs and uMMs separately in the 23 melts of the dataset and the properties of the selected melts are shown in *Figure 1-7*.

We selected the same melts for CSs and uMMs and we added one additional melt for uMMs, in which uMMs turned out to be fully extracted. For the CSs, the 3 selected melts, DC06-07, DC06-08 and DC06-09, share similar m (≈0.16 $\mu g.kg^{-1}$) and n (≈0.14 L^{-1}). One other melt, DC06-04, presents lower $m=0.09\ \mu g.kg^{-1}$ and $n=0.07\ L^{-1}$ and was thus considered not fully counted. The 4 selected uMMs melts, DC06-07, DC06-08, DC06-09 and DC06-11, displayed more spread values of m and n, ranging from 0.7 to 0.14 $\mu g.kg^{-1}$ and 0.7 to 0.33 L^{-1} respectively. This wider variation is attributed to the difficulty to identify and collect uMMs in a filter due to their non-spherical shape, in comparison to the CSs. The selected dataset is referred as the dataset #1. In total, the selected set contains 657 uMMs and 328 CSs.

Besides these selected melts in which the particle extraction was exhaustive, we recovered many CSs and uMMs from the 19 other melts. The collection protocols from these melts were identical to those of the selected melts. From these 19 additional melts, we extracted 480 CSs and 623 uMMs (see *Table 1-3*). The average number of particles per kg of snow in these additional melts was lower than that found in the selected melts mentioned above, due to incomplete scanning of the filters. However, the size distribution of particles within these additional melts was found compatible with that of the selected melts, indicating that there was no significant size bias between the two sets of data (dataset #1 and additional). We used the dataset #1 to infer the absolute value of the fluxes, and the complete set of data (dataset #1 + additional melts) to infer the global size and mass distributions. The global mass influx distributions were then normalized to the absolute values of the flux inferred from the selected melts.

For the uMM and CS selected melts, the average exposure parameters and masses of particles per kilograms of snow are: $<S_{uMM}>$ = 33.0 m^2.yr, $<m_{uMM}>$ = 0.103 µg.kg^{-1} and $<S_{CS}>$ = 22.4 m^2.yr, $<m_{CS}>$ = 0.163 µg.kg^{-1}. If one computes the total m and n obtained by summing the selected melts of uMM and CS separately (*i.e.* as if the selected melts were 2 global melts of uMMs and CSs), one gets similar values: S_{uMM} = 131.9 m^2.yr, m_{uMM} = 0.107 µg.kg^{-1} and S_{CS} = 89.6 m^2.yr, m_{CS} = 0.162 µg.kg^{-1}.

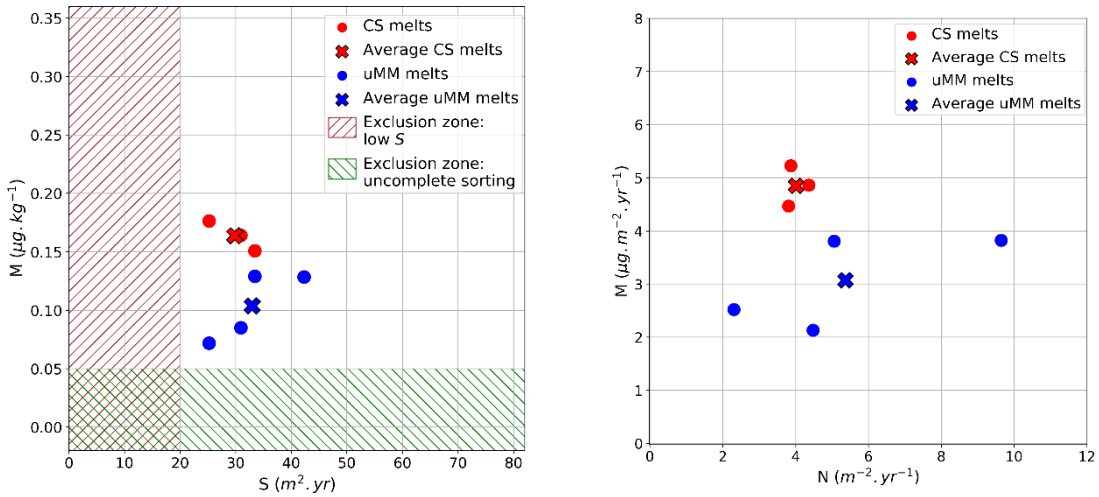

Figure 1-7. Melt selection graphics. Left, total mass of uMMs (blue dots) and CSs (red dots) per kg of snow M plotted against the exposure parameter S for the melts forming the selected dataset. Each point stands for a single melt. CSs and uMMs are treated separately. The exclusion zone in dashed brown (left) indicates the region where S is too low (< 20 m².yr) to perform an accurate measurement. The exclusion zone in green (bottom) indicates the region where M is significantly lower (< 0.05 µg.kg^{-1}) than its average value (0.163 and 0.103 µg.kg^{-1} for CSs and uMMs respectively) confirming the incomplete extraction/identification of the particles in the filters. The average <M>, average<S> and total S are reported as colored crosses. Right: mass flux (µg.m^{-2}.yr^{-1}) versus abundance flux (particles.m^{-2}.yr^{-1}) for the selected melts of CS and uMM, corrected from Q. These fluxes are derived from the sum of the mass in the melt divided by the exposure parameter.

	Date (mm/dd)	Name	N_{uMMs}	N_{CSs}	M_{uMMs} (µg)	M_{CSs} (µg)	Mass of snow (kg)	S (m^2.yr)	n_{uMMs} (part.kg^{-1})	n_{CSs} (part.kg^{-1})	m_{uMMs} (µg.kg^{-1})	m_{CSs} (µg.kg^{-1})	Flux (µg.m^{-2}.yr^{-1})		Selected melts
2006	01/14	DC06-04	59	42	14	43	639	23.7	0.092	0.066	0.022	0.067	-		NO
	01/16	DC06-05	63	50	4	44	384	14.2	0.164	0.130	0.010	0.115	-		NO
	01/19	DC06-07	103	89	49	120	681	25.2	0.151	0.131	0.072	0.176	2.1	5.2	**YES**
	01/21	DC06-08	65	123	71	136	835	30.9	0.078	0.147	0.085	0.163	2.5	4.8	**YES**
	01/23	DC06-09	294	116	116	136	903	33.4	0.326	0.128	0.128	0.151	3.8	4.6	**YES**
	01/26	DC06-10	33	31	9	27	721	26.7	0.046	0.043	0.012	0.037	-		NO
	01/27	DC06-11	195	0	146	0	1142	42.3	0.171	0	0.128	0	3.8	-	**YES (only uMMs)**
2002		DC02-01	6	6	6	11	304	11.3	0.020	0.020	0.020	0.036	-		NO
		DC02-02	4	8	2	17	206	7.6	0.019	0.039	0.010	0.083	-		NO
		DC02-03	20	16	16	41	283	10.5	0.071	0.057	0.057	0.145	-		NO
		DC02-04	15	17	52	31	280	10.4	0.054	0.061	0.186	0.111	-		NO
		DC02-05	5	7	4	12	195	7.2	0.026	0.036	0.021	0.062	-		NO
		DC02-06	28	21	28	15	608	22.5	0.046	0.035	0.046	0.025	-		NO
		DC02-07	37	35	9	70	257	9.5	0.144	0.136	0.035	0.272	-		NO
		DC02-08	31	17	34	22	170	6.3	0.182	0.100	0.200	0.129	-		NO
		DC02-09	49	21	22	23	212	7.9	0.231	0.099	0.104	0.108	-		NO
		DC02-10	57	23	17	28	408	15.1	0.140	0.056	0.042	0.069	-		NO
		DC02-11	18	12	14	17	455	16.9	0.040	0.026	0.031	0.037	-		NO
		DC02-12	14	16	3	35	242	9.0	0.058	0.066	0.012	0.145	-		NO
2016	01/06	DC16-06	8	1	2	3	1244	46.1	0.006	0.001	0.002	0.002	-		NO
	01/08	DC16-08	64	120	32	166	1530	56.7	0.042	0.078	0.021	0.108	-		NO
	01/14	DC16-11	30	10	33	1	2111	78.2	0.014	0.005	0.016	0.000	-		NO
	01/20	DC16-14	83	25	67	41	1983	73.4	0.042	0.013	0.034	0.021	-		NO

Table 1-3: List of individual melts forming part of the dataset used in this work. Individual mass fluxes are indicated for the selected melts. They are given by the sum of the particles mass divided by the exposure parameter S and the collection efficiency Q.

1.4.4. Flux size and mass distributions

The size distributions of uMMs and CSs from the complete data set are reported in *Figure 1-8*. The uMMs and CSs exhibit a maximum flux in number of particles at D_{eq} = 50 µm. The cumulative size distributions and mass fraction derived from the overall data set are also shown in *Figure 1-8*. Both size and mass cumulative distribution exhibit a strong decrease with the equivalent diameter, but a single power law cannot describe them over the entire interval in size reported. The cumulative distributions of uMMs and CSs can be approached by a function $f = b \cdot {D_{eq}}^{-a}$ between 80 and 200 µm with a_{uMM}= -3.2 and a_{CS} = -2.9 for uMM and CS respectively.

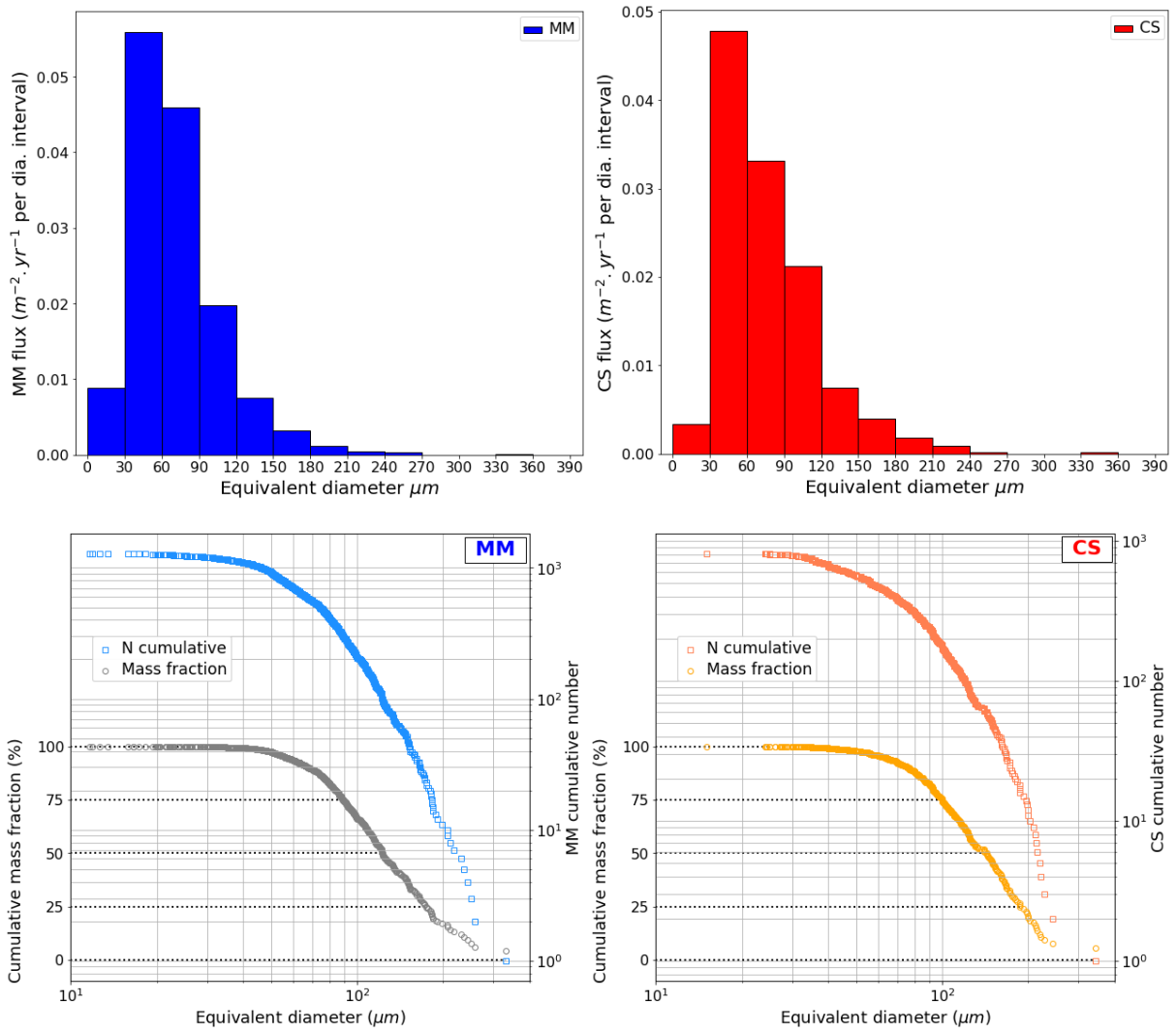

Figure 1-8: Histograms of MMs (blue) and CSs (red) size distributions using equivalent diameter bins of 30 µm (top panels). Cumulative number and mass distributions of MMs (blue and grey) and CSs (red and orange) (bottom panels). The numbers are reported on the right vertical axis and mass fractions on the left vertical axis

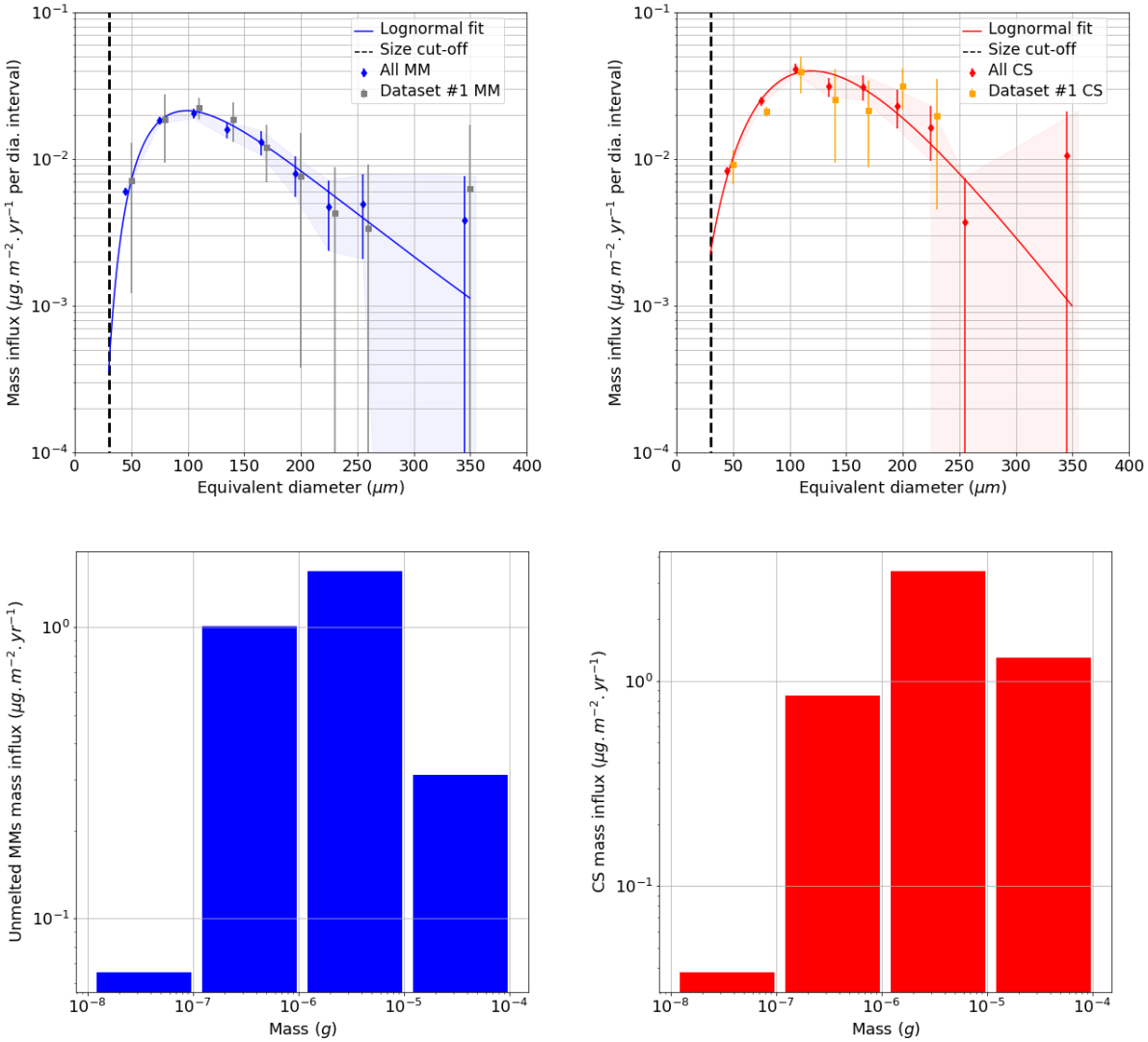

Figure 1-9: (top panels) Size and Mass distributions for MMs (left) and CSs (right) given as mass influxes using 30 µm bins in equivalent diameter and logarithmic bins in mass. The sizes distributions of MMs and CSs from the selected melts (Dataset #1) are reported in grey and orange symbols, and that considering the full dataset in blue and red symbols. The uncertainties of the MM and CS size distributions of the full dataset are outlined in the shaded areas. (bottom panels) Mass distributions for MMs (left) and CSs (right) deduced from the full dataset.

In *Figure 1-9*, we report the uMM and CS mass influx distributions from the selected melts (dataset #1) and the complete dataset using 30 µm diameter bins (in the upper panels of *Figure 1-8*, grey and orange squares for the selected melts, and blue and red for the complete dataset) along with their fits assuming log-normal laws. The shape of the particles' size distribution of the complete data set is compatible with that of the selected melts data (dataset #1), confirming the absence of significant size bias due to the incomplete sorting the filters in the complete data set.

The mass fluxes derived from the integration of the fit of dataset #1 points by log-normal laws are equal to 2.7 $\mu g.m^{-2}.yr^{-1}$ for uMMs and 5.2 $\mu g.m^{-2}.yr^{-1}$ for CSs. These values, which are corrected from *Q*, provide the absolute mass flux within the diameter range where these measurements were performed, i.e. between 30 to 240 µm. We used these absolute values to normalize the log-normal

laws fitted on the complete dataset (in the D_{eq} = 30 and 240 µm range). Data points from the selected and complete data sets are reported in Table 1-4.

Taking these normalized log-normal fits and assuming that their behavior stays relevant below and above the measured interval of the dataset (30 -350 µm), one can deduce the global mass flux over a broader size range. Considering a lower cut-off at 12 µm and an upper cut-off at 700 µm, the inferred global values for uMMs and CSs are Φ_{uMM} = 3.0 ± 1.0 µg.m^{-2}. yr^{-1} and Φ_{CS} = 5.7 ± 1.5 µg.m^{-2}. yr^{-1}, respectively (see Table 1-4). The errors are derived assuming that the number of influx particles follows Poisson statistics.

The mass distributions of uMMs and CSs respectively reach their maxima at D_{eq} = 100 µm and D_{eq} = 120 µm. These sizes correspond to uMMs and CSs of masses around 0.8 and 2.7 µg (*Figure 1-9* bottom panels). For masses above 10 µg, uMMs contribute 10 times less than CSs to the mass influx. The total mass is not sensitive to the broad cut-off considered here (12 -700 µm) as long as their values are chosen sufficiently far from the mass distribution maxima. If one restricts the integration to the range in which particles are actually recovered in the complete dataset, i.e. from 30 µm to 350 µm, the mass influxes are respectively 3.0 ± 1.0 µg.m^{-2}.yr^{-1} and 5.6 ± 1.5 µg.m^{-2}.yr^{-1} for uMMs and CSs, i.e. about 2% lower than the total mass flux inferred from the normalized log-normal fit over the whole size range for CSs (12-700 µm).

As detailed in Table 1-4, about 75% of the uMMs and CSs in the CONCORDIA collection are within the 30-100 µm size range, but they account for less than 30% of the mass influx. uMMs and CSs with diameters ranging from 100 up to 200 µm account for 15% to 20% of the total numbers of particles, but represent about half of the total mass influx. Finally, particles with D_{eq} > 200 µm are rare (a few % in numbers) but their contribution to the mass influx is still significant, close to 20%. Due to their scarcity, the uncertainties on the contribution of these large particles to the mass influx are higher compared to those in the 30-100 µm range.

At their entry in the terrestrial atmosphere, the meteoroids of large size/mass tend to reach higher temperature than the small ones. That effect becomes pronounced for particles with diameters above a few 100-200 µm. As a result, the proportion of CS is expected to dominate the mass flux in a size range that is not well sampled by our measurement (i.e. > 200 µm). The Concordia Collection allows having an accurate control on the absolute flux over a limited size range that is relevant for uMM but not for CS at sizes above 200 µm (because of their too low statistics). The extrapolation of the global CSs flux for particles at size above 200 µm is thus expected to be less accurate and probably tends to underestimate their actual proportion. By contrast, other collection such as that performed in SPWW is expected to have an accurate control on the shape of that distribution for sizes ranging from 200-300 µm up to about 700 µm (Taylor et al., 1998). We show below, that a global CS mass flux can be deduced from the gathering of these two complementary measurements (see section 1.5.1).

D	< 30µm		30µm - 100µm		100 µm - 200µm		> 200µm		TOTAL	
	Dataset #1	*All*	*Dataset #1*	*All*	*Dataset #1*	*All*	*Dataset #1*	*All*	*Dataset #1*	*All*
N_{CS}	5	23	264	614	55	160	4	11	328	808
N_{uMM}	18	79	532	997	102	194	5	10	657	1280
M_{CS} (µg)	< 1	1	112	292	228	624	67	224	407	1141
M_{uMM} (µg)	< 1	1	126	243	144	357	65	116	335	717
Flux with efficiency correction ($\mu g.m^{-2}.yr^{-1}$)									**30–240 µm**	**12-700 µm**
Φ_{CS} (fit)	< 0.1		1.3		3.3		1.1		5.2	$5.7^{\dagger}$ /7.1^{*}
Φ_{uMMs} (fit)	< 0.1		0.9		1.5		0.6		2.7	3.0

*Table 1-4: Numbers and mass of uMMs and CSs extracted from selected melts (Dataset#1) and from the complete data set (All) in 3 different size ranges (<30 µm, 30-100 µm, 100-200 µm, > 200 µm). The 2 last rows indicate their corresponding contributions to the mass flux, taking account of the collection efficiency (see text). Particles in the 100-200 µm size range make the highest contribution to the mass flux. The uMM and CS distributions from the complete data set are normalized to the selected data set between 30 and 240 µm in diameter. The inferred total mass influx from both uMMs and CSs in the 30-240 µm range and on a global range (12 - 700 µm) are reported in the last columns. For CSs, we indicate their mass influx considering the Dome C data alone (noted †) and that (noted *) considering the merging of the distribution from this work with that from the SPWW collection (Taylor et al.) for diameters > 200 µm (see section 1.5.1).*

1.5 Discussion

In this section, the results obtained with the CONCORDIA Collection are compared with previous works on similar collections from Antarctica (*Figure 1-10*). The global flux of CS is deduced over the (12 – 700 µm) range by combining the results from this work with that obtained by Taylor et al. (1998) using the South Pole water well micrometeorite collection. Finally, the implication of this work on the flux of carbonaceous material on Earth and the asymmetry distribution of the particles are discussed.

1.5.1. Comparison with previous works, the DC-SPWW complementarity

Yada et al. (2004) performed 5 independent collections in 3 different blue ice fields around the Yamato Mountains (Antarctica). The mass distributions, including both CSs and uMMs, exhibit a maximum between 100 and 200 µm, slightly higher than that determined in the present work for uMMs (100 µm), and in relative agreement with that for CSs (120 µm). The global micrometeorite (CSs and uMMs) flux measured in this work is, within uncertainties, in broad agreement with that measured by Yada et al. (2004) in locations J09 and J01, but is lower than that in the 3 other locations. The variations between the flux measured in distinct blue ice field locations may be explained by the differences in snow accumulation rate and erosion leading to an uncertainty in the *S* parameter associated with each collection site, and/or by possible variations of the extraterrestrial influx over long periods of time (several 10 kyrs, see section 1.4.1)

Taylor et al. (1998) performed a collection of CSs in the 50 – 700 µm diameter range from material recovered at the bottom of the South Pole water well (SPWW) of the South Pole Scott-Amundsen station, allowing the recovery of a large number of particles with sizes mainly above a few hundred µm, up to 700 µm. More recently, Suttle and Folco (2020) reported a flux value and size distributions

of thousands extraterrestrial particles gathered from a collection performed in a sediment trap in the Transantarctic Mountains (TAM). The maxima in the size distributions inferred from both the SPWW and TAM collections are located on a significantly larger range (D_{eq} = 200 - 300 µm) than that reported in this work.

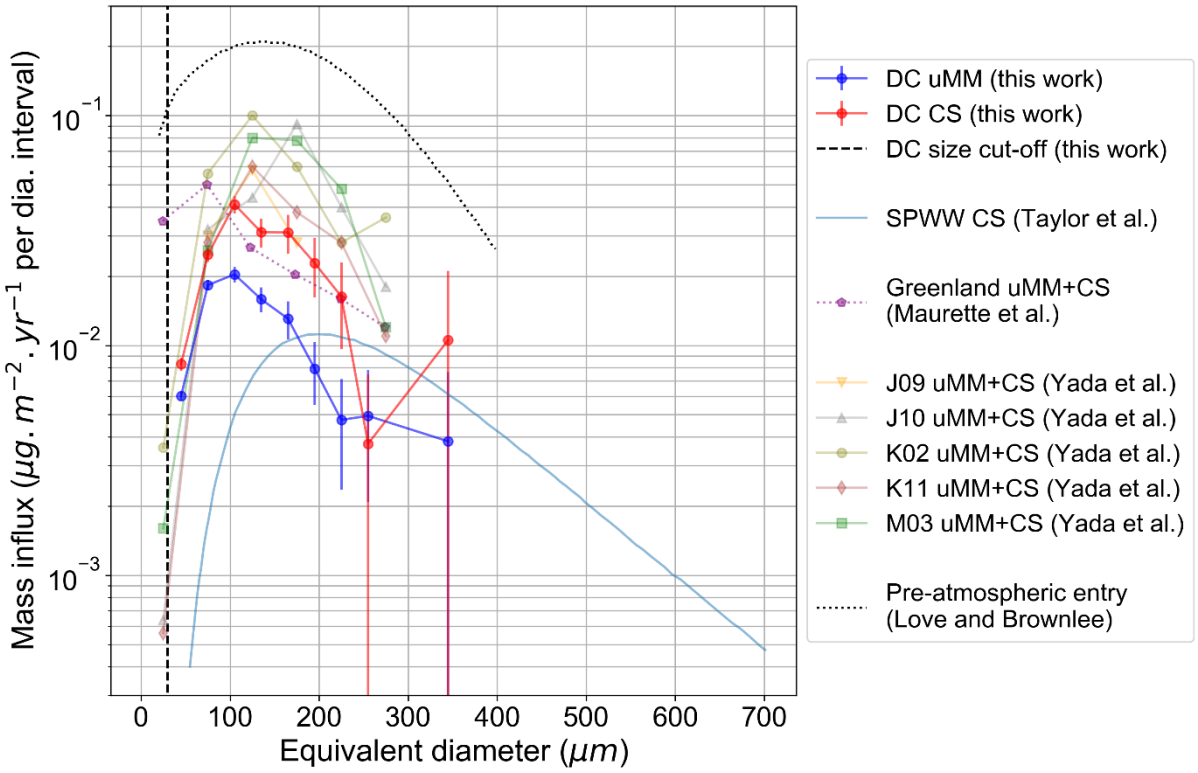

Figure 1-10: Comparison of the mass distributions of cosmic spherules and unmelted micrometeorites collected in Antarctica and Greenland ices and snows. The pre-atmospheric entry distribution of dust measured by Love and Brownlee (1993) is plotted for indication.

The high statistics of both the SPWW and TAM collections for large particles allows a precise size distribution to be inferred but only above 200 µm. The contribution of smaller particles is more uncertain in these two collections due to lower statistics and uncertainties in the *Q* value. The transport and settling of the particles within the SPWW geometry and the accumulation in the TAM sediment trap are complex processes resulting in uncertainties in the *S* and thus on the absolute value of the CS flux.

The present work on the Concordia Collection is thus complementary to the SPWW and TAM measurements as it provides an accurate constraint on the absolute value of the flux and on its mass/size distribution for both uMMs and CSs below 200 µm. In the right panel of *Figure 1-11* we combine the DC distribution for the low size range with the SPWW distribution for the higher size range (> 200 µm), in order to infer a global CS distribution in the overall diameter range (12 – 700 µm). The uncertainties (the envelope in red) were deduced by shifting vertically the SPWW distribution, but constraining its values to stay consistent with the DC CS experimental points at 195 µm and 225 µm. Such an error range on the absolute value of the SPWW flux is conceivable given the uncertainties on *Q* and *S* for this collection. While the flux deduced only from the DC collection yielded an underestimated mass flux of 5.7±1.5 $\mu g.m^{-2}.yr^{-1}$ for CSs, taking into account the SPWW data, the integration of the resulting distribution over the total range (12 – 700 µm) yields a total CS flux of 7.1

$\pm\ ^{2.0}_{1.4}$ µg.m^{-2}.yr^{-1}, which is a 25% increase of the flux derived from the DC CSs only. By extrapolating this result to the Earth surface, one gets 3,600$\pm^{1000}_{700}$ tons.yr^{-1}.

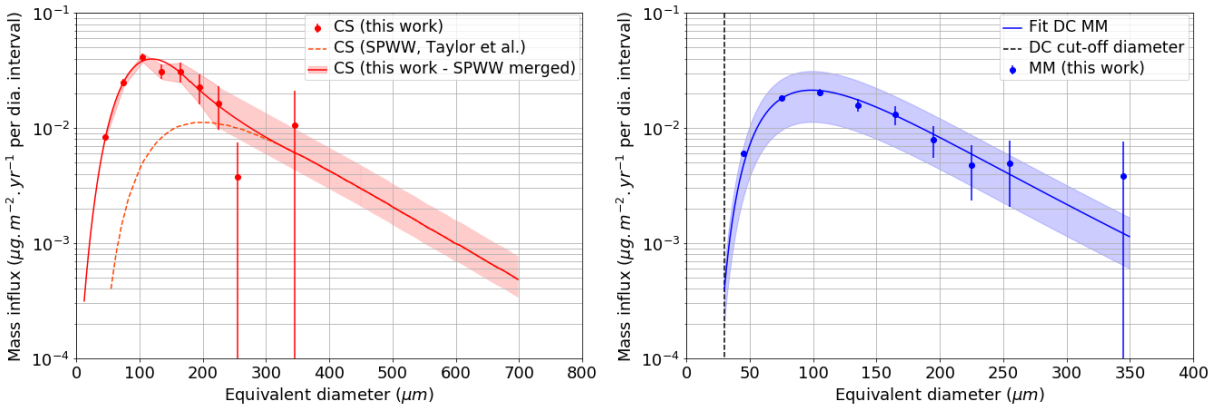

Figure 1-11. Left: global distribution of CSs inferred from the DC data (this work) for D<200 µm and SPWW (Taylor et al. 1998) data for CS with D>200 µm. The two datasets consider fully melted particles (CSs) recovered from melted Antarctic snow. The shaded area outlines the uncertainties in the global distribution. Right: uMMs distribution. The blue envelope indicates the impact of the mass density of uMMs on the uMM mass influx distribution, the lower and upper limits of the envelope correspond to uMM average densities of 0.8 and 2.2 g.cm^{-3}.

1.5.2. The Impact of the density of MMs on the flux measurement

A CS average density of 3.0 g.cm^{-3} is considered by most authors (Murrell et al., 1980; Yada et al., 2004). The uncertainty on that value is lower than for uMMs as CSs are mainly composed of the same components (silicates, metals and oxides) and do not exhibit significant porosity. By contrast, uMMs can exhibit a wide range of porosities, which may be related to their parent bodies' characteristics (cometary or asteroidal). Their average densities can vary between 0.8 g.cm^{-3} and 2.2 g.cm^{-3} for cometary and asteroidal end-members as discussed in section 1.3.2. Left panel of *Figure 1-11* shows the range of variation (blue envelope) of the uMM mass distribution for these two density values. Assuming a median density of 1,5 g.cm, and extrapolating over the entire Earth's surface, the global flux of uMMs is 1,600 ± 500 tons.yr^{-1} (4.4 ± 1.4 tons.d^{-1}). Considering the two end-members densities (0.8 g.cm^{-3} and 2.2 g.cm^{-3}, the annual global uMM flux on Earth would be shifted by about 45%, that is 800 and 2,400 tons.yr^{-1}, for average densities expected for cometary and asteroidal particles respectively. As a result, the inferred total flux of micrometeorites on Earth is estimated at 5,200$\pm^{1500}_{1200}$ tons.yr^{-1}, with 3,600$\pm^{1000}_{700}$ tons.yr^{-1} from CSs and 1,600±500 tons.yr^{-1} from uMMs.

1.5.3. The flux before the atmospheric entry, previous measurements and models

Love and Brownlee (1993) reported a measurement of the interplanetary dust flux prior the atmospheric entry by measuring and counting hypervelocity craters on the solar panels of the *Long Duration Exposure Facility* (LDEF) spacecraft. Their size distribution is plotted on *Figure 1-10*. The large difference between the ground-based measurements and this space-based measurement confirm that a significant part of the particles is ablated at the atmospheric entry. However, it is worth keeping in mind that the derivation of the mass of the incoming particles from the craters is highly sensitive on assumptions on both the speed and density of the particles before their impact that might lead to large uncertainties (see section 1.1.1, and Cremonese et al. (2012)). The size distributions of uMMs and CSs

from our work were compared with results from the CAMBOD-ZoDy model that simulate the position and velocity vectors of dust originating from different sources (Jupiter family comets, Halley-type comets and main belt asteroids) combined them with an ablation model of meteoroids at the atmospheric entry (Carrillo-Sánchez et al., 2016; Carrillo-Sánchez et al., 2015; Nesvorný et al., 2011). By constraining the model with the flux measurements on Earth, the model predicts the flux before the atmospheric entry and its possible origins. Based on the Concordia flux measurments, the CABMOD-ZoDy model predicts that the flux before the atmospheric entry is ranging from 10,000 to 20,000 tons·yr^{-1}, with the majority of the dust particles coming from the Jupiter family comets (Rojas et al., 2021).

1.5.4. Estimation of the carbon flux on Earth

Based on the flux estimation from the Concordia collection and the carbon (C) content of micrometeorites, it is possible to estimate the carbon flux on Earth carried by sub-millimeter particles. One part of the carbon flux reaches the Earth surface carried by particles that did not suffer from high temperature at atmospheric entry (unaltered carbon C_{unalt}) while another part the altered (altered carbon C_{alt}) is carried by CSs or uMMs that suffered various degrees of heating at atmospheric entry. C_{unalt} is carried by the fine-grained uMMs (Fg-uMMs) and the Ultra-Carbonaceous Antarctic micrometeorites (UCAMMs) with extreme C concentrations (see Chapter 2). The Fg-uMM mass flux represents ~40% of the uMM flux and their C concentration, [C], is similar to that in carbonaceous chondritic material. Considering an average [C] = (3±2) wt% (Matrajt et al., 2003), their global Carbon flux is (19±13) tons.yr^{-1}. The C/Si ratio in UCAMMs varies over a wide range from 10 to 10^3 (Dartois et al., 2018). Considering an average [C]=(60±30)wt% and that the mass of UCAMM is 0.7% of that of uMMs in the CONCORDIA collection, their associated C flux is (7±3) tons.yrs^{-1}. The resulting global flux of C_{unalt} is thus (26±16) tons.yr^{-1}. Considering an average [C] of (0.6±0.4)wt% for CSs and (1±0.8)wt% for non-Fg uMMs (Matrajt et al., 2003), the total flux of C_{alt} is (31±22) tons.yr^{-1}, with ~70% carried by CSs and ~30% by partially heated uMMs. Given these uncertainties, the total C flux shows a quite large range of variation (20-100 tons.yr^{-1}), with up to half of this C flux being in form of C_{unalt}. Noticeably, the flux of C from UCAMMs represents about 25% of the C_{unalt} flux, indicating that a substantial part of the interplanetary organics reaching Earth surface can originate from the specific cometary reservoir that is the parent body of UCAMMs.

1.5.5. The asymmetry factor distributions

The equivalent diameter and asymmetry distributions of the different types of uMMs and CSs from the Concordia collection are reported on Figure 1-12 and Figure 1-13. Asymmetry factors of uMMs, which have experienced no or little heating during atmospheric entry, are representative of a population of dust in the interplanetary medium. Conversely, CSs have been largely heated when going through the atmosphere, leaving no clue of their original shape.

The equivalent diameter distributions of uMMs and CSs do not exhibit substantial differences, all peaking around 30 and 60 µm. The distributions of asymmetry factors for the different types of particles are shown in Figure 1-13. CSs are characterized by *As* close to 1, reflecting their spherical shapes, while uMMs have mostly non-spherical geometry with *As* ranging from 0.2 to 1. The *As* distributions exhibit a maximum at 0.7 and no significant differences is observed between the different types of uMMs.

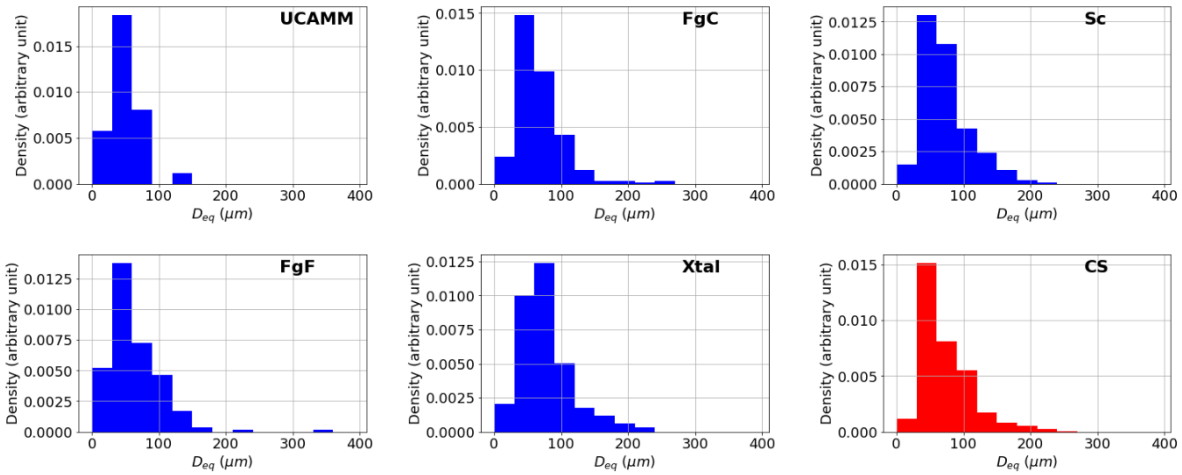

Figure 1-12: Distributions of equivalent diameter for the different types of particles (DC06 and DC16 data).

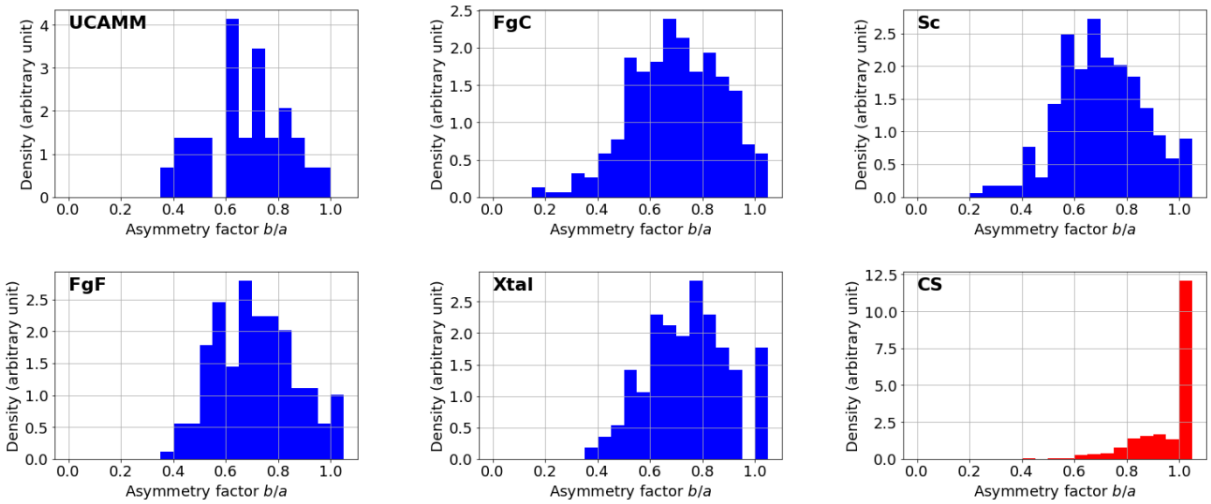

Figure 1-13: Distributions of asymmetry parameter for the different types of particles (DC06 and DC16 data).

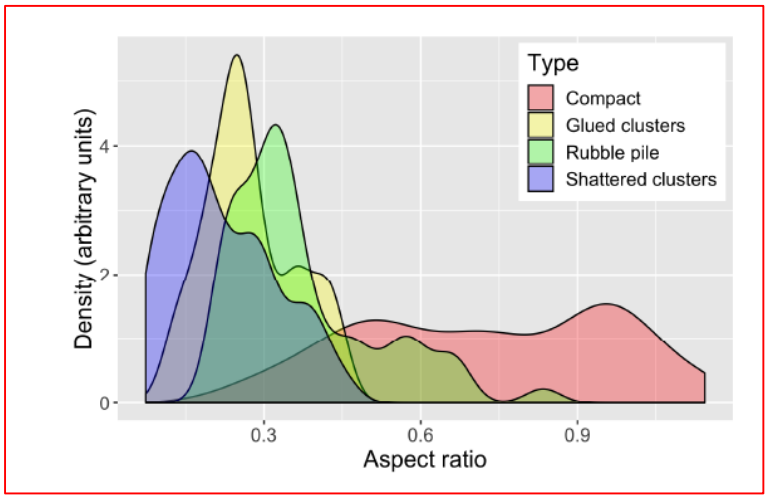

Figure 1-14: Aspect ratio distribution of different types of grains sampled by the COSIMA instrument onboard Rosetta. From Lasue et al., 2019.

The COSIMA instrument onboard Rosetta spacecraft was able to measure the projected area and the orthogonal height of individual cometary grains ejected from the comet 67P/Chryumov-Gerasimenko. An aspect ratio, defined as $\frac{height}{\sqrt{area}}$, was computed for each grain and aspect ratio distributions were derived for different types of grains (Langevin et al., 2015; Lasue et al., 2019). The cometary grains measured by COSIMA impacted the collection plate with velocities ranging from 1 to 15 m.s^{-1}, enough to flatten or crumble some of the original particles (Langevin et al., 2015). The asymmetry factor and the aspect ratio are not strictly equivalent since the later may exceed 1. Nevertheless, they both are a measurement of the asymmetric shape of a particle.

Aspect ratios of compact grain type share a same variation range, from 0.4 to 1, with the asymmetry factors of the uMMs, suggesting a similar general behavior. Though compact grains aspect ratios peak at 0.5 and 1 while uMMs *As* peak at 0.7 (Table 1-5). It is possible that the fluffier aggregates reported by COSIMA (Lasue et al., 2019) cannot reach the Earth surface undamaged and thus are not represented in the uMM asymmetry ratio distributions. A potential breakdown of these particles at the atmospheric deceleration could either destroy or split them in smaller fragments not collected or identified by the today collections. These geometrical properties of grains will be the subject of a dedicated forthcoming study as the present work provides new constraints on these distributions for grains with low sizes (i.e. below 100 µm) that are of interest in aggregation models of dust in protoplanetary disks.

Table 1-5: Mean values and standard deviations of D_{eq} and As for the 6 types of micrometeorites.

Type	UCAMM	FgF	FgC	Xtal	Sc	CS
D_{eq} ± σ (µm)	52 ± 23	65 ± 39	67 ± 34	77 ± 38	73 ± 35	72 ± 39
As ± σ	0.67 ± 0.15	0.71 ± 0.15	0.70 ± 0.17	0.74 ± 0.15	0.70 ± 0.16	0.94 ± 0.10

1.6 Exposure factor dependence

The influx of extraterrestrial material on our planet is a key parameter in many fields beside cosmochemistry (e.g. space science, geochemistry, atmospheric physics, glaciology). It is and will be the subject of large numbers of new attempts to precise its value. Most of these studies have to take into account the statistical fluctuations induced by the finite number of micrometeorites collected. The mass/size distributions obtained above allows modeling the number (and mass) expected to fall on a given surface·time. We present below Monte-Carlo simulations to quantify these statistical fluctuations. Such a study will be relevant to future collects as they provide a direct estimation of the statistical uncertainty related to a given exposure parameter.

1.6.1. Modeling ET flux sampling

Using the total mass distributions of *Figure 1-9*, we considered a nominal flux Φ_0 given by Φ_{uMM} and Φ_{CS}, carried by uMms and CSs. The statistical variation on the number of particles collected with a sufficiently large *S* (S_{ref} = 10^5 m². yr) is negligible and allows to infer the average number of uMMs and CSs per unit of surface and time within the 12-700 µm diameter range: N_{ref}(uMM) = 4.3 m^{-2}. yr^{-1} and N_{ref}(CS) = 3.6 m^{-2}. yr^{-1}.

We then simulated the number N_{simu} of collected particles for a set of exposure parameter *S.* For each simulation, the N_{simu} value was sorted with a binomial law of parameters ($n = N_{ref}$, $p = \frac{S}{S_{ref}}$). The masses M_{simu} of the N_{simu} particles were subsequently randomly chosen using the global uMM and CS mass distributions reported in *Figure 1-9*. A numerical measured flux was then computed with M_{simu}, the sum of the masses as $\Phi = \frac{M_{simu}}{S}$. For each *S*, we simulated 10^5 numerical measured fluxes Φ, to infer their median values and their 10-90% and 25-75% variations from the nominal flux Φ_0. The resulting distributions as function of *S* are presented in the *Figure 1-15* left panel, for *S* ranging from 10^{-1} to 10^5 m².yr.

Figure 1-15 right illustrates the probability, for a collection on a given exposure parameter S, to estimate the real flux Φ_0 with a relative uncertainty (Φ - Φ_0)/Φ_0 smaller than 10%, 20% and 30% (respectively P10, P20 and P30). The accuracy of a flux measurement for a given *S* is monitored by the median Φ/Φ_0 ratio and its variations at the first and last quartile (25-75%) and decile (10-90%).

For *S* lower than 1 m^2.yr, more than 75% of the simulated fluxes have relative uncertainties greater than 30% (*Figure 1-15*, right), preventing reliable measurements. The left panel in *Figure 1-15* also demonstrates that collections performed with *S* lower than a few m^2.yr are subjects to a systematic bias toward an underestimation of the real flux. This feature is due to the fact that, for such low *S*, the collection statistically misses a significant number of large size particles so that the masses collected tend to be lower than expected from the real mass distribution. For *S* greater than a few tens of m^2.yr, this systematic effect becomes negligible (the median Φ/Φ_0 approaches 1), and variations on the measured flux substantially decrease.

For $S \approx 100$ $m^2.yr$, there is a probability of about 90% (about 2 σ) that the relative difference between the measured flux Φ and the real flux Φ_0 is less than 20%. We report on *Figure 1-15* the exposure parameter of the sum of the selected melts (dataset #1) for CSs and uMMs (S = 89.6 m^2.yr for CSs and S = 131.9 m^2.yr for uMMs). *Figure 1-15* is helpful for evaluating the statistical biases inherent in a collection for a given exposure parameter.

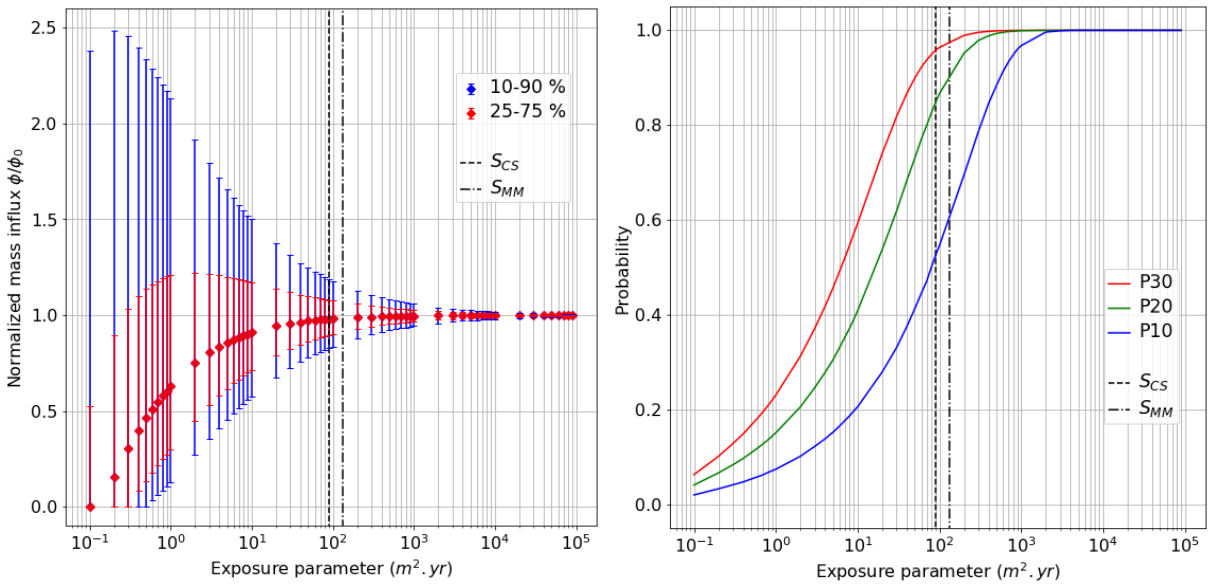

Figure 1-15. Impact of the exposure parameter on flux measurements. Left: Variation of the ratio between the measured flux (Φ) and the nominal input flux Φ_0 for different percentile ranges and recovery probability as a function of the exposure parameter S. Right: P30, P20 and P10 are the probabilities (depending on the exposure parameter) that the nominal input flux is estimated to have with less than 30%, 20% or 10% uncertainty, respectively. The vertical dashed lines indicate the exposure parameters S_{CS} and S_{MM} of the CS and MM collection from this work are indicated by the vertical dashed lines.

1.6.2. Selected melt validation

We used the results of these Monte-Carlo simulations to verify that the spread of the flux estimations from the selected melts were consistent with statistical fluctuations of the number of particles collected. Melts from the dataset #1 were simulated according to the protocol detailed in section 1.6.1. Based on the *S* value associated to each melt, we simulated N_{simu} collected particles with a binomial law ($n = N_{ref}$, $p = \frac{S}{S_{ref}}$). The mass of each particle was sorted with the global uMM and CS mass distributions. By repeating this operation 10^5 times for each melt (*i.e.* each *S*), we obtained the range of variation of the measured flux. The results of the simulations are shown in *Figure 1-16*. Blue shades represent the density of simulated measurements with a given mass influx. Red dotted lines indicate their 10th and 90th percentiles. Yellow lines are the actual flux measurements derived from the real data of the selected melts.

For uMMs, the spread selected is broadly consistent with expected statistical variations inherent to the exposure parameter *S* of each melt. The variations of the CS flux derived from the selected melts are less pronounced, most probably reflecting the fact that these particles are easier to identified in the filters and thus their actual number closer to the exact number located on the sampled surface. The CS flux variations are thus fully compatible with statistical variations of the number of infalling particles.

It is worth noting that, in the CSs' case, the mass influx derived from the sum of the selected melts (*Figure 1-16*, i) panel) 5.0 µg.m^{-2}.yr^{-1} is slightly lower than the actual real flux estimation, that is 5.7 µg.m^{-2}.yr^{-1}. Indeed, the real flux value is integrated over the 12-700 µm diameter range whereas, the CSs' selected melts do not contain particles with D_{eq} > 250 µm. Because the contribution of a limited number (sometimes only one) large particles is significant in the total mass budget of a melt, their absence tends to minimize the flux derived from the dataset #1.

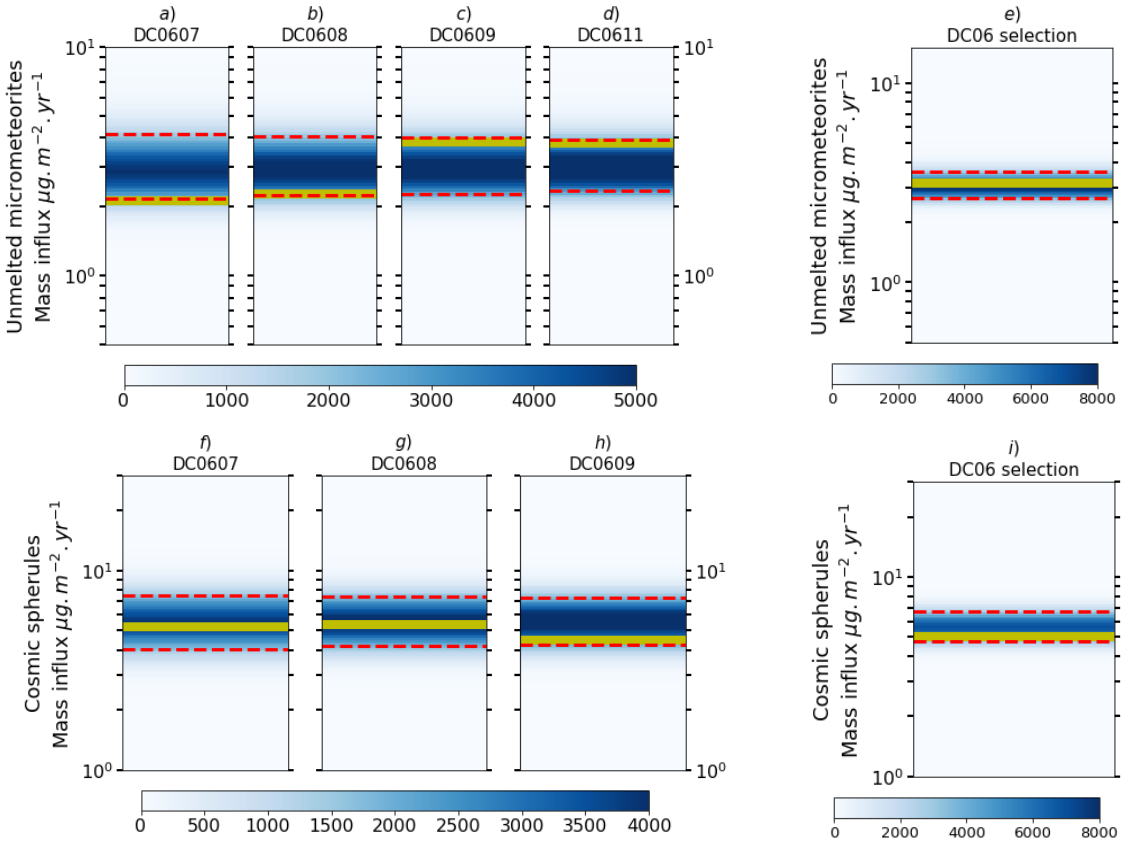

Figure 1-16: Measured flux values (yellow line) compared to simulated values obtained with the mass distributions from Figure 1-9. Red dotted lines indicate the 10th and 90th percentiles of the simulated values. Top: a,b,c,d are the selected melts for the MMs, and (e) is the sum of the selected MMs dataset, bottom: f, g, h are the selected melts for the CSs, and (i) is the sum of the selected CSs data set.

1.7 Summary

The work presented in this chapter is a comprehensive study on the flux of interplanetary sub-millimeter particles falling on Earth based on the Concordia Antarctic micrometeorites collection. The characteristics of the Concordia collection (location, weather conditions, field campaigns and collects protocols, types of particles, …) are presented. We show how both the exposure parameter *S* and collection efficiency *Q* are well controlled at Dome C and allow to obtain reliable sub-millimeter particles collections. A sub-set of melts form the Concordia collection is then selected, with high counting statistics, and the absolute mass distributions inferred, in the 12-700 µm diameter range, for both unmelted micrometeorites (uMM) and cosmic spherules (CS). The global micrometeorite flux on Earth is then extrapolated and discussed and compared with previous similar measurements from the literature. A global CS flux, in the 12-700 µm diameter range, is obtained by combining the Concordia CS flux distribution (accurate below ≈300 µm) with the SPWW CS flux distribution (accurate above ≈300 µm). The inferred total flux of micrometeorites on Earth is estimated at 5,200 tons.yr^{-1}, with 3600 tons.yr^{-1} from CSs and 1,600 ± 500 tons.yr^{-1} from uMMs. The flux of carbon on Earth carried by micrometeorites is estimated to range from 20 to 100 tons.yr^{-1}. Finally, a statistical study is developed in order to underline the intrinsic uncertainties related to the exposure parameter and the requirements and limitations for futures works on this subject. Collections with exposure parameters higher than 100 m²·yr have 90% chance to measure the flux with less than a 20% error.

2 Chapter 2: Isotopic composition of H, C and N in Ultra-Carbonaceous MicroMeteorites

2.1 The Ultra-Carbonaceous MicroMeteorites (UCAMMs)

Ultra-Carbonaceous Antarctic MicroMeteorites (UCAMMs) are carbon-rich micrometeorites collected in Antarctica. Among the diversity of extraterrestrial sub-millimeter particles (IDPs, micrometeorites), UCAMMs are the objects with the higher concentration in organic matter (Dartois et al., 2018). They were identified independently in the French and Japanese collections of Antarctic micrometeorites (Duprat et al., 2010; Nakamura et al., 2005).

The organic matter in UCAMMs is characterized by high N/C ratios, ranging from $4 \cdot 10^{-2}$ to $2 \cdot 10^{-1}$ (Dartois et al., 2018), higher than the ones measured in insoluble organic matter (IOM) extracted from meteorites and close to the interstellar medium (ISM) upper limit of $1.4 \cdot 10^{-1}$, determined by considering that the missing nitrogen in the diffuse medium is locked in carbonaceous dust (Dartois et al., 2018; Verstraete, 2011) (see *Figure 2-1*, left). The atomic carbon to silicon ratio (C/Si) of UCAMMs is also higher than the ones measured in meteorites and IDPs. Strikingly, its value lays above the value expected for interstellar dust (*Figure 2-1*, right), (Millar, 2015), suggesting that the organic matter of UCAMMs is not a phase directly inherited from the interstellar medium. A depletion in minerals of that magnitude can be explained by the synthesis of the organic matter of UCAMMs in a mineral-free environment such as ice mantles at the surface of small bodies, in cold regions of the solar system, where minerals are locked in depths (see Chapter 3). UCAMMs display a wide range of deuterium enrichments, with one particle exhibiting up to δD ≈ 30,000 ‰ and another δD ≈ 0 ‰ (Duprat et al., 2010; Yabuta et al., 2017).

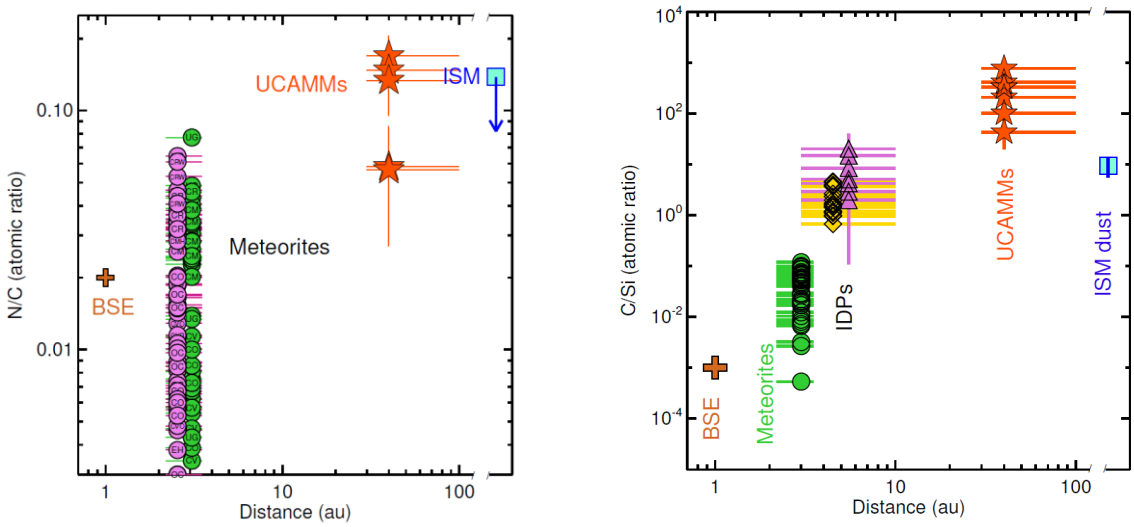

Figure 2-1 from Dartois et al. (2018). N/C ratios (left) and C/Si ratios (right) measured in UCAMMs (stars) compared to data measured in chondrites (purple and green circles from Kerridge (1985) and Alexander et al. (2007), respectively) and IDPs (triangles and diamonds). The bulk silicate Earth and interstellar medium values are indicated by an orange cross and a blue square.

The isotopic composition of light elements (H, C, N) is commonly used as a tool of classification of the extraterrestrial organic matters (see e.g. Floss et al. (2004); Alexander et al. (2007); Aléon et al. (2001) and references therein). It enables to identify possible links between interplanetary objects and heritage from different stages of evolution of the solar system. In this chapter, we report measurements of the H, C and N isotopic compositions of the organic matter of UCAMMs. Three UCAMMs were analyzed during this thesis: DC16-309 (hereafter DC309), DC06-18 (hereafter DC18) and DC06-43 (hereafter DC43). In addition, correlations of the H, C and N isotopic data are reported on another UCAMM, DC06-94 (hereafter DC94), analyzed by Bardin (2015).

2.2 The NanoSIMS technique

Isotopic data presented in this chapter were acquired by nanoscale secondary ions mass spectrometry (NanoSIMS). The NanoSIMS technique was developed by Pr. Georges Slodzian with the aim to perform *in-situ* mass spectrometry measurements with high mass resolution and lateral spatial resolution of 50 – 100 nanometers.

2.2.1. The NanoSIMS instrument

The Cameca NanoSIMS 50 instrument (*Figure 2-2*) couples a primary ion beam that sputters the surface of a sample to a mass spectrometer that collects the resulting secondary ions in order to analyze them. Primary ions are extracted from a cesium source (Cs^+) or an oxygen source (O^-). They are then guided through the primary and coaxial columns and impact the sample, leading to the extraction of neutral atoms, molecules and ions (secondary ions) from the sample. Secondary ions are collected under the action of a set of lenses and directed to the mass spectrometer via the coaxial column. Primary and secondary ions in the coaxial column travel in opposite directions and consequently have charges of opposite signs. The deviating plates P1 (*Figure 2-2*) allow the primary beam to enter the coaxial column and the secondary beam to enter the mass spectrometer (horizontal plane, in green in *Figure 2-2*). Nanoscale spatial resolution is achieved thanks to the coaxial column which allow a better precision than classical secondary ion mass spectrometry (SIMS) instruments.

Secondary ions' trajectories are selected at the entrance of the mass spectrometer by an entrance slit (ES) and an aperture slit (AS). An energetic and angular focusing of the ions is achieved with an electrostatic sector (SS100) and a magnetic prism (Magnet). The magnetic prism allows to select a set of ion masses that are detected by the multi-collection detectors (electron multipliers). Faraday cup detectors are also available for the detection of ions, however, they were not used during the NanoSIMS sessions described in this work since their time response is not compatible with imaging. The detectors stand on trolleys able to move horizontally along the focal plan of the magnetic prism to catch specific ions. The fine selection of a monochromatic ion beam (made of ions of a same mass) is performed by the combination of the action of the deflectors (Pd) and the positioning of the exit slits (ExS) before the detectors. Up to seven electron multiplier detectors (depending on the instrument) allow to record simultaneously the signals of different ions. The mass resolution of the NanoSIMS enables the separation of isotopologs such as $^{12}C^{15}N^-$ and $^{13}C^{14}N^-$ with very similar masses.

Ion images are acquired with the NanoSIMS by rastering the primary beam on the sample. A sub-micron scale resolution is achieved thank to the synchronized addressing of the primary and secondary ion beams (dynamic transfer, Slodzian et al. (2017)). The coupling of the dynamical transfer and the high resolution/multi-collection mass spectrometer allows to derive ratio images that can be used to measure elemental abundances (e.g. $^{12}C^{14}N/^{12}C_2$ ratio image for the N/C elemental ratio) or isotopic ratios (e.g. $^{12}C^{15}N/^{12}C^{14}N$ ratio image).

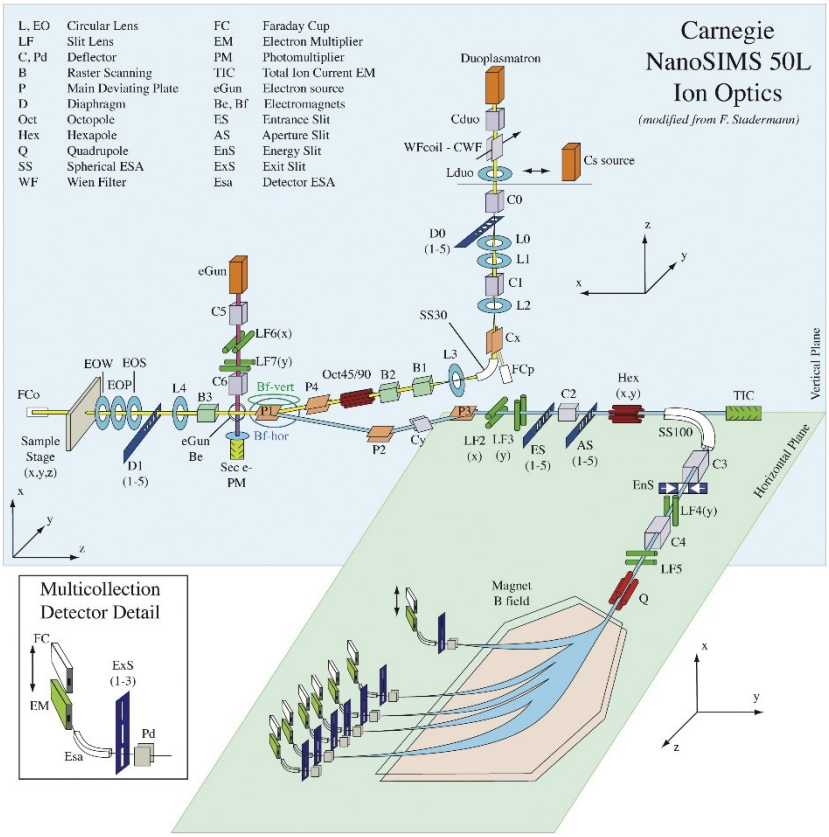

Figure 2-2: schematic diagram of the Cameca NanoSIMS 50L instrument at the Earth and Planets Laboratory (EPL, Carnegie institution) from Hauri et al. (2016). Ions of the primary beam are produced from the duoplasmatron (O^-) or the cesium source (Cs^+). The primary ions are guided through the primary and coaxial columns and impact the sample. By doing so, they lead to the production of secondary ions from the sample that are collected and sent to the mass spectrometer via the coaxial and secondary columns. Because the primary and secondary ions travel along the coaxial column in opposite directions, they must have charge of opposite sign.

2.2.2. Data treatment

Ion images are formed pixel by pixel by rastering the primary beam on the sample surface and collecting the locally extracted ions. After receiving an ion, an electron multiplier is not able to detect another impact during the so-called “dead-time”. This results on an underestimation of the number of ions collected by the detector and can be corrected as follow:

$$N_{corr} = \frac{N}{1 - N\frac{\tau}{S_{rate}}}$$

where N is the recorded number of ions per pixel, N_{corr} the number of ions per pixel corrected from the dead-time, τ the dead-time and S_{rate} the dwell-time (i.e. the time of residence of the primary beam on each pixel).

Slodzian et al. (2004) reported that in the case of important production rate of secondary ions by the primary beam, several ions are likely to impact a detector at the exact same time. Because the electron multipliers are not able to distinguish single or multiple ions impacts, this causes an underestimation of the counted ions. This effect is referred as quasi-simultaneous arrivals effect (QSA). The QSA effect can impact importantly the isotopic ratio images since it is expected to induced an underestimation of the number of the more abundant isotope/isotopolog and marginally affect the less abundant. Thus, a mass fractionation caused by the QSA effect enhances isotopic ratios (minor isotopolog/major isotopolog). A correction of the QSA can be made at the first order as follow (Slodzian et al., 2004):

$$N_{corr} = N \cdot (1 + \frac{1}{2}K)$$

where N is the measured number of secondary ions, N_{corr} the number of secondary ions corrected from the QSA effect and K the average number of secondary ions ejected per primary ions. The QSA correction has to be applied after the dead-time correction. Typical values of K were $2 \cdot 10^{-2}$ for the $^{12}C^-$ emission, $3 \cdot 10^{-3}$ for the $^{12}C_2^-$ emission and $7 \cdot 10^{-4}$ for the $^{12}C^{14}N^-$ emission.

Measurements of elemental or isotopic ratios with the NanoSIMS are also subject to instrumental mass fractionation (IMF). The IMF is often controlled by measuring standard samples with known compositions, leading to the IMF correction factor $\alpha = \frac{R_{exp}}{R_{st}}$ with R_{exp} and R_{st} the measured and calibrated ratios (isotopic or elemental) of the standard sample respectively. The ratios measured on unknown samples are then divided by α.

Isotopic images presented in this work were corrected from the dead-time, the QSA effect and the IMF.

Several notations are used to report isotopic ratio values:

- Ratio of the more abundant to the less abundant isotopes, e.g. H/D, $^{14}N/^{15}N$, $^{12}C/^{13}C$.
- Ratio of the less abundant to the more abundant isotopes, e.g. D/H, $^{15}N/^{14}N$, $^{13}C/^{12}C$.
- Delta (δ) notation expressing the difference between a measured ratio $(a/A)_{meas}$ and a reference value $(a/A)_{ref}$, e.g. δD, $\delta^{15}N$, $\delta^{13}C$. For instance, for two isotopes a (less abundant) and A (most abundant), one has:

$$\delta a = \left(\frac{(a/A)_{meas}}{(a/A)_{ref}} - 1 \right) \times 1000$$

  The δ values are expressed in permil (‰).

In this chapter, we report isotopic ratios with the second and third notations. The reference values for the δ notation are the VSMOW (Vienna Standard Mean Ocean Water, $D/H = 1.558 \cdot 10^{-4}$), ATM (atmospheric N_2, $^{15}N/^{14}N = 3.676 \cdot 10^{-3}$) and VPDB (Vienna Pee Dee Belemnite, $^{13}C/^{12}C = 1.124 \cdot 10^{-2}$) values. The terms “enrichment” or “depletion” refer to enrichment or depletion relatively to the VSMOW, ATM and VPDB values if not specified otherwise.

2.3 Isotopic analyses of UCAMMs

2.3.1. UCAMMs analyzed at the Earth and Planets Laboratory (Washington)

In April 2019, in collaboration with Dr. Nittler, we performed isotopic maps on 3 UCAMMs at the Carnegie Earth and Planets Laboratory (EPL, Washington DC, USA). The goal of this session was to acquire correlated maps of the D/H, $^{15}N/^{14}N$ and $^{13}C/^{12}C$ ratios on the 3 UCAMMs. Five fragments were prepared for analysis. In the following sections, the individual fragments and their isotopic maps are presented. We could not perform isotopic maps on an additional sample, the DC18 FIB section, due to its loss during the analysis, though, for the sake of completeness, the preparation procedure is detailed in annex 5.1.1.

Two settings of the NanoSIMS instrument were used. The D/H maps were obtained by collecting H^-, D^-, CH^-, OH^- ions and the $^{15}N/^{14}N$ and $^{13}C/^{12}C$ maps by collecting $^{16}O^-$, $^{12}C_2^-$, $^{12}C^{13}C^-$, $^{12}C^{14}N^-$, $^{12}C^{15}N^-$, $^{32}S^-$ ions (Table 2-1). For the two settings, the intensity of the primary Cs^+ beam was 10 µA and the dwell time was set to 2 ms/pixel. The instrumental mass fractionation (IMF) affecting the D/H ratios was controlled by measuring an in-house organic standard $C_{30}H_{50}O$ with δD = -152‰. For carbon acquisitions, IMF was controlled thanks to a SiC standard ($\delta^{13}C$ = -22‰) and the IOM QUE 99177 ($\delta^{13}C$ = -20.8‰, Alexander et al. (2007)). A Si_3N_4 sample with $\delta^{15}N$ = 0‰ was used to correct the IMF on nitrogen. The IMF correction factors measured on standards are listed in annex 5.1.2. Isotopic maps and values reported hereafter are corrected from the IMF.

The full sorting of the data was performed in Orsay, starting from raw data extracted with the OpenMIMS software (open-source software funded by the NIH/NIBIB National Resource) and using a dedicated procedure written in Python programming language (Python Software Foundation, https://www.python.org/) during the course of this work.

Table 2-1: characteristics of the NanoSIMS analyses performed at the Earth and Planets Laboratory, Washington DC in April 2019. Five acquisitions on 3 UCAMMs samples are presented in this section

UCAMMs	**Analyzed Area**	**Session D H, D, CH, OH**		**Session ^{15}N, ^{13}C ^{16}O, $^{12}C_2$, $^{12}C^{13}C$, $^{12}C^{14}N$, $^{12}C^{15}N$, ^{32}S**	
		Raster (pixels)	**N frames**	**Raster (pixels)**	**N frames**
DC309	5x5 µm²	128x128	15	128x128	20
DC43 C1	12x12 µm²	128x128	26	256x256	10
DC18 A	50x50 µm²	512x512	30	512x512	35
DC18 B	45x45µm²	256x256	40	512x512	30
DC18 C	20x20 µm²	256x256	11	256x256	30

2.3.1.1. *UCAMM DC309 on a diamond cell*

Prior to the NanoSIMS analyses, the DC309 sample was the object of an extensive study by nanoscale infrared spectroscopy (AFMIR) reported in Mathurin et al. (2019). A fragment of the DC309 micrometeorite was embedded in sulfur and ultramicrotomed. The resulting slices were subsequently deposited on a diamond cell (Figure 2-3) and the remaining sulfur was removed by a slow annealing at 50°C. The nature of the slice was confirmed by far field IR measurements. For the purpose of NanoSIMS analyses, a 40 nm thick gold coating was deposited on the sample.

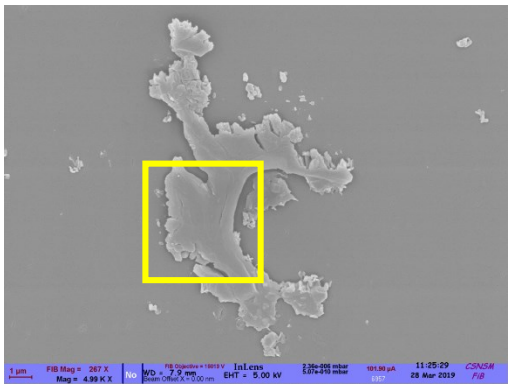

Figure 2-3: SEM image of the DC309 fragment. The yellow square was analyzed by NanoSIMS.

The analyzed zone, shown in Figure 2-3, consisted in a 5x5 µm² area imaged on a 128x128 pixels raster (see Table 2-1). Isotopic images of the DC309 section are shown in *Figure 2-4* along with a CH^- image. The CH^- image show no apparent difference in structure within the sample, as confirmed by the SEM image (Figure 2-3). The bulk composition was determined to be $\delta^{15}N$ = -125 ± 31‰, $\delta^{13}C$ = 27 ± 16‰ and δD = 6800 ± 500‰, depleted in ^{15}N in comparison with the Earth atmosphere and with a high deuterium abundance. Two regions with distinct D/H and $^{15}N/^{14}N$ ratios are observed. The region at the left has lower D and higher ^{15}N composition (δD≈4200‰, $\delta^{15}N$≈-69‰) than the region at the right (δD≈8700‰, $\delta^{15}N$≈-178‰). Measurements on specific regions of interest (ROI), drawn in white and yellow in *Figure 2-4*, are detailed in Table 2-2 and plotted in *Figure 2-9*.

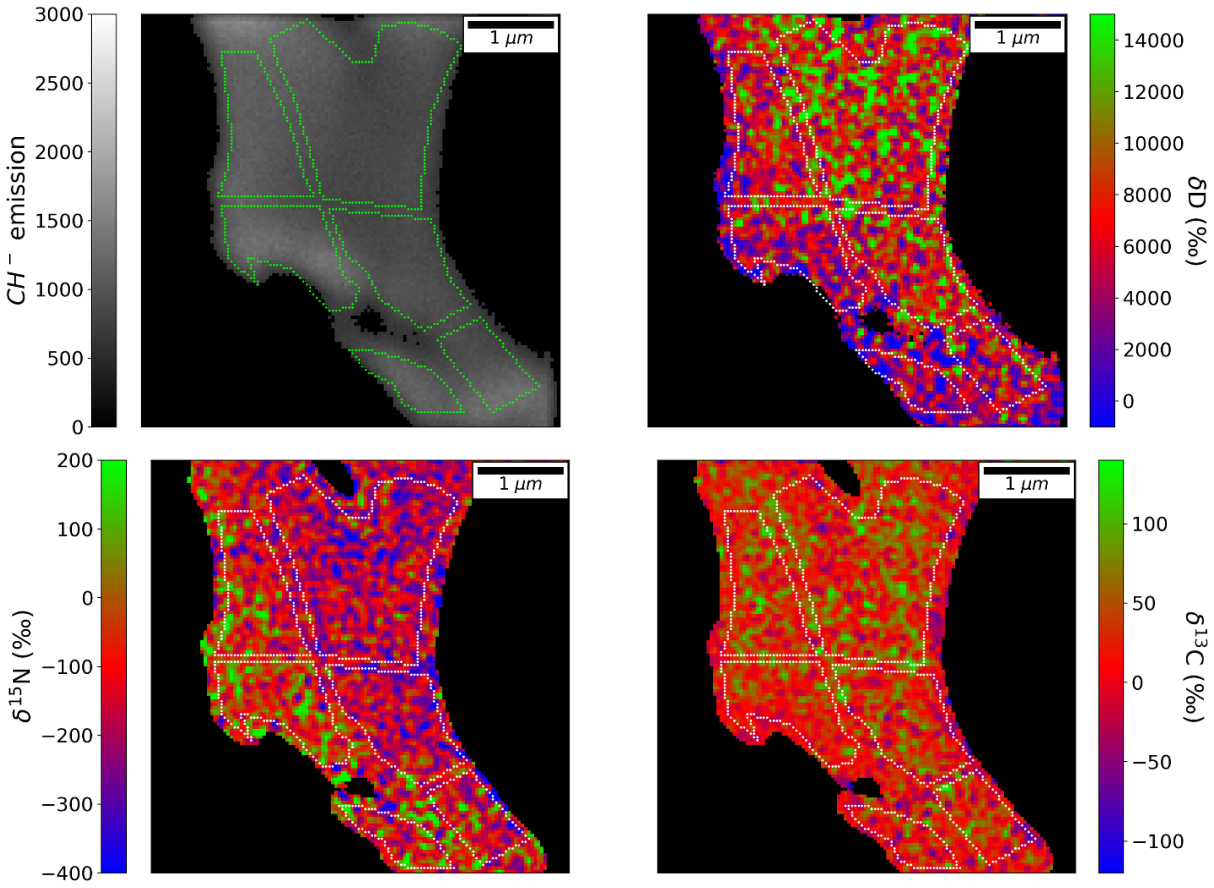

Figure 2-4. Top left: CH^- (counts) image of the zone of the DC309 section analyzed by NanoSIMS. Top right, bottom left and bottom right: δD, $\delta^{15}N$ and $\delta^{13}C$ images. Regions of interest are drawn in white in yellow. Two zones with different isotopic composition δD and $\delta^{15}N$ are observed. The $^{13}C/^{12}C$ ratios do not present significant variations.

2.3.1.2. *UCAMM DC43 on a diamond cell*

The DC43 sample analyzed at EPL was prepared by pressing a fragment of UCAMM DC43 between two diamond windows in a dedicated cell. An image of the resulting C1 fragment, measuring 9µm by 5µm is shown in *Figure 2-5*. A 20 nm gold layer was deposited at the surface of the sample prior the analyses. The H^- and D^- images were acquired on a 12x12µm² area over 128x128 pixels. Images of the $^{12}C_2^-$, $^{12}C^{13}C^-$, $^{12}C^{14}N^-$, $^{12}C^{15}N^-$ ions were measured on the same zone with a 256x256 pixels raster (Table 2-1).

Figure 2-6 shows the CH^- and the δD, $\delta^{15}N$, $\delta^{13}C$ images of the DC43 C1 fragment. For the δD image, the contour of the particle was defined on the basis of the CH^- emission. The bulk isotopic composition of DC43 C1 is $\delta^{15}N = 272 \pm 46‰$, $\delta^{13}C = -12 \pm 18‰$ and $\delta D = 3100 \pm 300‰$. Three regions were spotted with $\delta^{13}C$ below -40‰ (see Table 2-2 and *Figure 2-9*). One present richer ^{15}N-composition ($\delta^{15}N \approx 610‰$) and a bulk-like D/H (δD≈3400‰), another a higher D/H ratio (δD≈6500‰) and a bulk-like $^{15}N/^{14}N$ ratio ($\delta^{15}N \approx 350‰$) and the third one has low D/H and $^{15}N/^{14}N$ ratios (δD≈500‰, $\delta^{15}N \approx 41‰$).

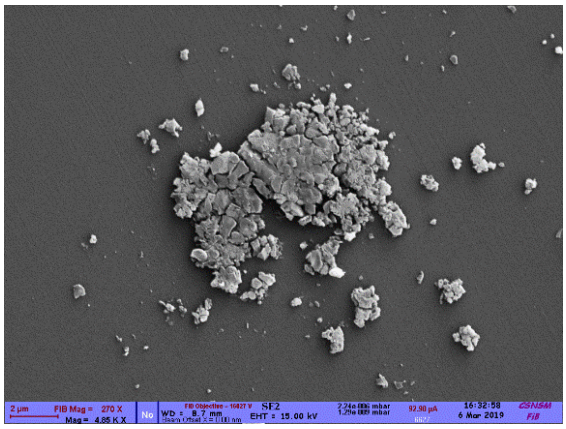

Figure 2-5. SEM image of the DC43 fragment C1 analyzed by NanoSIMS. The fragment was deposited on a diamond cell and pressed. The dimensions of the fragment are 9x5 µm.

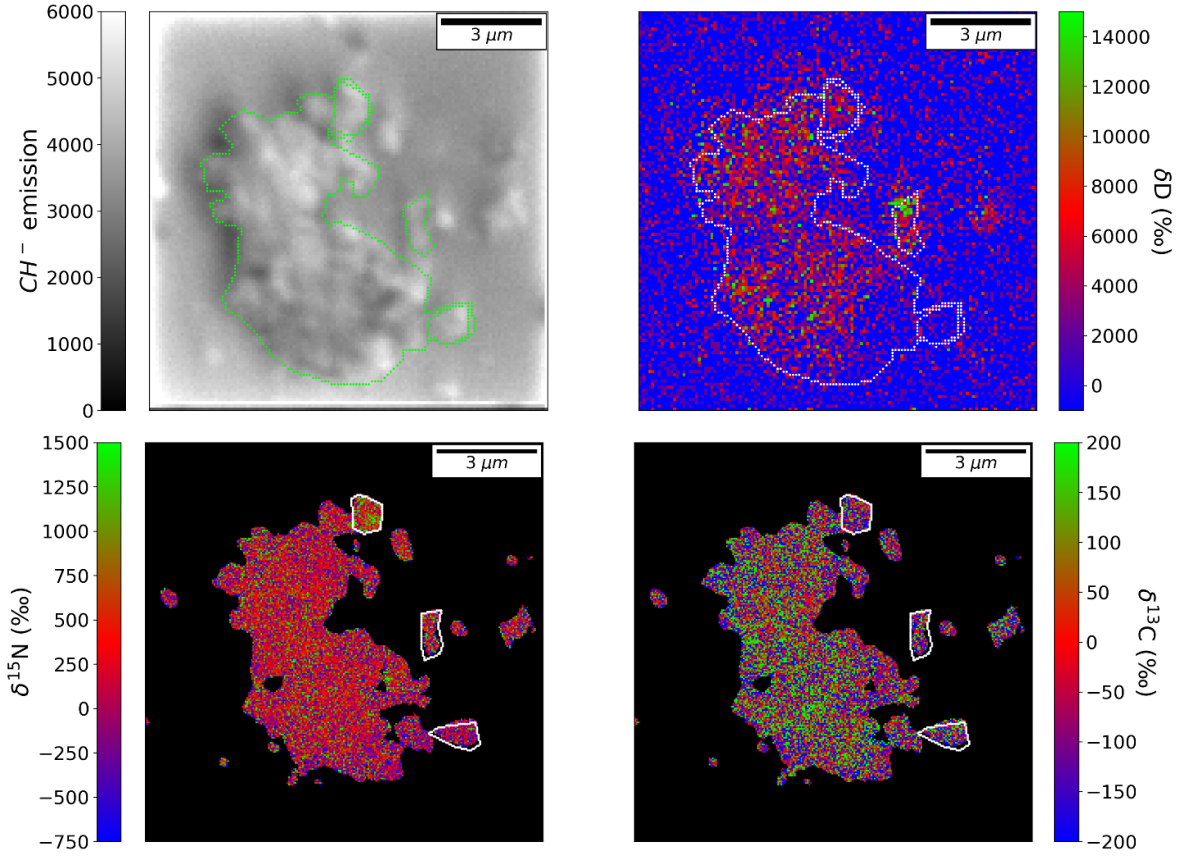

Figure 2-6: Top left: CH^- image of the DC43 C1 fragment analyzed by NanoSIMS. Top right, bottom left and bottom right: δD, $\delta^{15}N$ and $\delta^{13}C$ images. Three regions of interest are drawn in white in yellow where abnormal isotopic compositions are observed.

2.3.1.3. *UCAMM DC18 in a gold foil*

Three fragments of the DC18 UCAMM deposited on a gold foil were analyzed by NanoSIMS. Secondary electron microscopy images of the three fragments labeled A, B and C are shown in *Figure 2-7*. Fragment A is a single piece, 40µm long and 17µm large, fragment B consists of several small pieces of matter grouped on a 27x20 µm² area, and fragment C is made of two pieces with a total dimension of 18x7 µm².

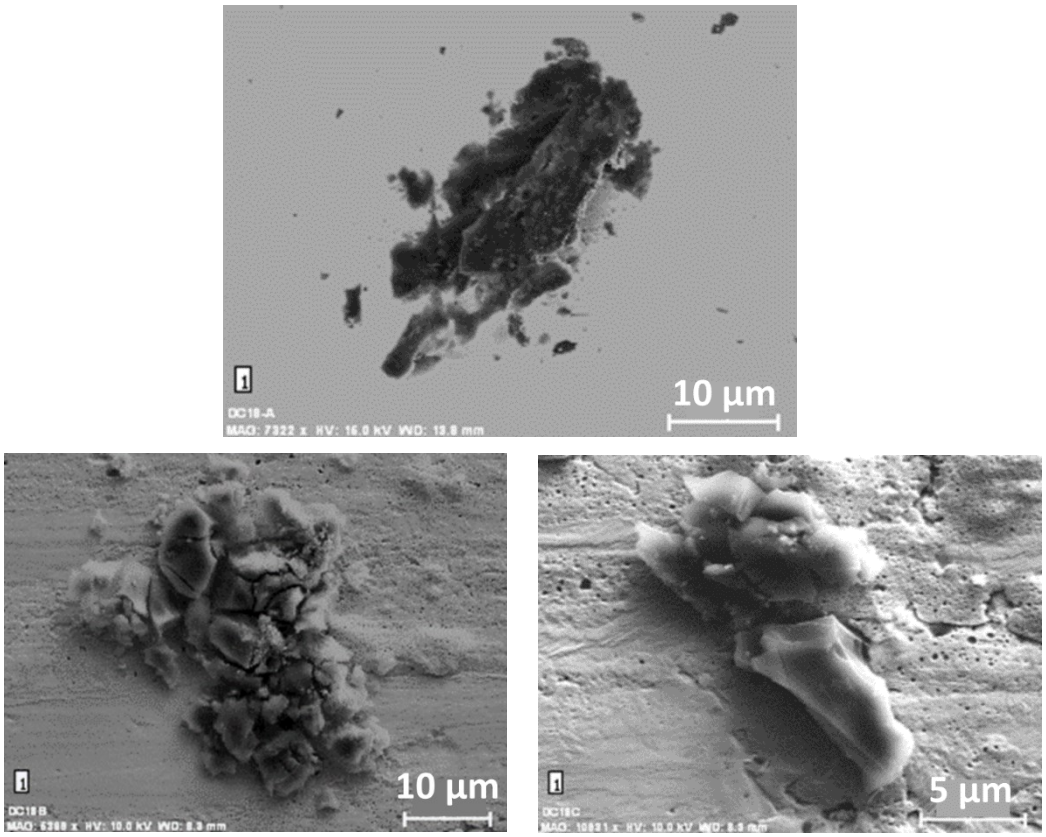

Figure 2-7: SEM images of DC18 fragments A (top), B (bottom left) and C (bottom right) analyzed by NanoSIMS. They were deposited on a gold foil.

The isotopic maps of hydrogen and nitrogen on the fragment B are reported on *Figure 2-8*. The isotopic maps on fragments A and C are detailed in the annex 5.1.3. Carbon isotopic images on DC18 are not reported due to an interruption of the monitoring of the magnetic field (magnet, *Figure 2-2*) during the acquisition. Nitrogen data were validated by re-measuring the fragments and the Si_3N_4 standards subsequently. Unfortunately, the carbon standards could not be measured.

The three fragments present very similar bulk D/H and $^{15}N/^{14}N$ ratio: $\delta D \approx 960‰$, $\delta^{15}N \approx -120‰$ (*Figure 2-9* and Table 2-2). A peculiar grain of fragment C measured with an ROI has $\delta D = -60 \pm 70‰$ and $\delta^{15}N = -58 \pm 70‰$. Based on several ROIs (drawn in yellow and white on *Figure 2-8* and on the annex 5.1.3 figures), DC18 seems to show a correlation between the lower δD and higher $\delta^{15}N$ values relative to its bulk composition, as observed in DC309 over a larger range of variation. The bulk D/H of DC18 is the lowest one measured in UCAMMs from the Concordia collection so far.

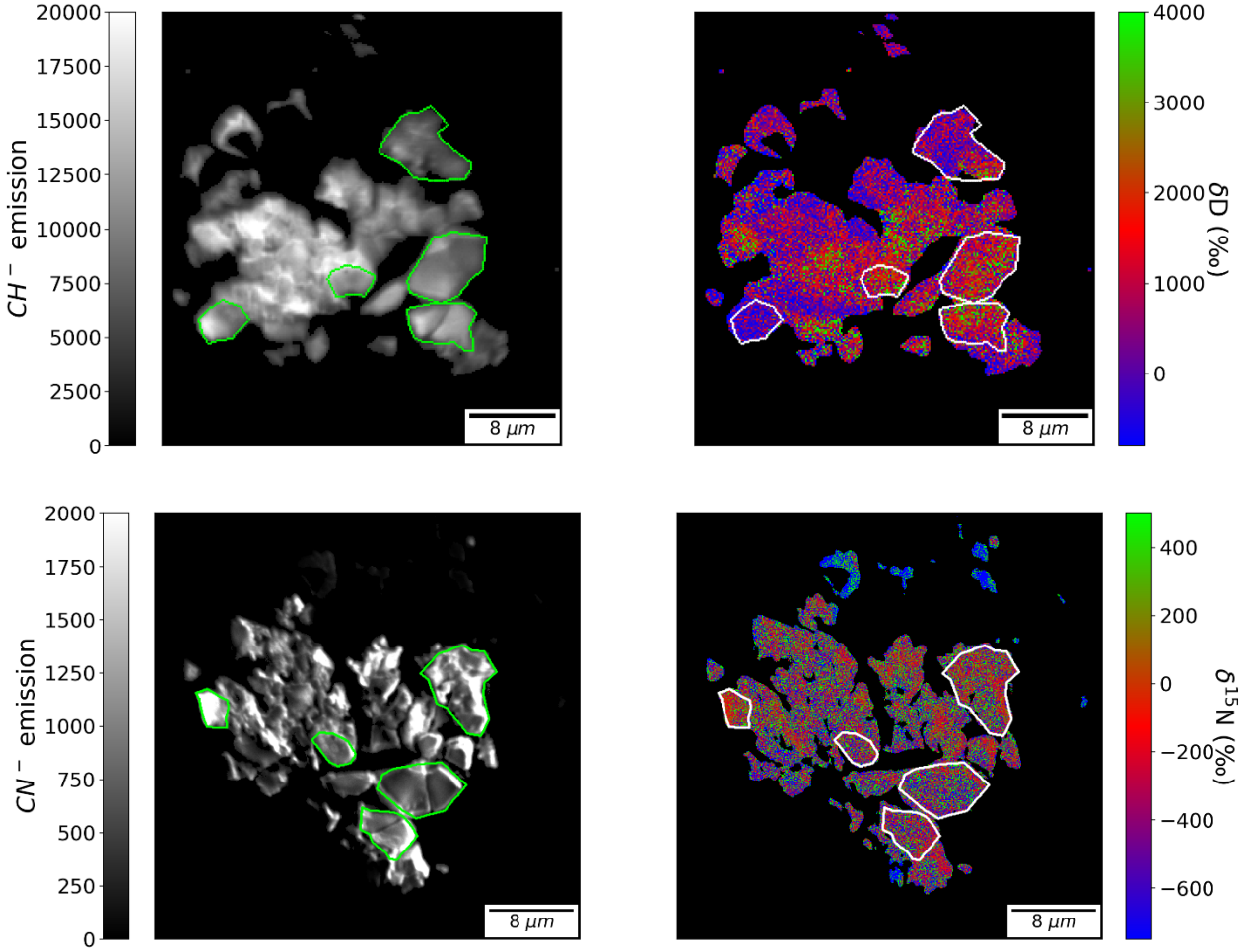

Figure 2-8: Top left: CH^- image of the DC18 B fragment analyzed by NanoSIMS. Top right: δD image of DC18 B. Bottom left: CN- image of DC18 B. Bottom right: $\delta^{15}N$ image of DC18 B. Five regions of interest are drawn in white in yellow. The ROI at the left side of the image sample an organic matter with a deuterium composition close to the SMOW value and $^{15}N/^{14}N$ higher than the bulk composition.

2.3.1.4. *The UCAMMs analyzed at EPL: summary*

The three UCAMMs analyzed at Carnegie EPL present distinct bulk isotopic compositions (*Figure 2-9*). Although DC18 and DC309 share a same low ^{15}N-nitrogen composition, below -100‰, the organic matter of DC309 is 6 to 7 times more enriched in D than DC18. DC43 has a ^{15}N-rich composition, with a substantial D-enrichment. It also contains anomalous grains bearing different isotopic signatures. Carbon fractionation in DC309 and DC43 slightly varies from 30‰ to -12‰. These results are discussed in chapter 4.

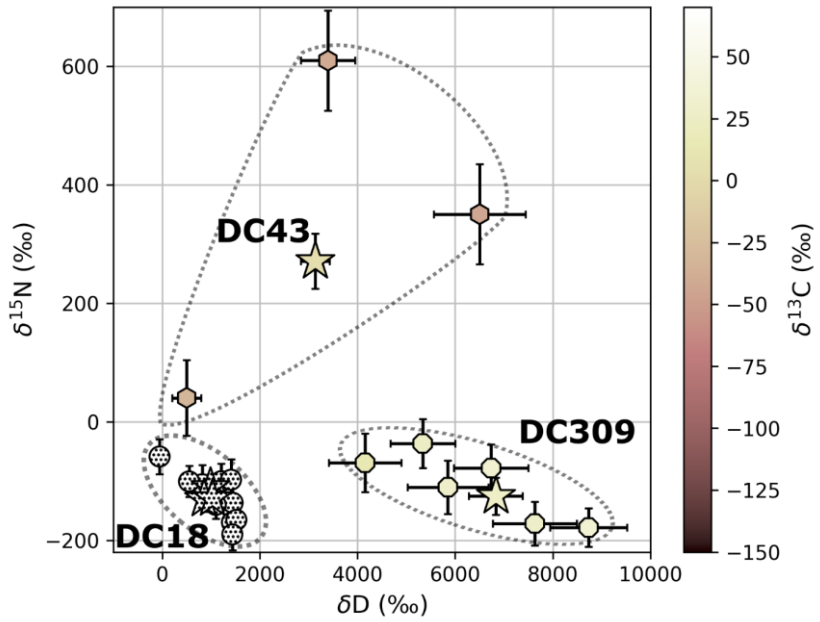

Figure 2-9. The D, ^{15}N and ^{13}C enrichments measured in UCAMMs DC309, DC43 and DC18 at Carnegie EPL. The δ^{13}C composition is given by the pink color bar. The bulk isotopic bulk values of the UCAMMs are indicated by stars. Solid circles, hexagons and octagons account for isotopic values measured on ROIs on DC18, DC43 and DC309 respectively. The ^{13}C/^{12}C ratios of DC18 are not available (see section 2.3.1.3).

Table 2-2: D/H, $^{15}N/^{14}N$ and $^{13}C/^{12}C$ ratios measured in DC309, DC43, DC18A, DC18B and DC18C. Isotopic ratios are also indicated with the δ notation. Errors at 1σ are computed by combining the error on the IMF correction factor and the errors on the statistics on the image. $^{13}C/^{12}C$ ratios on DC18 are not available (see section 2.3.1.3).

UCAMM		D/H ($x10^{-4}$)	δD (‰)	$^{15}N/^{14}N$ ($x10^{-3}$)	$\delta^{15}N$ (‰)	$^{13}C/^{12}C$ ($x10^{-2}$)	$\delta^{13}C$ (‰)
DC309	Bulk	12.2 ± 0.9	6800 ± 500	3.22 ± 0.12	-125 ± 31	1.154 ± 0.018	27 ± 16
	1	15.2 ± 1.2	8700 ± 800	3.02 ± 0.12	-178 ± 32	1.162 ± 0.020	34 ± 16
	2	13.4 ± 1.3	7600 ± 900	3.05 ± 0.14	-171 ± 37	1.155 ± 0.021	28 ± 16
	3	11.0 ± 1.3	5800 ± 800	3.30 ± 0.17	-110 ± 45	1.155 ± 0.024	28 ± 16
	4	8.0 ± 1.2	4200 ± 700	3.42 ± 0.18	-69 ± 50	1.139 ± 0.024	14 ± 16
	5	12.0 ± 1.2	6700 ± 800	3.39 ± 0.15	-78 ± 40	1.161 ± 0.021	33 ± 16
	6	9.9 ± 1.0	5300 ± 700	3.54 ± 0.15	-36 ± 41	1.151 ± 0.021	25 ± 16
DC43	Bulk	6.4 ± 0.5	3100 ± 300	4.67 ± 0.17	272 ± 46	1.111 ± 0.021	-12 ± 18
	1	6.8 ± 0.9	3400 ± 600	5.92 ± 0.31	610 ± 85	1.066 ± 0.028	-51 ± 25
	2	11.7 ± 1.5	6500 ± 900	4.97 ± 0.31	350 ± 84	1.064 ± 0.030	-54 ± 27
	3	2.3 ± 0.5	500 ± 300	3.83 ± 0.24	41 ± 64	1.076 ± 0.030	-42 ± 26
DC18A	Bulk	3.1 ± 0.1	990 ± 80	3.27 ± 0.08	-110 ± 23	-	-
	1	3.8 ± 0.2	1440 ± 110	3.17 ± 0.11	-136 ± 29	-	-
	2	3.4 ± 0.2	1200 ± 100	3.31 ± 0.11	-100 ± 30	-	-
	3	2.8 ± 0.1	820 ± 90	3.29 ± 0.12	-105 ± 32	-	-
	4	3.7 ± 0.2	1400 ± 110	3.32 ± 0.13	-98 ± 35	-	-
DC18B	Bulk	2.9 ± 0.1	850 ± 80	3.20 ± 0.08	-130 ± 21	-	-
	1	2.8 ± 0.2	1420 ± 120	3.05 ± 0.10	-170 ± 27	-	-
	2	2.4 ± 0.1	550 ± 80	3.31 ± 0.10	-100 ± 26	-	-
	3	3.9 ± 0.2	1510 ± 160	3.07 ± 0.12	-165 ± 33	-	-
	4	3.8 ± 0.2	1430 ± 130	2.98 ± 0.10	-190 ± 27	-	-
	5	1.5 ± 0.1	-60 ± 70	3.46 ± 0.11	-58 ± 30	-	-
DC18C	Bulk	3.2 ± 0.1	1030 ± 90	3.20 ± 0.08	-129 ± 22	-	-
	1	3.3 ± 0.2	1090 ± 110	3.16 ± 0.09	-140 ± 23	-	-
	2	3.1 ± 0.2	1010 ± 100	3.22 ± 0.09	-124 ± 24	-	-

2.4 C, H and N isotopic analyses on UCAMM DC94

Four NanoSIMS sessions were performed, between October 2012 and February 2014, to acquire D/H, $^{15}N/^{14}N$ and $^{13}C/^{12}C$ images on the DC94 UCAMM fragment (see Table 2-3). The D/H and $^{15}N/^{14}N$ acquisitions were performed within the course of N. Bardin Ph.D. thesis (2012-2015), on the same 50x50 µm² areas at Institut Curie (Orsay, France) while the $^{13}C/^{12}C$ measurements were made on 20x20 µm² areas at IMPMC-MNHN (Paris, France). In order to obtain a comprehensive dataset on the correlations between H, N and C isotopic compositions, this work presents a new analysis of these data on a selected set of acquisitions. The processing of DC94 data was performed from the raw data and using the same dedicated procedure developed for the UCAMMs analyzed at EPL (see section 2.3.1) that combined the OpenMIMS software and specially developed routines in Python programming language.

A presentation of the DC94 is made and the Carbon acquisitions are detailed, followed by the presentation of the Deuterium and Nitrogen acquisitions. Then, the three sets of data are combined to get systematic measurements of the isotopic composition of the DC94 fragment.

2.4.1. Anterior analyses on DC94

The DC94 UCAMM was identified in the 5th filter of the 2006 Antarctic expedition. The particle originally measured 53x66 µm and was fragmented in more than 20 fragments which were used to perform various characterizations such as Raman and IR spectroscopy (Dartois et al., 2013; Dartois et al., 2018), TOF-SIMS (Briani et al., 2012) and SEM/EDX.

A DC94 fragment was deposited and crunched on a gold foil in order to perform NanoSIMS analyses. *Figure 2-10* shows an image of the fragment acquired by secondary electrons microscopy. After preparation, its size was 125x125 µm². The characteristics of the DC94 fragment have been previously reported by Bardin (2015). The fragment has been analyzed several times with the NanoSIMS instrument at Institut Curie (October 2012, July 2013) and IMPMC-MNHN (January 2014) resulting in hydrogen, carbon and nitrogen isotopic maps (Table 2-3). Its H and N isotopic composition was extensively studied in N. Bardin Ph.D. thesis. However, the carbon data were not fully analyzed and reported. Here we summarize the results of her work and present new analysis on the carbon data as well as correlations between the H, N and C isotopic data.

On the *Figure 2-10*, areas analyzed during the $^{13}C/^{12}C$ sessions are represented by white squares whereas areas of the $^{15}N/^{14}N$ and D/H sessions, analyzed during the N. Bardin Ph.D. thesis are reported in blue. The zones where the $^{13}C/^{12}C$, D/H and $^{15}N/^{14}N$ acquisitions overlap define the zones A, B, C and D discussed in this section. Details on these zones are given in Table 2-3. Acquisitions are named by their corresponding number followed by the first letters of the element investigated (Carb for carbon, Nit for nitrogen and Deut for deuterium). The 5-Deut and 5-Nit acquisitions included C_2^- images which were used to align the two set of data. The sub-section A, B and C were defined by comparing the $^{12}C^-$ images of acquisitions 7-8-Carb, 7-9-Carb and 7-10-Carb with the C_2^- images of 5-Deut and 5-Nit. For the zone 6, we used the C_2H^- image of 6-Deut to perform the alignment with the C_2^- image of 6-Nit and the $^{12}C^-$ image of 6-1-Carb.

In a first approach, a set of regions of interest (ROI) was defined based on identifiable structures on the C_2^-, $^{12}C^-$ and C_2H^- images to measure correlated isotopic ratios. The isotopic composition of carbon in the ROIs is first reported for A, B, C and D regions. Deuterium and nitrogen 15 enrichments are then reported in the corresponding ROIs. In the last section, the Carbon acquisitions are rotated in order to

overlap with the Deuterium and Nitrogen acquisitions. Isotopic ratios are then measured following a hexagonal mesh in the zone A, B and C. Due to strong distortions observed in zone D between the images of 7-6-Carb and 6-Deut and 6-Nit, the latter procedure was not applied to that zone.

Table 2-3: characteristics of the NanoSIMS sessions performed on zones A, B, C and D shown in Figure 2-10. For each session, the name and the date of the acquisition is listed in the column "Acquisition". The "Original size" column indicates the dimension of the sampled area (µm²) and the raster size (pixel², in parentheses). Sub-selection of the NanoSIMS maps were needed to match the different acquisitions. The size of the sub-selection is indicated in the column "Restricted size".

Zone	Session $^{13}C/^{12}C$			Session D/H			Session $^{15}N/^{14}N$		
	Acquisition	Original size	Restricted size	Acquisition	Original size	Restricted size	Acquisition	Original size	Restricted size
A	7-9-Carb 02.03.2014	20x20 (256x256)	20x20 (256x256)	5-Deut 07.22.2013	50x50 (512x512)	22x24 (222x247)	5-Nit 07.29.2013	50x50 512x512	22x24 (222x247)
B	7-10-Carb 02.03.2014	20x20 (256x256)	20x11 (256 x140)	5-Deut 07.22.2013	50x50 (512x512)	21x13 (218x132)	5-Nit 07.29.2013	50x50 512x512	21x13 (218x132)
C	7-8-Carb 02.03.2014	20x20 (256x256)	20x17 (256 x216)	5-Deut 07.22.2013	50x50 (512x512)	21x19 (216x196)	5-Nit 07.29.2013	50x50 512x512	21x19 (216x196)
D	7-6-Carb 01.31.2014	20x20 (256x256)	20x20 (256x256)	6-Deut 10.30.2012	50x50 (512x512)	23x23 (234x234)	6-Nit 07.29.2013	50x50 512x512	23x23 (234x234)

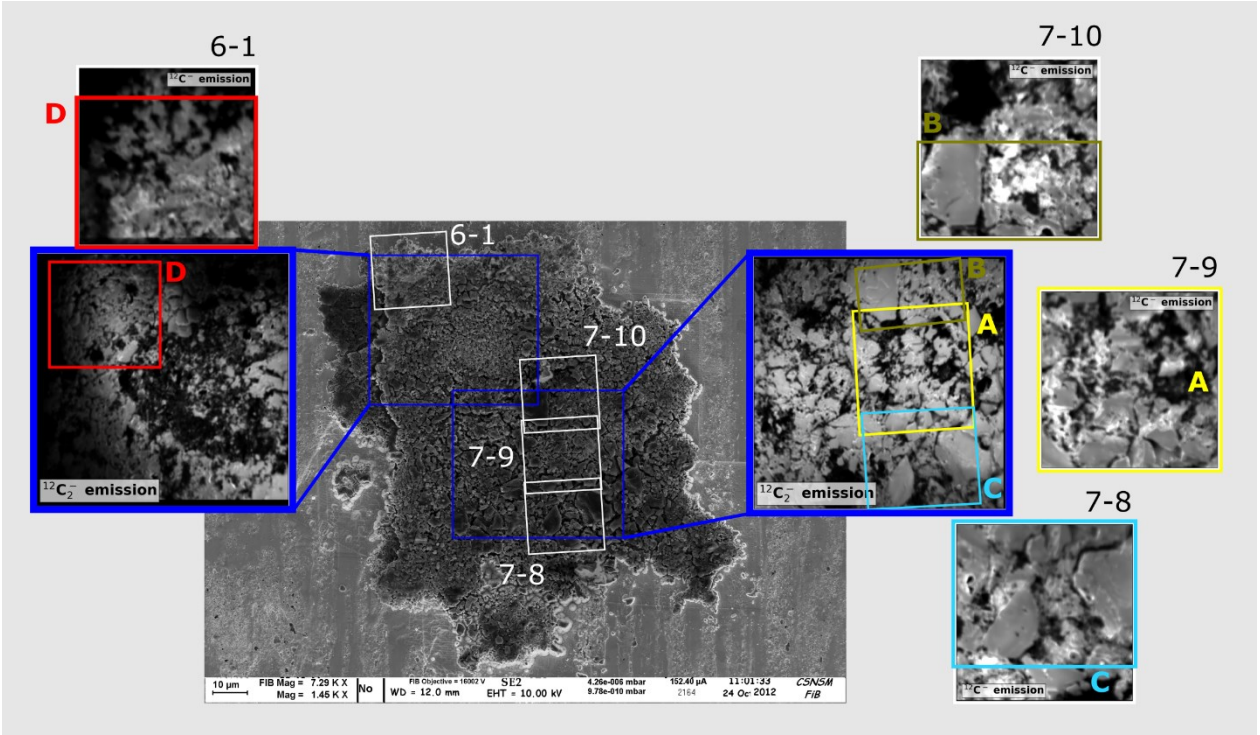

Figure 2-10: SEM image of the analyzed DC94 fragment (from Bardin (2015)). The image is flipped to match with the NanoSIMS maps' orientation. Dark blue squares represent the region where H and N isotopic ratios were measured. White squares indicate the regions where C isotopic ratio were measured. Zone A, B, C and D were defined on regions where the hydrogen, nitrogen and carbon acquisitions overlap.

2.4.2. $^{13}C/^{12}C$ data on DC94

The isotopic images on the zone 6-1, 7-8, 7-9 and 7-10 were acquired in January and February 2014 at IMPMC-MNHN (Paris, France). Acquisitions were made on 20 µm size zones sampled on 256x256 pixels. For each zone, a set of 200 consecutive plans of $^{12}C^-$, $^{13}C^-$, $^{16}O^-$, $^{17}O^-$, $^{18}O^-$ ions were collected with a primary Cs^+ ion probe of 1.0 pA. The dwell time was 1.0 ms/pixel. All the images were corrected from dead time and quasi simultaneous (QSA) effects. During the analyses, the instrumental mass fractionation (IMF) affecting the $^{13}C/^{12}C$ ratio was controlled with a kerogen standard (see annex 5.1.2). Results presented in the following section are corrected from the IMF. In order to maximize the counting statistics, the 200 consecutive plans were aligned and summed. The alignment procedure consisted in simple translations. It was based on the $^{12}C^-$ consecutive plans and the transformation matrix was subsequently applied to the $^{13}C^-$ sequence.

A set of regions of interest (ROIs) were used to measure the $^{13}C/^{12}C$ content on specific areas of zone A, B, C and D. A more systematic analysis was completed by applying a hexagonal mesh to the $^{13}C^-$ and $^{12}C^-$ maps. The isotopic ratio of an ROI or an individual mesh i was given by the ratio of the sum of $^{12}C^-$ and $^{13}C^-$ counts:

$$R_i = \frac{\sum_{pixels} N(^{13}C^-)}{\sum_{pixels} N(^{12}C^-)}$$

Hexagonal meshes are made 624 pixels, *i.e.* 3.8 µm², given the spatial definition of the acquisitions. Relative errors related to the counting statistics on the ROIs are often lower than 0.5 %.

2.4.2.1. *DC94, $^{13}C/^{12}C$: zone A*

The 7-9-Carb acquisition zone overlap entirely with the Zone A. *Figure 2-10* and Figure 2-11 show the $^{12}C^-$ emission image resulting from the sum of the 200 consecutive plans of acquisition 7-9-Carb. Several patches of matter appear on the $^{12}C^-$ image (see Figure 2-11, left). These patches, homogeneous on the $^{12}C^-$ image were used to define 13 ROIs, labeled from A-1 to A-13, where the $^{13}C/^{12}C$ ratio was measured (see Figure 2-11 right and Table 2-4).

In addition to the 13 ROIs, a hexagonal mesh was applied to the zone 7-9 in order to derive the ^{13}C-abundance independently from the structures visible on the $^{12}C^-$ image (*Figure 2-12*, left). The measured $\delta^{13}C$ values are shown in *Figure 2-12*, right, with the ROI and mesh measurements represented in dark and light blue respectively.

Based on the hexagonal mesh, the median value of the $\delta^{13}C$-image is -99‰. However, two populations of mesh units appear: one with the lowest $\delta^{13}C$, ranging from -100 ‰ to -160 ‰ and the other with $\delta^{13}C$ ranging from -50 ‰ to -110 ‰. The low $\delta^{13}C$ are associated with slightly higher $^{12}C^-$ emission and mainly correspond to the patches of organic matter. The ROIs with highest $\delta^{13}C$ correspond to matter that present a fluffier aspect on the $^{12}C^-$ images excepted for the A-12 ROI (-64 ± 10 ‰) which have a smooth aspect.

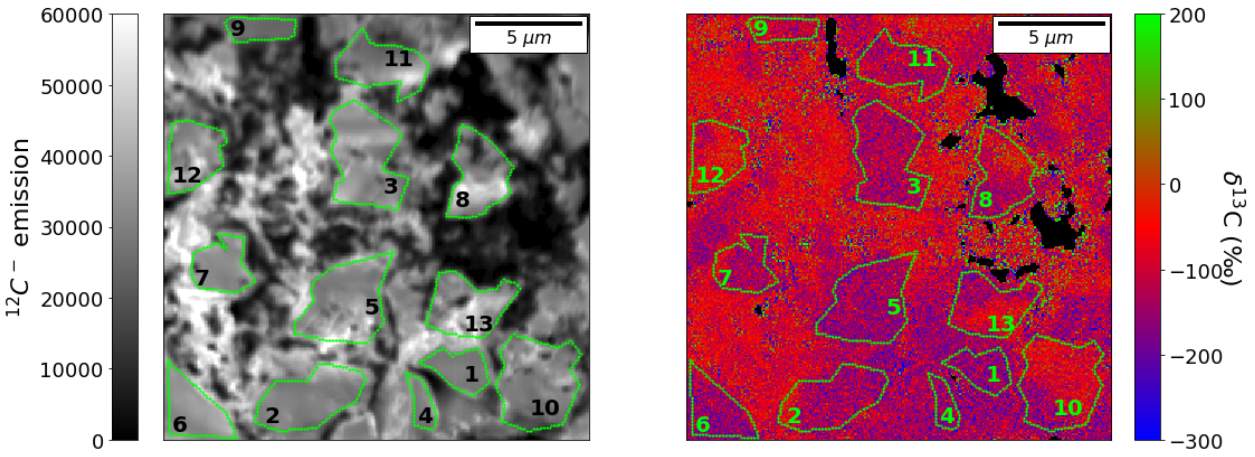

Figure 2-11. Left: $^{12}C^-$ emission image of the 7-9 zone resulting from the sum of 200 plans. Right: $\delta^{13}C$ map on zone 7-9. The isotopic map is masked at 3%.

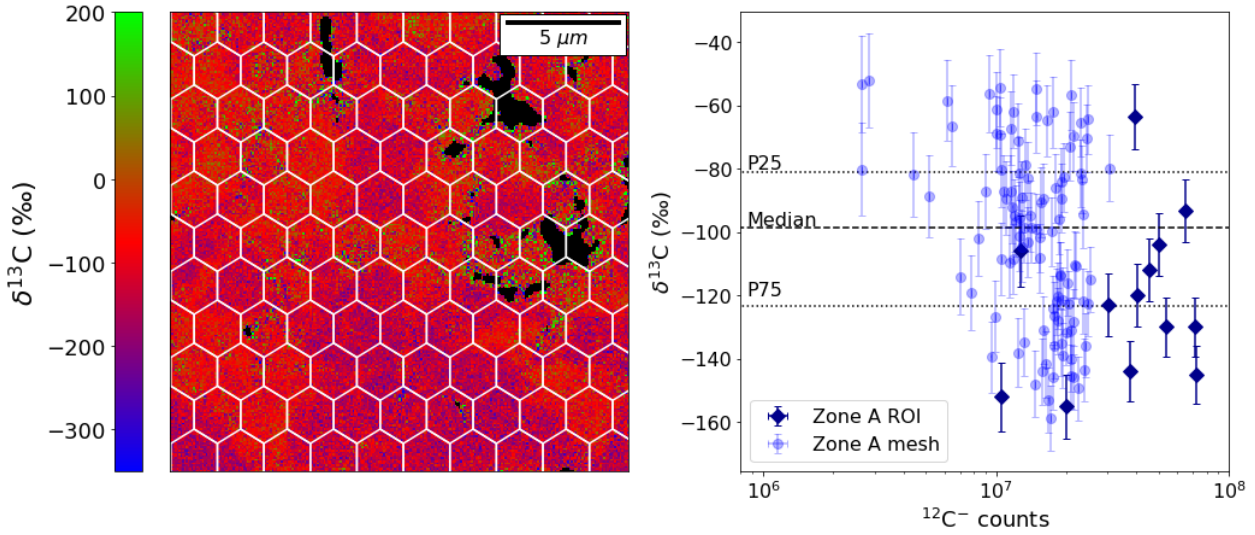

Figure 2-12. Left: hexagonal mesh on the $\delta^{13}C$ map of zone 7-9. The cells of the mesh are made of 624 pixels. Right: $\delta^{13}C$ values against the total number of 12C- ions collected for the cells of the hexagonal mesh (light blue) and the 13 ROIs (dark blue). The isotopic map is masked at 3%.

2.4.2.2. *DC94, $^{13}C/^{12}C$: zone B*

Zone B corresponds to a sub-section of the 7-10-Carb acquisition. *Figure 2-13* shows the $^{12}C^-$ emission of 7-10-Carb (left) and the selected sub-section matching with zone B (top right). Four ROIs (B-1 to B-4) were defined in structures visible on the $^{12}C^-$ image. They all display low ^{13}C-abundance, with $\delta^{13}C$ ranging from -55‰ to -127‰. An extremely low $\delta^{13}C$ value equal to -127 ± 9 ‰ is observed in B-1 which correspond to a large patch of organic matter. The isotopic image (*Figure 2-13*, bottom right) shows that this patch of matter displays a homogeneous ^{13}C-low composition. A hexagonal mesh applied to zone B highlight the presence of two distinct populations, as in zone A (*Figure 2-14*), with $\delta^{13}C$ ranging from -40‰ to -100‰ for the hotter and from -100‰ to -160‰ for the colder. The median value of the $\delta^{13}C$ image is -96‰, laying between its two poles.

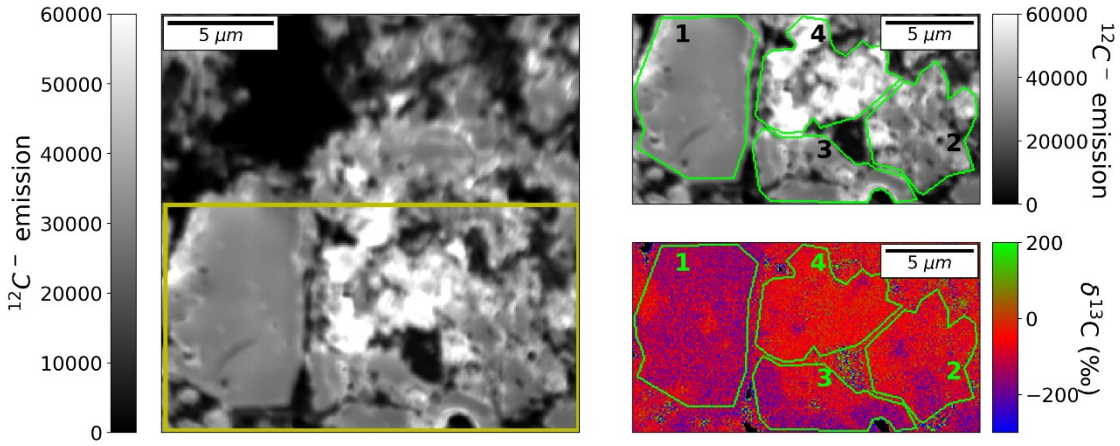

Figure 2-13. Left: $^{12}C^-$ emission image of the 7-10 zone. The yellow rectangle shows the region B. Top right: zone B, fraction of the image analyzed in this section. $^{13}C/^{12}C$ mesurments have been limited to this region for comparisons with the D/H and $^{15}N/^{14}N$ measurements. Bottom right: $\delta^{13}C$ image of the zone B.

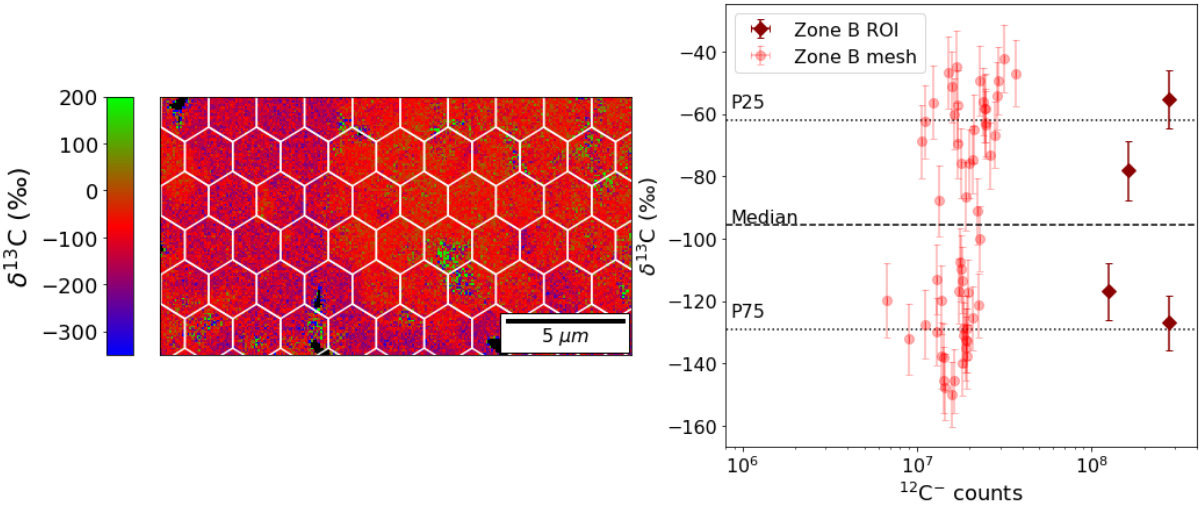

Figure 2-14. Left: hexagonal mesh applied on zone B. Right: $\delta^{13}C$ values against the total number of $^{12}C^-$ ions collected for the cells of the hexagonal mesh (light red) and the 4 ROIs (dark red).

2.4.2.3. *DC94, $^{13}C/^{12}C$: zone C*

Acquisition 7-8-Carb overlaps with zone C as indicated on *Figure 2-15* (yellow square). The $^{13}C/^{12}C$ ratios were measured on 9 ROIs (C-1 to C-9) drawn on the $^{12}C^-$ image. Isotopic $^{13}C/^{12}C$ ratios were measured in the whole zone C thanks to a hexagonal mesh (*Figure 2-16*). As observed in zone A and B, the ^{13}C-low ratios are correlated with large patch of organic matter (*Figure 2-15* and *Figure 2-16*). However, the two distinct populations of pixels visible on *Figure 2-12* and *Figure 2-14* (right) are not fully resolved on *Figure 2-16*. This might be due to the presence of very large patches of ^{13}C-depleted matter (ROIs 1 and 2) in the image that dominate the pixel distribution. The median value of $\delta^{13}C$ on zone C is -105 ‰.

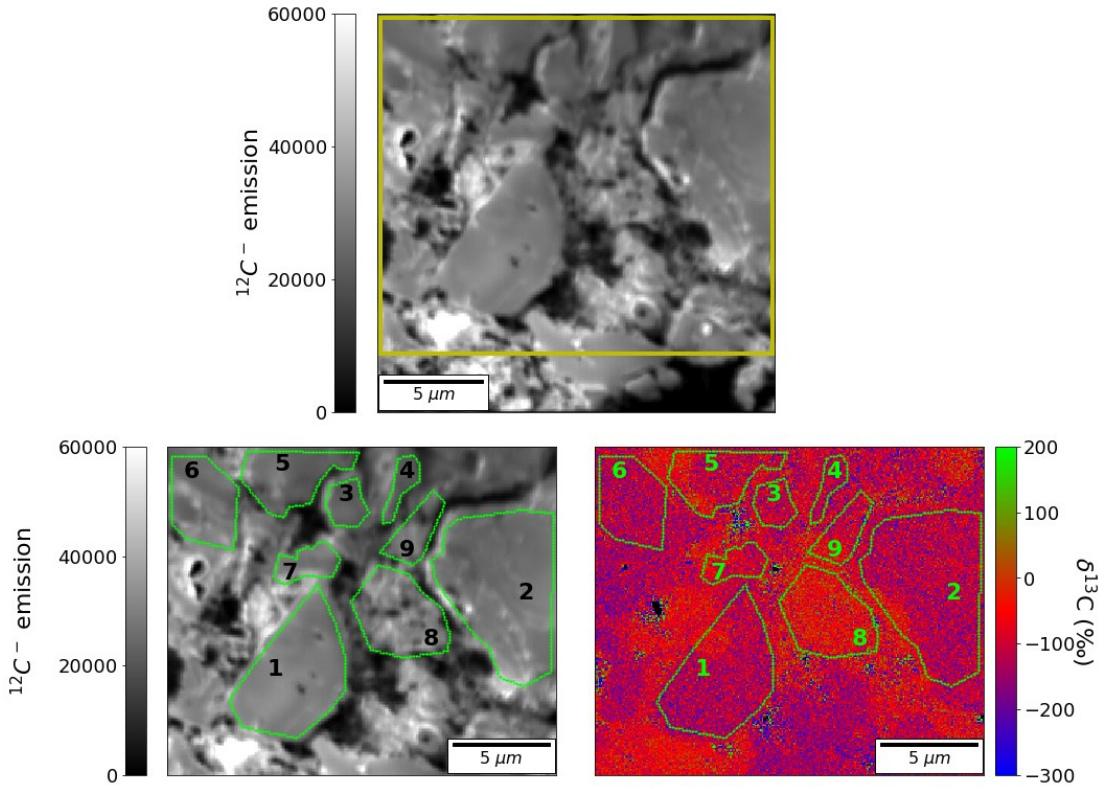

Figure 2-15: Top: $^{12}C^-$ emission image of the 7-8-Carb acquisition. The yellow rectangle shows the zone C, where $^{13}C/^{12}C$, D/H and $^{15}N/^{14}N$ measurements are performed. Bottom left: $^{12}C^-$ emission in zone C. Bottom right: $\delta^{13}C$ image of the zone C.

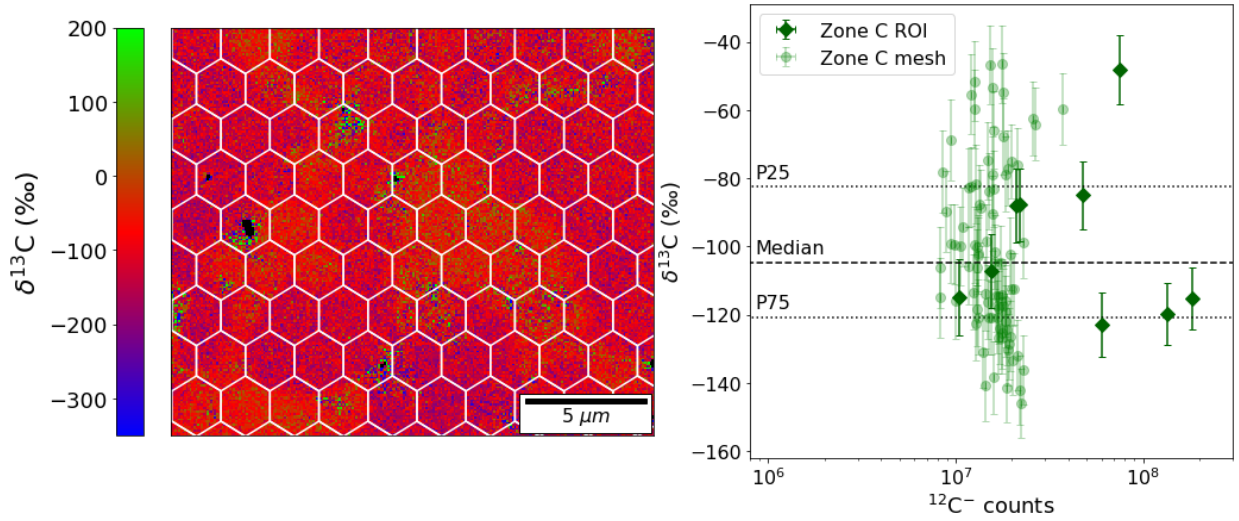

Figure 2-16. Left: hexagonal mesh applied on the zone C. Right: $\delta^{13}C$ values against the total number of $^{12}C^-$ ions collected for the cells of the hexagonal mesh (light red) and the 9 ROIs (dark red).

2.4.2.4. *DC94, $^{13}C/^{12}C$: zone D*

The zone D corresponds to the bottom part of acquisition 6-1-Carb. We defined 7 ROIs based on $^{12}C^-$ image (Figure 2-17). The $\delta^{13}C$ values measured in these ROIs are ranging from -25‰ to -100‰, lower than in the zone A, B and C. This general feature was confirmed by measurements made with a hexagonal mesh on the zone D. Half of the individual mesh have $\delta^{13}C$ values comprised between -26‰ and -52‰, with a median value at -41‰. These values are compatible with the low pole observed on zone A, B and C. A small area, at the right of ROI 5 and the left of ROI 7 displays a $\delta^{13}C$ below -100‰. Zone D does not exhibit the large patches of organic matter observed in the other zones. The ROIs of zone D correspond to less compact units of organic matter.

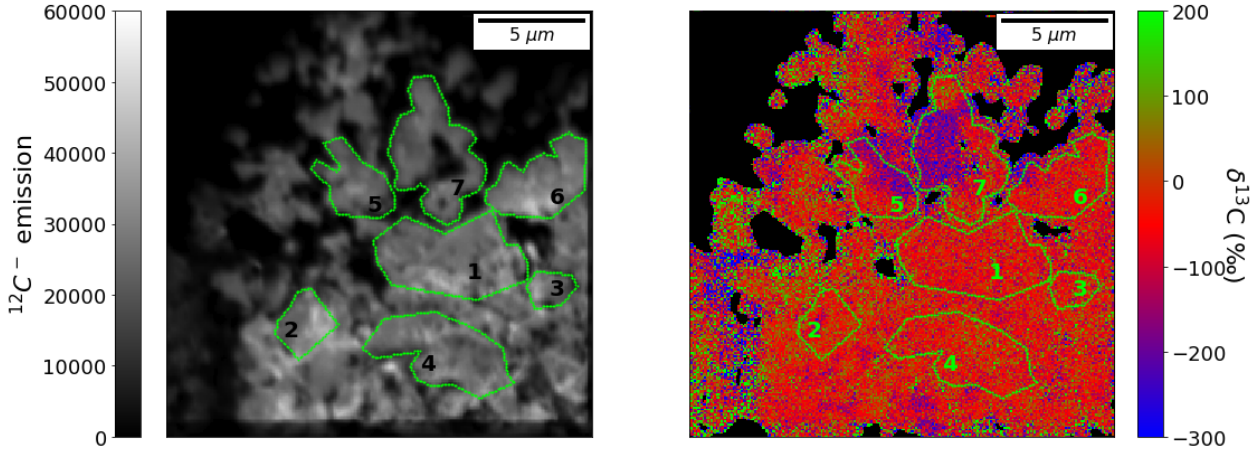

Figure 2-17. Right: $^{12}C^-$ emission image of the zone 6-1. Left: $\delta^{13}C$ image on the same zone.

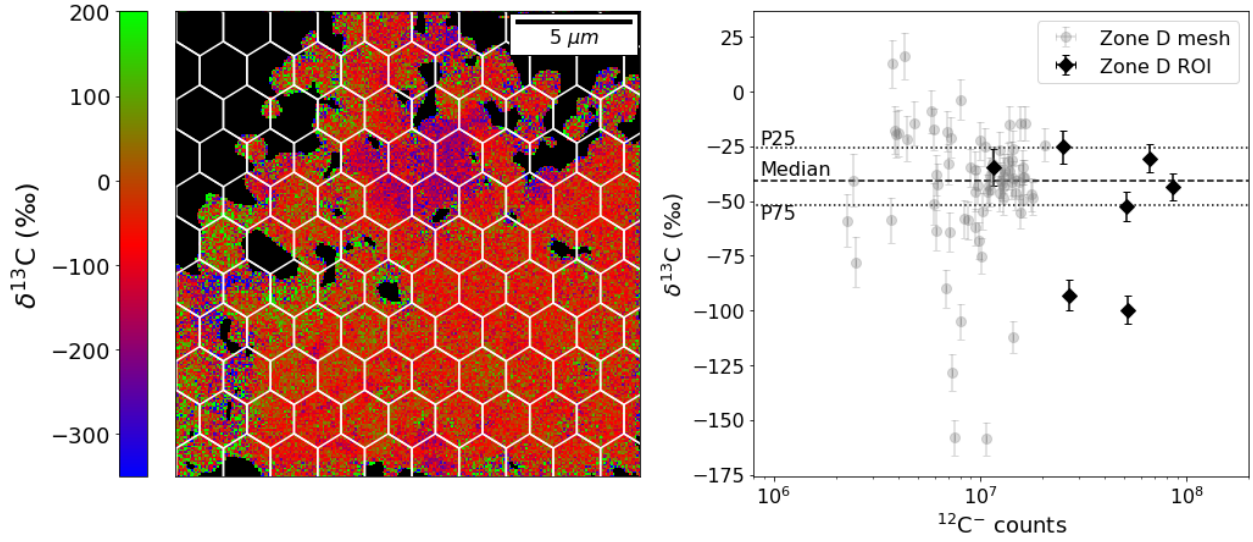

Figure 2-18. Left: hexagonal mesh on the zone D. Right: $\delta^{13}C$ values against the total number of $^{12}C^-$ ions collected for the cells of the hexagonal mesh (light gray) and the 7 ROIs (black).

2.4.2.5. *UCAMM DC94, $^{13}C/^{12}C$ summary*

Isotopic mapping of $^{13}C/^{12}C$ abundances in 4 zones of the DC94 UCAMM reveal a ^{13}C-depleted organic matter. Two distinct poles of organic matter are observed. The ^{13}C-cold matter is characterized by $\delta^{13}C$ values ranging between - 100‰ and -150‰. It is mostly present in the zone A, B and C under the form of large and smooth patches of carbonaceous matter. Low $\delta^{13}C$ values are also observed on zone D but in much lower abundance and without being associated with a patch structure. Zone D exhibits a matter with larger $^{13}C/^{12}C$ ratios, with $\delta^{13}C$ values ranging from -26‰ to - 52‰. This pole is also observed on the zone A, B and C as a fluffier matter with a broader spread which can reach -100‰.

The bulk median $\delta^{13}C$ values of zone A, B and C are very close the one another, around -100‰, resulting from a mix of the two poles of matter. Conversely, the bulk median value of zone D is -41‰ consisting in matter with a higher $\delta^{13}C$ value.

Table 2-4: Measurements of the $^{13}C/^{12}C$ ratios on the ROI on the zone A, B, C and D. Values reported are corrected from the IMF. Errors are indicated at 1σ.

ROI	$^{13}C/^{12}C \pm Err$ (x 10^{-3})	$\delta^{13}C \pm Err$ (‰)
A-1	9.50 ± 0.11	-155 ± 10
A-2	9.77 ± 0.11	-130 ± 9
A-3	9.78 ± 0.10	-129 ± 9
A-4	9.53 ± 0.12	-152 ± 11
A-5	9.61 ± 0.10	-145 ± 9
A-6	9.62 ± 0.11	-144 ± 10
A-7	9.86 ± 0.11	-123 ± 10
A-8	9.98 ± 0.11	-112 ± 10
A-9	10.05 ± 0.13	-106 ± 11
A-10	10.19 ± 0.11	-93 ± 10
A-11	9.89 ± 0.11	-120 ± 10
A-12	10.52 ± 0.12	-64 ± 10
A-13	10.07 ± 0.11	-104 ± 10
B-1	9.81 ± 0.10	-127 ± 9
B-2	10.36 ± 0.11	-78 ± 9
B-3	9.92 ± 0.10	-117 ± 9
B-4	10.62 ± 0.11	-55 ± 9
C-1	9.89 ± 0.10	-120 ± 9
C-2	9.94 ± 0.10	-115 ± 9
C-3	10.03 ± 0.12	-107 ± 11
C-4	9.95 ± 0.13	-114 ± 11
C-5	10.28 ± 0.11	-85 ± 10
C-6	9.86 ± 0.10	-123 ± 9
C-7	10.25 ± 0.12	-88 ± 11
C-8	10.69 ± 0.11	-48 ± 10
C-9	10.25 ± 0.12	-88 ± 11
D-1	10.75 ± 0.07	-44 ± 6
D-2	10.95 ± 0.08	-25 ± 7
D-3	10.85 ± 0.09	-34 ± 8
D-4	10.89 ± 0.07	-31 ± 7
D-5	10.19 ± 0.08	-93 ± 7
D-6	10.65 ± 0.07	-52 ± 6
D-7	10.12 ± 0.07	-100 ± 6

2.4.3. D/H and $^{15}N/^{14}N$ in DC94

Hydrogen and nitrogen isotopic ratios of DC94 were measured during 3 sessions in 2012 and 2013, at Institut Curie (Orsay, France) and were presented in details in N. Bardin Ph.D. thesis. For the purpose of this study, we summarize here the set of data on two zones, named 5 and 6, overlapping with zones A, B, C and D (Table 2-5 and blue squares on *Figure 2-10*). In this section, the D and ^{15}N enrichments measured on the ROIs corresponding to the ones defined for the carbon acquisition (see section 2.4.2) are presented. Measurements based on a hexagonal mesh are presented in the section 2.4.4, along with the rotated maps of the carbon acquisitions.

Table 2-5: Analytical conditions of the NanoSIMS sessions on the DC94 fragment.

Date	Ions	Zone	Primary current (pA)	Dwell time (ms/pix)	N plans	Laboratory
07.22.2013	$^{12}CH^-$, $^{12}C_2^-$, $^{12}C_2H^-$, $^{12}C_2D^-$	5	11.5	0.5	119 (120)	Institut Curie
10.30.2012	$^{12}C_2H^-$, $^{12}C_2D^-$, $^{12}OH^-$, $^{12}OD^-$	6	7.7	1.0	30	Institut Curie
07.29.2013	$^{12}CH^-$, $^{12}C_2^-$, $^{12}C^{14}N^-$, $^{12}C^{15}N^-$	5	10.0	0.5	118 (120)	Institut Curie
07.29.2013	$^{12}CH^-$, $^{12}C_2^-$, $^{12}C^{14}N^-$, $^{12}C^{15}N^-$	6	10.0	0.5	160	Institut Curie

2.4.3.1. *DC94, zone 5 (zone A, B and C)*

The zone 5 was analyzed in July 2013 (5-Deut and 5-Nit sessions, see Table 2-3). It consists on a 512x512 pixels image on a 50x50 µm² area. The 5-Deut session consisted in the multi-collection of the $^{12}CH^-$, $^{12}C_2^-$, $^{12}C_2H^-$, $^{12}C_2D^-$ ions extracted with a 11.5 pA primary ion probe. The dwell-time was set to 0.5 ms/pixel. One hundred and twenty plans were accumulated from which one was removed due to the presence of artifacts. Ions $^{12}CH^-$, $^{12}C_2^-$, $^{12}C^{14}N^-$, $^{12}C^{15}N^-$ were collected during the 5-Nit session on the same area (same raster) with a primary current set to 10.0 pA and a dwell time of 0.5 ms/pixel. From the 120 plans acquired, 2 were removed. For the two sessions, the individual ion images were corrected from dead-time and QSA prior to be summed. The instrumental mass fractionation (IMF) for the D/H and $^{15}N/^{14}N$ ratios were controlled by measuring the terrestrial anthracite DonH8 and a dedicated deuterated polystyren standard as detailed in annex 5.1.2 (Bardin et al., 2015; Sangely, 2004).

Figure 2-19 shows the C_2^- emission images acquired during the 5-Deut (left) and 5-Nit (right) sessions. Collored squares indicate the corresponding 7-8, 7-9 and 7-10 areas analyzed during the carbon sessions. The analyses presented in this section were restricted to these areas (see Table 2-3). Sizes of zone A, B and C are 222x247 pixel², 218x132 pixel² and 216x196 pixel² respectively.

The δD and $\delta^{15}N$ images of the zone A, B and C are shown on Figure 2-21, Figure 2-22 and Figure 2-23. Regions of interest defined on the 3 zones correpond to the regions of interest defined in section 2.4.2. Although the ROIs were chosen to fit as well as possible for the 5-Deut, 5-Nit and Carb sessions, they can still differ marginally. The differences are mainly caused by the evolution of the area under the succesive NanoSIMS sessions and by the variability in the aspect of the structures imaged with the $^{12}C^-$ and $^{12}C_2^-$ ions. Isotopic enrichments in D and ^{15}N in the ROIs are reported in Table 2-6.

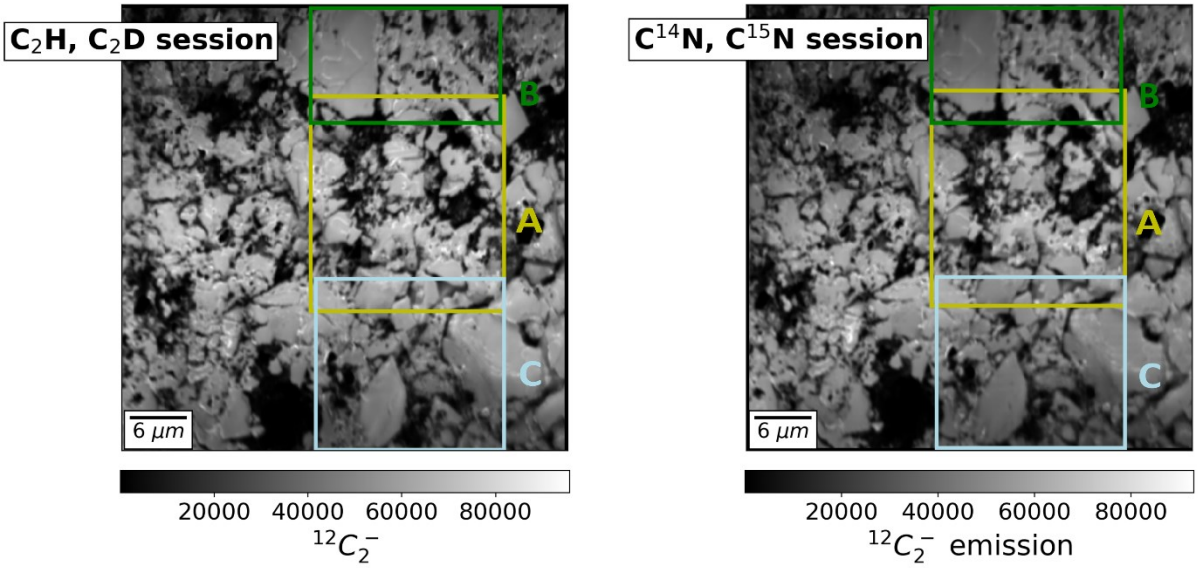

Figure 2-19: Zone 5. C_2^- images acquired by the NanoSIMS during the 5-Deut (left) and 5-Nit (right) sessions. The yellow, green and blue squares indicate the zones A, B and C where carbon measurements were performed.

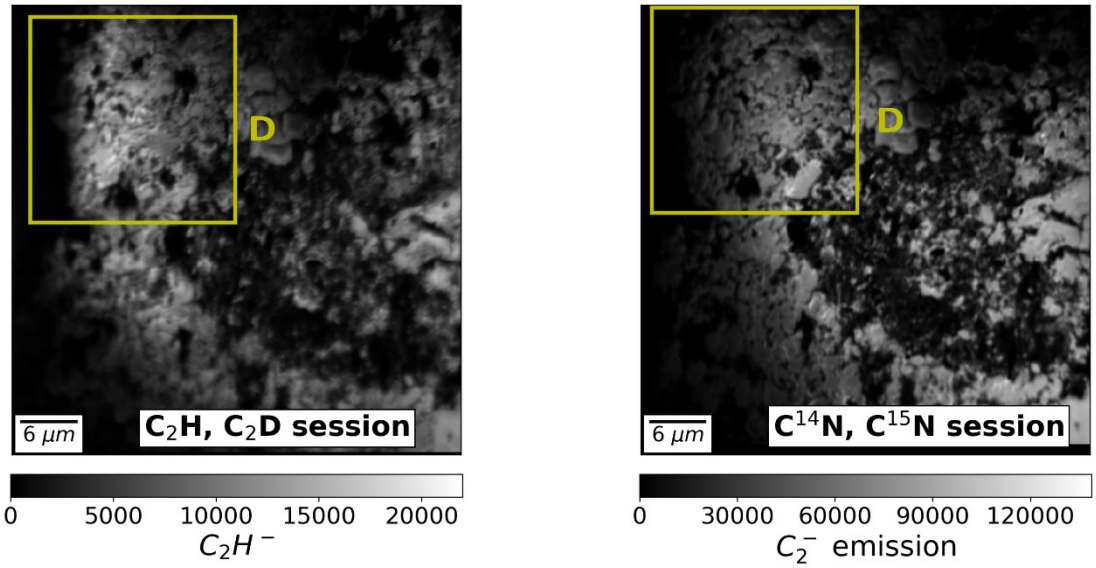

Figure 2-20: Zone 6. C_2^- images acquired during the C_2H-C_2D session in October 2012 (left) and during the $C^{14}N$-$C^{15}N$ session in July 2013 (right). The yellow square indicates the zone C where ^{13}C and ^{12}C measurements were performed. C_2^- acquisition was not performed during the October 2012 session.

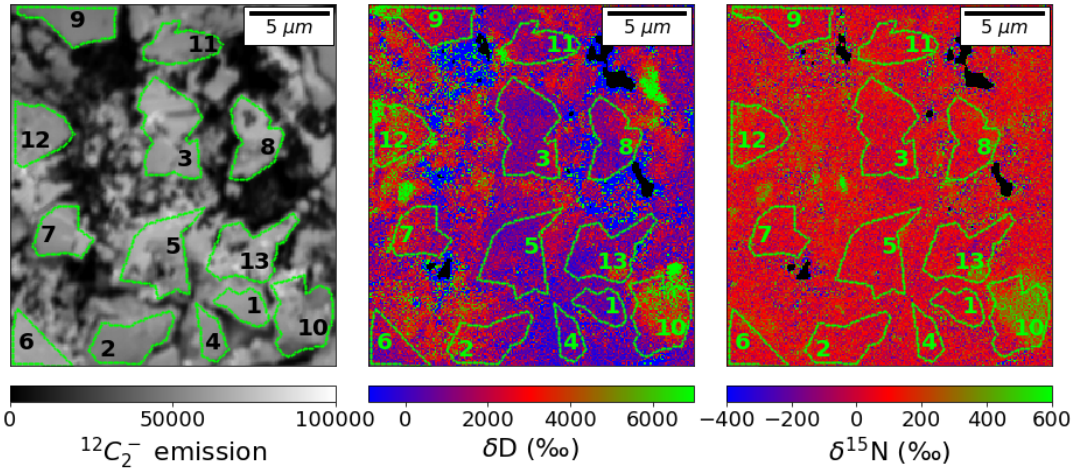

Figure 2-21. Left: regions of interest (ROI) on the zone A (C_2^- emission image). δD (center) and δ^{15}N (right) maps on zone A.

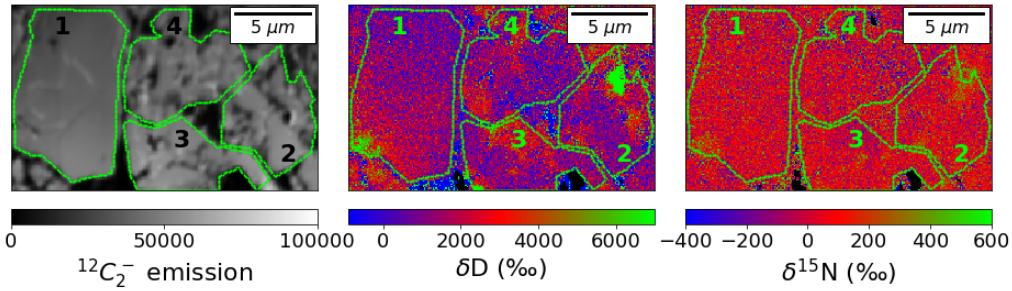

Figure 2-22. C_2^- image of zone B with its 4 ROIs (left). δD (center) and δ^{15}N (right) maps on zone B.

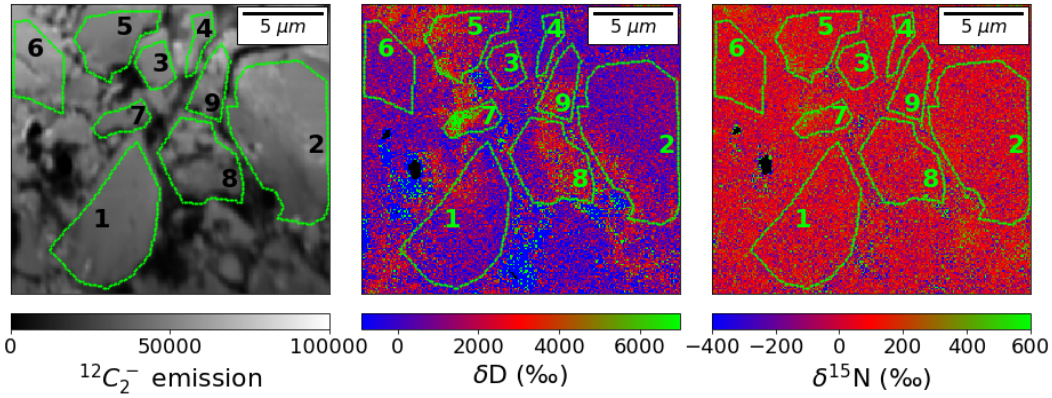

Figure 2-23. Left: C_2^- image of zone C with its 9 ROIs. δD (center) and δ^{15}N (right) maps on zone C.

2.4.3.2. *DC94 zone 6 (zone D)*

The hydrogen isotopic composition on zone 6 which overlaps with zone D was analyzed during a first session in October 2012. Ions $^{12}C_2H^-$, $^{12}C_2D^-$, $^{12}OH^-$, $^{12}OD^-$ were collected on a 50x50 µm² area (512x512 pixels) with a 7.7 pA ion probe. The dwell time was set to 1.0 ms/pixel. All the consecutive 30 plans were corrected from dead-time and QSA effects and summed. A Don-H8 sample and a deuterated polystyrene standard (Bardin et al., 2015) were used to control the IMF.

The nitrogen isotopic content of zone 6 was measured in another session in July 2013, consecutively to the analysis of zone 5 (see section 2.4.3.1 and Table 2-5). The 6-Nit acquisition consisted in 160 consecutive plans recording the $^{12}CH^-$, $^{12}C_2^-$, $^{12}C^{14}N^-$, $^{12}C^{15}N^-$ signals with a 10.0 pA ion probe. The dwell time was set to 0.5 ms/pixel. A dead-time and QSA correction was applied to all the individual plans before summing them. As for the zone 5, the IMF was controlled with the Don-H8 sample.

Because $^{12}C_2^-$ ions were not collected during the 6-Deut acquisitions, the identifications of structures and ROIs are based on comparisons between the C_2H^- image from 6-Deut and the C_2^- image from 6-Nit. Figure 2-24 shows the ion images associated with the δD and $\delta^{15}N$ maps.

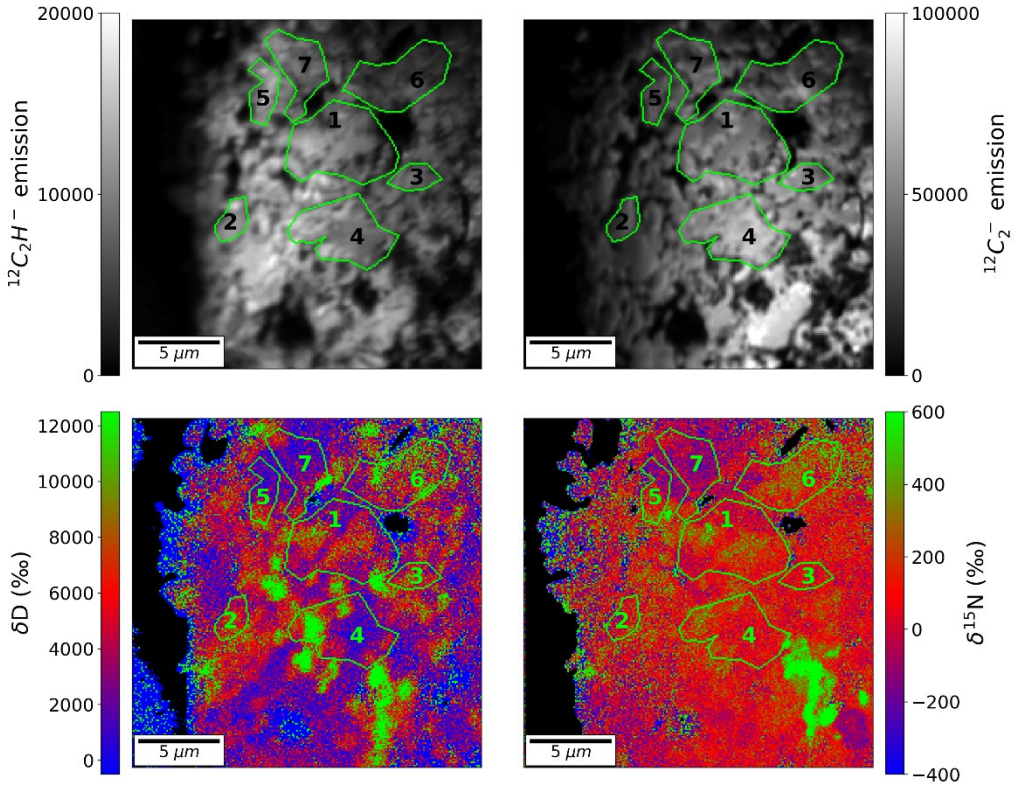

Figure 2-24. Left: C_2H^- images of zone D with the 7 ROI analyzed (top) and δD image on the corresponding zone (bottom). Right: C_2^- image of the zone C (top) and the corresponding $\delta^{15}N$ image (bottom).

2.4.3.3. *UCAMM DC94, D/H and 15N/14N summary*

Isotopic mapping of D/H in 4 zones of DC94 allow to identify a heterogeneous D-rich signature of the organic matter with δD values ranging between about 500‰ and 6000‰. Zones A, B and C present the lower δD value (lower than 4000‰, measured in ROIs) while δD up to 6000‰ are observed in zone D. Local D/H heterogeneities appear to be more frequent in zone D (Figure 2-24) than in zones A, B and C (Figure 2-21, Figure 2-22, Figure 2-23). The $\delta^{15}N$ values in the zones A, B, C and D are fairly homogeneous with a mean value of $\delta^{15}N_{mean}$ = 63‰ and isolated hotspots (e.g. $\delta^{15}N$ = 264 ± 7‰, ROI A-10 in Table 2-6).

Table 2-6: D/H and $^{15}N/^{14}N$ ratios measured in the ROIs on zones A, B, C and D . Ratios have been corrected from the IMF. Errors are indicated at 1σ.

ROI	D/H ± err (10^{-4})	δD ± err (‰)	$^{15}N/^{14}N$ ± err (10^{-3})	$\delta^{15}N$ ± err (‰)
A-1	2.71 ± 0.08	740 ± 51	3.79 ± 0.03	30 ± 8
A-2	4.50 ± 0.10	1892 ± 69	3.89 ± 0.02	59 ± 7
A-3	3.31 ± 0.06	1123 ± 41	3.87 ± 0.02	52 ± 6
A-4	2.41 ± 0.08	544 ± 54	3.82 ± 0.03	40 ± 9
A-5	3.03 ± 0.06	948 ± 41	3.85 ± 0.02	48 ± 6
A-6	3.82 ± 0.10	1454 ± 62	3.93 ± 0.03	70 ± 7
A-7	4.85 ± 0.11	2112 ± 71	3.87 ± 0.03	52 ± 7
A-8	3.64 ± 0.08	1336 ± 51	4.01 ± 0.02	90 ± 6
A-9	4.88 ± 0.10	2131 ± 67	3.91 ± 0.03	62 ± 7
A-10	6.82 ± 0.13	3376 ± 84	4.65 ± 0.03	264 ± 7
A-11	3.94 ± 0.09	1527 ± 60	3.94 ± 0.03	71 ± 7
A-12	7.12 ± 0.14	3574 ± 92	4.08 ± 0.03	110 ± 7
A-13	3.39 ± 0.08	1179 ± 49	3.92 ± 0.02	67 ± 6
B-1	3.96 ± 0.06	1545 ± 40	3.85 ± 0.02	48 ± 5
B-2	4.72 ± 0.08	2031 ± 54	3.94 ± 0.02	71 ± 5
B-3	4.31 ± 0.08	1764 ± 48	3.85 ± 0.02	48 ± 5
B-4	3.94 ± 0.07	1529 ± 46	3.80 ± 0.02	33 ± 6
C-1	3.06 ± 0.06	966 ± 40	3.83 ± 0.02	42 ± 5
C-2	3.05 ± 0.05	957 ± 35	3.84 ± 0.03	45 ± 5
C-3	3.12 ± 0.10	1003 ± 66	3.83 ± 0.04	41 ± 8
C-4	2.31 ± 0.09	484 ± 56	3.80 ± 0.03	33 ± 9
C-5	4.95 ± 0.11	2178 ± 71	3.97 ± 0.02	80 ± 6
C-6	3.29 ± 0.07	1114 ± 47	3.84 ± 0.02	45 ± 6
C-7	7.32 ± 0.19	3700 ± 123	4.13 ± 0.04	123 ± 10
C-8	4.50 ± 0.10	1888 ± 64	3.84 ± 0.02	43 ± 6
C-9	3.55 ± 0.10	1281 ± 64	3.78 ± 0.03	27 ± 7
D-1	9.46 ± 0.48	5072 ± 306	3.98 ± 0.02	83 ± 5
D-2	10.34 ± 0.61	5641 ± 391	3.80 ± 0.04	32 ± 11
D-3	10.66 ± 0.66	5844 ± 422	3.81 ± 0.03	37 ± 8
D-4	10.04 ± 0.51	5445 ± 324	3.99 ± 0.02	86 ± 6
D-5	6.21 ± 0.40	2983 ± 256	3.65 ± 0.03	-6 ± 9
D-6	11.25 ± 0.60	6222 ± 387	4.14 ± 0.03	126 ± 7
D-7	6.37 ± 0.38	3091 ± 245	3.30 ± 0.02	-101 ± 6

2.4.4. Correlation of H, C and N isotopic maps on DC94

In the following section, the $\delta^{13}C$, $\delta^{15}N$ and δD maps on DC94 are compared.

2.4.4.1. *Correlation between $\delta^{13}C$, $\delta^{15}N$ and δD measured in the ROIs*

Isotopic measurements based on the ROIs detailed in Table 2-4 and Table 2-6 are combined to investigate isotopic correlations on the zones A, B, C and D. Results are presented with colored error bars on the $\delta^{13}C$ against $\delta^{15}N$ and $\delta^{13}C$ against δD graphs on *Figure 2-26*.

The $\delta^{15}N$ values in the regions of interest appears to be homogeneous, ranging from 30‰ to 100‰. Two anomalous spots are observed on ROIs A-10 and D-7 with $\delta^{15}N$ equal to 264 ± 7 ‰ and -101 ± 6 ‰ respectively. No correlation is observed between the $\delta^{15}N$ and $\delta^{13}C$ or δD variations.

Deuterium enrichments on DC94 range from about 500‰ to 6000‰. The right panel of *Figure 2-26* shows the positive correlation between the $\delta^{13}C$ and δD values measured in the ROIs (dotted line, Pearson correlation coefficient of 0.802). Whereas zones A, B and C seem to sample a similar matter with $\delta^{13}C$ in the [-150‰ ; -50‰] interval and δD in the [500‰ ; 4000‰] interval, zone D is characterized by higher ^{13}C and D contents ranging from -60‰ to -20‰ and 4500‰ to 6000‰ respectively at the exception of ROIs D-5 and D-7 that display low $\delta^{13}C$ and δD comparable with those observed on zones A, B and C.

2.4.4.2. *Correlation between $\delta^{13}C$, $\delta^{15}N$ and δD maps using a mesh*

In order to perform a complete comparison between the images, the 7-8-Carb, 7-9-Carb and 7-10-Carb acquisitions were resized and rotated to match with the 5-Nit and 5-Deut acquisitions on zones A, B and C (see *Figure 2-25*). The sizes of $^{12}C^-$ images of zones A, B and C were rescaled by a factor 0.90 ± 0.04 to match with the sizes of the zones in the 5-Nit and 5-Deut sets (Table 2-3). In the rescaled images, pixels resulting from the merging of two or more pixels were filled with the average value of the original pixels. Once rescaled, the images were rotated without performing interpolation. Structures visible on the C_2^- images from 5-Nit and 5-Deut served as references to adjust the rotation. The accuracy of the operation was estimated by comparing the position of the structures on the modified $^{12}C^-$ images and C_2^- images. The same processing was applied to the $^{13}C^-$ images. Isotopic ratio images were subsequently derived. No transformations were applied on the 5-Nit and 5-Deut datasets

A hexagonal mesh was applied to the Carb, Deut and Nit acquisitions on zone A, B and C (*Figure 2-25*). Figure 5-4 in annex 5.1.4 shows the mesh on the isotopic images. Each mesh cell is made of 624 pixels accounting for 5.95 µm², based on the 5-Deut and 5-Nit spatial definition. The $\delta^{13}C$, $\delta^{15}N$ and δD values are plotted on *Figure 2-26*. Small shifts are still visible from one acquisition to the other, as a perfect overlapping of these maps is not achievable without introducing non-linear distortions of the images. Moreover, the erosion of zone A, B and C induced by the successive NanoSIMS sessions, along with the nature of the collected ions, are expected to impact the apparent structures, highlighting the necessity of a careful approach when comparing the H, C and N datasets. Still, when compared to the size of the hexagonal cells, the residual shifts resulting from the alignment process appear negligible.

For the zone D, a hexagonal mesh was applied on the deuterium and nitrogen maps but not on the carbon map. The correlation of the deuterium, nitrogen and carbon isotopic compositions in zone D is based on the ROIs.

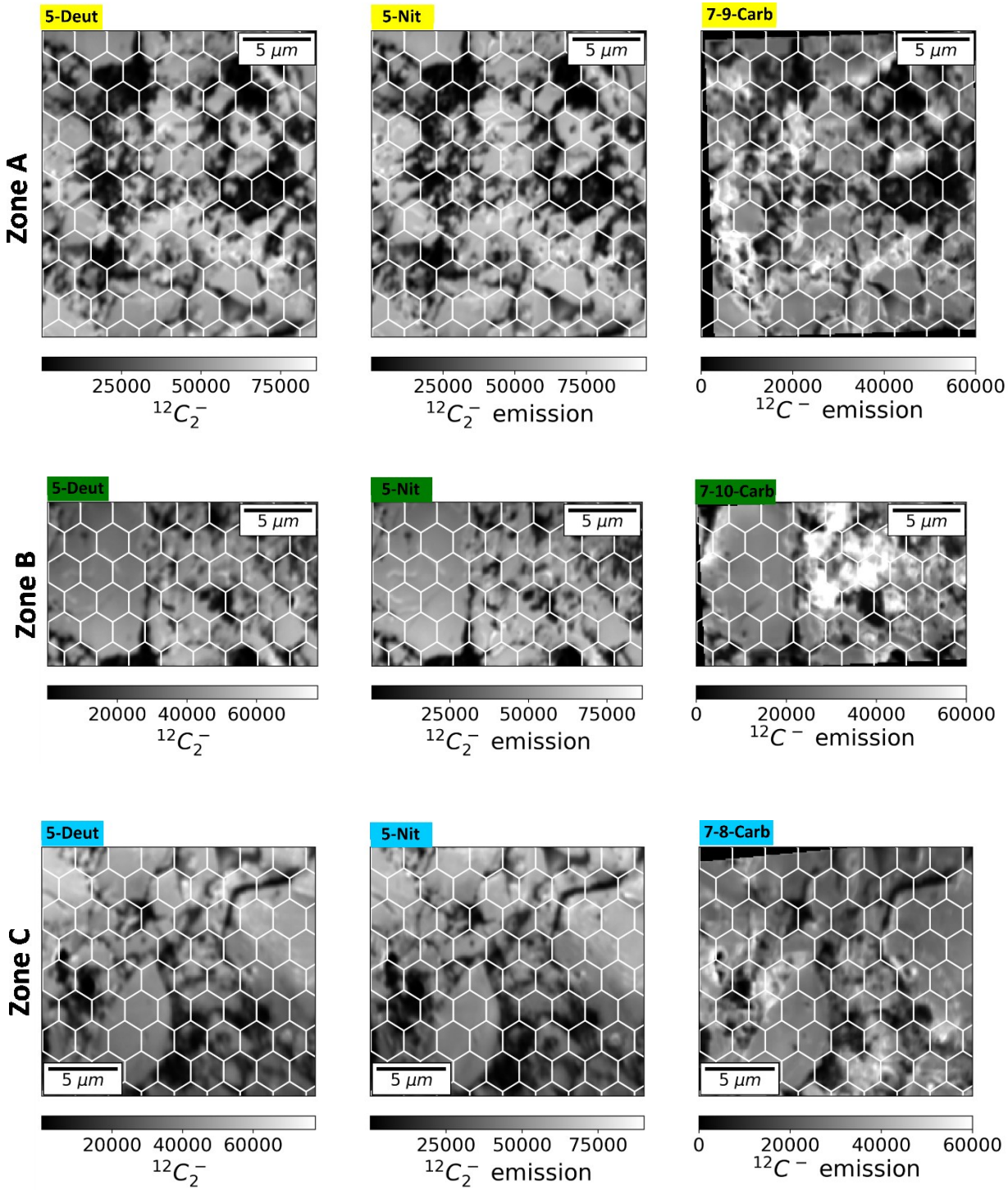

Figure 2-25: $^{12}C_2^-$ images from 5-Deut (left column), 5-Nit (middle column) and $^{12}C^-$ images from Carb acquisitions (right column) for zones A (top row), B (middle row) and C (bottom row). The transformation applied on $^{12}C^-$ data only consisted in linear operations without interpolation. $^{12}C^-$ image from the Carb acquisitions have been downsized and rotated in order to overlap the $^{12}C_2^-$ images from Deut- and Nit- acquisitions (see text). The hexagonal mesh is used to derive the correlations between $\delta^{13}C$, $\delta^{15}N$ and δD maps. The transformation applied on $^{12}C^-$ data only consisted in linear operation without interpolation.

The measurements derived from the hexagonal mesh are presented by gray error bars on *Figure 2-26*. The spread of ^{13}C, ^{15}N and D enrichments are characterized by the mean value, 0.1 and 0.9 quantiles as follow:

- $\delta^{13}C_{mean}$ = -87‰ ; $\delta^{13}C_{0.1}$ = -135‰ ; $\delta^{13}C_{0.9}$ = -58‰
- δD_{mean} = 2521‰ ; $\delta D_{0.1}$ = 836‰ ; $\delta D_{0.9}$ = 3179‰
- $\delta^{15}N_{mean}$ = 63‰ ; $\delta^{15}N_{0.1}$ = 17‰ ; $\delta^{15}N_{0.9}$ = 87‰

As observed with the ROIs' measurements and on the isotopic maps, the nitrogen isotopic composition is rather homogeneous. A single region of zone A, around ROI A-10 display an ^{15}N-enriched composition with $\delta^{15}N$ above 200‰.

The positive correlation between ^{13}C and D enrichments is confirmed by the mesh sampling, however, *Figure 2-26* (top right) indicates that the population of organic matter with higher $^{13}C/^{12}C$ ratios is statistically less sampled by the ROIs approach. This arises from the selection of ROIs on the basis of patches of matter identified on the ion images ($^{12}C^-$ and $^{12}C_2^-$): a low ^{13}C-content was preferentially sampled in comparison to the fluffy interstitial matter with, in average, higher ^{13}C-content.

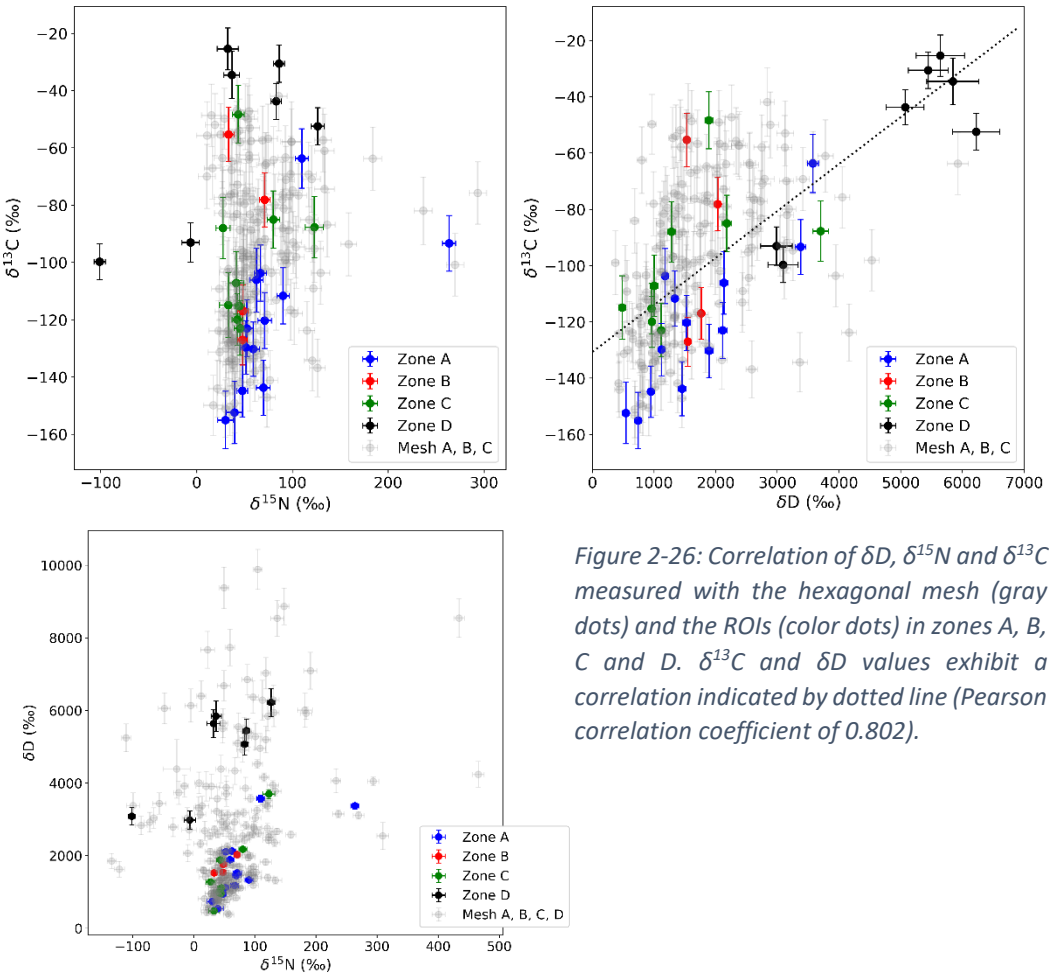

Figure 2-26: Correlation of δD, $\delta^{15}N$ and $\delta^{13}C$ measured with the hexagonal mesh (gray dots) and the ROIs (color dots) in zones A, B, C and D. $\delta^{13}C$ and δD values exhibit a correlation indicated by dotted line (Pearson correlation coefficient of 0.802).

2.5 Summary

This chapter presents analyses of the H, N and C isotopic compositions of the organic matter of UCAMMs. Isotopic imaging was performed on 5 fragments of 3 UCAMMs (DC43, DC309 and DC18) and data acquired prior this Ph.D. on another UCAMM (DC94) were sorted, in order to present the first comprehensive study of correlated D/H, $^{13}C/^{12}C$, $^{15}N/^{14}N$ ratios on several fragments of these rare particles. The bulk isotopic composition substantially differs from one UCAMM to another and large variations can also be observed within individual UCAMM fragments (*Figure 2-27*). Some isotopic heterogeneities exhibit linear correlations while others appear as isolated anomalous spots. These linear correlations are observed on UCAMM DC309 ($\delta^{15}N$ vs. δD) between a cold component [$\delta^{15}N \approx$-200‰;$\delta D \approx$8500‰] and a ^{15}N-richer component [$\delta^{15}N \approx$-30‰;$\delta D \approx$4000‰] (thick gray line in *Figure 2-27*) and on UCAMM DC94 ($\delta^{13}C$ vs. δD) between a cold $\delta^{13}C$ component [$\delta^{13}C \approx$-150‰;$\delta D \approx$800‰] and a ^{13}C-richer component [$\delta^{13}C \approx$-30‰;$\delta D \approx$6000‰] (dotted line in *Figure 2-26*). Chapter 3 presents a series of new experiment to show that the irradiation of isotopically heterogeneous ice mixtures can produce organic matter with large isotopic heterogeneities comparable to that reported in this chapter. Chapter 4 will compare the H, N and C isotopic compositions of UCAMMs to the isotopic compositions of other solar system objects and predictions of theoretical models of molecular reservoirs in the protoplanetary disk.

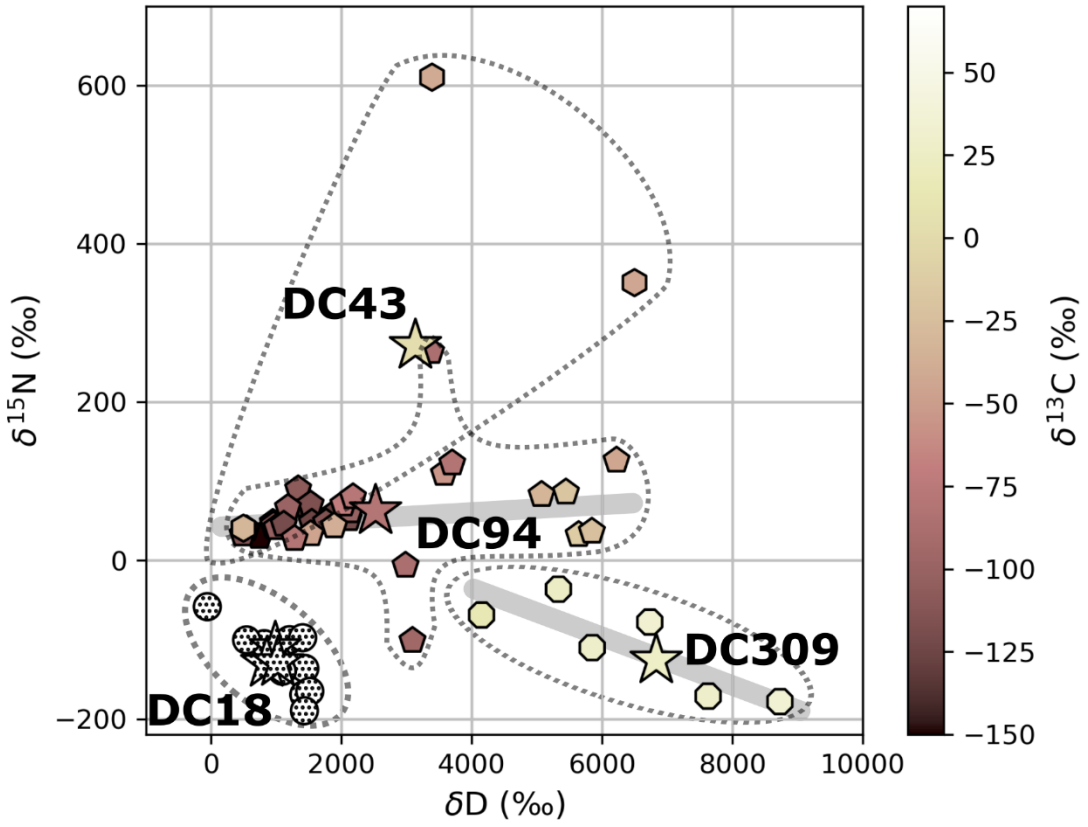

Figure 2-27: summary of the δD, $\delta^{15}N$ and $\delta^{13}C$ measured on DC309, DC18, DC43 and DC94. The color scale indicates the $\delta^{13}C$ values. Bulk composition are plotted with stars and measurements on ROIs by circles (DC18), octagons (DC309), hexagons (DC43) and pentagons (DC94). The linear correlations observed in DC309 and DC94 are represented by gray thick lines.

3 Chapter 3: Irradiation of cometary surfaces by Galactic Cosmic Rays, an experimental approach

3.1 The production and isotopic study of irradiation-induced residues

3.1.1. Motivation and experimental approach

Irradiation experiments of nitrogen-rich ice films by swift ions (energetic ions for which the electronic stopping power dominates over the nuclear stopping power) demonstrated that the irradiation of nitrogen-rich ice mantles followed by a slow annealing was able to form an organic matter with an infrared (IR) signature similar to the one of UCAMMs (*Figure 3-1*, Augé et al. (2016)). However, Augé et al. (2019) showed that the Hydrogen isotopic fractionation induced by the irradiation process itself cannot explain the large deuterium heterogeneities observed in the organic matter of UCAMMs. The isotopic heterogeneities in H, N and C in the organic matter of UCAMMs (Chapter 2) might thus be inherited from the nature of parent reservoirs.

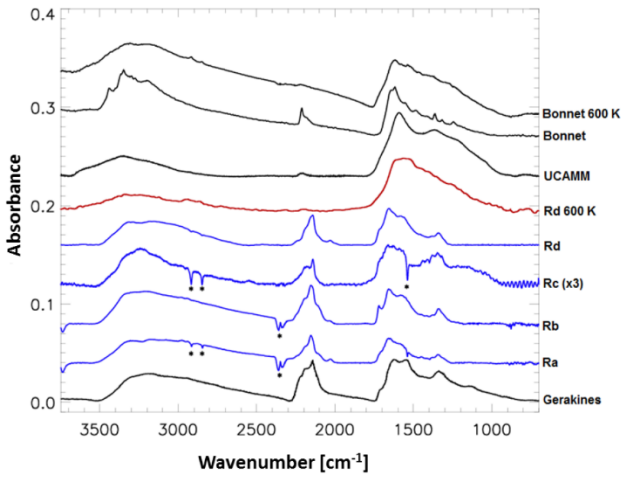

Figure 3-1 : FTIR spectra of organic residues compared to the spectrum of an UCAMM from Augé et al. (2016). The red spectrum corresponds to an organic residue formed from the irradiation of a N_2-CH_4 ice mixture subsequently annealed to 600K in order to simulate the heating experienced by UCAMMs during their atmospheric entry. The UCAMM spectrum was reported by Dartois et al. (2013). Blue spectra: residues "a" to "d" produced in Augé et al. (2016) after irradiation and annealing to 300 K. Black spectra, top: poly-HCN before and after annealing to 600 K (Bonnet et al., 2015). Bottom: pure HCN ice after irradiation with 0.8 MeV protons from Gerakines et al. (2004).

The experimental approach described in this chapter aims to reproduce the formation of organic matter induced by irradiation of nitrogen and carbon rich ices of relevance to the solar system, by swift ions. Such a process is experienced by the surface of icy bodies submitted to the GCR in the cold outer regions of the solar system. The experiments performed at GANIL are in the follow-up of the work described in Augé et al. (2016) and Augé et al. (2019).

N-rich complex organic residues can be formed by the slow annealing (0.1 – 0.5 K/min) of N-rich ices mixed with hydrocarbons ices after they have been irradiated by swift ions. The infrared signature of the residues present similarities with that of UCAMMs. Augé et al. (2019) showed that the D/H isotopic fractionation associated with the swift ion-irradiation itself remains marginal (i.e. lower than a few ten percent) and thus cannot account for the large D/H fractionation (*i.e*. from 10 to 20 times the SMOW value) observed in UCAMMs' organic matter. In the same study, Augé et al. (2019) showed that the irradiation of a mixture of ices with a high local isotopic heterogeneity in D, induces a residue that exhibits isotopic heterogeneities, suggesting that the isotopic heterogeneities observed in UCAMMs may be related to isotopic heterogeneities of the original ices layers at the surface of their icy parent body/bodies.

The aim of the experiments performed during this thesis is to extend these previous works to:

- Irradiate D, ^{15}N and ^{13}C labeled ices to study correlated H, C and N isotopic heterogeneities
- Compare the organic residues induced by irradiation of different ice composition representative of icy bodies orbiting in different regions of the solar system (N_2-CH_4 for external regions, NH_3-CH_4 for internal) or that may have lost the more volatile N_2 in the subsurface after thermal events (e.g. triggered by impacts).

In order to study the transfer of isotopic heterogeneities from the ice to the organic residue, we deposited an isotopically labeled thin ice layer (*Figure 3-2*, red layer) within an unlabeled ice film (*Figure 3-2*, light-blue volume). We chose the chemical composition of the labeled layer as close as possible to the composition of the main ice film to avoid chemical driven fractionations. Though, we introduced in some of them slight variations of the composition to explore perturbative effects induced by the composition. Prior irradiation, the isotopically labeled and unlabeled ices were deposited sequentially in order to be spatially well separated (*Figure 3-2*).

Molecular nitrogen and ammonia are two species observed at large heliocentric distances that can be a relevant source of the nitrogen observed in the cometary organic matter. Methane ice is also observed at the surface of Pluto (Grundy et al., 2016) and is a carbon provider, essential for the formation of organic matter. Its concentration in the ice will determine the maximum quantity of organic matter that can be formed.

Two main compositions of ice were explored, composed of nitrogen rich molecules (N_2 or NH_3) and mixed with a fraction of carbon-bearing simple ice precursors (CH_4):

- N_2 ices mixed with 10% of CH_4: N_2 – CH_4 (90:10).
- NH_3 ices mixed with 10% of CH_4: NH_3 – CH_4 (90:10).

The deposited ice film thickness was about ≈10µm (see section 3.1.3.1). This chosen thickness ensured that the heavy ion energy was sufficiently high to deposit energy within the ice without stopping (and therefore implanting ions) within the ice sandwich. The irradiation doses were ranging from 8 to 25 eV·molec^{-1}, the values after which no more significant chemical recombination are observed through the infrared monitoring of the ice (Augé et al., 2016). A slow annealing of the processed ice was subsequently performed in order to sublimate the remaining unprocessed volatile species and condensate the refractive materials on the windows (*Figure 3-2*, bottom). After each experiment, the windows with the organic refractive residues obtained at room temperature (300K) were quickly extracted from the chamber, stored in vacuum cells and brought back to Orsay to be analyzed by NanoSIMS at Institute Curie.

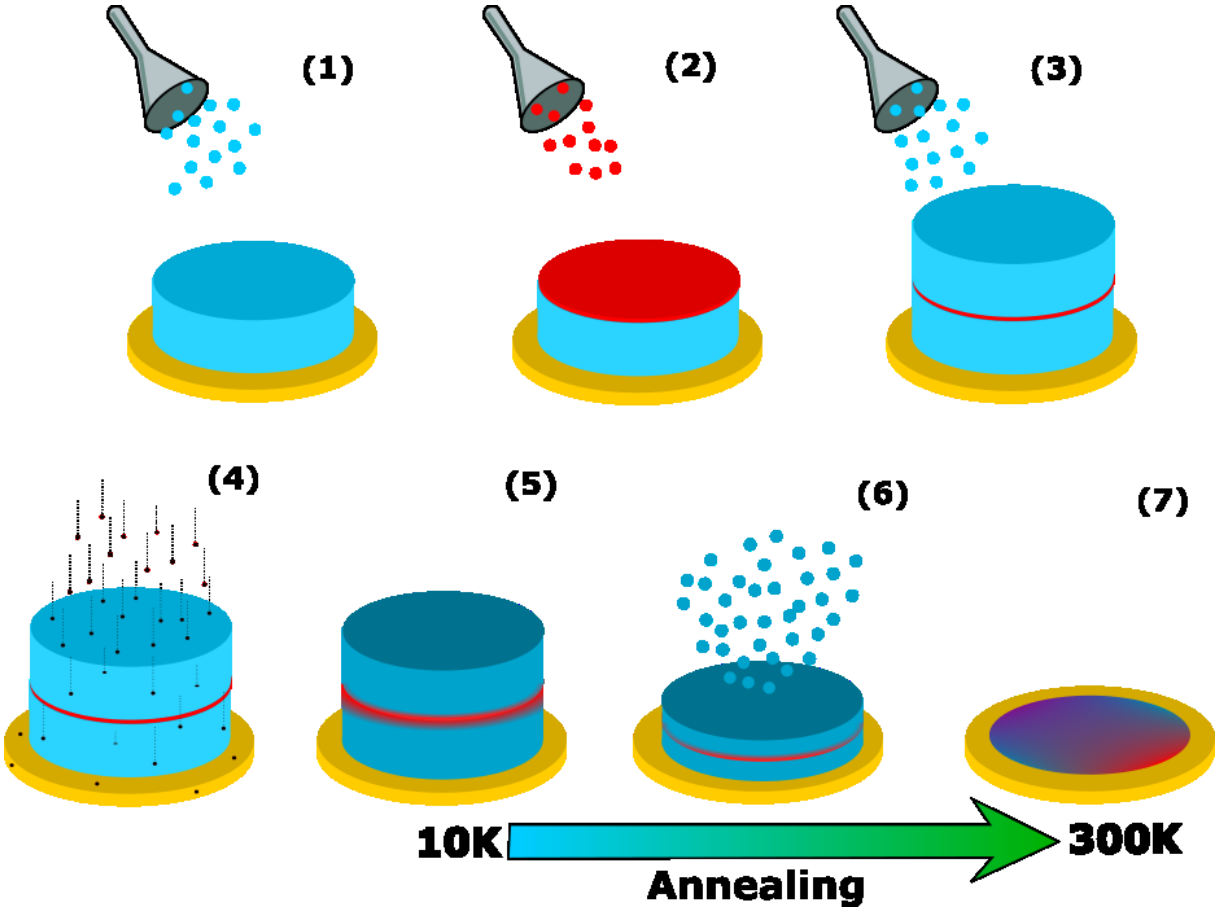

Figure 3-2 : Principle of ice irradiation experiments. A N-rich ice film is formed at 10K by the deposition on a substrate window (in yellow) of 2 istopically unlabeled ice layers (in light blue, step 1 and 3) surrounding an isotopically labeled ice layer (in red, step 2). The resulting 10 µm thick ice film is then irradiated by swift ions (step 4) until the formation of new chemical species (step 5). At the end of the irradiation , the ice film is very slowly warmed-up to 300K in order to concentrate the refractive species as an organic residue on the window (step 7). During the annealing, the remaining volatile ice and light radiolytic products sublimate (step 6). The ≈10µm-thick ice films are mainly composed of isotopically unlabeled N-rich molecules mixed with methane N_2—CH_4 (90:10) or NH_3—CH_4 (90:10). The final organic residue is about 50 – 150 nm thick.

3.1.2. The IGLIAS set-up at GANIL (CIMAP)

Ice irradiation experiments were conducted at the large heavy ions accelerator GANIL (Grand Accélérateur National d'Ions lourd, Caen, France). GANIL is a national facility built for experimental nuclear physics involving ions with energies ranging from 1 to 10^2 MeV/amu. Ions are extracted from a plasma formed by the heating of a gaseous or solid source and subsequently injected in a first cyclotron C0 where they are accelerated to an energy of about 1 MeV/amu. The lower energy beams in the range covered are directly sent to IRRSUD at the exit of C0 (Figure 3-3). Beams with higher energies can be achieved through two additional cyclotrons CSS1 and CSS2, up to 10^2 MeV/amu. The experiments described in this chapter were all performed with the low energy ion beam IRRSUD (0.5 – 1 MeV/amu).

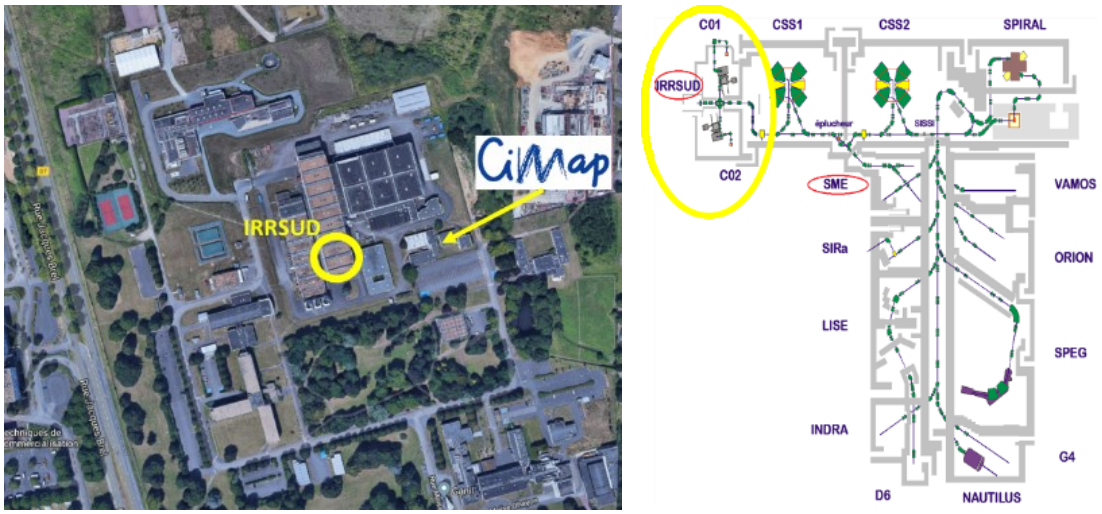

Figure 3-3: left, aerial view of the GANIL facility. Right, map of the beamlines and cyclotrons C0, C1, CSS1 and CSS2 at GANIL. Yellow circles indicate the IRRSUD beamline where the IGLIAS experimental set-up was installed.The other installations are mainly used fo nuclear physics experiments.

IGLIAS (Irradiation de GLaces d'Intérêt Astrophysique) is an experimental set-up designed at the CIMAP (Centre de recherche sur les Ions, les MAtériaux et la Photonique) for the irradiation of ice of astrophysical interest (Augé et al., 2018; Augé et al., 2019). It consists of an Ultra High Vacuum (UHV) chamber connected to the beam line where ices can be deposited and irradiated (Figure 3-4). Up to three IR transparent windows can be set on the holder (see *Figure 3-5*) and cooled down to 9K by a cryogenic head equipped with a closed system helium cryostat. A Lake Shore temperature controller allows adjusting the temperature of the holder between 9K and 300K, with a precision better than a few Kelvins.
The experiments are monitored *in situ* with 3 instruments:

- a Fourier transform infrared (FTIR) spectrometer (Brucker Vertex 70v) that follows the evolution of the ice film during the irradiation, in the 500 to 6000 cm^{-1} wavenumber range.
- a quadrupolar mass spectrometer (QMS, Microvision 2 MKS104) that measures the gas phase in the chamber in the 1 to 70 mass to charge ratio (m/z) with a rate of 4.6 scans per minute.
- a visible-ultraviolet (Vis-UV) spectrometer to monitor the ice evolution. We did not use it during our experiments; it is thus not represented in Figure 3-4.

During the experiment, the substrate windows can be aligned in 2 positions: one for the ice film deposition facing the gas injection system and the second for the ion irradiation coupled to the infrared

measurements. This is achieved by rotating the entire sample holder head in the chamber. IGLIAS main chamber is represented in *Figure 3-4*.

The ice films are formed by condensation of a specific gas mixture on the cold substrate windows (*Figure 3-2*, *Figure 3-4*). A mobile needle can be translated up to 15 mm from the window to inject the gas with a minimum spread around the target to minimize background vacuum contamination. A mixing chamber (not visible on *Figure 3-4*) is located before the gas injection needle to prepare the mixture of gases prior injection.

The IGLIAS main chamber is connected to the beam line through a differential pumping chamber in order to preserve a pressure of $2 \cdot 10^{-10}$ mbar with a cryogenic pump (Augé et al., 2018). In position of irradiation, the window is aligned with the laser beam to perform IR spectra (*Figure 3-4*). The angle of incidence of the IR beam with the normal direction of the windows is $\Theta_{IR} = 12°$. The substrate windows we used in the experiments were first ZnSe and then Si high purity windows that are both transparent to IR to achieve the monitoring with the IR transmission spectra.

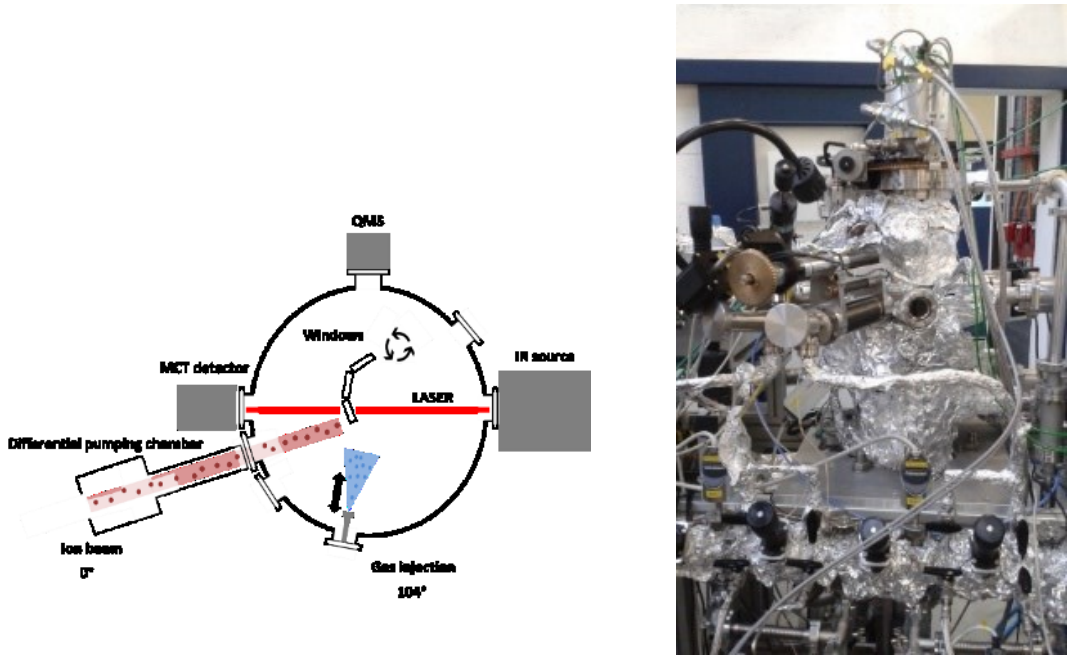

Figure 3-4: left, technical scheme of the IGLIAS chamber. Right, picture of the IGLIAS chamber installed at IRRSUD. The windows are attached to a cold finger system. An ice sample is formed by the condensation of gaz injected on the window cooled by the cold finger. The ion beam irradiation of the window models the GCR irradiation of ice mantles. A quadrupolar mass spectrometer (QMS) and a Fourier Transform InfraRed spectrometer (FTIR) are used to monitor the evolution of the ice during the irradiation.

Figure 3-5: The IGLIAS window holder. Three 20 mm diameter windows can be mounted simultaneously in the holder (only one is present in the picture). Inside the IGLIAS chamber, the holder is cooled down to 9K by a cold finger.

3.1.3. Synthesis of refractory organic residue by heavy ion irradiation

3.1.3.1. *Ice sandwiches condensation and IR monitoring*

Ice films were deposited on substrate windows at a temperature ranging from 9K to 12K following a three-step procedure (*Figure 3-2*, top):

1. A first lower thick layer of unlabeled ice (N_2-CH_4 or NH_3-CH_4) was deposited.
2. An isotopically (D, ^{13}C, ^{15}N) labeled thin ice layer with a thickness accounting from about 1 to 5% of the total thickness of the ice sandwich was added.
3. The upper unlabeled layer (identical to the first layer) was deposited.

The ice deposition was controlled by recording IR spectra of the intermediate deposited ice layers and final deposited films. IR spectra are recorded to measure the transmittance T, *i.e.* the ratio of transmitted (through the film) and the bare window incident radiant fluxes, Φ_t and Φ_i respectively. In this chapter, transmission spectra were converted into optical depth spectra. The optical depth τ is derived from the transmittance as follow:

$$\tau = -\ln(T) = -\ln\left(\frac{\Phi_t}{\Phi_i}\right) \quad (1)$$

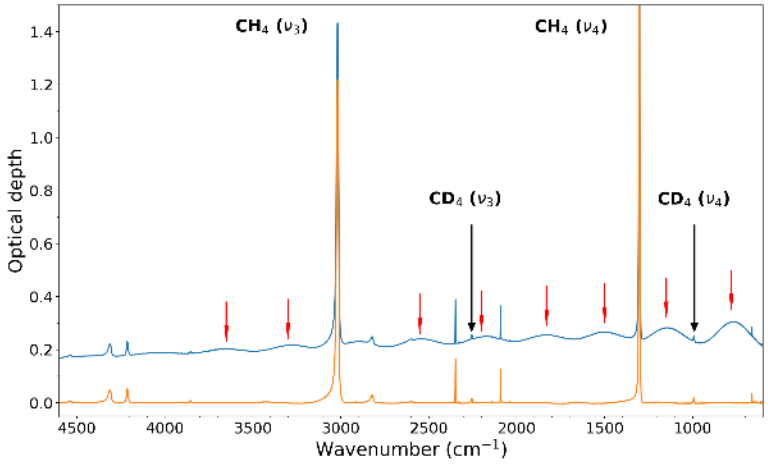

Figure 3-6: IR spectrum of a N_2-CH_4 ice sample prior irradiation (Sd3, see section 3.2). The blue curve shows the raw spectrum before correction. The slope and the oscillations of the baseline were corrected using an empirical function. The period of the oscillations, indicated by red vertical arrows, was used to estimate the thickness of the ice sample d = 11.1 ± 0.5 µm. Orange line is the corrected spectrum. Bands of CH_4 and CD_4 were used to estimate the D/H bulk ratio.

In the case of identified vibrational bands (*e.g.* the ν_3 and ν_4 CH_4 stretching and deformation bands in *Figure 3-6*), the column density of the corresponding molecule was calculated from the known integrated absorption band strength *A* and the integrated optical depth *S* as follow:

$$N(molecule \cdot cm^{-2}) = \frac{1}{A} \times \int_{\nu_{min}}^{\nu_{max}} \tau d\nu = \frac{S(cm^{-1})}{A(cm \cdot molecule^{-1})} \quad (2)$$

Numerous authors have reported the band positions and integrated absorption band strengths of pure molecule ices at low temperature *i.e.* below 25 K, such as CH_4, NH_3, CO, CO_2. However, there are few reported oscillator strength measurements for the isotopolog molecules (*i.e.* with the ^{15}N, ^{13}C and D isotopes). When the band strengths of isotopically labeled molecules such as CD_4, $^{13}CD_4$ and $^{15}ND_3$ were

not documented in the literature, we estimated them by applying a linear correction linked to the shift of the corresponding vibrational band following from the change in reduced mass:

$$A(mol, \tilde{\nu}_i) = A(MOL, \nu_i) \times \frac{\tilde{\nu}_i}{\nu_i} \quad (3)$$

where mol is the isotopically labeled molecule, MOL the isotopically unlabeled molecule and $\tilde{\nu}_i$ and ν_i the position of the two corresponding bands in cm^{-1}.

An IR spectrum was acquired at the end of the deposition process to control the overall thickness and composition of the ice sandwich (*Figure 3-6*). Periodic oscillations are observed on the IR spectra; they are related to reflections at the interfaces of the ice deposits (Fabry-Perot effect) and are inversely proportional to its thickness. Following Domingo et al. (2007), the thickness d_{osc} of the ice film can be derived from the period $\Delta\nu$ of the oscillations with the equation:

$$d_{osc} = \frac{1}{2n \cdot \Delta\nu \cdot \cos\theta_{IR}} \quad (4)$$

with:

- n the refractive index of the ice, with n_{N2} = 1.2 for N_2 ices (Satorre et al., 2008) and n_{NH3} = 1.38 for NH_3 ices (Satorre et al., 2013).
- Θ_{IR} = 12° the angle of incidence of IR beam on the window.

The quantity of gas injected in the chamber was given by the pressure differential in the mixing chamber $\Delta P = P_{fin} - P_{ini}$ with P_{ini} *and* P_{fin} the pressure in the mixing chamber respectively before and after the injection of gas.

When the IR spectra were subject to high uncertainties, *i.e.* for the 2020 experimental session (see below), a calibration factor k_1 had to be introduced to relate the differential pressures and the thickness of the ice deposits, based on the thickness measurements performed in the previous experiments. The calibration factor $k = \frac{d}{\Delta P}$ was equal to $k_1 = 1.14$ for N_2-CH_4 (90:10) mixtures and $k_2 = 0.77$ for NH_3-CH_4 (90:10) mixtures.

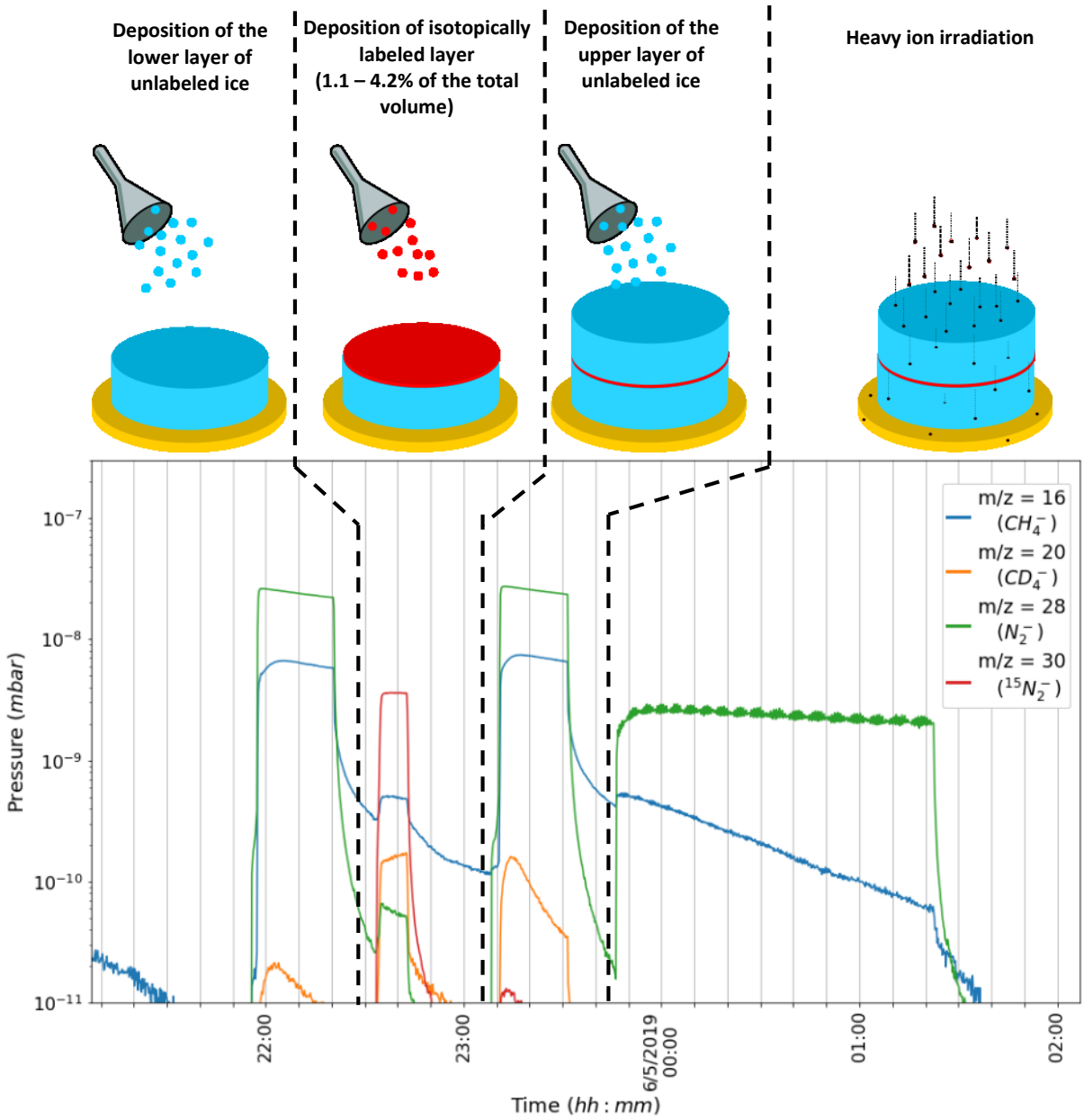

Figure 3-7. Top: sequential view of the formation and irradiation of an ice sample. The ice sandwich is formed by the deposition of three ice layers. The upper and lower layers are made of isotopically unlabeled ice. The central layer, isotopically labeled account for 1% to 5% of the total volume of the ice sample. Bottom: QMS spectra obtained during the experiment at GANIL monitoring the ice deposition and irradiation of W#3 2019 (sd3) consisting in N_2-CH_4 and $^{15}N_2$ -CD_4. The deposition of the unlabeled layers is characterized by a high signal of the m/z = 28 and 16 (respectively accounting for the CH_4^- and N_2^- ions). The labeled ice layer was made of $^{15}N_2$ and CD_4 and is characterized by a high signal of m/z = 30 and 20.

3.1.3.2. *QMS monitoring*

The quadrupolar mass spectrometer allows to access to the composition of the deposited ices in the chamber by ionizing molecules in the gas phase during the deposition and collecting the resulting ions.

Ionization is achieved by electron impacts leading to a fragmentation pattern including smaller ionized fragments, which are subsequently detected according to their mass to charge ratio *m/z*. The ions collection by the QMS results in a mass spectrum, *i.e.* the abundance of the ions signals against their *m/z* values.

We used the QMS set with an electron-impact ionization energy of 70 eV and recorded a mass spectrum in the *m/z* = 1—70 range each 13 seconds. Output files consisted in cubes of data containing the relative abundance of each *m/z* signal in function of the scan and thus the time (*Figure 3-8*). In this chapter, QMS data are represented under the form of a mass spectrum from the integration of multiple scans (*Figure 3-9*) or under the form of abundances vs. time graphs (*Figure 3-7*, bottom).

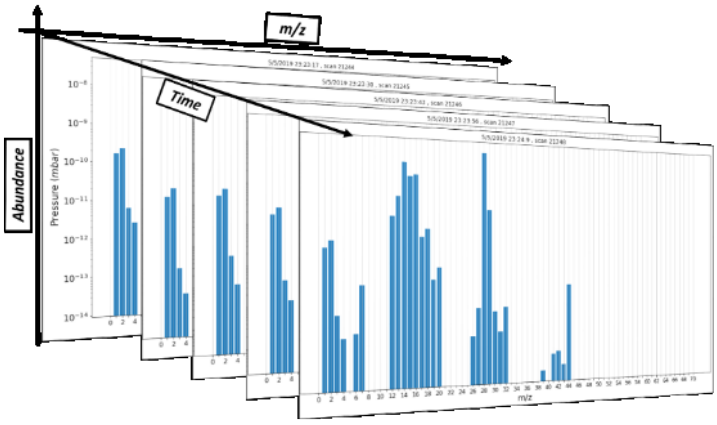

Figure 3-8: graphical representation of the QMS data structure. A QMS data file is made of the compilation of QMS scans, each of them containing a mass spectrum ranging from m/z = 1 to 70. The duration of a scan is 13 seconds. Data can be visualized as single mass spectrum as shown here and in Figure 3-9***Erreur ! Source du renvoi introuvable.*** *or as the evolution of specific m/z signals over time (Figure 3-7, bottom).*

Figure 3-7, bottom shows the correspondence between the steps of the deposition sequence and the QMS signal of major species contributing to the layers in the case of the sandwich Sd3 (2019, see section 3.2). N_2-CH_4 deposits are characterized by strong signals at m/z = 28 ($^{14}N_2^-$), m/z = 14 ($^{14}N^-$, $^{12}CH_2^-$) and m/z = 16 ($^{12}CH_4^-$) whereas the isotopically labeled layer made of $^{15}N_2$-CD_4-^{13}CO (80:10:10) is characterized by signals at m/z = 30 ($^{15}N_2^-$), m/z = 15 ($^{15}N^-$), m/z = 20 ($^{12}CD_4^-$) and m/z = 29 ($^{13}CO^-$).

The nature of the fragmentation patterns and the relative abundance follow probabilistic laws and varies with the electron energy. The signal contribution and abundance for a given molecule is obtained from its fragmentation pattern. We performed internal calibrations to derive the fragmentation pattern $f(X,m/z)$ of an initial molecule *X* with *m/z* fragments (Dartois et al., 2020):

$$f(X,{}^{m}/_{z}) = \frac{I({}^{m}/_{z})}{\sum_{\frac{m}{z}=X_{fragments}} I({}^{m}/_{z})} \quad (5)$$

with $I(m/z)$ the measured intensities of the *m/z* fragments. We assumed that the fragmentation patterns of a molecule and its isotopologs are the same. When internal calibrations were not possible, we used the fragmentation pattern from the NIST database (https://webbook.nist.gov/chemistry/). The errors on the fragmentation patterns' coefficients were estimated to range from 20% to 30% by comparing the calibrations' results from one experiment to another.

Mass spectra acquired during the deposition process resulted in the addition of the signals from multiple species present in the gas phase. In order to identify and quantify these components, we numerically modelled the experimental mass spectra $I_{exp}(m/z)$ with linear combinations of the fragmentation patterns of the species likely to be present in the gas phase (*Figure 3-9*, top). The simulated

intensity $I_{simu}(m/z)$ of a m/z value in a mass spectrum was reconstructed from the fragmentation patterns $f(X_j,m/z)$ of species contributing to this m/z value and their scaling factor $\alpha(X_j)$ by the relation:

$$I_{simu}(^{m}/_{z}) = \sum_{X_j} \alpha(X_j) \cdot f(X_j, ^{m}/_{z}) \tag{6}$$

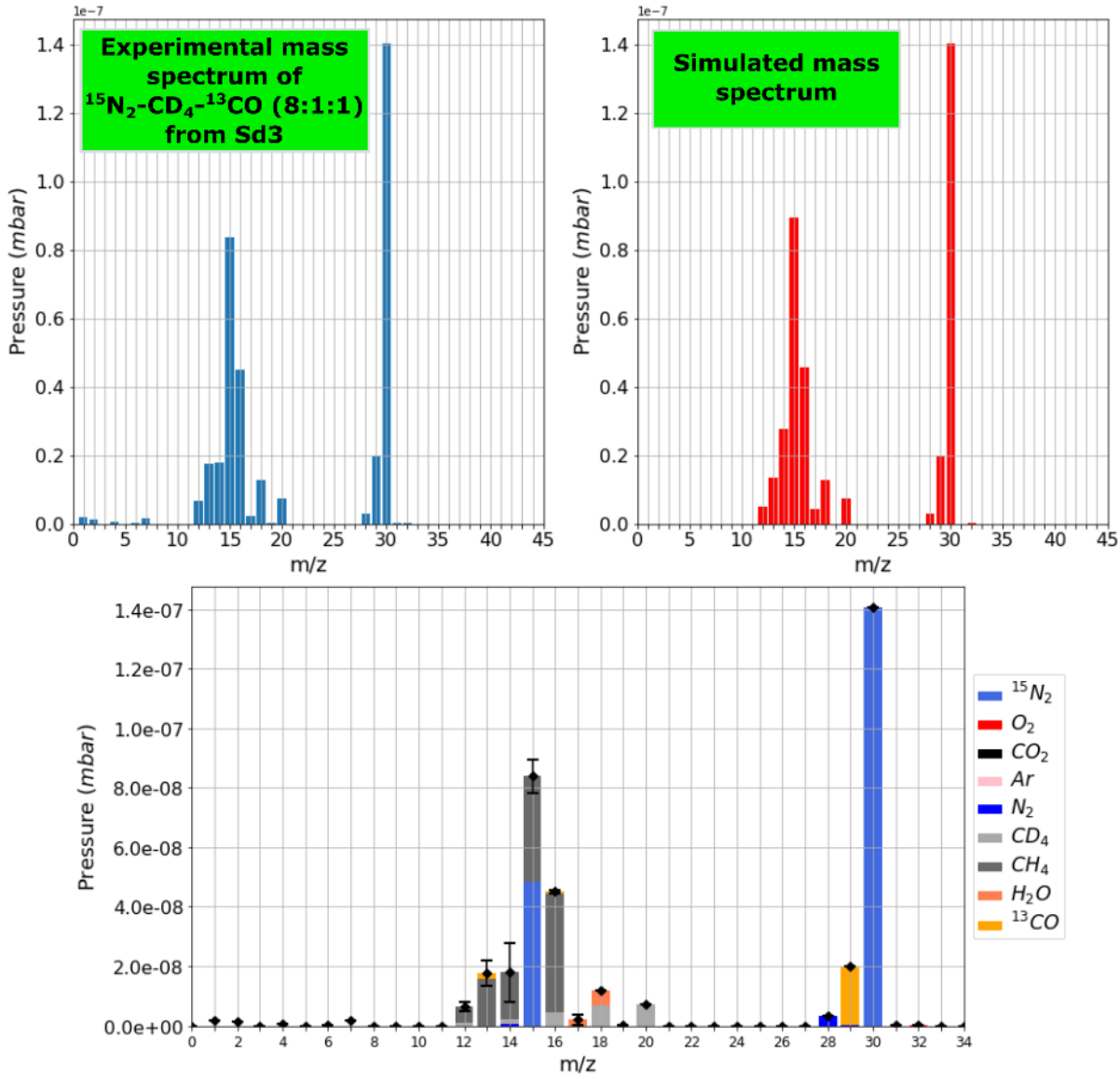

Figure 3-9: upper left, experimental mass spectrum integrated over the labeled layer deposition. It consists on the collection of the $I_{exp}(m/z)$ intensities for each m/z. Upper right, simulated mass spectrum aiming to reproduce the experimental spectrum by a linear combination of the fragmentation patterns of the molecules assumed to be present. The simulated intensities are referred as $I_{simu}(m/z)$. Bottom, final mass spectrum with the estimated contribution of each species $I_{est}(X_j,m/z)$. Error bars are estimated from the difference between the experimental and simulated mass spectra.

The associated error was given by:

$$\delta(m/z) = \frac{|I_{simu} - I_{exp}|}{I_{exp}} \quad (7)$$

Therefore, the simulated contribution of the X_j species in the total intensity $I_{simu}(m/z)$ is:

$$i_{simu}(X_j, m/z) = \alpha(X_j) \cdot f(X_j, m/z) \quad (8)$$

and the estimated abundance of the X_j species from the m/z intensity (*Figure 3-9* bottom, bars of the same color) is given by:

$$i_{est}(X_j, m/z) = \frac{i_{simu}(X_j, m/z)}{I_{simu}(m/z)} \cdot I_{exp}(m/z) \quad (9)$$

The relative abundances $A(Xj)$ were computed by averaging the abundances derived from each m/z intensities associated with a same species X_j:

$$A(X_j) = \frac{1}{N_{frag}} \cdot \frac{1}{\sigma_{impact}(X_j)} \cdot \sum_{N_{frag}} \frac{i_{est}(m/z)}{f(X_j, m/z)} \quad (10)$$

with N_{frag} the number of fragments of the molecule X_j and $\sigma_{impact}(X_j)$ the electron-impact ionization cross section of the molecule X_j at 70 eV (NIST database).

Bulk isotopic ratios of the sandwiches were computed from the abundances integrated over the different layers of the ice sandwich. *Figure 3-9* shows the integrated mass spectrum recorded during the labeled ice layer condensation of Sd3 (top left), the corresponding simulated mass spectrum (top right) and the identification of each contributing species (bottom) computed following this procedure.

3.1.3.3. *Heavy-ion irradiation*

Galactic cosmic rays mainly consist in protons (87%) and helium ions (11%). The remaining 2% of the GCR flux is driven by heavier ions accelerated during violent events such as supernovae. However, light ions such as protons and helium do not carry high kinetic energy due to their low mass. Rare and heavier ions, conversely, can reach energies high enough to compete with protons in term of doses deposited into solid targets as ices (*Figure 3-10*, left, and *Figure 3-11*). The GCR flux reaches its maximum for ions with about 60 MeV/amu (*Figure 3-11*). Our experiments used low-energy ion beams (0.5 MeV/amu) to model the impact of the GCR on nitrogen-rich ices. Despite the difference between the energies of the GCR ions and the ones reached in the accelerator, scaling factors in the energy deposition allow the experimental model to be adjusted.

When passing through the ice, ions deposit energy via elastic and non-elastic collisions with the ice molecules. A non-elastic collision corresponds to the interaction between the electron clouds of the ion and the molecule/solid. The energy transferred via such collisions per unit of distance is referred to as electronic stopping power S_e and is responsible for the chemical radiolysis of the ice. Elastic collisions result from coulomb interactions of the ion with the repulsive potential of the atoms constitutive of the solid and the associated energy deposit is called nuclear stopping power S_n. The values of the electronic and nuclear stopping powers depend on the energy of the ion. Thus, in specific energy regime, one component

can be cancelled (see *Figure 3-10*, right). The stopping power (in MeV/µm) of an ion with an energy E is the sum of the electronic and nuclear stopping power:

$$S(E) = -\frac{\mathrm{d}E}{\mathrm{d}x} = S_e(E) + S_n(E) \tag{11}$$

S depends on the nature of the ion, its initial energy and the nature of the target material. Bringa (2003) reported that iron ions in the energy range representative of the GCR deposit hundred times more energy than protons in water ice (*Figure 3-10*, left). Since the stopping power depends on the energy of the ion (*Figure 3-10*, right), the dose deposited in a target is given by the combination of the energy distribution of the GCR and the relative abundance of the ions of the GCR (*Figure 3-11*).

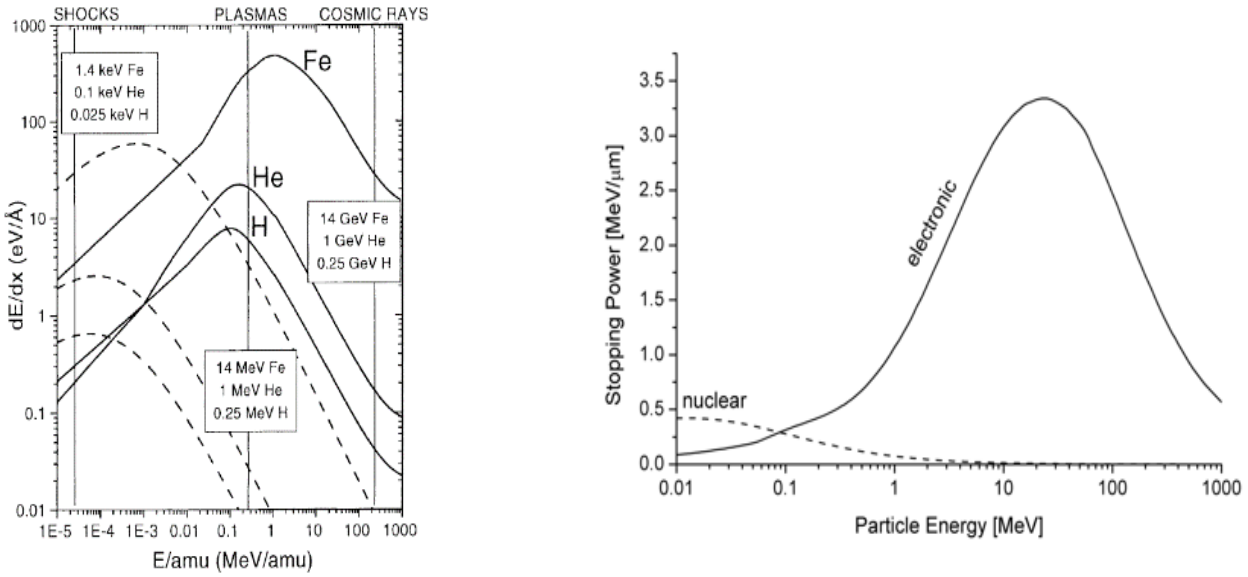

Figure 3-10. Left : stopping power of H, He and Fe in water ice from Bringa (2003). The nuclear stopping power is indicated by dashed lines and the electronic stopping power with solid lines. Right: nuclear and electronic stopping power of Al ions in an aluminum target (credit H. Paul).

The ion penetration distance R in the target before stopping can be computed as follow at the first order:

$$R = \int_0^{E_{ini}} \frac{1}{S(E)} \mathrm{d}E \tag{12}$$

However, energy loss and deviation factors that will affect the ion trajectory can be taken into account in a more refined approach. The effective penetration distance of the ion in the target is given by the projected range R_p. During the 3 experimental sessions, we irradiated the ice films with 3 different ions: $^{58}Ni^{9+}$ (33 MeV), $^{136}Xe^{19+}$ (75 MeV) and $^{86}Kr^{15+}$ (74 MeV). We computed the stopping power $S(E)$ and the projected range R_p associated to these ions with the SRIM software (Ziegler et al., 2010). In our experiments, the thicknesses of the irradiated ices were chosen in order to prevent ion implantation within the ice, ensuring a fair homogeneity in the deposited energy and the domination of electronic energy

deposition over nuclear energy deposition (*Figure 3-12*). Ions deposit their energy in the ice and their implantation occurs eventually in the substrate window behind.

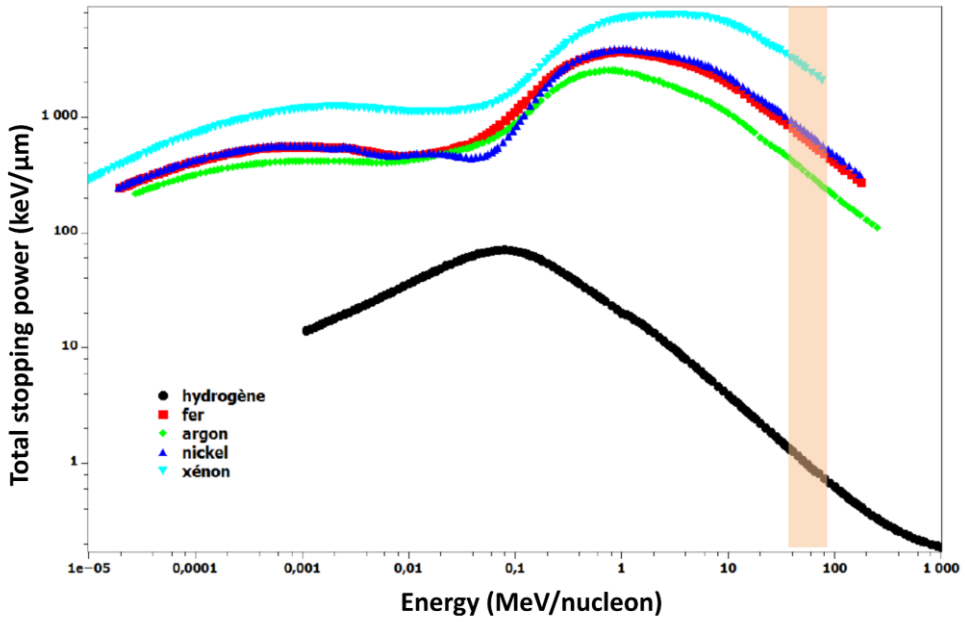

Figure 3-11 : Ion stopping power in keV/µm as a function of the projectile energy for various accelerated ions from Augé (2017)). The colored band correspond to the energies for which the GCR flux is maximal.

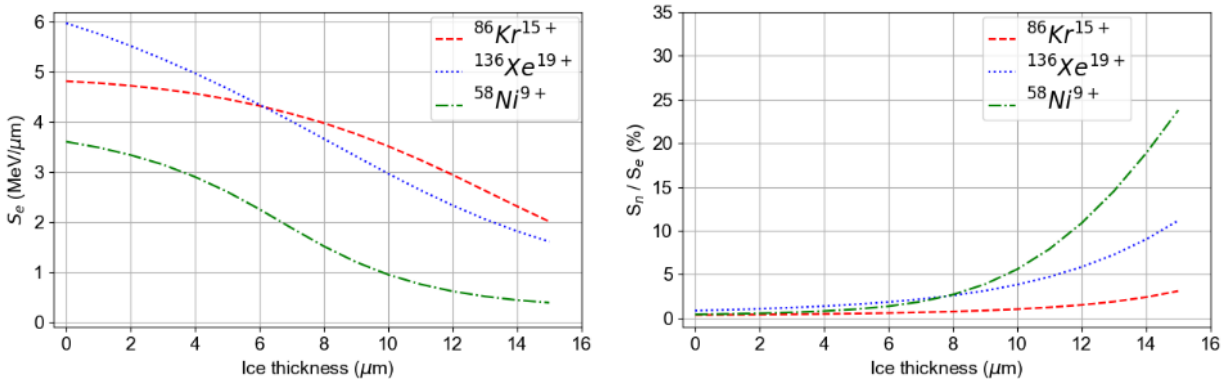

Figure 3-12, left: electronic stopping power of the 3 ions used during the experimental sessions plotted against the thickness of an N_2-CH_4 (90:10) ice. The deposited energy in the ice decreases with the thickness, i.e. with the energy of the ion. The thicknesses of the ice films were established to avoid ion implantation in the ice. Right: evolution of the ratio between the nuclear and electronic stopping powers in function of the ice thickness for the 3 ions used in the experimental sessions. For thickness below 12 µm, the nuclear stopping power remains 10 times lower than the electronic stopping power for the 3 considered ions.

The quantification of the ice processing by irradiation is determined through the dose D (in eV·molecule^{-1}) *i.e.* the energy deposited per molecule. It is given by the fluence Φt (the quantity of ions

per cm² that have impacted the ice over time), the mean stopping power in the ice $\langle S \rangle$ (in MeV/µm), the Avogadro constant N_A, the density ρ (in g.cm^{-3}) and the molar mass M (g.mol^{-1}) of the target:

$$D = \Phi t \cdot \langle S \rangle \cdot \frac{M}{\rho N_A} \cdot 10^{10} \quad eV \cdot molecule^{-1} \tag{13}$$

In our case, the mean stopping power $\langle S \rangle$ is largely dominated by the mean electronic stopping power $\langle S_e \rangle$ due to the negligible values of the nuclear stopping power (see *Figure 3-12*, right). The evolution of the ice was monitored *in situ* with the infrared spectrometer and the irradiation was stopped at a dose D_{tot}, ranging from 8.2 to 21.8 eV·molecule^{-1}. Such doses correspond to several million years of exposure in the outer solar system (Augé et al., 2016).

3.1.3.4. *Annealing process*

Despite the formation of organic radicals (*i.e.* reactive chemical species formed by the irradiation process), at the end of the irradiation ices and volatile radiolytic products remain major components in the film (*e.g.* Augé et al. (2019) and references therein). A slow annealing from 10 K to room temperature (*i.e.* 300K) was performed to sublimate the remaining ice allowing to concentrate the refractive molecules on the substrate windows. It is mandatory to use a very slow temperature ramp (<0.5 K/min) to, somehow, simulate a slow evolution in a space environment and to avoid explosive events due to fast sublimation of gas, which could blow the whole residue by volcano effect (Burke and Brown, 2010).

Thanks to the QMS and IR monitoring, we identified on-line the temperature of sublimation of some major components within the ice all along the annealing process (from 20 to 28 hours). The simplest species were identified for the purpose of the presented analysis, but a comprehensive identification of all chemical species released during the ice sublimation was not performed yet due to the complexity of the identification of such complex mixture in the QMS data.

3.1.4. NanoSIMS isotopic mapping of the residues

Organic refractory residues formed at GANIL were analyzed by NanoSIMS to map their isotopic heterogeneities. The NanoSIMS sessions took place at Institut Curie (Orsay, France) during the summers 2019, 2020, 2021, with the NanoSIMS-CAMECA 50 instrument in collaboration with Dr. T.-D. Wu (*Figure 3-13*).

3.1.4.1. *The NanoSIMS sample preparation*

We used a Cs^+ primary ion beam to analyze the residues with the NanoSIMS instrument. At the impact, molecules, atoms and electrons are ejected from the surface. An electric field extracts the ionized fraction and inject it into the mass spectrometer (see section 2.2). This process implies the potential accumulation of local electric charges on the sample surface that need to be evacuated. An inefficient evacuation of the charges is likely to give rise to an interfering electric field which can deteriorate or impede the continuity of the analysis (see annex 5.2).

To prevent analytical issues due to charge accumulation, the samples were coated with a 40 nm thick layer of gold by plasma deposition. When possible, half of the substrate window was left uncoated to perform subsequent complementary analyses (*Figure 3-13*, right). As charging effects occurred during the first experimental session (2019) due to the insulating nature of the ZnSe substrate windows, we opted for more conductive Si substrate windows for the 2020 and 2021 experiments. The nature of the substrate windows had to satisfy the requirements associated with both transparency in IR spectroscopy and NanoSIMS mass spectrometry.

Figure 3-13: left, picture of the NanoSIMS at Institut Curie, Orsay, France. Right, ZnSe window in the NanoSIMS dedicated holder prior the analysis in June 2019. Half of the substrat window has been gold-coated.

3.1.4.2. *The NanoSIMS analytical conditions*

The goal of the NanoSIMS analyses was to map simultaneously the D/H, $^{15}N/^{14}N$ and $^{13}C/^{12}C$ heterogeneities in the refractory residue. It was achieved by multi-collection of ions $^{13}C^{14}N^-$, $^{12}C^{15}N^-$, $^{12}C^{14}N^-$, $^{12}CD^-$ and $^{12}CH^-$. Since $^{13}C^{14}N^-$ and $^{12}C^{15}N^-$ ions are both located at m/z =27, we used a switching mode to collect alternatively the two ions, as described in *Figure 3-14*. Mass spectra at mass 14 and 27 acquired on the Sd4 sample are shown in the *Figure 3-15*. Peaks of the different ions at these masses are well separated allowing measurements to be performed.

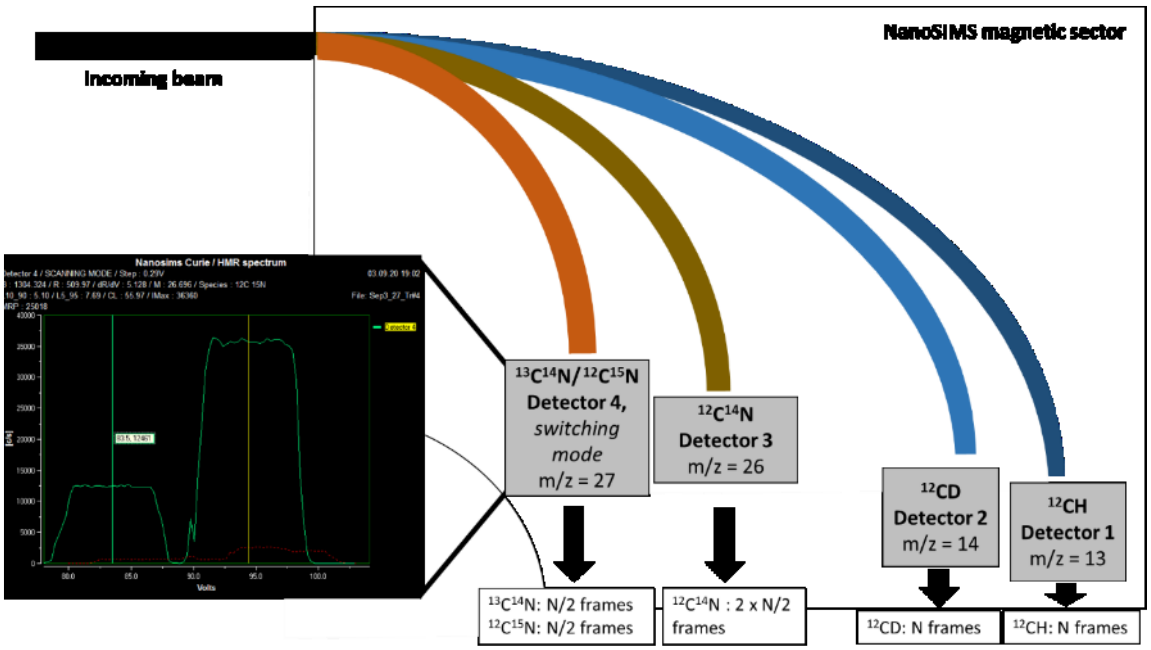

Figure 3-14: Acquisition mode used to monitor simultaneously the D/H, $^{13}C/^{12}C$ and $^{15}N/^{14}N$ ratios in a same area of the organic residue. The detector 4 acquired alternatively $^{13}C^{14}N$ and $^{12}C^{15}N$ maps by switching the voltage of the exit plates. $^{12}C^{14}N$ maps measured by the detector 3 were used to compute the $^{13}C/^{12}C$ and $^{15}N/^{14}N$ ratios.

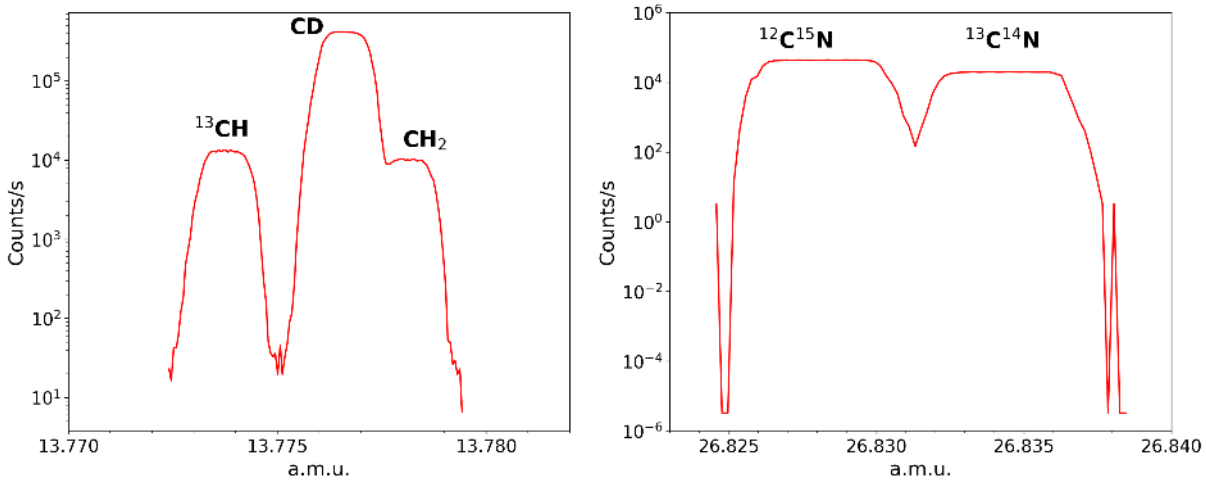

Figure 3-15: NanoSIMS mass spectrum around the mass 14 (left) and 27 (right) acquired during the 2020 experimental session at Institut Curie. $^{13}CH^-$, CD^- and CH_2^- have very close positions but are well separated. $^{12}C^{15}N^-$ and $^{13}C^{14}N^-$ ions are well separated, no pollution of $^{11}B^{16}O^-$ was observed in the samples.

3.2 The 3 experimental sessions at GANIL

3.2.1. The irradiation conditions for the different ices mixtures

The irradiation experiments took place at GANIL during about a week in May 2019, February 2020 and May 2021 (see *Table 3-1*). Each experimental session was conducted with the ions available at the time of the session at GANIL, different for the 3 experimental sessions. We thus adapted the ion fluence to the ion stopping power, to remain in the same range of doses deposited in the ice. Each ice film was formed with the same protocol as described in section 3.1.3.1. The isotopically labeled layer at the center of the ice film accounted for 1.1 to 4.2 % of the total ice volume. Labeled layer proportions in the total ice sandwich were kept low enough to provide a well-defined spatial heterogeneity but high enough to allow sufficient counting in the NanoSIMS images.

Due to alignment issues of the FTIR IR spot and high levels of water in the MCT detector during the 2020 session, the *in-situ* IR spectra of the residues were not exploitable in that session. In 2021, the spatial distribution of the produced residues formed from NH_3-dominated ices was too irregular to obtain IR spectra during the annealing (see section 3.2.3.2). Additional IR spectra of the residues Sd5, Sd7 and Sd8 were thus taken with a FTIR microscope spectrometer after extraction of the substrate windows from the IGLIAS chamber. These spectra allowed to compare the compositions of each residue formed during the different experimental sessions.

Date GANIL	**May 2019**			**February 2020**			**May 2021**		
Ion beam [a]	$^{58}Ni^{9+}$ (33 MeV)			$^{136}Xe^{19+}$ (75 MeV)			$^{86}Kr^{15+}$ (74 MeV)		
Sample name [b]	Sd1	Sd2	Sd3	Sd4	Sd5	Sd6	Sd7	Sd8	Sd9
Main ice [c]	N_2-CH_4 (90:10)	N_2-CH_4 (90:10)	N_2-CH_4 (90:10)	N_2-CH_4 (90:10)	N_2-CH_4 (90:10)	N_2-CH_4 (90:10)	N_2-CH_4 (90:10)	NH_3-CH_4 (89:11)	NH_3-CH_4 (89:11)
Labeled ice [d]	$^{15}N_2$-CD_4 (89:11)	$^{15}N_2$-CD_4 (89:11)	$^{15}N_2$-CD_4-^{13}CO (9:1:1)	$^{15}N_2$-$^{13}CD_4$ (88:12)	$^{15}N_2$-^{13}CO (88:12)	$^{15}ND_3$-$^{13}CD_4$ (1:1)	$^{15}N_2$-CD_4-^{13}CO (73.7: 12.5: 13.8)	$^{15}ND_3$-$^{13}CH_4$ (89:11)	$^{15}ND_3$-$^{13}CH_4$ (1:1)
Ice film thickness [e] (µm)	8.3 (*)	11.6 (*)	11.7 (*)	8.3 (†)	11.8 (†)	11.8 (†)	13.4 (*)	8.0 (*)	7.7 (*)
Labeled ice contrib. [f]	1.1 %	1.8 %	1.7 %	4.0 %	2.9 %	> 3.5 %	3.6 – 4.2 %	3.6 %	3.4 %
Mean stopping power (Mev/µm) [g]	2.9	2.4	2.4	5.1	4.4	4.4	4.15	4.95	4.95
Projected range (µm) [h]	23	23	23	26	26	26	29	27	27
Dose [i] (eV.molec^{-1})	8.2	11.3	9.9	25.2	17.4	21.8	15.3	16.4	16.8
µ-FTIR data [j]	-	-	-	-	Jun. 2021	-	Jun. 2021	Jun. 2021	-
Date NanoSIMS [k]	-	June 2019	Aug. 2019	Sep. 2020	Sep. 2020	Sep. 2020	July 2021	July 2021	-
Substrate windows [l]	ZnSe Ø 20mm	ZnSe Ø 20mm	ZnSe Ø 20mm	7 × Si Ø 5mm	7 × Si Ø 5mm	7 × Si Ø 5mm	Si Ø 20mm	Si Ø 20mm	Si Ø 20mm

Table 3-1: Summary of the 3 experimental sessions of ice irradiation at GANIL. (a) ion used during ice irradiations, with the total energy of the ion. (b) Name of the sample. (c) Composition of the main ice in the deposit. (d) Composition of the isotopically labeled ice. (e) Thickness of the whole ice film estimated with IR measurements (*) or by pressure difference (†). (f) Proportion of the isotopically labeled layer in the ice film estimated by pressure difference ratios. (g) Mean stopping power of the ion within the ice computed with SRIM. (h) Projected range computed with SRIM. (i) Dose deposited in the ice film. (j) Additional μ-FTIR data acquired after the GANIL experiment. (k) Dates of the NanoSIMS analyses of the refractory residues. (l) Nature and diameter of the substrate windows used for the irradiation experiments.

3.2.2. The chemical and isotopic composition of the ice mixtures

3.2.2.1. *N_2-dominated ices*

Infrared spectra of N_2-CH_4-dominated ice films (*i.e.* Sd1, 2, 3, 4, 5, 6, 7) display a limited number of bands (see e.g. Sd7 spectrum in black in *Figure 3-16*) due to the low absorption of the N_2 molecule (de Barros et al., 2015). Similarly, no bands are associated with the $^{15}N_2$ molecule when present in the isotopically labeled layer. The strongest bands are due to the CH_4 modes and their combinations. CD_4 bands were observed at 11K (Augé et al., 2019; He et al., 2010). The relative optical depths *S* of the CD_4 bands at 2251 cm^{-1} (ν_3) and 990 cm^{-1} (ν_4) and the CH_4 bands at 3021 cm^{-1} (ν_3) and 1305 cm^{-1} (ν_4) were used to estimate the D/H ratio of the ice sandwiches prior irradiation, following the equations 2 and 3 (Augé et al., 2019):

$$\left(\frac{D}{H}\right)_{IR} \approx \frac{S_{CD_4}}{S_{CH_4}} \times \frac{\nu_{CH_4}}{\nu_{CD_4}} \tag{14}$$

In the Sd4 ice sandwich, $^{13}CD_4$ was used instead of CD_4. The ν_3 and ν_4 bands were found close to that of CD_4 at 2249 cm^{-1} and 991 cm^{-1} respectively. Equation (14) was used to derive the $^{13}C/^{12}C$ ratio since the ^{13}C and D were carried by the same $^{13}CD_4$ molecule.

In Sd3, 5 and 7, the presence of ^{13}CO was indicated by the band at 2092 cm^{-1} (Gerakines et al., 1995). The $^{13}C/^{12}C$ ratio is derived by the integration of the CH_4 band at 1305 cm^{-1} and the ^{13}CO band at 2092 cm^{-1}:

$$\left(\frac{^{13}C}{^{12}C}\right)_{IR} = \frac{S_{^{13}CO}}{A(^{13}CO, 2092\ cm^{-1})} \Bigg/ \left(\frac{S_{CH_4}}{A(CH_4, 1305\ cm^{-1})} + \sum_{Add\ ^{12}C} \frac{S_i}{A_i}\right) \tag{15}$$

where *S* are the optical depths, *A* the band strengths and the summing term accounts for the contribution of the minor ^{12}C-bearing molecules (CD_4, CO and CO_2 contamination). In all ice sandwiches, the CO_2 bands at 660 cm^{-1} and 2343 cm^{-1} were used to quantify the CO_2 ice contamination. CO contamination was estimated with the band at 2139 cm^{-1}.

All the identified bands are reported in the Table 3-2 along with their band strength when documented.

At the end of the ion irradiation of the ices, at a temperature of about 10K, the complex signatures of the irradiation-induced compounds are observed in the spectra (*Figure 3-18*, left). These new molecules are formed from the reaction of the N_2 and CH_4 atoms when processed by the ions. ^{13}CO incorporated in the ice sandwich as well as CO and CO_2 contamination in the chamber are observed with the bands at 2092

cm^{-1}, 2139 cm^{-1} and 2343 cm^{-1}. They lead to the formation of oxygenated molecules such as HNCO (2260 cm^{-1}) and OCN^- (2170 cm^{-1}) (Augé et al., 2019; Muñoz Caro and Schutte, 2003; Schutte, 2002)

3.2.2.2. *NH_3-dominated ices*

Ice films made of the NH_3-CH_4 mixture present a more complex IR signature as shown on the *Figure 3-16* (Sd8, red line). The 3 main features of the NH_3 ice at 10K were reported in the literature (Bouilloud et al., 2015; D'Hendecourt and Allamandola, 1986; Holt et al., 2004). They are observed at (ν_3- ν_1) = 3420-3120 cm^{-1}, ν_4 = 1626 cm^{-1} and ν_2 = 1070 cm^{-1} on Figure 3-17 and Figure 3-16. A spectrum of NH_3-CH_4 (9:1) ice was recorded after the deposition of the first half of the lower layer of Sd8 (*Figure 3-17*, *Figure 3-7*, step 1). The column densities derived from the ν_3- ν_1, ν_4 and ν_2 features are in good agreement: $N(\nu_4) = 5.7 \cdot 10^{18}$ cm^{-2}, $N(\nu_3 - \nu_1) = 5.7 \cdot 10^{18}$ cm^{-2}, $N(\nu_2) = 6.0 \cdot 10^{18}$ cm^{-2}. Assuming an ice density of $\rho(NH_3) = 0.67$ $g.cm^{-3}$ (Satorre et al., 2013) and a molecular mass $M(NH_3) = 17.0$ $g.mol^{-1}$, we derived the ice thickness $\langle d_{IR} \rangle = 2.5 \pm 0.5$ µm. The thickness d_{osc} estimated from the oscillation pattern (see section 3.1.3.1) was $d_{osc} = 2.3 \pm 0.1$ µm. These three features allow to quantify the NH_3 column density in the ice films. In the complete ice films Sd8 and Sd9, the (ν_3- ν_1) and ν_2 bands were saturated, thus NH_3 quantification was performed with the ν_4 band.

The positions of the corresponding bands for the $^{15}ND_3$ molecule were derived from the ND_3 bands reported by Holt et al. (2004) at 25 K since the shift in wavenumber is not expected to be larger than 10 cm^{-1}. In the Table 3-2, first column, the bands associated with the ND_3 molecule are reported together with the band positions attributed to the $^{15}ND_3$ in the Sd8 and Sd9 spectra. The column density of $^{15}ND_3$, $N(^{15}ND_3)$, was derived from the bands at ν_3 = 2490 cm^{-1} and ν_2 = 833 cm^{-1} with the equation 2. The uncertainty on the determination of $N(^{15}ND_3)$ is given by the difference between the results from the two bands. The D/H and $^{15}N/^{14}N$ ratios were then determined as follow:

$$\left(\frac{D}{H}\right)_{IR} = \frac{N(^{15}ND_3)}{\left(N(NH_3) + \frac{4}{3}N(CH_4)\right)} \quad (16)$$

$$\left(\frac{^{15}N}{^{14}N}\right)_{IR} = \frac{N(^{15}ND_3)}{N(NH_3)} \quad (17)$$

In Sd6, Sd8 and Sd9, the ^{13}C-carriers were $^{13}CH_4$ molecules. No specific bands of $^{13}CH_4$ were identified due to their small shift with respect to the bands of CH_4. Measurements of the $^{13}C/^{12}C$ ratio in these samples were thus not achievable with the IR spectra. No signature of oxygen bearing molecules were observed in the ice spectra.

At the end of the irradiation, signatures of irradiation-induced compounds are observed (*Figure 3-18*). The identified bands are listed in the Table 3-2. Based on the ν_2 and ν_3 NH_3 bands, about the half of the ammonia molecules are still present in the irradiated ice film.

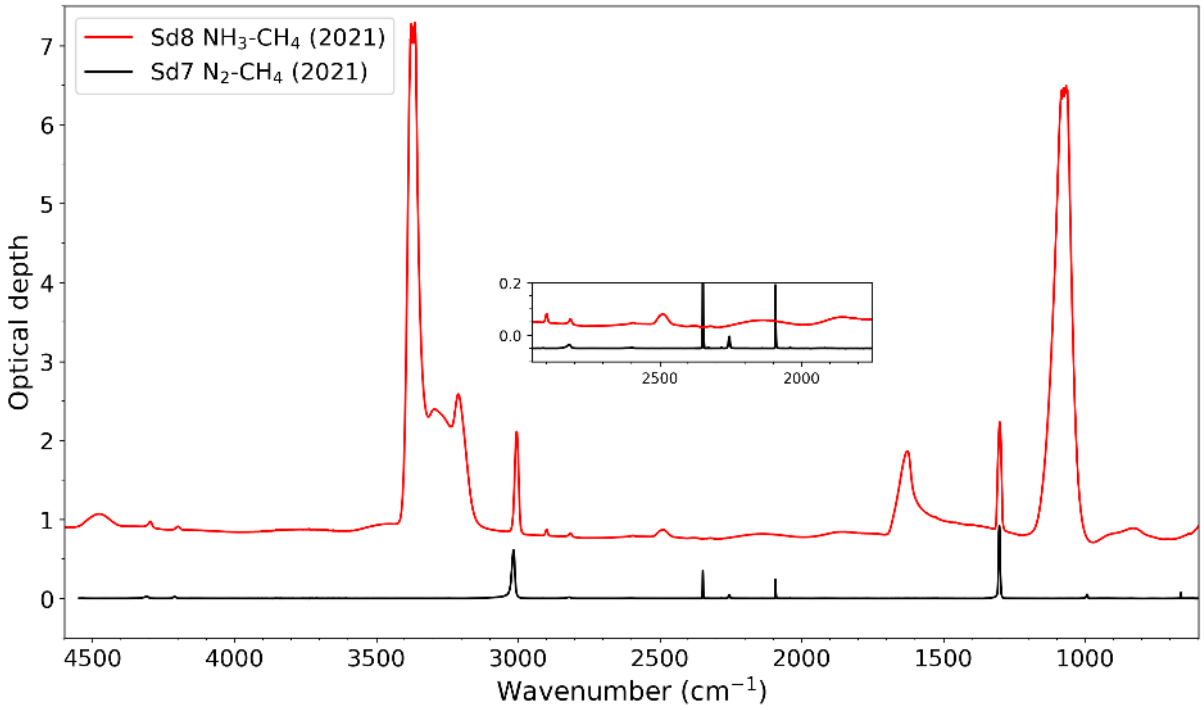

Figure 3-16: Comparison of the IR spectra of the Sd8 (main ice NH_3-CH_4) (red) and Sd7 (main ice N_2-CH_4) (black) ice sandwiches. Bands associated with the NH_3 molecules dominate the Sd8 spectrum (see Figure 3-17). Bands of ^{13}CO, $^{13}CO_2$ and CO_2 are visible in the Sd7 spectrum (zoom box). CH_4 bands appear in both spectra.

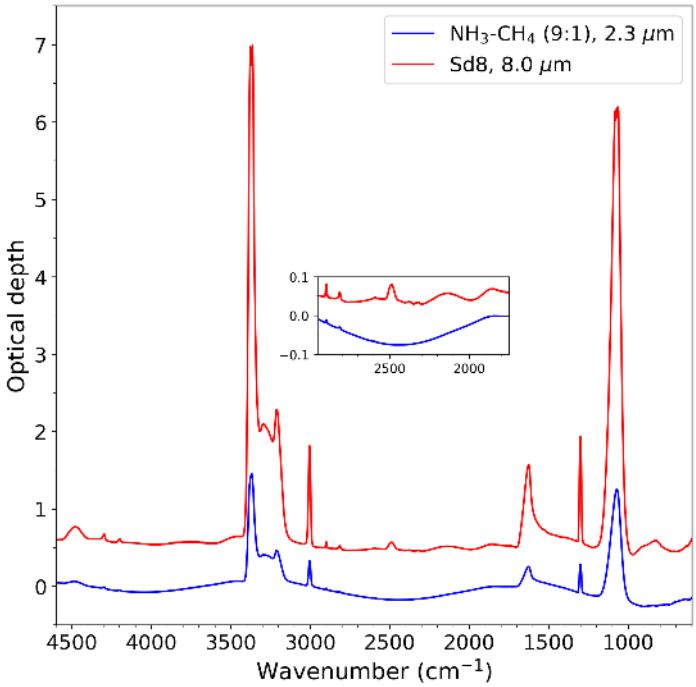

Figure 3-17: IR spectra of a partial (blue) and full (red) ice layer. The first layer (thickness 2.3 µm) of NH_3-CH_4 ice (blue) and of the whole ice on Sd8 prior irradiation (red) before baseline substraction. The 3 main bands associated with the NH_3 ice are observed at 1626 cm^{-1}, 1070 cm^{-1} and between 3420-3120 cm^{-1}(see text). Their integrations allow to derive the column density of NH_3. All of them were found relevant to provide measurements of the column density. In the Sd8 spectrum, the 3420-3120 cm^{-1} and 1070 cm^{-1} were saturated. The quantification of NH_3 was made with the 1626 cm^{-1} band. Comparison between the blue and red spectra allows to identify bands associated with the $^{15}ND_3$ of the labeled layer at 2489 cm^{-1} (zoom box) and 816 cm^{-1}.

Table 3-2: List of the identified IR bands in the ice sandwich prior and after irradiation. (1) Position of the band in cm^{-1}. Values in parentheses correspond to the effective positions of the IR bands in the experimental spectra. (2) Molecule associated with band. (3) Assignment. (4) Oscillator strength (10^{-17} cm/molecule). (5) References where the bands have been identified. Adapted from Augé et al. (2019).

Wavenumber cm^{-1} (1)	Identification (2)	Assignement (3)	A $\times 10^{-17} \mathrm{cm \cdot molec^{-1}}$ (4)	References (5)
4538	CH_4	$\nu_2 + \nu_4$		a
4502	CD_4	$2\nu_3 + \nu_L$		b
4477	CD_4	$2\nu_3$		c
4337	CH_4	$\nu_3 + \nu_4$		a
4327	CH_4	$\nu_3 + \nu_4$		a
4318	CH_4	$\nu_3 + \nu_4$		a
4310	CH_4	$\nu_3 + \nu_4$		a
4194	CH_4	$\nu_3 + 2\nu_4$		c
4122	CH_4	$2\nu_1 + \nu_4$		a
3852	CH_4	$3\nu_4$		a
3708 (3710)	CO_2	$\nu_1 + \nu_3$	0.14	t, u
3371 (3369)	NH_3	ν_3	1.1	q
3420-3120	NH_3	Large band	2.2-3.0	q, r
3270	H-C=C-R	ν(C-H)		d
3226	CD_4	$\nu_3 + \nu_4$		c
3217 (3211)	NH_3	ν_1		s
3091	CD_4	$\nu_1 + \nu_4$		c
3087	CD_4	$\nu_1 + \nu_4$		c
3010	CH_4	ν_3	0.64	q
2985	C_2H_6	ν_{10}		d
2983	CHD_3	ν_1		c
2926	CD_4	$3\nu_4$		c
2914	CH_4	ν_1		a
2832	CH_4	$\nu_2 + \nu_4$		a
2827	CH_4	$\nu_2 + \nu_4$		a
2826	CH_4	$\nu_2 + \nu_4$		a
2820	CH_4	$\nu_2 + \nu_4$		a
2814	CH_4	$\nu_2 + \nu_4$		a
2617	CH_4	$\nu_2 + \nu_4$		a
2602	CH_4	$2\nu_4$		a
2597	CH_4	$2\nu_4$		a
2503 (2489)	ND_3 ($^{15}ND_3$)	ν_3		s
2402	C_2D_2	ν_3		e
2347	N_2	ν_1	0.0015	f
2343 (2348)	CO_2	ν_3	7.6	
2328	N_2	ν_1	0.00022	f
2326 (2321)	ND_3 ($^{15}ND_3$)	ν_1		s
2283	$^{13}CO_2$	ν_3	7.8	t
2251 (2256)	CD_4	ν_3		c
2242	CD_4	ν_3		c

2237	$^{13}CD_4$	ν_3		c
2212	$C_2H_4N_4$			g
2139	CO		1.1	h
2100	HCN			i
2092	^{13}CO		1.3	t, u
2091	CN^-			j
2073	CD_4	$\nu_2 + \nu_4$		c
2040	associated with ^{13}CO			t
2036	HNC	ν_3		k
1975	CD_4	$2\nu_4$		c
1918				
1887	C_2HD	ν_2		e
1656	N_3		0.0072	l
1626	NH_3	ν_4	0.47 - 0.56	m
1465	C_2H_6		0.416	n
1454	NH_4^+	ν_4		o
1305	CH_4	ν_4	0.61	a
1070 (1073)	NH_3	ν_2	2.1 – 1.7	m, r
990	CD_4	ν_4		c
833 (816)	ND_3 ($^{15}ND_3$)	ν_2	5.6	s
825	C_2H_6	ν_{12}	1.6	p
757	C_3H_8			d
660 (662)	CO_2	ν_2	1.1	T, u

(a) Bennett and Kaiser (2007) (b) Calvani et al. (1989) (c) He et al. (2010) (d) Gerakines et al. (1996) (e) Bottger and Eggers (1964) (f) de Barros et al. (2015) (g) Gerakines et al. (2004) (h) Palumbo and Strazzulla (1993) (i) Burgdorf et al. (2010) (j) Moore and Hudson (2003) (k) Wu et al. (2013) (l) Hudson and Moore (2002) (m) Sandford and Allamandola (1993) (n) Moore and Hudson (1998) (o) Schutte and Khanna (2003) (p) Öberg et al. (2009) (q) D'Hendecourt and Allamandola (1986) (r) Bouilloud et al. (2015) (s) Holt et al. (2004) (t) Gerakines et al. (1995) (u) Isokoski et al. (2013).

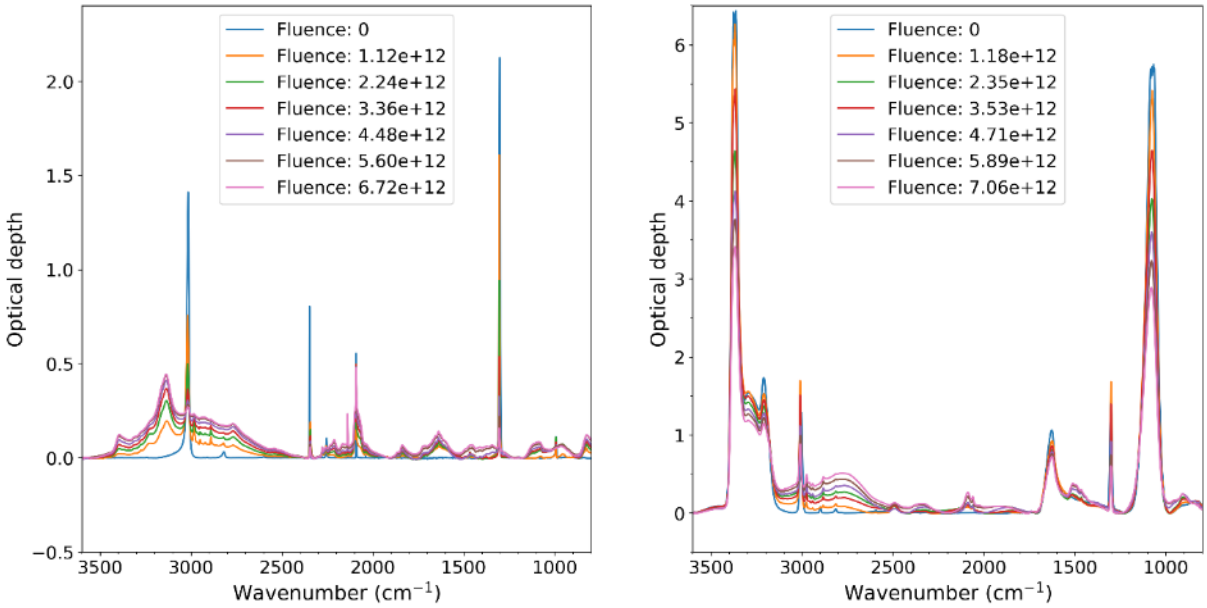

Figure 3-18: Evolution of the Sd7 (left) and Sd8 (right) ice films under irradiation up to ~7x10^{12} ions/cm^2. At the end of the irradiation, complex compounds have formed. Large quantities of NH_3 remains in the case of Sd8.

3.2.3. Characterization of the residues

3.2.3.1. *Residues from N_2-dominated ice films.*

All the organic residues obtained from the different irradiation sessions of N_2-dominated ices (Sd1, 2, 3, 4, 5, 6, 7) share similar IR spectra, showing that the chemical nature of the residue is driven by the nature of the ice mixture (Figure 3-19).

However, the morphology of the residues changed from one experimental session to another (Figure 3-20). Residues Sd1, 2 and 3 from the 2019 session display a compact and homogeneous structure divided in islands with thicker organic residue and valleys with thinner material. Measurements of the Sd2 residue with an atomic force microscope (AFM) indicated a typical heights $h_{islands}$= 130-160 nm and $h_{valleys}$= 30-60 nm for the islands and the valleys respectively. The residues Sd4, 5 and 6 from 2020 experiment exhibit larger patches of matter separated by empty furrows. The furrows' lateral thickness slightly varies in the residue. Particularly, in the Sd4 residue, small concentric holes are observed (see Sd4, Figure 3-20). These holes are most probably due to the formation of bubbles during the slow sublimation process at the end of the experiment. The occurrence of such bubbles is most probably due to an imperfect thermal conductivity between the small 5 mm Si windows used in the sample holder. During the 2020 experimental session, several 5 mm Si windows did not exhibit any residue at the end of the annealing process, strongly suggesting an imperfect thermal contact that may have causes an uncontrolled rapid heating of the ices and a brutal volatilization or/and removal of both the ices and the irradiation-induced residue precursors. Notably, around the holes of Sd4 residues, smaller patches of organic matter are observed; we will come back to these peculiar patches in section 3.3.1.

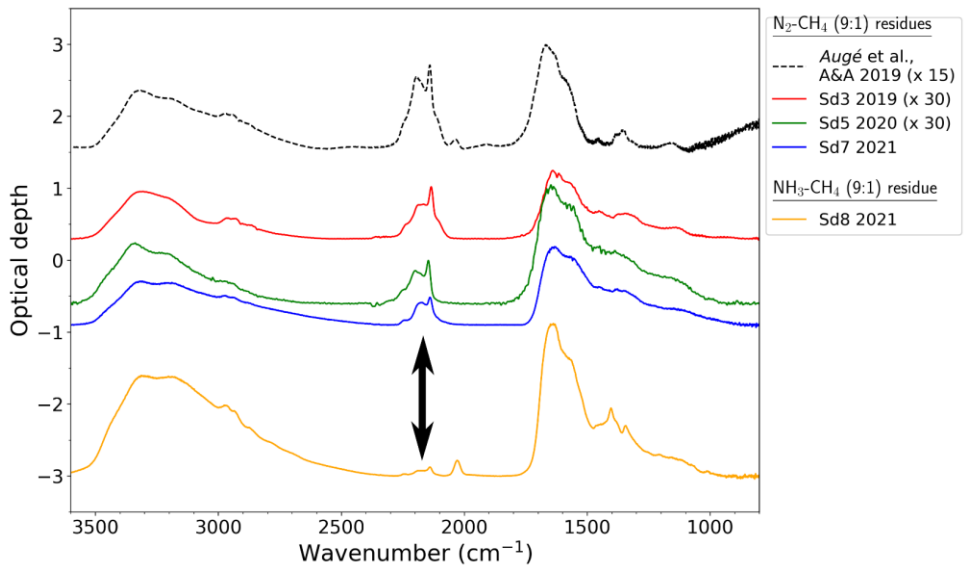

Figure 3-19: IR spectra of organic residues formed from the ion-iradiation of ices. Spectra of residues formed from N_2-CH_4 ices are similar. The spectrum reported by Augé et al. (2019) is plotted with dashed lines for comparison. The IR spectrum of Sd8 has a feature between 2100 and 2300 cm^{-1} (C≡N/N≡C) showing that the residue present a chemical composition different from the other residues (black arrow).

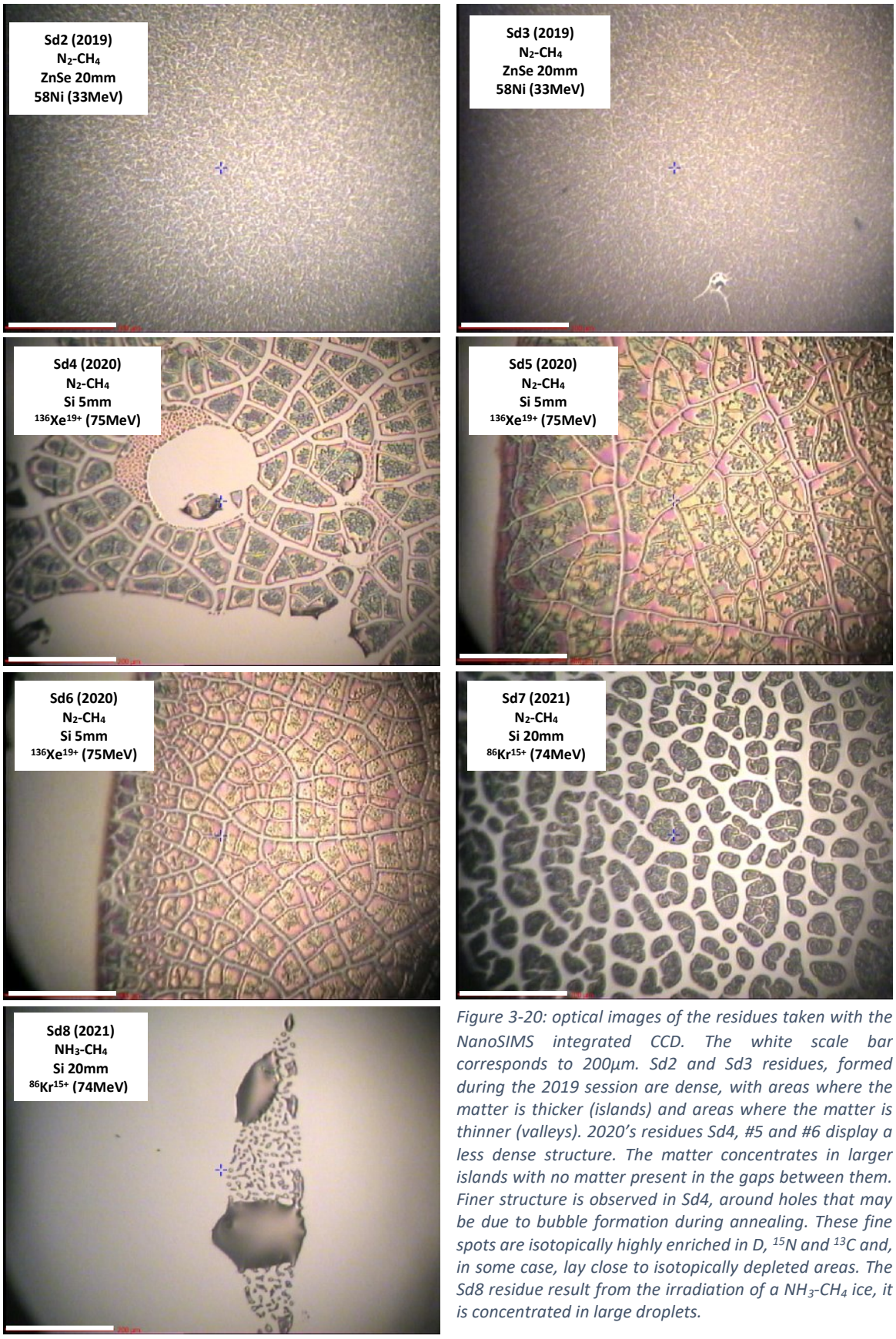

Figure 3-20: optical images of the residues taken with the NanoSIMS integrated CCD. The white scale bar corresponds to 200µm. Sd2 and Sd3 residues, formed during the 2019 session are dense, with areas where the matter is thicker (islands) and areas where the matter is thinner (valleys). 2020's residues Sd4, #5 and #6 display a less dense structure. The matter concentrates in larger islands with no matter present in the gaps between them. Finer structure is observed in Sd4, around holes that may be due to bubble formation during annealing. These fine spots are isotopically highly enriched in D, ^{15}N and ^{13}C and, in some case, lay close to isotopically depleted areas. The Sd8 residue result from the irradiation of a NH_3-CH_4 ice, it is concentrated in large droplets.

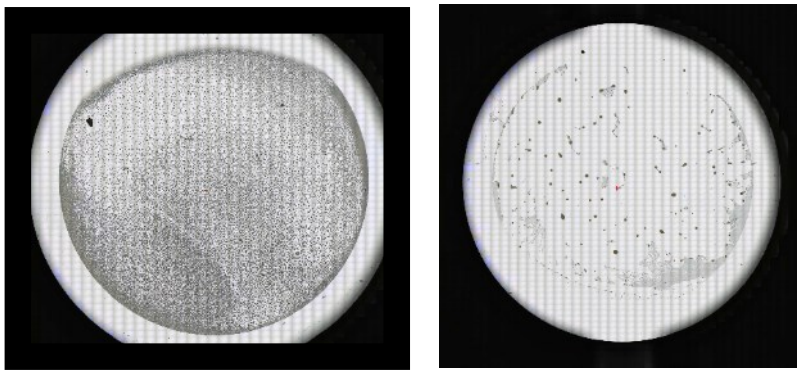

Figure 3-21: optical mosaic of the 2021 residues Sd7 (left) and Sd8 (right) on the 20 mm large Si substrate windows. Sd7 residue has the characteristic shape of residue obtained with N_2-dominated ices with a homogeneous structure on the substrate window. Sd8 residue is the one obtained with NH_3-dominated ice, the matter is concentrated around smaller spots but much thicker, up to 5 µm in height.

3.2.3.2. *Residues from NH_3-dominated ice films*

The annealing of sandwiches Sd8 and Sd9, made of NH_3-dominated ice, led to the formation of several hundred microns large patches of organic residues separated by large empty areas (*Figure 3-21*, right) preventing the recording of relevant *in-situ* IR spectra due to the lack of homogeneous film of material in the line of sight. Subsequent IR measurements and optical images of Sd8 residue were taken with a µ-FTIR spectrometer after extraction of the substrate windows from the IGLIAS chamber (see *Figure 3-21*, left and Figure 3-19). Figure 3-19, bottom shows the spectrum of a spot of matter of the Sd8 residue. Following the methodology described in section 3.1.3.1, the thickness of the spot can be derived from the fringe pattern observed between 5000 and 3600 cm^{-1}. Assuming a refractive index n = 1.55 for the Sd8 residue, classical of poly-HCN residue (Khare et al., 1994), one gets a thickness of 5.7 µm. The spots of residue formed from NH_3-dominated ice are therefore scattered over the window, but up to 30 times thicker than the more homogeneously distributed residues formed from N_2-dominated ice during the same experimental session (*Figure 3-21*, left).

3.2.4. Isotopic mapping of the residues

Isotopic mappings of the residues were obtained at the NanoSIMS instrument at Institut Curie during 4 sessions in 2019, 2020 and 2021. The analytical conditions of the different NanoSIMS sessions are detailed in the annex 5.2.1. The analyses of samples Sd2 and Sd3 were limited to about 300 frames' acquisitions due to the charging effects (see annex 5.2). After 300 frames, the residual charges on the samples caused the deviation of the secondary ion beam resulting in the extinction of the image. This issue was resolved in the 2020 and 2021 experiments by replacing the ZnSe substrate windows by conducting Si substrate windows. Thanks to these new windows, the 2020 and 2021 NanoSIMS sessions were remarkably stable allowing acquisitions of more than 1000 frames on a given area. In order to obtain a sufficient counting statistic on isotopic images, CH^- and CD^- frames were stacked by 100 while $^{12}C^{14}N^-$,

$^{13}C^{14}N^-$, $^{12}C^{15}N^-$ frames were stacked by 50. Given that measurements with the switching mode presented in section 3.1.4.2 result in 2 times more CH^- and CD^- frames than $^{12}C^{14}N^-$, $^{13}C^{14}N^-$, $^{12}C^{15}N^-$ frames, the synchronization of the two group of stacked frames was preserved.

3.2.4.1. *Isotopic images of residues from N_2-CH_4 ices.*

Sd3 and Sd7 ice films had the same layer composition: $^{15}N_2$-CD_4-^{13}CO.

Residue Sd3 (N_2-CH_4 ; $^{15}N_2$-CD_4-13CO)

The concentration of labeled ice in Sd3 was about 1.7% (Table 3-1) but the NanoSIMS secondary CD^- emission was too low to measure precisely the D/H ratio over 300 frames. Longer NanoSIMS analyses to increase the CD^- counting were not possible due to the charging effects. $^{15}N/^{14}N$ and $^{13}C/^{12}C$ have been measured in the 2 first stacks of the analyses. The islands and valleys visible on the CCD images (see *Figure 3-20*) appear on the ratio images, revealing that these two features have different isotopic compositions. Though, valleys are made of lower quantities of matter allowing measurements only in the 2 first stacks of the acquisition.

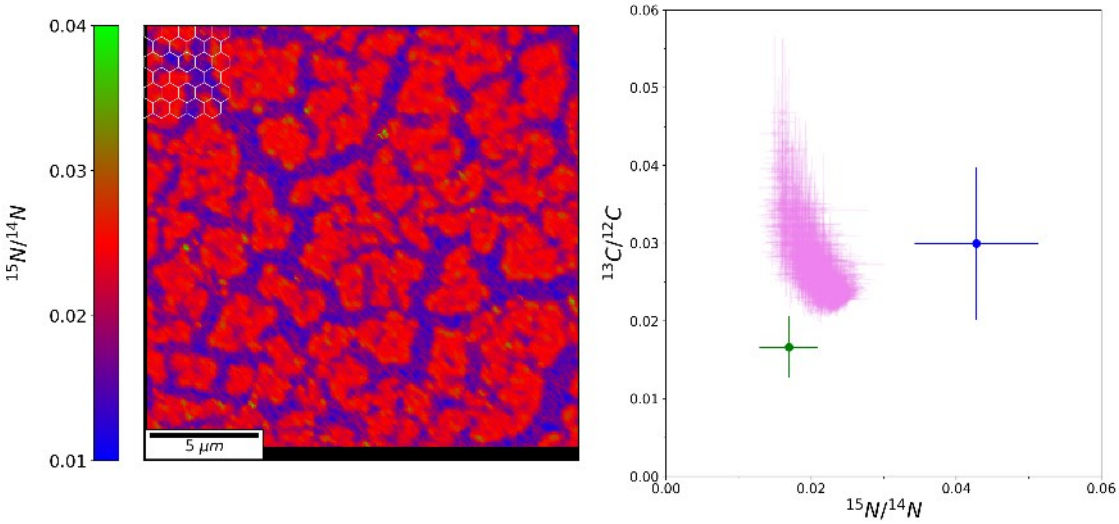

Figure 3-22. Left: $^{15}N/^{14}N$ ratio image of the Sd3 residue. Measurements of the $^{13}C/^{12}C$ and $^{15}N/^{14}N$ ratios were made according to a hexagonal mesh (top left of the image). Right: mean $^{13}C/^{12}C$ and $^{15}N/^{14}N$ ratios measured in the cells of the hexagonal mesh. The error bars are equal to the standard deviation of the cells' values. The approximate isotopic ratios of the initial ice film estimated from the QMS data and partial pressure are reported in blue and green.

Figure 3-22 is based on the analysis of the second stack. Points reported in the right panel are the mean values of the pixels contained in the mesh cells on the ratio images (left panel). An anti-correlation of the $^{13}C/^{12}C$ and $^{15}N/^{14}N$ ratios is observed: valleys are enriched in ^{13}C and depleted in ^{15}N whereas islands are richer in ^{15}N and depleted in ^{13}C. However, this peculiar behavior was not observed in the other residues from this work (see below) and thus, given the difficult analysis conditions on that window, it remains to be confirmed by future experiments. In the islands, the mean ratios are well defined: $\langle^{15}N/^{14}N\rangle_{islands}$ = $(2.4\pm0.2)\cdot10^{-2}$, $\langle^{13}C/^{12}C\rangle_{islands}$ = $(2.4\pm0.2)\cdot10^{-2}$. The nitrogen isotopic composition of the valley is well constrained with $\langle^{15}N/^{14}N\rangle_{valleys}$ = $(1.8\pm0.3)\cdot10^{-2}$, but its $^{13}C/^{12}C$ composition is less well constrained and ranges from 0.03 to 0.05. The ratios measured in the Sd3 residue are in fair agreement with the

approximate bulk ratios estimated from the QMS data and the partial pressure measurements (respectively blue and green error bars on *Figure 3-22. Left: $^{15N}/_{14N}$ ratio image of the Sd3 residue.Figure 3-22*).

Residue Sd7 (N_2-CH_4 ; 15N2-CD_4-^{13}CO)

Four analyses were performed in different areas of the Sd7 residue. They revealed a diversity of isotopic ratios as shown in *Figure 3-23*. Three main isotopic poles are identified:

- A cold endmember with $(^{15}N/^{14}N)_{cold} = (3.0 - 8.0)\cdot10^{-2}$, $(^{13}C/^{12}C)_{cold} = (2.0 - 4.0)\cdot10^{-2}$ and $(D/H)_{cold} = (1.0 - 5.0)\cdot10^{-2}$.
- A medium dominant component with $(^{15}N/^{14}N)_{medium} = (10.0 - 15.0)\cdot10^{-2}$, $(^{13}C/^{12}C)_{medium} = (4.0 - 7.0)\cdot10^{-2}$ and $(D/H)_{medium} = (5.0 - 9.0)\cdot10^{-2}$.
- A hot endmember with $(^{15}N/^{14}N)_{hot} = (17.0 - 20.0)\cdot10^{-2}$, $(^{13}C/^{12}C)_{hot} = (7.0 - 8.0)\cdot10^{-2}$ and $(D/H)_{hot} = (10.0 - 12.0)\cdot10^{-2}$.

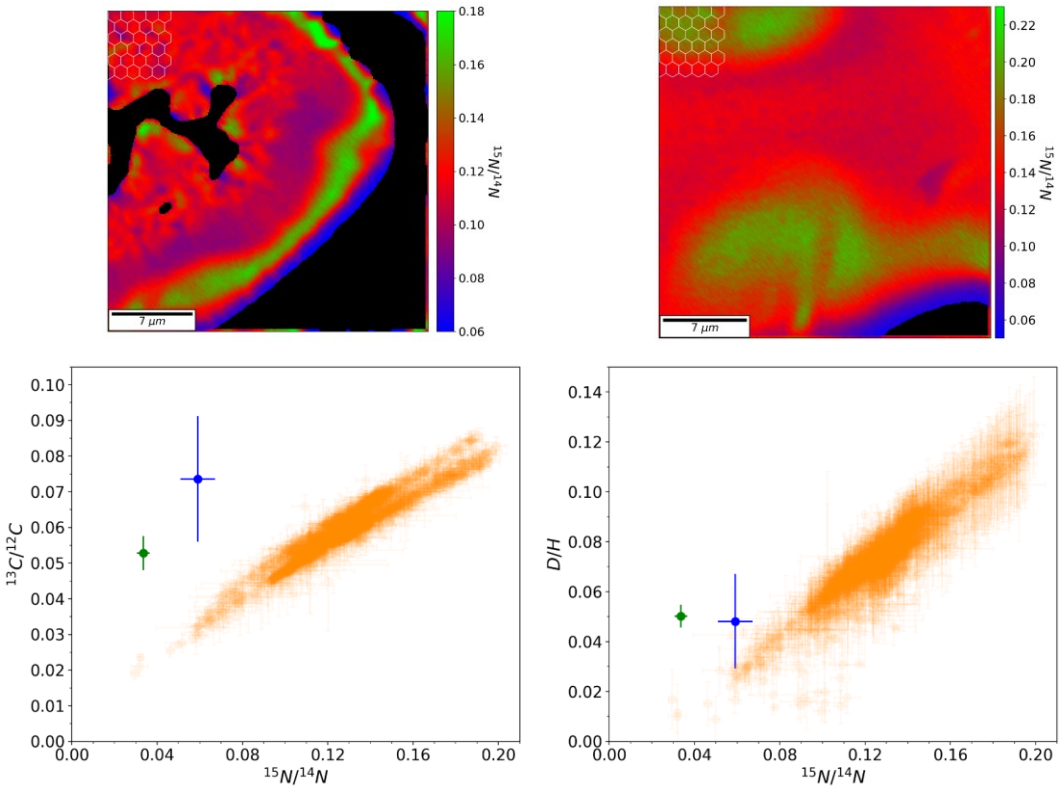

Figure 3-23. Top left and right: $^{15}N/^{14}N$ ratio images of 2 zones of the Sd7 residue. Bottom: $^{13}C/^{12}C$ (left), D/H (right) and $^{15}N/^{14}N$ ratios measured in the 4 analyzed zones of the Sd7 residues according to the hexagonal mesh (see text). Estimated isotopic ratios of the ice film are reported in blue (QMS) and green (partial pressure).

In Sd7, the enrichments in $^{15}N/^{14}N$, $^{13}C/^{12}C$ and D/H are clearly correlated and spread along straight lines (*Figure 3-23*, bottom panels) defining mixing lines between the main isotopic composition and the ^{15}N, ^{13}C and D rich end-members. Such feature indicates that the residue keeps the memory of the layered structure of the original ice film. D/H values exhibit a larger spread compared with $^{15}N/^{14}N$ and $^{13}C/^{12}C$ that might be the result to the lower mobility of the D and H atoms in the ice during the irradiation and the warming sequence.

While the average $^{13}C/^{12}C$ and D/H ratios measured in the residue are close to the estimated bulk ratio of the ice film (blue and green error bars in *Figure 3-23*), the $^{15}N/^{14}N$ ratios measured in the residue are substantially higher than those estimated from the bulk ratio of the ice film. This underestimation of the $^{15}N_2$ in Sd7 may result from an observed small leak between the volumes of $^{15}N_2$ and N_2-CH_4 in the mixing line during the 2021 experimental session.

Residue Sd4 (N_2-CH_4 ; $^{15}N_2$-$^{13}CD_4$)

The labeled ice layer of Sd4 was made of a $^{15}N_2$-$^{13}CD_4$ (9:1) mix. The vast majority of the residue consists in islands of matter (*Figure 3-20*) that exhibit homogeneous isotopic compositions. Strikingly, large isotopic heterogeneities are observed in patches of matter at the vicinity of holes (Sd4 on *Figure 3-20* and *Figure 3-24*). Two NanoSIMS analyses performed in these regions revealed 3 well-defined isotopic poles, stable along the analyses (*Figure 3-24* and *Figure 3-25*):

- A cold endmember with $(^{15}N/^{14}N)_{cold} = (1.0 - 2.0)\cdot10^{-2}$, $(^{13}C/^{12}C)_{cold} = (1.5 - 2.0)\cdot10^{-2}$ and $(D/H)_{cold} = (0.2 - 0.8)\cdot10^{-2}$.
- A medium dominant component with $(^{15}N/^{14}N)_{medium} = (3.5 - 6.5)\cdot10^{-2}$, $(^{13}C/^{12}C)_{medium} = (3.0 - 6.0)\cdot10^{-2}$ and $(D/H)_{medium} = (1.5 - 3.5)\cdot10^{-2}$.
- A hot endmember with $(^{15}N/^{14}N)_{hot} = (8.0 - 10.0)\cdot10^{-2}$, $(^{13}C/^{12}C)_{hot} = (8.0 - 9.5)\cdot10^{-2}$ and $(D/H)_{hot} = (1.5 - 5.0)\cdot10^{-2}$.

The distributions of the isotopic ratio values in the first image are presented as 2-dimensionsal histograms in *Figure 3-24*. To each stack in abscissa is associated the pixel ratio distribution which density is given by a black color scale. Such 2-dimensionsal histograms allow to see the evolution of the isotopic ratios during the NanoSIMS analyses as well as the presence of isotopic heterogeneities in the images.

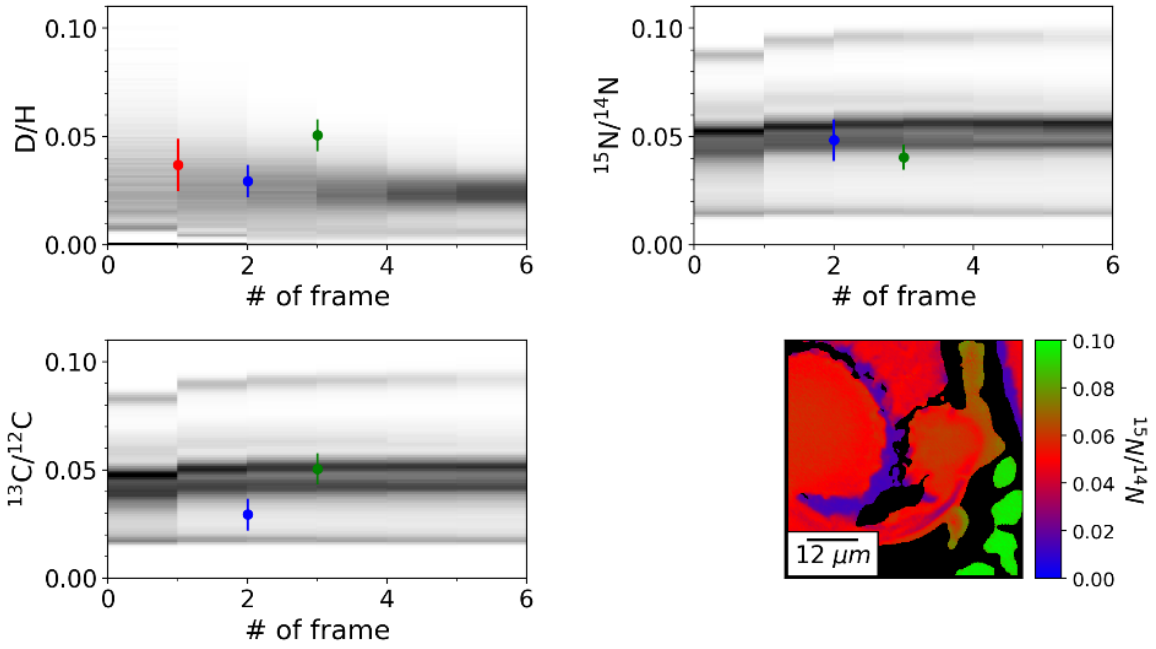

Figure 3-24: Evolution of the D/H (top left), $^{15}N/^{14}N$ (top right) and $^{13}C/^{12}C$ (bottom left) ratios along the NanoSIMS analysis of the Sd4 residue. Red, blue and green error bars indicate the ratios derived from IR, QMS and partial pressure measurements respectively. Three isotopic poles are revealed by the analysis.

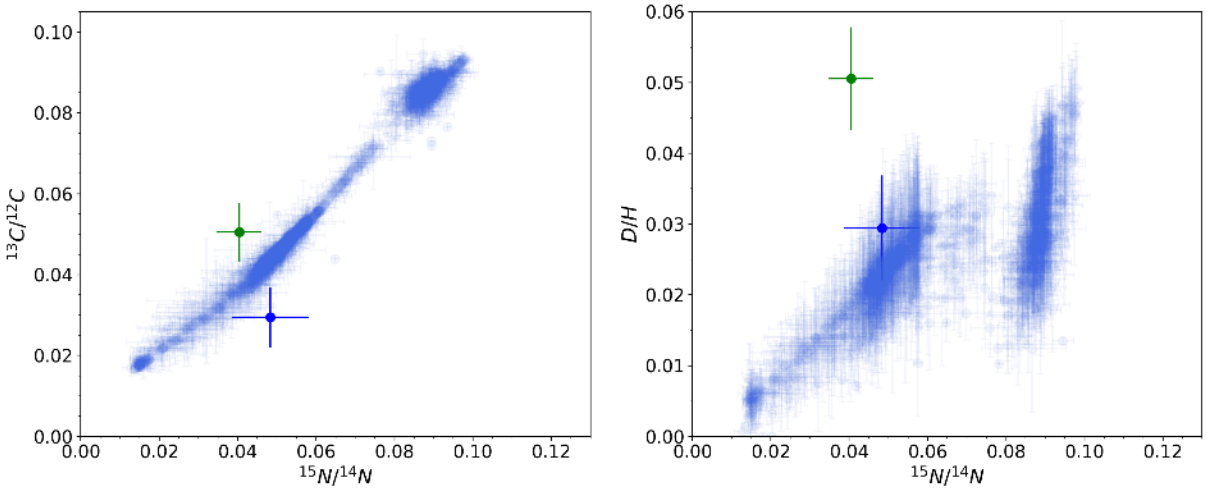

Figure 3-25: $^{13}C/^{12}C$ $^{15}N/^{14}N$ (left), $^{15}N/^{14}N$ vs D/H (right) spatial correlations measured in the Sd4 residue with a hexagonal mesh. The estimated bulk ratio of the initial ice film are indicated by the dark blue (QMS) and green (partial pressure) error bars.

As observed in the Sd7 residue, the correlation between the enrichments in ^{15}N, ^{13}C and D indicate that the residue keeps the memory of the ice isotopic heterogeneities. The spread of the D/H values that extend on a more restricted range of variation indicates a more effective diffusion of the D and H atoms in the ice during either the irradiation of the ice and/or the residue formation process.

Residue Sd5 (N_2-CH_4 ; $^{15}N_2$ -13CO)

Residue Sd5 was labeled by a $^{15}N_2$-^{13}CO ice layer. The isotopic mapping of the residue displays a homogeneous isotopic composition (see *Figure 3-26*). As in the Sd4 and Sd7 residues, the ^{13}C and ^{15}N enrichments are spatially correlated. The mean isotopic ratios are $^{15}N/^{14}N = (4.1 \pm 0.3)\cdot 10^{-2}$ and $^{13}C/^{12}C = (3.9 \pm 0.2)\cdot 10^{-2}$.

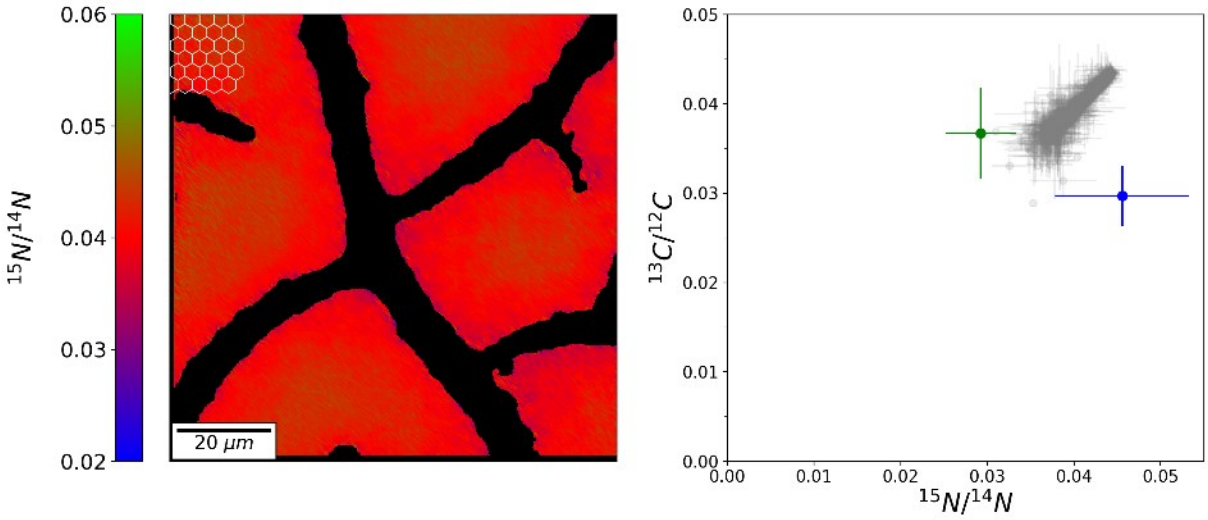

Figure 3-26: Left: $^{15}N/^{14}N$ ratio image of the Sd5 residue. Right: mean $^{13}C/^{12}C$ vs $^{15}N/^{14}N$ ratios measured in the cells of the hexagonal mesh (see upper left). The error bars are equal to the standard deviation of the cells' counting values. Isotopic ratios of the initial ice film are reported in blue (QMS) and green (partial pressure).

Residue Sd8 (NH_3-CH_4 ; $^{15}ND_3$-$^{13}CH_4$).

NanoSIMS isotopic maps of the Sd8 residue reveal an isotopically very homogeneous matter with limited spatial variations, suggesting an efficient mixing either during the irradiation and/or the annealing of the ice, or an efficient dissociation of NH_3 compared to N_2. Most of the residue display constant isotopic ratios with low dispersion around the mean values:

- $D/H = (8.0 \pm 0.8)\cdot 10^{-3}$
- $^{15}N/^{14}N = (3.5 \pm 0.1)\cdot 10^{-2}$
- $^{13}C/^{12}C = (3.5 \pm 0.1)\cdot 10^{-2}$

Errors corresponds to one standard deviation and were measured on the 6th frame.

Bottom panels of *Figure 3-27* compare the distribution of isotopic ratios with the bulk isotopic ratio of the ice film estimated with the QMS (dark blue), partial pressure (green) and the IR spectra (red). $^{13}C/^{12}C$ and $^{15}N/^{14}N$ ratios derived from the partial pressures are comparable with the ratios measured in the residue, however, the D/H value of the residue is lower than the estimations from partial pressures.

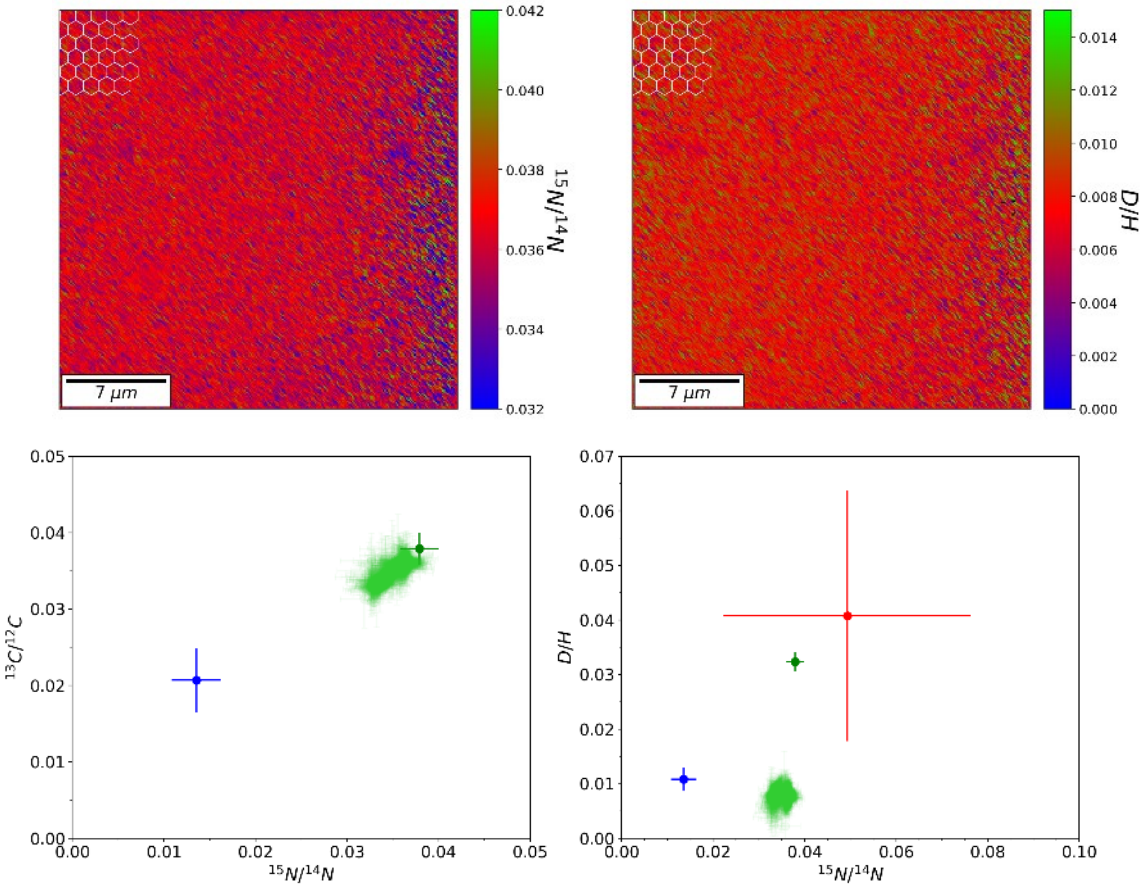

Figure 3-27. Top: $^{15}N/^{14}N$ (left) and D/H (right) maps of a droplet of the Sd8 residue. Bottom: spatially correlated $^{13}C/^{12}C$ (left), D/H (right) and $^{15}N/^{14}N$ ratios measured in the Sd4 residue with a hexagonal mesh. Estimated bulk ratio of the ice film are indicated by the dark blue (QMS), green (partial pressure) and red (IR) error bars.

3.3 Discussion

3.3.1. Formation of isotopic heterogeneities in the residues

Figure 3-28 shows the H, N and C isotopic ratios measured in 5 organic residues. The spread of the isotopic ratios varies from one residue to another but is often distributed along a mixing line. Strikingly, the residues formed from the irradiation of N_2-CH_4 ices have more heterogeneous isotopic compositions than the residue formed from the irradiation of a NH_3-CH_4 ice (Sd8 in green in *Figure 3-28*). The bulk composition of Sd4 is indicated with blue dashed ellipses. Although patches of matter with high and low isotopic ratios are observed in Sd4, they are all spatially localized around holes (see section 3.2.3) and do not reflect the bulk composition of Sd4 (that exhibit much lower isotopic fractionation). Sd3 presents a specific isotopic composition with an anti-correlation of the $^{13}C/^{12}C$ and $^{15}N/^{14}N$ ratios. However, due to charging effects on that residue during the NanoSIMS acquisitions, we were not able to deepen the analysis. This feature was not observed in the residue Sd7 synthetized from an initial ice sandwich with the same composition and remain thus to be confirmed. The average values of the $^{13}C/^{12}C$ and $^{15}N/^{14}N$ in Sd3 are on the trends observed for other mixtures but their dispersion should be taken with caution and deserve further investigations to be confirmed.

Organic residues Sd7 and Sd8 were formed during the same experimental session at GANIL in 2021, with the same $^{86}Kr^{15+}$ (74 MeV) ion beam, starting from two different ice mixtures: N_2-CH_4 and NH_3-CH_4 respectively. They experienced the exact same annealing procedure and still present very distinct structures and isotopic spatial distributions. The large isotopic heterogeneities in Sd7 (red crosses in *Figure 3-28*) are observed at scales ranging from 1 to 10 microns (*Figure 3-23*). Unlike in the Sd4 residue, they are not spatially localized in limited zones and constitute a global feature. Conversely the Sd8 residue (green crosses in *Figure 3-28*) is characterized by a much more homogeneous composition. NanoSIMS analyses on Sd8 were performed on different residue droplets of matter separated by several millimeters on the substrate window (see *Figure 3-20* and *Figure 3-21*) and all revealed the same homogeneous isotopic composition in H, N and C. The absence of heterogeneities in Sd8 most probably derives from the chemical specific nature of the NH_3-CH_4 initial ice mixture.

Several studies on the formation of organic residues from the UV-irradiation of H_2O-CH_3OH-NH_3 ice mixtures at low temperature (10K) (Piani et al., 2017; Tachibana et al., 2017) evidenced the formation of several microns large bubbles when warming-up the ice films. These bubbles were associated with the formation of H_2 from the processing of NH_3 and CH_3OH during the irradiation, with a correlation between the number of bubbles and the abundances of these two molecules in the initial mixture. In an investigation on the annealing of NH_3-H_2O ice films (not containing C-bearing molecules) irradiated by 100 keV protons, Loeffler and Baragiola (2012) observed H_2 outbursts interpreted as resulting from the formation of bubbles in the processed ices. The high abundance of hydrogen atoms from the NH_3 molecules in the Sd8 ice film and an efficient radiolytic production of H_2 might thus be responsible for the structure of the residue. Before the evaporation of the remaining volatile species, irradiated ice films display a liquid-like behavior (Tachibana et al., 2017). An extensive mixing of the synthetized radicals during this phase might have occurred in the case of Sd8 leading to an efficient mixing of the initial heterogeneous isotopic composition of the ice layers. The large size of the residue droplets in Sd8 suggest a different retracting dynamic of this residue (compared to the N_2-CH_4 residue) during the annealing. The fact that the mixing is less effective in the case of the N_2-CH_4 ice films may be due to a lower mobility (*i.e*. a higher "viscosity") of the irradiated mixture (Piani et al., 2017), linked to the lower abundance of hydrogen atoms.

Organic residues formed from the ion-irradiation of H, N and C isotopically heterogeneous ice films present isotopic heterogeneities at the 1 – 10 microns scale (corresponding to the typical thickness of the initial ice films). The structure of the residue and the transmission of isotopic heterogeneities from the ice mixture depend on several factors including: the nature and roughness of the substrate window, the energy of the ions used for the irradiation and the pace of the annealing ramp. Still, when formed under the very same conditions, residues derived from N_2-CH_4 or NH_3-CH_4 ice mixtures display distinct isotopic compositions and structures. This indicates that the chemical nature of the irradiated ice has a direct and crucial influence on the inheritance of H, N and C isotopic heterogeneities from the initial ice to the organic residue.

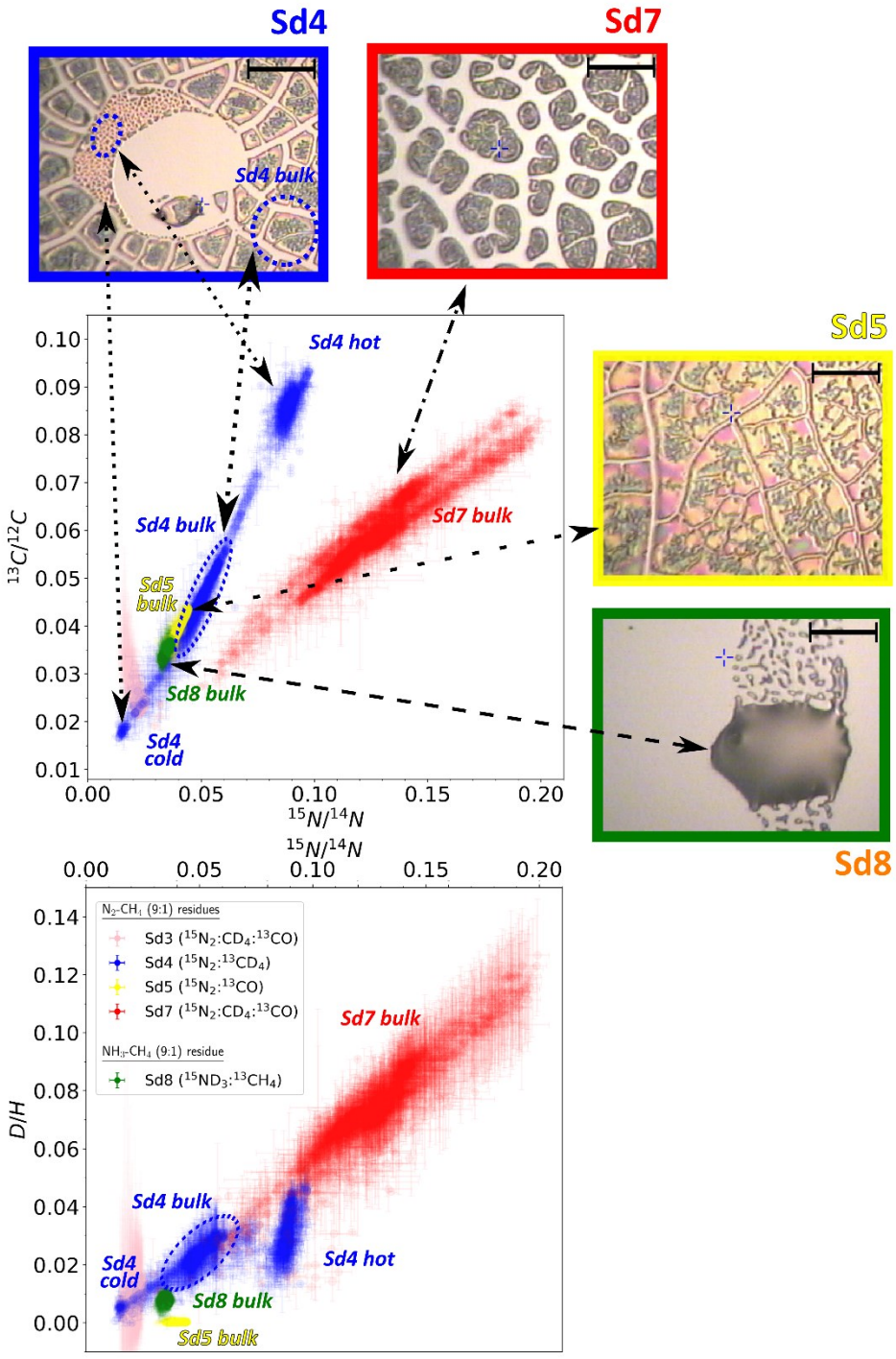

Figure 3-28 : $^{15}N/^{14}N$ vs $^{13}C/^{12}C$ (bottom) and D/H (top) ratios measured in 5 residues formed from the irradiation of N_2-CH_4 (gray, blue, yellow, red) and NH_3-CH_4 (green) ices. The composition of the inner labeled ice layer for each residue is indicated in parenthesis in the legend. Sd4 exhibit localized zones with high isotopic heterogeneities. The bulk composition of Sd4 is located within blue dotted ovals.

The formation of localized patches of matter with D/H, $^{15}N/^{14}N$ and $^{13}C/^{12}C$ ratios very different from the bulk ratios (Sd4, Figure 3-24) shows the possibility to concentrate a specific composition in the residue to give rise to highly fractionated small areas, *i.e.* "hotspots". This process may be controlled by the matrix mobility and kinetics during the annealing. This hypothesis is supported by the fact that the Sd4 residue is the only residue where the tiny droplets with large isotopic anomalies (^{15}N, ^{13}C and D) inherited from the initial ice mixture are observed. Strikingly, Sd4 is also the only residue where we observed the holes, most probably due a perturbed heating. The perturbed annealing may have induced rapid changes in the matrix mobility and kinetics resulting in isolation of portions of the residue.

The overall physico-chemical processes leading to the formation of such residues is highly complex and its deeper understanding would require detailed studies that are, by far, beyond the scope of the present work. However, even if many ice mixture compositions, other stratification of the ice layers, and processes remain to be explored further, the present work demonstrates that irradiation by swift ions of ices produces, after annealing, refractory organics with various type of isotopic heterogeneities. The mere observation of such diverse isotopic heterogeneities opens a path for a better understanding of the formation of organics at the surface of icy bodies.

3.3.2. Implications on irradiation-induced organics at the surface of icy bodies

Organic residues formed from the processing of C-bearing ice films are often considered to be convincing analogs of the organic matter formed in space (Bonnet et al., 2015; Gerakines et al., 2004; Mahjoub et al., 2021). More specifically, Augé et al. (2016) showed that the IR signature of UCAMMs can be fairly reproduced by heating up to 600K an organic residue synthetized from the ion-irradiation of a N_2-CH_4 ice mixture. Such heating episode can be experienced by UCAMMs during their high-velocity entry in Earth atmosphere. N_2, CH_4 and CO ices were observed at the surface of several Kuiper Belt objects (KBOs, Figure 3-30 and *Figure 3-29*) (Douté et al., 1999; Grundy et al., 2016), where the different species are mixed. The GCRs and UVs processing of such nitrogen-rich ice mantles can produce the organic matter of UCAMMs. Based on a time-dependent atmospheric escape model, Schaller and Brown (2007) were able to explain the persistence of N_2, CH_4 and CO ices at the surface of large and cold KBOs (*Figure 3-29*). The chemical nature of the ices condensed at the surfaces of KBOs in the early ages of the solar system depends on their radial position in the disk relatively to the various volatiles species snowlines. Brown et al. (2011b) proposed that the nature of the organic crust formed on the surface of KBOs by the irradiation processes depends on the initial ice composition and the exposure time to solar radiation (Figure 3-30, left). In such a scenario, the ice mantles can be formed above 10 A.U. and progressively depleted from volatile species by atmospheric escape (within about 10 Myr, depending on their distance to the sun). It is likely that small bodies experienced several ice condensation and irradiation during their evolution in the early solar system, especially if they radially drifted in the disk. This would have resulted in the formation of a complex organic crust formed from the irradiation of a mixture of several (heterogeneous) ices.

The remote observation of the disk around TW Hya (Figure 3-30, right, Qi et al. (2013)), an analog of the young solar disk, allowed to identify the CO snowlines at ≈30 A.U. from the emission of N_2H^+ that is efficiently destroyed when in presence of gaseous CO. This observation along with atmospheric escape models allow to infer that the ice mantles that can give rise to the formation of the organic matter in UCAMMs were most probably formed in regions above 10 A.U. Their processing by UV and GCR were most probably continuous over time, enabling the continuous formation of newly condensed ices resulting from

the radial mixing. Still, the chemical composition and the degree of mixing of the initial ices are poorly constrained. Investigating the transmission of isotopic heterogeneities from the initial ice to the organic residue can provide additional elements for the understanding of the formation of the organic matter of UCAMMs

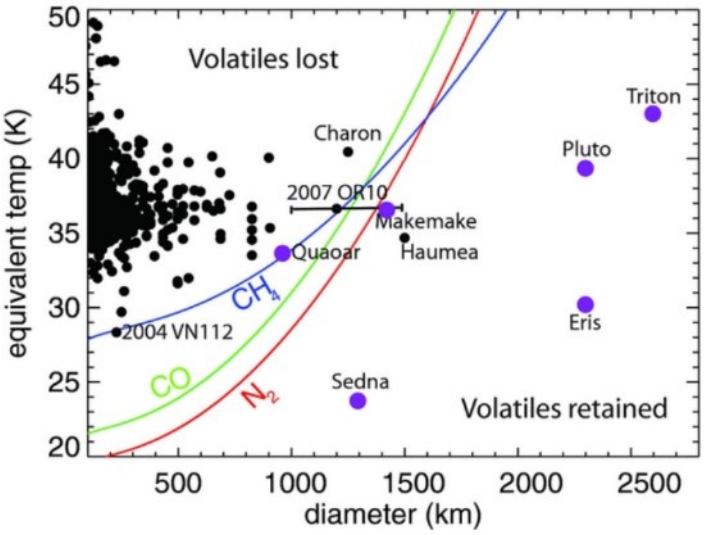

Figure 3-29: condensation lines of CH_4, CO and N_2 on small bodies as function of the diameter of the bodies and the equivalent temperature from Brown et al. (2011a). Black dots are Kuiper Belt objects (KBO). Purple dots are KBOs where CH_4 have been observed. The presence of volatile ice mantles on the KBOs is fairly well described by a model of time-dependent atmospheric escape. In earlier ages of the solar system, smaller bodies may have been able to retain volatile ices.

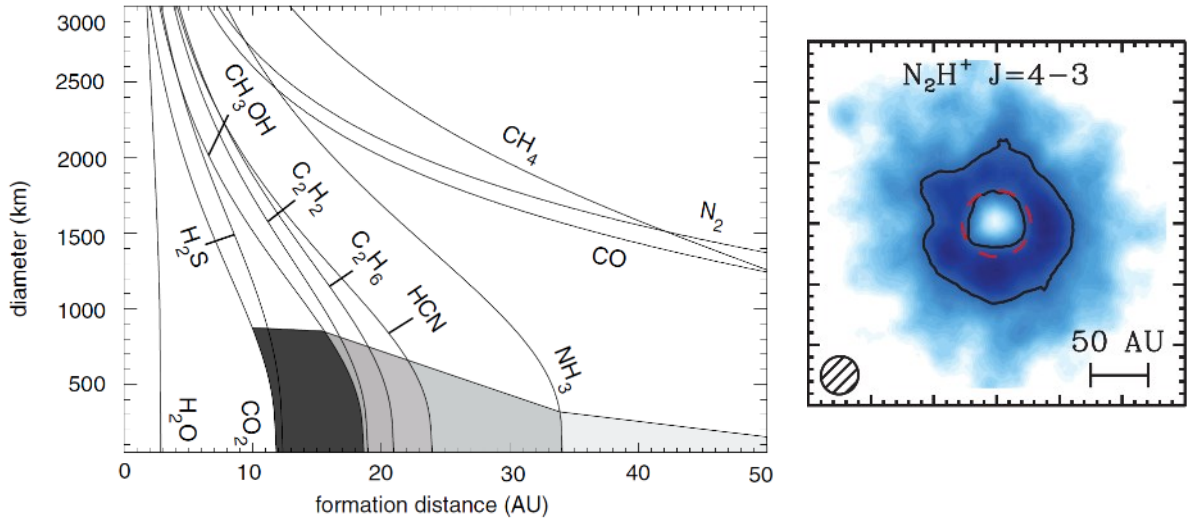

Figure 3-30. Left: depletion lines of volatile species at the surface of solar system bodies after an exposition of 10 Myrs to the sunlights (from Brown et al. (2011b)). Right: N_2H^+ emission in the disk around TW Hya, an analog of the solar nebula, from Qi et al. (2013). The presence of N_2H^+ in the disk is correlated to the freeze out of the CO reservoir, preventing its destruction. The CO snow line is estimated to stand at ≈ 30 AU, at temperature below 17K, from the emission of N_2H^+ in the disk.

Augé et al. (2019) reported the spatial variations of the D/H ratios at a micron scale in organic residues formed from an N_2-CH_4 ice films with a local D-rich ice layer of pure CD_4. Results presented in this work indicate that nitrogen and carbon isotopic heterogeneities can be formed in organic residues resulting

from the irradiation of isotopically heterogeneous ice mixtures. However, the formation of such heterogeneities in the residues is highly dependent on the chemical nature of the initial ice. Thus the existence of isotopic heterogeneities at a micron scale in UCAMMs (see Chapter 2) may allow to rule out some parent ice reservoirs. At the surface of small bodies, in the outer cold regions of the solar system, the low mobility of radicals formed by irradiation of ice mantles would favor the formation of H, N and C isotopic heterogeneities in the organic matter of UCAMMs. The present experiments suggest that a NH_3-CH_4 ice mixture is less favorable than a N_2-CH_4 ice mixture. However, ice mantles on small objects may consist in more complex ice mixture including additional chemical species (Douté et al., 1999).

3.3.3. Time of irradiation of cometary surfaces

The processing of ices in the interplanetary medium is driven by the energy deposition by UV photons, solar particles and the Galactic cosmic rays (see section 3.1.3.3). While photons can penetrate in the first tens to hundreds nanometers below the ice surface, GCRs (protons and heavier ions) can reach depths ranging from several micrometers to few meters (Moore et al., 2001). The dose deposited in ice mantles can thus vary with the nature of the UV and GCR flux and with the depth.

In the hypothesis of the irradiation of ice mantles at the surface of a cometary parent body residing at a large heliocentric distance, the GCRs most likely dominate the depth energy deposition as UV photons do not penetrate deep in the sub-surface. Several works evaluated that the dose deposited by GCR protons within the first 20 cm of ice mantles at the surface comets stored in the Oort cloud during 4.6 Gyr is of about 40 eV.molecule^{-1} (see the Oort cloud dose in Donn (1976), Moore et al. (1983) and Gerakines et al. (2000)). However, this value is derived from the dose necessary to process ice film with protons during laboratory experiments and it may not be fully constrained by astrophysical considerations. Based on theoretical derivations on the GCRs' energy distribution, Strazzulla and Johnson (1991) and Moore et al. (2001) estimate an order of magnitude higher dose, i.e. about 600 eV.molecule^{-1} and 150 eV.molecule^{-1} (respectively) deposited within the first 10 cm of cometary ice mantles exposed for 4.6 Gyr, leading to the formation of a "primordial refractory mantle" (Strazzulla and Johnson, 1991). Nevertheless, the dose deposited in ice mantles is depth-dependent (Figure 3-31) and lower doses correspond to the processing experienced by deeper ice layers within the same period of time. Cooper et al. (2003) predict that the first 1 µm of an ice mantle exposed to the GCR protons outside the heliosphere (that is relevant for objects in the Oort cloud) may receive a 100 eV/16-amu dose in about 2 Myr (Figure 3-31, left) while it will take about 1 Gyr to deposit the same dose at a 1 cm depth. The dependence of the energy deposition with the depth will thus affect the productions of radicals able to form refractory organic molecules in different ice layers, as shown by Strazzulla and Johnson (1991) (Figure 3-31, right). The lower fraction of altered carbon in the deeper layers will thus lead to a lower yield of the formation of refractory material.

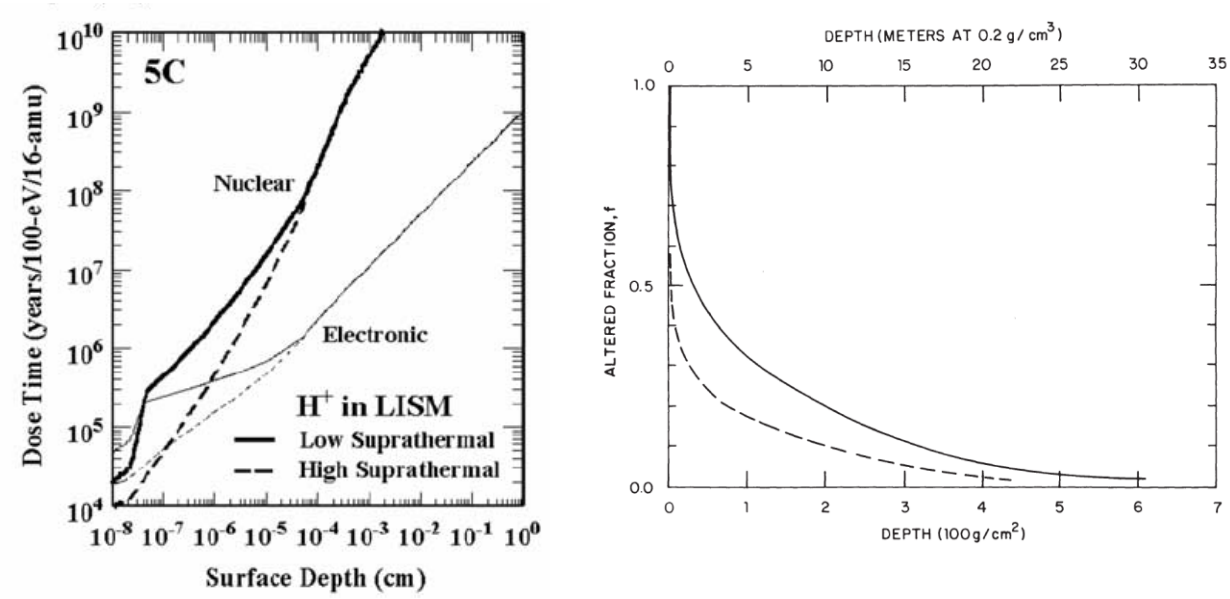

Figure 3-31. Left: time necessary to deposit 100 eV/16-amu with protons in the local interstellar medium (LISM) as function of the depth, from Cooper et al. (2003). Polymerized fraction of carbon as function of the depth into a comet exposed for 4.6 Gyr to GCR protons, from Strazzulla and Johnson (1991)

According to these considerations, the dose achieved in the ice irradiation experiments presented in this work would correspond to a lower limit on the time of irradiation by the GCRs of about 60 Myr and an upper limit of about 3 Gyr (based on the 10-20 cm estimations). Although these estimations span a large range, these values indicate that the doses considered in our experiments are consistent with that deposited at several depths during the lifetime of comets in the Oort cloud. If one considers the typical size of the organic phase in UCAMMs (≈10^{-3} cm) and an irradiated-ice/refractory-residue conversion yield of 1% (see section XX and Muñoz Caro and Schutte (2003)) a typical thickness of the parent ice mantle would be about 10^{-1} cm. The estimation of the thickness of the organic residue can be scaled to match the yield of other ice chemical compositions. A surface ice mantle with such thickness would receive a 20 eV.molecule^{-1} dose over ≈50 Myr based on Figure 3-31, left. However, because cometary surfaces are evolving structures, the processing of cometary matter most probably result in different ice mantles irradiated, since their formation, about 4 Gyr ago. Finally, it has to be noted that the irradiation by GCR ions heavier than hydrogen is likely to play an important role in the processing of the ice layers at depths of about 10-500 µm, where they still penetrate and deposit locally more energy than protons (see section 3.1.3.3). At such depths, the energy deposition by heavy ions can reach about the half of the total energy deposition by the GCR, besides their much lower abundance. In the thickness range investigated in the irradiation experiments (that is about 10 µm), the higher stopping power of heavy ions allows to reach large cumulated dose (that would require a higher flux if performed with protons).

Although the organic matter of UCAMMs was most likely induced by the irradiation of cometary ice mantles at large heliocentric distances, irradiation of small icy grains in the dense core phase may also have played an important role in the synthesis of organic matter available in the early stages of the solar system. Shen et al. (2004) developed a theoretical model to investigate the energy deposition of UVs and GCRs in grains of ≈ 0.1 µm radii in dense environments. By integrating the energy distribution of the GCRs in the [1 MeV; 10^4 MeV] range, including protons and heavier ions, Shen et al. (2004) estimated that GCRs

deposit about $6 \cdot 10^{-15}$ eV.molecule^{-1}.s^{-1} within the grains. Given the dose required to process icy grains, this dose correspond to an exposure to the GCR of about 10^2 Myr. In dense environments, the UV field, which is induced by the GCRs interaction with the gaseous phase (i.e. mainly hydrogen atoms) is thought to dominate the energy deposition by one order of magnitude (Moore et al., 2001). In that case, the required dose represents a 10 Myr exposure time to the GCRs and the induced UV field, that is consistent with the estimated lifetime of the protoplanetary disk (Charnoz and Morbidelli, 2007; Raymond and Morbidelli, 2020; Reipurth, 2005).

3.4 Summary

The scenario of formation of the organic matter of UCAMMs by the irradiation of icy mantles on the surface of small bodies, in cold regions of the disk, is summarized on the Figure 3-32. Small bodies in cold regions (as comets) are made of a mineral and water-ice-rich nucleus surrounded by an ice mantle of more volatile species (step 1, (Malamud and Prialnik, 2015; Neveu et al., 2015)). The irradiation of the surface ice mantle by the galactic cosmic rays produces radicals (step 2) that form a refractory organic crust (*i.e.* not volatile at temperatures reached during the approach in the inner solar system) once the ice mantle sublimates (step 3). Because the minerals are locked in the nucleus, the surface organic crust is expected to be depleted in minerals.

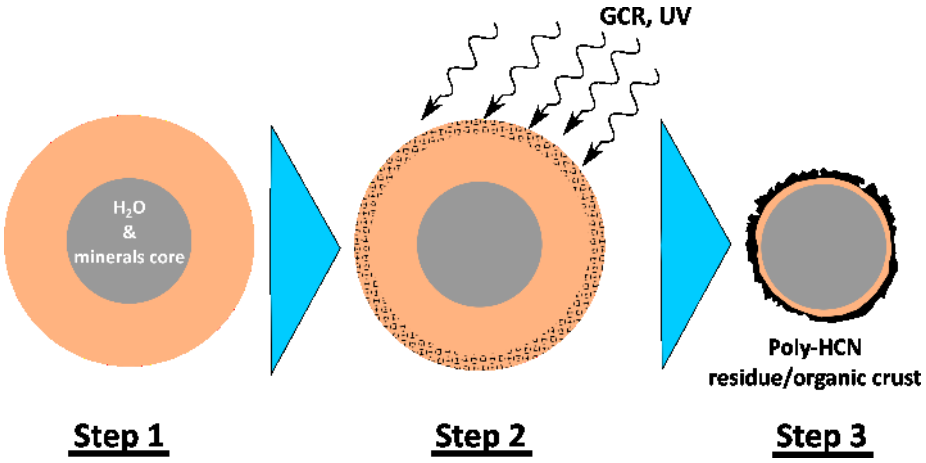

Figure 3-32: schematic view of the formation of the organic matter of UCAMMs by the irradiation of volatile ice mantles by GCRs and UVs.

The irradiation experiments presented in this chapter extend the comprehension of the transmission of H, N and C isotopic heterogeneities from the initial ice mixture with isotopically labeled ice layers to the resulting organic residues. Two main chemical composition of ice were investigated (N_2-CH_4 and NH_3-CH_4). Irradiation of isotopically heterogeneous N_2-CH_4 ice mixtures induce residues with potentially large micron scale isotopic heterogeneities, plotting along mixing lines, while residues formed from the irradiation of isotopically heterogeneous NH_3-CH_4 ice mixtures present reduced isotopic heterogeneities. The structure of the organic residues depends on the radiolysis efficiency, related to the chemical composition of the ice. In the highly hydrogenated NH_3-dominated ice mixture, the higher sublimation temperature provides a larger time of recombination of the radicals formed from the irradiation (Tachibana et al., 2017). This tends to produce a more homogeneous, extensively mixed, isotopic composition. The low sublimation

temperature of N_2 and the lower abundance of hydrogen atoms in the N_2-dominated ice mixture might allow a better conservation of the isotopic heterogeneities inherited from the initial ice film in the organic residue, leading to an organic component with higher isotopic variations. However, the 3 experimental sessions conducted with same mixtures and different annealing ramps suggest that the efficiency of such freezing depends on the effective duration of the annealing. A sufficiently low annealing might allow to lead to a homogeneous composition, even for N_2-CH_4 ices. Finally, the experiments also showed that it is possible to form localized patches of matter with extreme isotopic anomalies inherited from the labelled layer, some of them likely linked to sporadic events during the annealing.

4 Chapter 4: Discussion and perspectives

4.1 Comparison of the UCAMMs with other solar system materials

The isotopic diversity of the organic matter of UCAMMs is a multiscale feature, D/H, $^{15}N/^{14}N$ and $^{13}C/^{12}C$ heterogeneities being observed from one UCAMM to another or within one, at a micron scale. Heterogeneities observed at the scale of several microns in DC94 and, to a lower extent, in DC309 show that a single UCAMM is likely to contain entities originating from various reservoirs, suggesting a complex formation history. In this chapter, we compare the isotopic composition of UCAMMs with that of other solar system materials and models to propose hypotheses on the origin of the different organic matter components of UCAMMs.

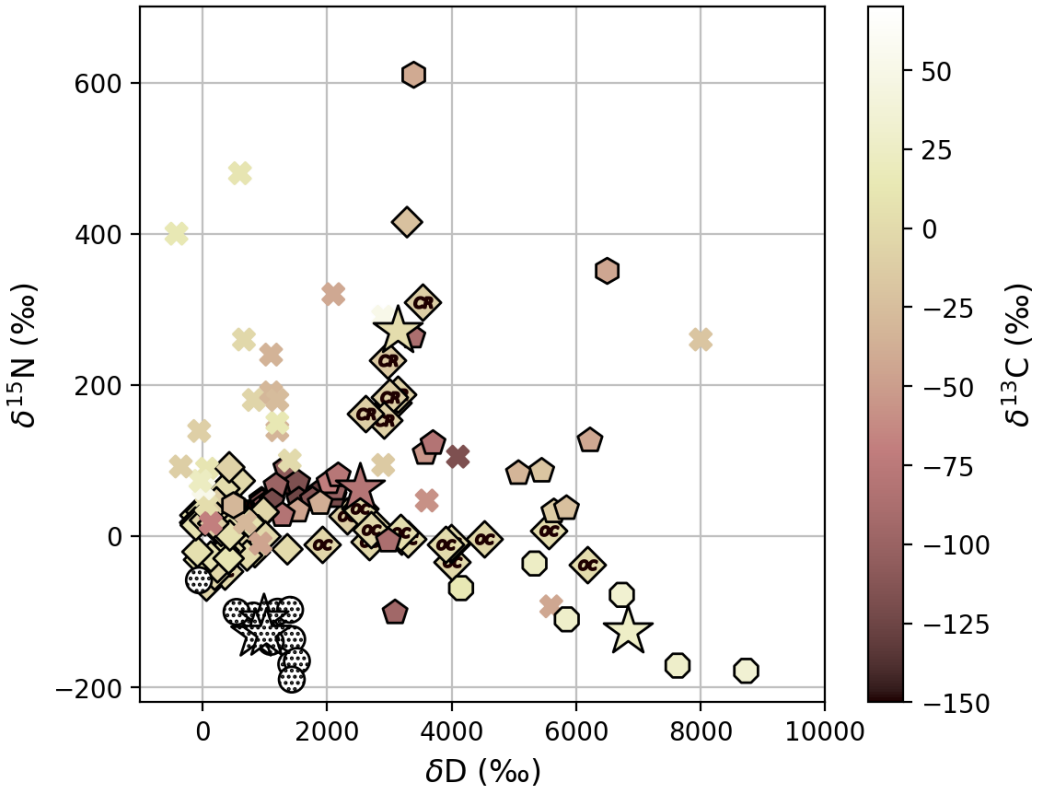

Figure 4-1. Comparisons of correlated D, ^{15}N and ^{13}C enrichments measured in UCAMMs (this study), IDPs (crosses, Messenger (2000)) and IOM of meteorites (diamonds, Alexander et al. (2007)). IOM from OC and CR chondrites are specified with the labels OC and CR. $\delta^{13}C$ values are indicated by the color scale and black dots when not available (DC18). Bulk isotopic compositions of UCAMMs are reported by stars, ROIs by circles (DC18), octagons (DC309), hexagons (DC43) and pentagons (DC94). The bulk isotopic composition of UCAMMs differ one from another, but some spots of DC94 (pentagons) present D and ^{15}N content similar to the bulk composition of DC43. DC43 shares noticeable isotopic similarities in D, ^{15}N and ^{13}C with the IOM of CR chondrites.

4.1.1. The D/H ratios of UCAMMs

The organic matter of UCAMMs often shows enhanced D/H bulk compositions with regard to the majority of the extraterrestrial objects (*Figure 4-1* and *Figure 4-3*). Still, the magnitude of these D-enrichments varies from one UCAMM to another. The D/H ratio of DC18 (the UCAMM with the lower bulk $\delta D = 990 \pm 80‰$), is comparable with values measured in the IOM extracted from chondrites and in chondritic porous IDPs (CP-IDPs) (Aléon et al., 2001; Alexander et al., 2007; Ceccarelli et al., 2014; Messenger, 2000). DC43 and DC94 have higher bulk D enrichments, above 2500‰, in the range of variation of the D/H ratio observed in the IOM of Renazzo-type chondrites (CR) and ordinary chondrites (OC). DC309 present the larger D/H bulk ratio of the 4 UCAMMs analyzed in this work ($\delta D = 6800‰$).

In addition to their D-rich bulk composition, UCAMMs display localized extreme D enrichments, as reported by Duprat et al. (2010) and Bardin (2015). These enrichments can reach 30 times the mean ocean water value in areas much larger (1 – 10 µm) than the extend of hotspots identified in IDPs (*Figure 4-2*).

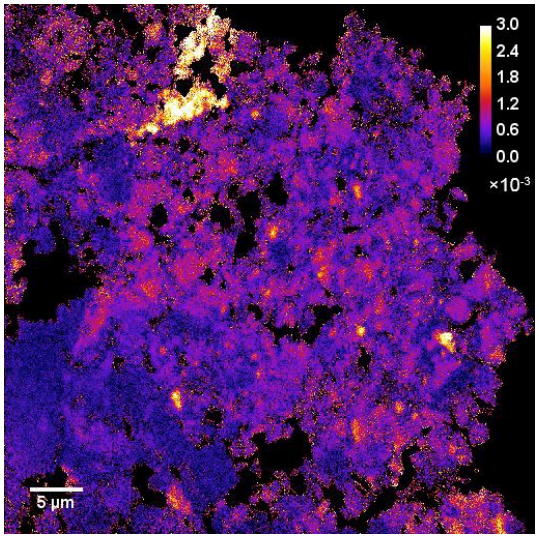

Figure 4-2: extreme D/H enrichments in a several microns large area on UCAMM DC94 (from Bardin (2015)). The color scale indicates the D/H value.

The diversity of the D/H ratios observed in the solar system has been investigated extensively, (see e.g. Altwegg et al. (2015); Ceccarelli et al. (2014)), highlighting the large differences between the protosolar nebula composition and a diversity of extraterrestrial objects (*Figure 4-3*). Oort cloud comets (OCC), originating from the outer regions of the solar system were thought to have higher D/H ratios than the more internal Jupiter family comets (JFC). However, *in-situ* measurements on the JFC comet 67P/Churyumov-Gerasimenko, with the ROSINA instrument on board Rosetta spacecraft, revealed a D/H ratio equal to $(5.3 \pm 0.7)\cdot10^{-4}$, (i.e. $\delta D \approx 2400‰$), higher than in OCC and comparable to the bulk values of DC43 and DC94 (colored triangles in *Figure 4-3*). The bulk D/H ratios of DC18 is comparable the values measured in cometary water by remote sensing of comets

(Biver et al., 2007; Bockelée-Morvan et al., 1997; Meier et al., 1998; Weaver et al., 2008), that are also in broad agreement with the bulk values of DC43 and DC18. DC309 sets apart with a higher bulk D content. However, water and organic matter are distinct reservoirs, formed through different chemical pathways and the comparison of their D/H is thus limited. In their review, Bockelée-Morvan et al. (2015) highlighted that C-bearing molecules originating from comets were systematically enriched in deuterium ($\approx 10^{-3} - 10^{-1}$) in comparison to water ($\approx 10^{-4}$).

Large D excesses (up to D/H $\approx 10^{-2}$) are expected to rise in molecular reservoirs in cold dense regions at the early stages of the solar system formation (Aikawa et al., 2012; Ceccarelli et al., 2014). UCAMMs obviously sampled a D-rich reservoir, maybe similar to that of OCCs and some JFCs. Still, the D-enrichments measured in the CR and OC chondrites suggest that high D/H is not an unambiguous tracer of a material formed in the outer cold regions of the disk. Moreover, Yabuta et al. (2017) reported D/H close to the terrestrial value in one UCAMM from the Japanese Antarctic collection, meaning that the large D-excesses may not be an ubiquitous characteristic of all UCAMMs.

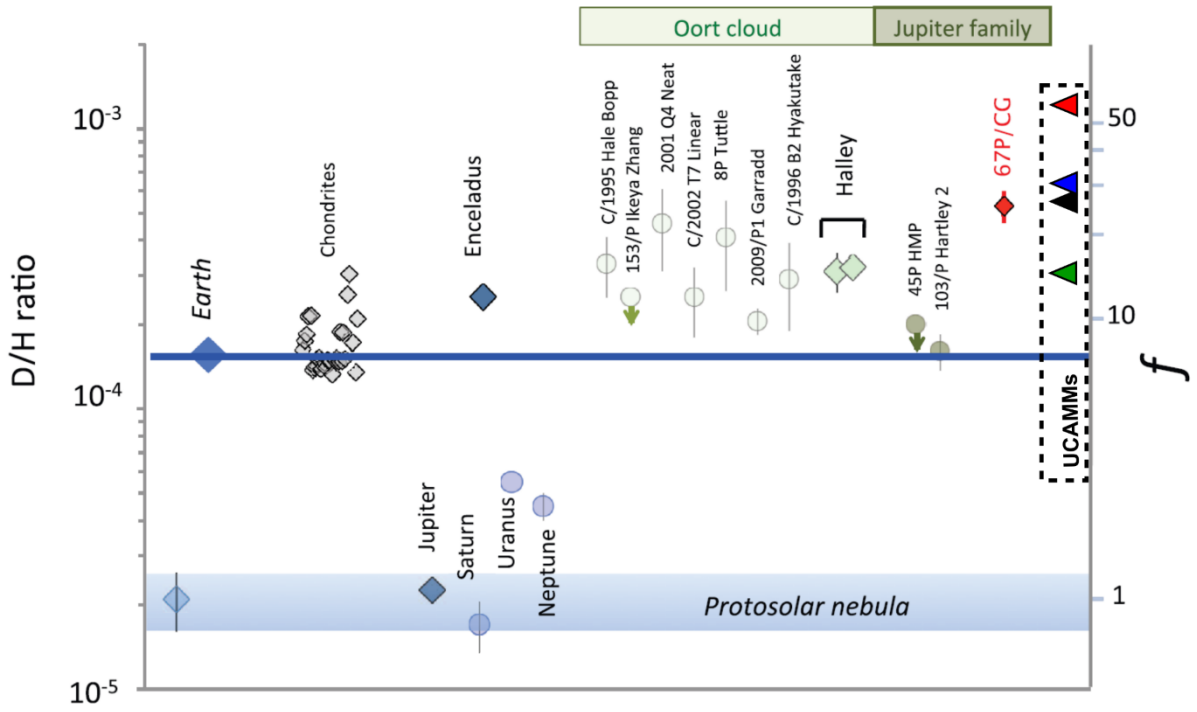

Figure 4-3: the D/H ratios in the solar system, adapted from Altwegg et al. (2015). UCAMMs bulk D/H are reported with red (DC309), blue (DC43), black (DC94) and green (DC18) triangles

4.1.2. The main UCAMM organic reservoir (DC43)

The bulk H, C, N, isotopic composition of the organic matter in UCAMM DC43 is comparable (with slightly higher $\delta^{15}N$ values) to that of IOM from CR chondrites (*Figure 4-1* and yellow patch on *Figure 4-4*, Alexander et al. (2007)). These values are also consistent with whole rock isotopic measurements of the Renazzo CR chondrite (Kerridge, 1985), even though the latter might include contributions that do not belong to the organic phases. Among meteorites, CR chondrites are thought to bear the most primitive IOM (Alexander et al., 2007; Floss and Stadermann, 2009; Weisberg et al., 1993). The comparison between the organic matter of CR chondrites and DC43 will be discussed in more details in section 4.2.

The D/H bulk composition of DC43 is higher than in most CP-IDPs. While high D-enrichments observed in extraterrestrial samples are often found in hotspots, UCAMMs distinguish themselves by displaying large bulk D/H ratios and extreme D-rich zones. Some IDPs and cluster porous IDPs (Aléon et al., 2003; Floss et al., 2006; Messenger, 2000) also display $^{15}N/^{14}N$ and/or $^{13}C/^{12}C$ values comparable to that of DC43. The existence of D-rich hotspots in CP-IDPs and the similarities of their ^{13}C and ^{15}N composition with DC43 indicate that the main organic component of UCAMMs is similar to that of previously reported IDPs and IOM from specific meteorites.

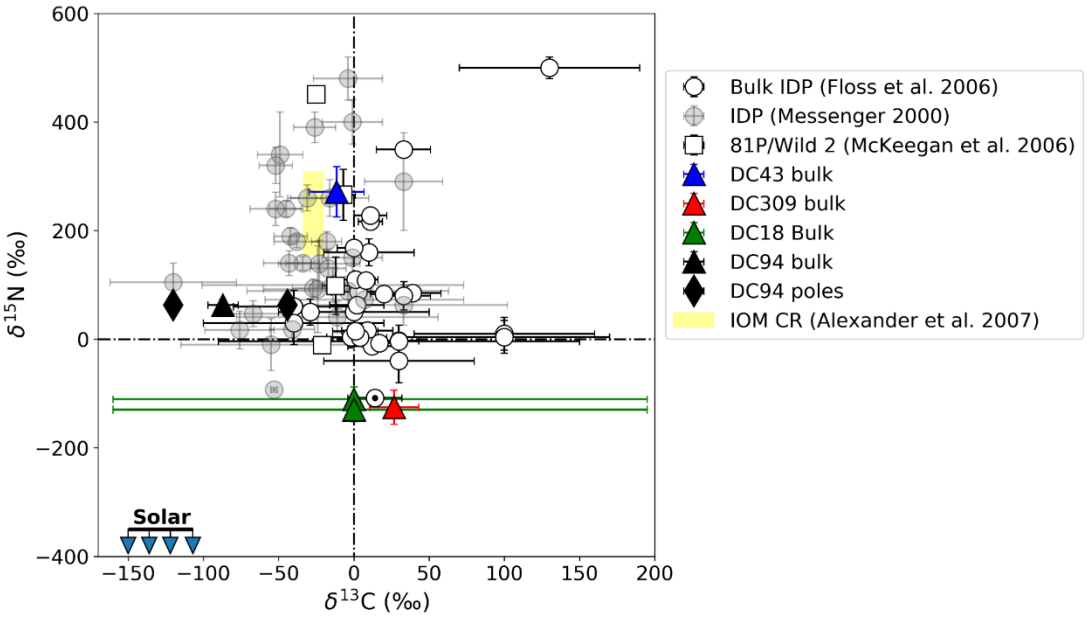

Figure 4-4. Comparison of the bulk $^{15}N/^{14}N$ and $^{13}C/^{12}C$ ratios measured in UCAMMs and in other extraterrestrial samples adapted from Hashizume et al. (2004). The $\delta^{13}C$ value of DC18 is unknown. Bulk values of UCAMMs are plotted with triangles of different colors. The two "poles" with distinct $\delta^{13}C$ in DC94 are shown with black diamonds. Bulk composition of CP-IDPs (Floss et al., 2006) are plotted with white circles. The organic matter rich CP-IDP Eliot is shown as dotted circle (with a ^{15}N-depleted, ^{13}C-enriched composition similar to that of DC309). Data on CP-IDPs from (Messenger, 2000) are reported by light-gray circles (including "hotspots" and "coldspots"), they have the closest $\delta^{13}C$ and $\delta^{15}N$ values to that of DC94. The isotopic data of grains of comet 81P/Wild 2 returned by the Stardust mission (McKeegan, 2006) are represented by white squares. The IOM of CR chondrites (Alexander et al., 2007) are indicated by a light yellow patch. These values are close the DC43 isotopic bulk. The solar ^{13}C and ^{15}N isotopic composition inferred by (Hashizume et al., 2004; Marty et al., 2011) is indicated as blue arrows.

4.1.3. ^{13}C-poor organic matter (DC94)

Due to its large dimensions, DC94 was extensively characterized, first by Bardin et al. (2014), then in this work, allowing the identification of isotopic variations at a micron scale. We discuss here the two types of organic matter with the distinct $^{13}C/^{12}C$ ratios, reported in chapter 2:

- Large platelets of organic matter present in zones A, B and C of DC94 present strong ^{13}C-depletions ($\delta^{13}C \approx -120‰$) and $\delta D \approx 1500‰$.
- The matter of zone D has a fluffier structure and is less depleted in ^{13}C and more D-rich with $\delta^{13}C \approx -40‰$ and $\delta D \approx 5500‰$.

The $\delta^{15}N$ composition is fairly constant (ca. + 60‰) in the 4 analyzed zones, with the exceptions of several "hotspots" in zone A and D.

Phases with $\delta^{13}C$ lower than -50‰ are not common in solar system materials. IOM extracted from meteorites have $\delta^{13}C$ values around -20‰, rarely below -35‰ (Alexander et al., 2007). Large bodies from the inner regions of the solar system (e.g. terrestrial and martian mantles) present $\delta^{13}C$ values at 5‰ and -7‰ respectively (Hashizume et al., 2004; Wright and Pillinger, 1994). The ^{13}C-poor organic matter of DC94 is thus noticeably different from the organics found in inner solar system bodies.

In their study of several IDPs, Messenger (2000) and Floss et al. (2006) reported the existence of particles with bulk $\delta^{13}C$ below -40‰, down to $\delta^{13}C = -120\pm42‰$ for the particle LD2009 D9 (Table 1, Messenger (2000)). These values are comparable to that measured in DC94. The slight ^{15}N enrichments are also in broad agreements with that measured in DC94, ranging from 0‰ to 100‰. The ROI D-7 in DC94 exhibits a specific ^{13}C-poor and ^{15}N-poor matter that is observed in one IDP (L2011 A3, Messenger (2000)). In addition, Aléon et al. (2001) measured $\delta^{13}C$ ranging from -59±27‰ to -92±47‰ in five IDPs compatible with the values in DC94. The similarities between the ^{13}C and ^{15}N compositions of DC94 and some IDPs and cluster IDPs suggest the existence of a specific reservoir with a low $^{13}C/^{12}C$ ratio at the origin of this organic matter component in UCAMMs and, possibly, in some IDPs (see section 4.3).

4.1.3.1. *The low solar $^{13}C/^{12}C$ ratio*

The existence of a carbon reservoir with a low $^{13}C/^{12}C$ ratio is suggested by measurements of the carbon isotopic ratio in the solar wind (Hashizume et al., 2004; Wimmer-Schweingruber et al., 2014) and observations of the CO absorptions lines in the solar photosphere (Lyons et al., 2018). Hashizume et al. (2004) measured the $^{13}C/^{12}C$ profile in lunar regolith samples and derived the contribution of the solar wind implantation. The authors concluded that (in absence of fractionation processes associated with the acceleration of the solar winds and the implantation) the protosolar carbon ratio likely ranges from -105‰ to -150‰. Based on the data of the Solar Wind Ion Composition Spectrometer (SWICS) onboard ACE spacecraft, Wimmer-Schweingruber et al. (2014) estimated a solar wind with $\delta^{13}C = -89 \pm 93‰$, compatible with the value mentioned above. However, observation of CO emission lines in the solar photosphere (Lyons et al., 2018) suggest a higher protosolar $^{13}C/^{12}C$ composition at $\delta^{13}C = -48‰ \pm 7‰$. Although the protosolar $^{13}C/^{12}C$ ratio remains uncertain, these works strongly suggest that its bulk $\delta^{13}C$ value was significantly negative, possibly below -100‰.

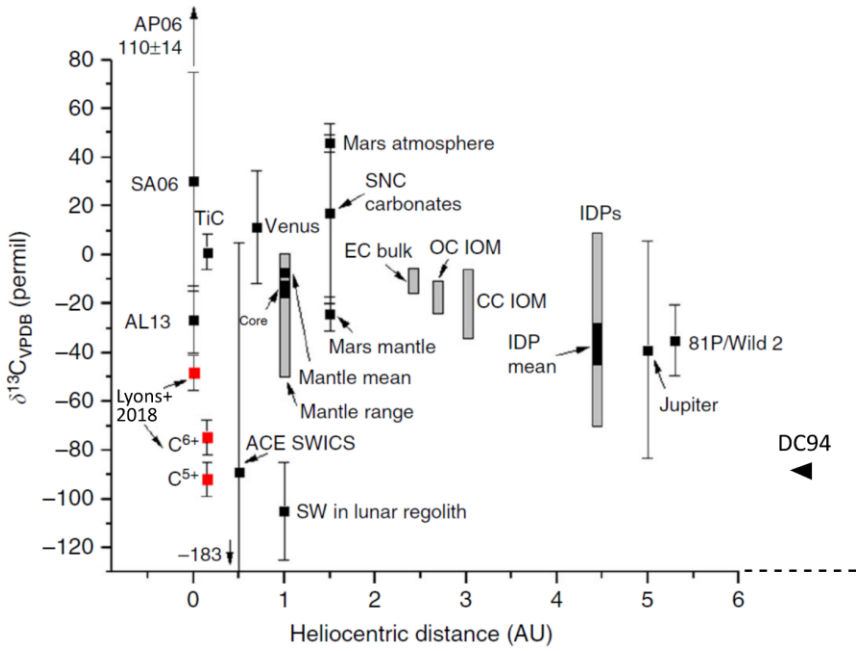

Figure 4-5: the diversity of ^{13}C-abundance measured in the solar system from Lyons et al. (2018). The low $^{13}C/^{12}C$ ratio measured in DC94 is similar to the one derived from measurements of solar wind implantation in the lunar regolith.

4.1.3.2. *Origin of the low ^{13}C component*

Hashizume et al. (2004) and Lyons et al. (2018) discuss the mechanisms that may give rise to carbon reservoirs with different isotopic compositions, including isotopic fractionation caused by CO self-shielding in photo-dissociation regions. In a CO cloud, the UV field ionize the ^{12}CO and ^{13}CO molecules at different wavelengths. Due to their much higher abundance, the ^{12}CO molecules saturate their corresponding UV lines and the ^{12}CO molecules in the inner regions of a dense cloud are self-shielded from photo-dissociation. By contrast, UV photons corresponding to efficient photo-dissociation of ^{13}CO molecules can penetrate deeper in the cloud allowing ^{13}CO molecules to be ionized. As a result, in the inner regions of the cloud or the disk, this process leads to the formation of a ^{13}C-depleted CO reservoir and a corresponding ^{13}C-rich reservoir of C^+ ions (van Dishoeck and Black, 1988; Visser et al., 2009; Warin et al., 1996). However, the fate of these gaseous carbon reservoirs is complex as exchange reactions at low temperatures (below 30K) may subsequently counterbalance the isotopic fractionation of the CO reservoir by efficiently enhancing its $^{13}C/^{12}C$ (Langer and Graedel, 1989; Watson et al., 1976). The persistence of a ^{13}C-depleted CO reservoir is thus depending on several factors including the vertical position above the disk mid-plane and/or specific processes that may freeze the exchange reactions. The condensation of the gaseous CO reservoir in ice mantles could preserve a low $^{13}C/^{12}C$ resulting from the self-shielding. Whether the carbon reservoir at the origin of the low ^{13}C isotopic composition of DC94 is CO or another species, it was possibly also sampled by several comets. The δ^{13}C values inferred from the observation of CN and HCN emission lines in comet C/1995 O1 (Hale-Bopp) by Arpigny et al. (2003) and Wyckoff et al. (2000), are ranging from -460±130‰ to -11±164‰. Although these measurements are subject to large uncertainties, they are in agreement with the existence of a ^{13}C depleted carbon reservoir in the comet forming regions.

4.1.3.3. *Correlation of D and ^{13}C heterogeneities in DC94*

The irradiation experiments reported in Chapter 3 demonstrate that spatial correlation of isotopic heterogeneities in the initial ice film can result in a residue with corresponding correlated heterogeneities. In DC94, the correlation between the $\delta^{13}C$ and δD values (*Figure 2-26*) may thus indicate that the H-bearing ices associated with the ^{13}C-depeleted ice should have lower D/H ratios than that the H-bearing ices associated with the ^{13}C-richer ice. ^{13}C-depeleted zones are also observed in DC43 but to a lesser extent, indicating that the organic matter of this UCAMM may also contain a component originating from the irradiation of such a ^{13}C-depleted ice reservoir.

4.1.4. The ^{15}N-poor organic matter (DC309 and DC18)

The bulk nitrogen isotopic composition of DC309 and DC18 ranges from -110‰ to -130‰. Such low $\delta^{15}N$ values are not common in organic matter of meteorites (*Figure 4-6*) but are observed in CP-IDPs and cometary grains sampled by the stardust mission (Floss et al., 2006; McKeegan, 2006; Messenger, 2000). These samples present classical $\delta^{13}C$ values ranging from -50‰ to 0‰ (*Figure 4-7*), lower than that measured in DC309 (bulk $\delta^{13}C$ = 27 ± 16‰). Strikingly, the CP-IDP Eliot, reported by Floss et al. (2006) exhibit similar isotopic bulk composition in both N and C ($\delta^{15}N$ = -108 ± 9‰ ; $\delta^{13}C$ = 14 ± 18‰) with DC309. This IDPs is described as a smooth matter similar to the structure of DC309 (dotted circle in *Figure 4-4*, *Figure 4-8*).

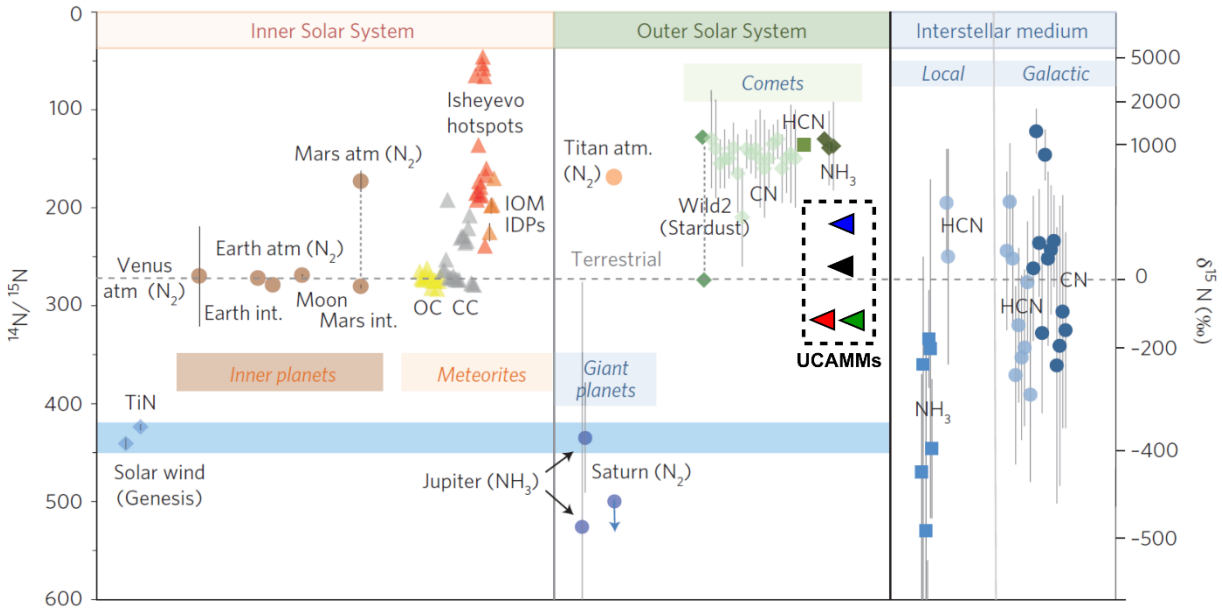

Figure 4-6: the diversity of the $\delta^{15}N$ measured in the solar system, from Füri and Marty (2015). UCAMMs are reported by blue (DC43), black (DC94), red (DC309) and green (DC18) triangles.

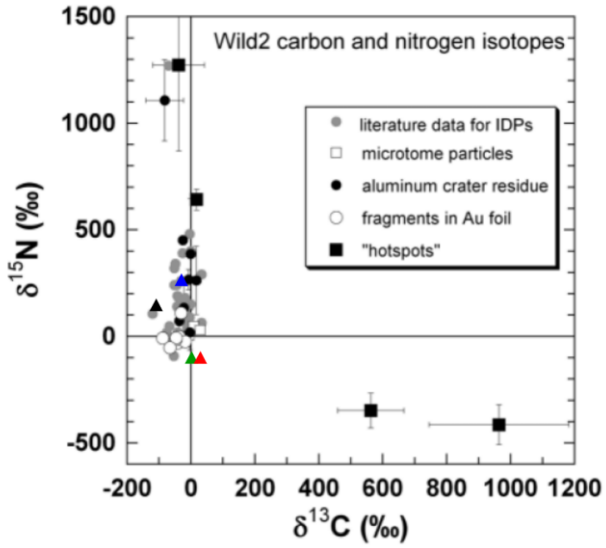

Figure 4-7 from McKeegan (2006). $\delta^{15}N$ and $\delta^{13}C$ measured in grains from 81P/Wild 2 comet returned by the Stardust mission. A diversity of $\delta^{15}N$ values are observed in the grains, echoing the various $\delta^{15}N$ measured in UCAMMs (see colored triangles and Figure 4-4). DC309, 18, 43 and 94 are plotted as red, green, blue and black triangles.

Remote observations of distant objects provide additional information on the various N reservoirs in the solar system. Based on observations of the CN violet band and the NH_2 optical band, comets appear to display a ^{15}N enriched composition, with $\delta^{15}N$ up to about 900 ‰ relative to the terrestrial atmospheric value (Bockelée-Morvan et al., 2008; Bockelée-Morvan et al., 2015; Füri and Marty, 2015; Shinnaka et al., 2016). By contrast, measurements of the sub-millimeter HCN emission lines of Hale-Bopp reported by Jewitt et al. (1997) indicated poorer ^{15}N composition down to $\delta^{15}N$ = -160 ± 120 ‰. However, a reanalysis of these data by Bockelée-Morvan et al. (2008) concluded that the HCN-derived $^{15}N/^{14}N$ ratios of comets were consistent with the high ratios mentioned above. The grain residues from the comet 81P/Wild 2 collected by the Stardust missions suggest that comets have distinct organic components with both ^{15}N-depleted and ^{15}N-rich composition (*Figure 4-7*, McKeegan et al. (2006)). Finally, the $\delta^{13}C$ values measured in comets (Jewitt et al., 1997; Lis et al., 1997; Wyckoff et al., 2000; Ziurys et al., 1999) lean towards a ^{13}C-depleted cometary matter, at the opposite of the composition of DC309 and CP-IDP Eliot.

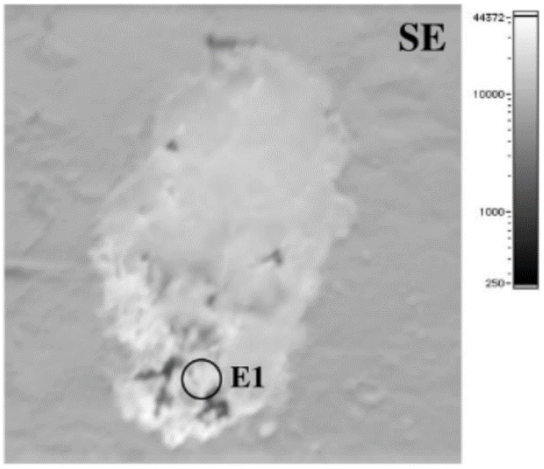

Figure 4-8: SEM image (20x20 µm) of the CP-IDP Eliot from Floss et al. (2006). Eliot is made of a smooth organic matter characterized by a low ^{15}N and slightly enriched ^{13}C composition comparable to that of DC309.

The origin of low $^{15}N/^{14}N$ ratios in UCAMMs is still puzzling. It might result from the inheritance of the proto-solar ^{15}N-depleted nitrogen reservoir not observed by spectroscopic measurements on comets.

Floss et al. (2006) suggested that such composition could be that of cometary nucleus ices. Large variation of the D/H ratios associated with the low ^{15}N-component in DC309 and DC18 suggest the possibility that several reservoirs with diverse D enrichments may be associated with low ^{15}N-ices.

4.2 Complementary information of the chemical and structural data of UCAMMs

In this section we put into perspective the results presented in this thesis with chemical and structural data from the literature and new results on UCAMMs from the B. Guérin Ph.D. thesis (2021).

Different types of organic matter are identified in UCAMMs (Engrand et al., 2018; Guérin et al., 2020):

- Type I and II are organic components with N/C atomic ratios in the 0<N/C<0.05 range compatible with that measured in the IOM from carbonaceous chondrites. Type I and II organic matters are spatially entangled and contain various minerals including high temperature crystalline phases originating from inner (*i.e.* hotter) regions of the solar system. Since these two types are often associated together, they might have formed simultaneously.
- Type III is a nitrogen rich organic component with N/C atomic ratios ranging from 0.08 to 0.2. This organic matter is essentially depleted in minerals, it is the key signature of UCAMMs. This type III component is the component that is most probably synthetized by irradiation of nitrogen-rich ice mantles in outer regions of the solar system.

The amount of type I, II and III organic matters varies from one UCAMM to another (Table 4-1, *Figure 4-9*). In some UCAMM fragments, type III organic matter dominates and forms structural units extending over several tens of µm wide surfaces (see *Figure 4-9*). An organic matter with such extent and fully depleted in minerals cannot form from the aggregation of micrometer-size grains and requires a specific formation process able to synthetized large patches of N-rich matter (over hundreds of µm^3). Conversely, types I and II organic matters dominate in several UCAMMs' fragments.

DC18 has a bulk N/C = 0.17±0.04, measured with an electron microprobe (Dartois et al., 2018). No bulk measurements were performed for DC309, though, STXM-XANES analyses showed than the type III organic matter is abundant in that UCAMM (*Figure 4-9*, Guérin et al. (2020), Guerin (2021)). High N/C ratios and/or high abundances of type III organic matter are consistent with organic matter synthesized in the cold regions of the disk by irradiation of a nitrogen-rich icy mantle (Augé et al., 2018). In cold regions, close to the disk midplane, these ice mantles (e.g. N_2-CH_4, N_2-CO) are expected to have low ^{15}N/^{14}N ratios and slightly enriched ^{13}C/^{12}C ratios (see section 4.3).

Conversely, DC43 and DC94 display lower N/C ratios, equal to 0.04±0.03 and $0.05\pm^{0.05}_{0.02}$ respectively (Bardin, 2015; Dartois et al., 2013). The STXM-XANES map on DC43 (*Figure 4-9*) also indicates a low abundance of type III organic matter in comparison to the types I and II. Such N/C ratios are comparable to those reported for the IOM of CR chondrites (0.032 - 0.044, Alexander et al. (2007) considered to be the most primitive organic matter observed in meteorites (Alexander et al., 2007; Floss and Stadermann, 2009; Weisberg et al., 1993). Studies on the structure of the organic matter of UCAMMs by Raman spectroscopy, measuring their carbonaceous structural order with the so-called D and G bands, highlighted their disordered nature, with band parameters overlapping that of the IOM of the most primitive meteorites, including CRs (Busemann et al., 2007; Dartois et al., 2018; Dobrică et al., 2011). The isotopic data on DC43 exhibit D/H, ^{15}N/^{14}N and ^{13}C/^{12}C ratios comparable to that of the CRs' IOM (*Figure 4-1*). The similarities of N/C ratios, disordered structures and isotopic compositions between DC43 and CRs suggest that these

objects sampled a similar organic matter reservoir. It has already been proposed that CRs may have a cometary heritage based on the similarities of their IOM with the CHON grains collected from the Halley comet by the Vega mission (Alexander et al., 2007; Krueger and Kissel, 1987). The identification of a carbon-rich clast within the CR2 chondrite LaPaz Icefield 02342 (Nittler et al., 2019), possibly a cometary building block, indicates that, at least, the CR parent body (or bodies) probably accreted matter from the cometary reservoir.

The coexistence of the 3 types of organic matter in individual UCAMMs, in addition to their different association with crystalline and amorphous minerals (B. Guerin Ph.D. thesis (2021)) confirm the existence of a radial and/or vertical mixing in the protoplanetary disk, gathering organic matters formed in different regions of the disk (B. Guérin Ph.D. thesis (2021)). More specifically, the type III organic matter is very unlikely to have formed in the same regions that the crystalline minerals. Several ice reservoirs are proposed in section 4.3 to explain the diversity of chemical and isotopic compositions of UCAMMs.

Table 4-1: N/C atomic ratios measured in fragments of the DC43, DC309, DC18 and DC94. (a) Bulk values measured by electron microprobe (EMPA) from Dartois et al. (2018). (b) N/C ratios measured in OM I, II and III by STXM-XANES from B. Guérin Ph.D. thesis (2021). (c) Bulk value measured by NanoSIMS from Dartois et al. (2013) and Bardin (2015).

	N/C			
UCAMM	Bulk	OM I	OM II	OM III
DC43	0.04±0.03 [(a)]	0.04 [(b)]	0.03 [(b)]	0.08 [(b)]
DC309	-	0.01 [(b)]	<0.01 [(b)]	0.07 [(b)]
DC18	0.17±0.04 [(a)]	<0.01 [(b)]	-	0.11 [(b)]
DC94	$0.05\pm^{0.05}_{0.02}$ [(c)]	-	-	-

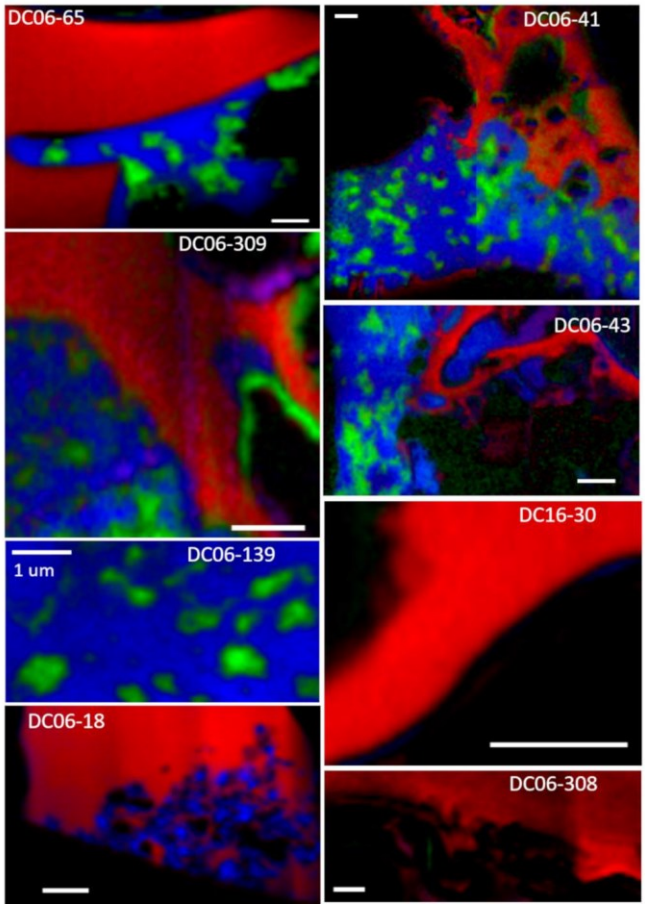

Figure 4-9 from B. Guérin Ph.D. thesis (2021). Hyperspectral maps on 8 UCAMMs acquired with STXM-XANES. The colors indicate the type of organic matter. Blue: type I, green: type II, red: type III. The relative abundances of the 3 types of organic matter vary from one UCAMM to another. Type III organic matter is more abundant in DC18 (DC06-18) and DC309 (DC06-309) than in DC43 (DC06-43), as expected from the bulk measurements (Table 4-1).

4.3 Formation of N-rich organic matter with various isotopic enrichments

The evolutions of $^{13}C/^{12}C$, $^{15}N/^{14}N$ and D/H ratios in molecular reservoirs depend on the interactions of H-, C- and N-bearing species in the protoplanetary disk (Visser et al., 2018). Models of protoplanetary disk formation including chemical formation pathways are developed to assert the composition and dynamics of molecular species in the young solar system (e.g. (Visser et al., 2018; Visser et al., 2009)). In the following section, we propose an interpretation of the diversity of the N, C and H isotopic composition observed in UCAMMs based on models of disk chemistry published by Visser et al. (2018) and Aikawa et al. (2012). The formation scenario is subsequently discussed with regard to the chemical characteristics reported for the 4 UCAMMs.

4.3.1. The N an C isotopic diversity in the young protoplanetary disk.

The DALI code (Dust And Lines) is a thermochemical 2D-axisymmetric model of the young (1 Myr) protoplanetary disk that computes the evolution of a chemical network based on physical characteristics of the disk (Bruderer et al., 2014; Miotello et al., 2014). The code includes the action of the interstellar UV field, the galactic cosmic rays, the stellar X-ray field and the stellar black body. The chemical network was optimized to include the species involved in the evolution of the CO reservoir (Miotello et al., 2014) and Visser et al. (2018) added the carbon and nitrogen isotopologs of a large numbers of molecules in order to

derive the spatial evolution of the $^{13}C/^{12}C$ and $^{15}N/^{14}N$ ratios of the different reservoirs. In the model, bulk isotopic compositions of the disk are set to $\delta^{15}N$=-380‰ and $\delta^{13}C$=290‰. While the $^{15}N/^{14}N$ ratio is consistent with the protosolar nebula value (Füri and Marty, 2015), the assumed $^{13}C/^{12}C$ ratio is high compared to the solar nebula estimation by Hashizume et al. (2004) and Lyons et al. (2018) (see section 4.1.3) and corresponds to the inferred value for the local interstellar medium by Milam et al. (2005). Although the absolute ratios derived in Visser et al. (2018) depends on the initial bulk ratio assumptions, the relative differences remain relevant when looking at fractionation originating from the chemical reactions between several reservoirs. It is worth noting that the authors emphasize that their model overestimate the $HC^{14}N/HC^{15}N$ ratio by about a factor of 2 compared to astronomical observations of disks. The discussion will thus focus on the comparison of relative isotopic fractionation rather than on the absolute isotopic ratios.

Results from Visser et al. (2018), are reported in the *Figure 4-10*, as a 2D representation of a slice of the protoplanetary disk. The results are presented as function of the radial distance R to the star and the vertical distance z/R from the disk mid-plane. The model predicts substantial C and N isotopic fractionations in the gas phase from one species to another and from one region to another. It is important to note that, on *Figure 4-10*, the color scale gives the ratio of the molecular species, meaning that for the molecular nitrogen N_2 (middle row, left panel), the ratio $N_2/N^{15}N$ has to be multiplied by a factor 2 of to be compared to $^{14}N/^{15}N$.

The fractionation processes affecting the dominant N_2 and CO reservoirs drive the distribution of the N and C isotopes. For the nitrogen, the isotope-selective photodissociation of N_2 (i.e. the self-shielding described in section 4.1.3) dominates the fractionation processes, leading to the ^{15}N-depletion of N_2 and, correspondingly, a ^{15}N-enhancement of the cyanides (HCN, HNC, CN). This fractionation occurs at intermediate depths from the surface of the disk ($z/R \approx 0.1 - 0.2$,) in the yellow region in the N_2 panel and the purple region in the HCN panel of *Figure 4-10* (middle row). At more important depths, closer to the disk midplane, the isotope-selective photodissociation is less effective due to the self-shielding of $N^{15}N$ UV lines and the N_2 and cyanide reservoir has $^{15}N/^{14}N$ ratios close to the bulk initial ratio ($\delta^{15}N$=-380‰). Low temperature exchange reactions do not play a significant role in the case of the nitrogen fractionation (Visser et al., 2018). Because NH_3 form from a chemical pathway distinct from the one of the cyanides, its $^{15}N/^{14}N$ ratio roughly follows the ratio of N_2. From a general point of view, one can note that the variations of the $^{15}N/^{14}N$ ratio are more pronounced in the cold outer regions than in the hotter inner regions. Between 5 and 100 A.U. (delimited by vertical dotted lines in *Figure 4-10*), the various molecular reservoirs are characterized by large variations both in the vertical and radial directions, mainly at intermediate depths region (purple region in the $HCN/HC^{15}N$ image). Importantly, the region between 5 and 100 A.U. is precisely that in which the parent body of UCAMM may originate from (see chapter 3, section 3.3.2).

The fractionation of the carbon reservoirs appears even more complex than that of nitrogen. The isotopic-selective photodissociation is expected to deplete the CO molecule in ^{13}C and produce a ^{12}C-rich CO reservoir in the outer mid-plane regions (see section 4.1.3.2). Correspondingly, the C^+ reservoir become enriched in $^{13}C^+$ ions that react with other carbon-molecules. However, in the case of CO, the low-temperature (<30K) exchange reactions are effective and can rapidly counterbalance the effects of the self-shielding. The $^{13}C/^{12}C$ ratios of the different reservoirs depend thus on the balance between these two processes (i.e. depending on the UV field and the temperature profile). The CO reservoir at the vicinity of the midplane is globally ^{13}C-enriched with slight enhancements between 10 and 100 A.U. because the low

temperature reactions dominate (bottom left panel of *Figure 4-10*). The $^{13}C/^{12}C$ ratio of the cyanides exhibit large radial and vertical variations close to the mid-plane at all distances between 10 and 100 AU.

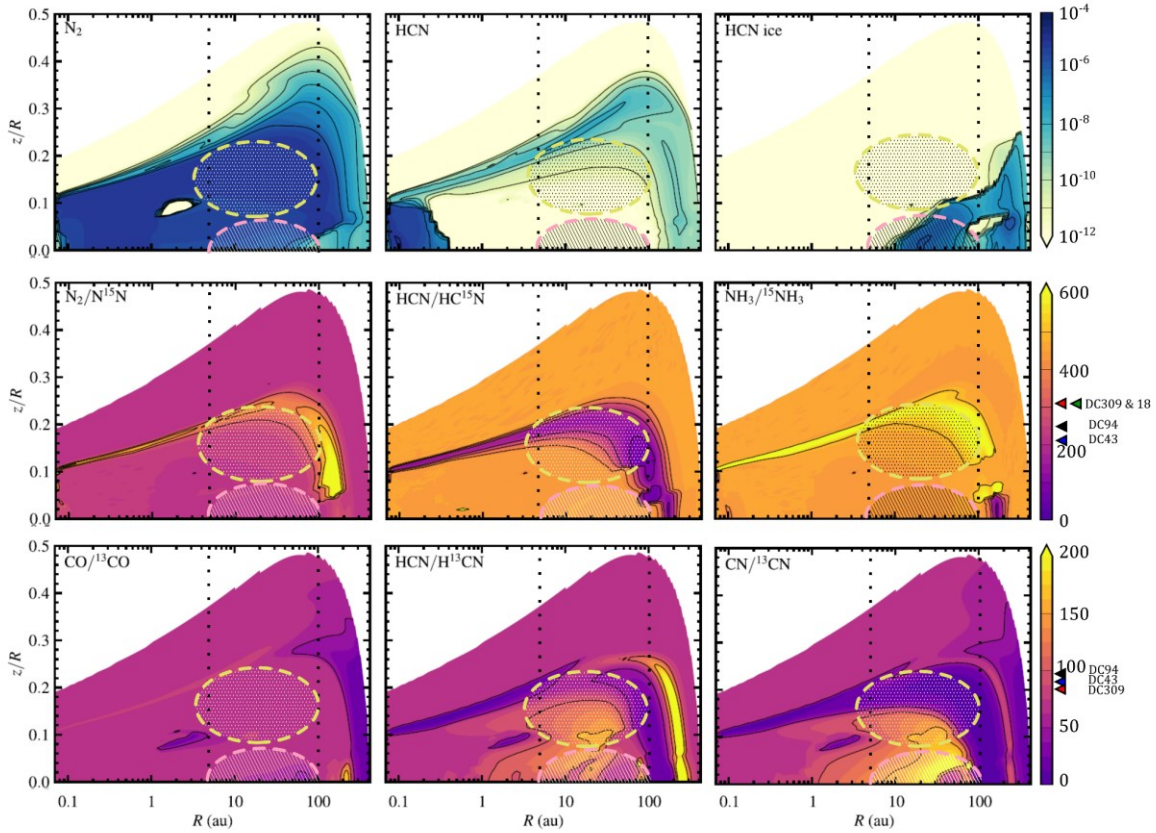

Figure 4-10: Nitrogen (middle row) and carbon (bottom row) isotopic composition of various chemical species in gas phase of the young protoplanetary disk (1 Myr) from Visser et al. (2018). The color scale gives the ratios of the major (^{14}N and ^{12}C) to minor (^{15}N and ^{13}C) isotopes (inverse notation to that use in the manuscript). The variations of the $\delta^{15}N$ and $\delta^{13}C$ are indicated for clarity but their absolute values are not discussed. Dashed vertical lines at 5 and 100 A.U. delimit a radius range where small bodies able to condensate ice mantles are expected to form. Hatched and dotted ovals underline possible regions of formation of the organic matter of UCAMMs based on their isotopic compositions. The pink hatched zone, deep in the midplane, is a region with the CO, N_2 and cyanide reservoirs with low $^{15}N/^{14}N$ and high $^{13}C/^{12}C$ ratios. The condensation and irradiation of ices with such composition can form the ^{15}N-depleted, ^{13}C-enriched matter of DC309. The green dotted zone is located at intermediate depth regions, where molecular reservoirs are more ^{15}N-rich. The condensation and irradiation of such ices could be at the origin of DC43 and DC94 organics. The predicted ^{13}C-depletion of cyanides in the lower part of this zone could explain the low $^{13}C/^{12}C$ observed in DC94.

4.3.2. Fractionation of hydrogen in the disk

Deuterium fractionation in the solar system is likely inherited from fractionation that happened in the early proto-stellar core stage, as shown by astronomical observations of proto-stellar objects (Bacmann et al., 2003; Crapsi et al., 2005; Pagani et al., 2007) and described by models (Aikawa et al., 2012; Furuya and Aikawa, 2018). Large D fractionation driven by gas-grain reactions can lead to the formation of deuterated molecular reservoirs (see e.g. HCOOH, CH_3CN, NH_3 in Figure 4-11 from Aikawa et al. (2012). D/H ratios in different molecular reservoirs in the proto-stellar core in function of the radius at t=-5.6·102 yr (thin lines), 4.3·102 yr (thick lines) and 9.3·104 yr (bold lines).Figure 4-11). Aikawa et al. (2012) predict that such enhancements can occur within 10^5 years after the formation of the proto-stellar core. The extreme deuterium excesses in UCAMMs, up to δD≈30,000‰ reported in Bardin (2015) and Duprat et al. (2010), indicate that the organic matter of UCAMMs inherited from a highly deuterated molecular reservoir. Moreover, the preservation of the deuterated signature of chemical species can depend on their gaseous or solid state during the solar system evolution (Piani et al., 2021). The parent reservoir of UCAMMs may thus have preserved its highly deuterated nature under the form of ice in cold regions of the protoplanetary disk. However, some UCAMM, such as DC18, or the UCAMM reported by Yabuta et al. (2017) present lower δD (lower than 1000‰), indicating that all UCAMMs may not have sample the same chemical reservoir. The diversity of the bulk hydrogen isotopic composition of the organic matter in UCAMMs may thus result from the condensation of chemical species at different heliocentric distances and/or different times (Ceccarelli et al., 2014; Piani et al., 2021). The bulk δD observed in the different UCAMMs analyzed in this work vary from about 1000‰ to 7000‰ that is consistent with the H-fractionation reached at different stages and locations in the disk in models (Aikawa et al., 2018; Aikawa et al., 2012). Additionally, large D/H fractionation, ranging from 0‰ to 6000‰ in DC94 and from 4000‰ to 9000‰ in DC94, are observed within individual UCAMM. In the hypothesis of a heritage of the isotopic composition of heterogeneous ice mantles, this would suggest that reservoirs with different H fractionation levels may have sequentially condensed on a same parent body. This could result from a sequential condensation at different heliocentric distances/temperatures.

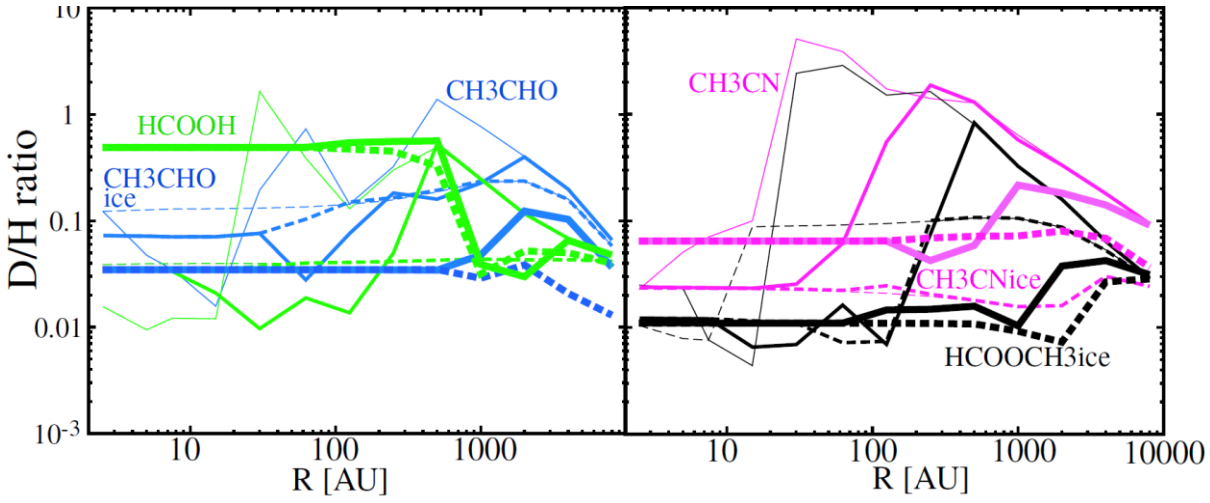

Figure 4-11 from Aikawa et al. (2012). D/H ratios in different molecular reservoirs in the proto-stellar core in function of the radius at t=-5.6·10² yr (thin lines), 4.3·10² yr (thick lines) and 9.3·10⁴ yr (bold lines).

4.3.3. Probing the radial and vertical isotopic diversity of the disk with UCAMMs?

The diversity of the UCAMMs isotopic compositions reported in this work may be related to the diversity of carbon and nitrogen isotopic compositions of the different molecular reservoirs described above. The mere variability of the isotopic compositions of UCAMMs is an additional indication that they most probably originate from the outer regions of the disk, that is the location where highly fractionated molecular reservoirs coexist. Such gaseous reservoirs can then condensate at the surface of UCAMMs parent bodies and, subsequent irradiation by GCR can form the isotopically heterogeneous organic matter. The feasibility of such a scenario, starting from chemically simple ice building blocks ubiquitous in the early solar system, is demonstrated by the GANIL experiments described in Chapter 3. The formation scenario of UCAMMs depends on the efficiency of condensing volatile species with different isotopic composition at the surface of small bodies. The abundance of HCN ice on grains plotted against the regions of the disk, in *Figure 4-10* (top right panel), indicates that, in the DALI model, HCN ice is not expected below 10 A.U. at 1 Myr. However, the condensation of volatile ices (HCN, N_2, CO, CH_4, …) is still possible at smaller radii on the surface of small bodies (Brown et al., 2011a), large enough to retain volatiles (see chapter 3, section 3.3.2).

The models of Visser et al. (2018) and Aikawa et al. (2012) indicate that different molecular reservoirs exhibit large isotopic fractionations in H, C and N that, once condensed at the surface of small bodies, can induce refractory organic compounds with the isotopic characteristics of UCAMMs. UCAMMs are a new type of interplanetary materials and, although this work gathers the most comprehensive isotopic survey on these objects, the constraints on their organic components remain limited. The theoretical reservoirs predicted by Visser et al. (2018) and Aikawa et al. (2012) display isotopic fractionations much larger than the one observed in UCAMMs and several combinations of these reservoirs can be considered as end-members from which the isotopic composition of UCAMMs may originate. Although not unique, we emphasize below a possible solution with two parent reservoirs for the irradiation-induced organic matter of UCAMMs (*Figure 4-10*, *Figure 4-12* and Table 4-2).

Midplane regions (the pink hatched zone):

In the outer midplane regions of the disk ($R \approx 5 – 100$ A.U., $z/R \leq 0.06$, pink hatched zone on *Figure 4-10*), the low temperature is expected to allow the formation of condensed ice mantles of relatively volatile ices (such as N_2 and CO) at the surface of small bodies. The DALI model predicts that the N_2 and CO reservoirs that are the most abundant in that region have low $^{15}N/^{14}N$ and moderate to high $^{13}C/^{12}C$ ratios. Thus the irradiation of such N_2-CO ice mantles would lead to the formation of an organic matter with high N/C ratio, low $^{15}N/^{14}N$ and high $^{13}C/^{12}C$ consistent with the chemical and isotopic data on DC309 and DC18. This hypothesis is supported by the fact that DC309 and DC18 are both dominated by the type III organic matter (see section 4.2). The CP-IDP Eliot (*Figure 4-8*, Floss et al. (2006)) may very well originates from the same region. DC309, DC18 and Eliot would be formed within that midplane region, by the irradiation of N_2-CO dominated ice mantles at very low temperatures. The characteristic isotopic fingerprint of the surface of small bodies with ices originating from that region would be low $^{15}N/^{14}N$ ratios and slightly enhanced $^{13}C/^{12}C$ (*Figure 4-12*).

Intermediate depth regions (the green dotted zone):

The lower N/C ratios in DC94 and DC43 (Table 4-1) suggest that their organic matters formed in a less N-rich environment than DC309 and DC18, possibly in hotter regions. The isotopic composition of DC94, uncommonly depleted in ^{13}C, suggests that its organic matter may have inherited a cyanide-like $^{13}C/^{12}C$ ratio found in regions at 0.08 < z/R < 0.20 (green dotted zone in Figure 4-10). Its $^{15}N/^{14}N$ composition, higher than the PSN value but lower than the one of DC43, may result from either a mix of two fractionated reservoirs or come from a single reservoir in a "transition" zone (e.g. the cyanide reservoir in the dotted zone in Figure 4-10). The DC43 parent reservoir could also originate from this intermediate depth regions, possibly at higher latitudes where the ^{15}N compositions of the cyanides are higher. Based on the similarities between DC43 and the IOM of CR chondrites and the CP-IDPs, the reservoir of DC43 would be more common and sampled by several classes of interplanetary objects.

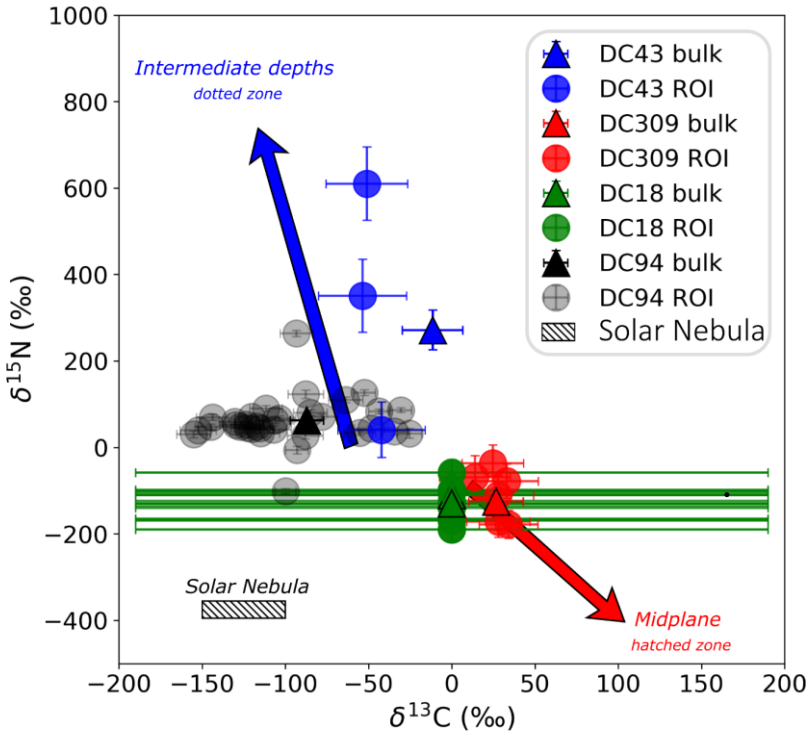

Figure 4-12: $\delta^{15}N$ vs $\delta^{13}C$ values in the 4 UCAMMs, bulk values are plotted with triangles and ROI with circles. The DC309 and DC18 may have formed from the irradiation of N_2-CO-rich ices originating from the cold regions around the midplane while DC43 and DC94 may have formed from the irradiation of cyanide ices originating from intermediate depth (and slightly less cold) regions.

Table 4-2. Summary of the isotopic and chemical compositions of the 4 UCAMMs (DC309, DC18, DC43, DC94) reported in this work and B. Guérin Ph.D. thesis (2021). (a) OM type refers to the dominant type of organic matter observed on STXM-XANES maps.

UCAMM	Isotopic composition (Bulk)			Chemical composition		Reservoir
	δD (‰)	$\delta^{15}N$ (‰)	$\delta^{13}C$ (‰)	OM type[(a)]	N/C	
DC309	6800	-125	27	I, II, III	-	Midplane *(hatched zone)*
DC18	990	-120	-	III	0.17	
DC43	3100	272	-12	I, II	0.04	Intermediate depths regions *(dotted zone)*
DC94	2520	63	-87	I, II	0.05	

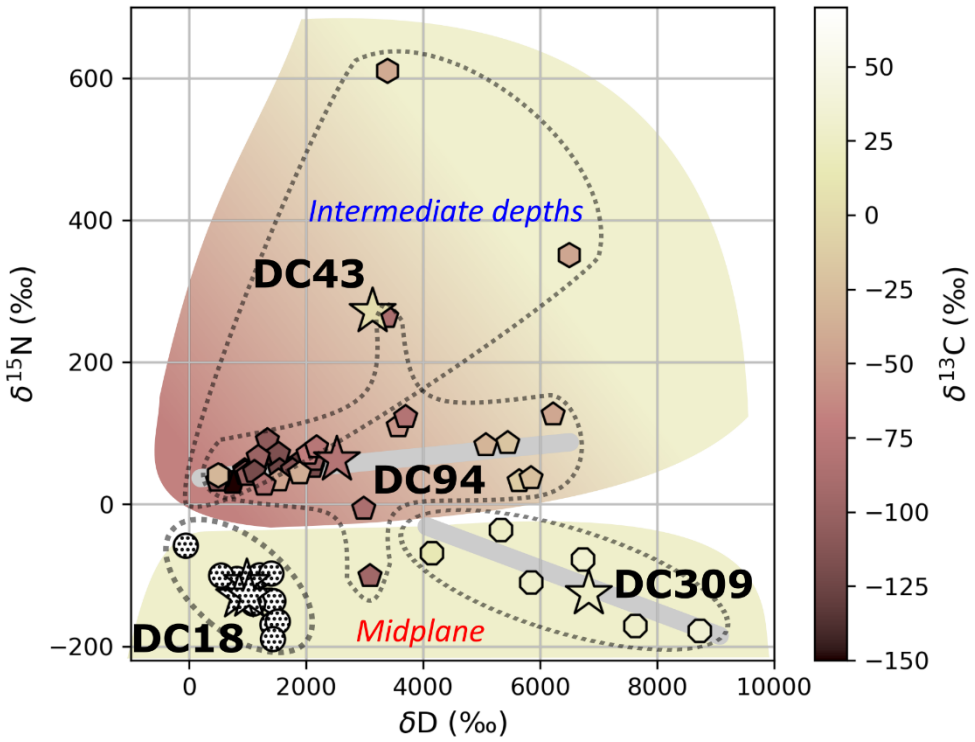

Figure 4-13: the two possible parent reservoirs of UCAMMs represented on a $\delta^{15}N$ vs δD vs $\delta^{13}C$ graph. The intermediate depths reservoir is characterized by positive $\delta^{15}N$ values and a δD values ranging from 0 ‰ to about 6000‰. The midplane reservoir has lower $\delta^{15}N$ and a wide range of δD from about 0 to 9000‰. Thick gray lines indicate correlations between $\delta^{15}N$ and δD in DC309 and $\delta^{13}C$ and δD in DC94 (section 2.5).

Mixing different reservoirs

Correlations between $\delta^{15}N$ and δD in DC309 and between $\delta^{13}C$ and δD in DC94 (thick gray lines in Figure 4-13) echo the mixing lines observed in the spatial distributions of isotopic enrichment in organic residues formed at GANIL (see Chapter 3 section 3.3.1). They may thus be interpreted as resulting from the isotopic heterogeneities within the initial ice mantles. The correlation associated to DC94 indicates that the reservoir with the low $\delta^{13}C$ component is probably associated with a low δD reservoir. By contrast, the correlation observed in DC309 connects an end-member with very high δD and low $\delta^{15}N$ with the main

reservoir of UCAMMs. The results obtained in Chapter 3 indicate that, under specific conditions of annealing, the irradiation-induced residues can exhibit linear correlations between the isotopic compositions of specific layers of ice. The isotopic composition of DC309 may be a result from the sequential condensation of layers of ice from the midplane and the intermediate depths reservoirs on the parent body/bodies of UCAMMs. The possible correlation between these two hypothetical reservoirs remains an open question and data on more UCAMMs need to be gathered to obtain extended isotopic and chemical constraints on the organic components present in UCAMMs and on the evolution of their mixing within individual particles.

The transfer of the characteristics of the parent reservoirs to the organic matter of UCAMMs requires the condensation of these reservoirs. However, the formation of small bodies condensing substantial ice mantles occurred at a more advanced stage than the one investigated by the models of Visser et al. (2018) and Aikawa et al. (2012). The heritage of the isotopic compositions of UCAMMs implies thus an intermediate step in which the isotopic compositions of these early molecular reservoirs are preserved, then transferred to the ice mantles on small bodies. This can have occurred through the condensation of the volatile reservoirs on small grains prior to their incorporation in larger parent bodies (Charnoz and Morbidelli, 2007). In such a scenario, subsequent surface/sub-surface processes could lead to the distillation of the icy grains at the parent body surface and segregate the mineral grains from the volatile compounds to form mineral-depleted ice mantles. An alternative possibility involves the young disk dynamics where, during their formation, large grains/pebbles might accrete volatiles along their journey toward the disk midplane. These intermediate size objects could then be incorporated in small bodies during their accretion phase and episodic accretion bursts may then sublimate/re-condensate the most volatile species on their surface (Bosman and Bergin, 2021). The subsequent irradiation of these icy mantles, however they formed, could then lead to the synthesis of an organic matter depleted in minerals as observed in UCAMM type III organic matter.

The existence of anomalous spots with isotopic compositions profoundly different from the bulk composition of the UCAMMs may result from the mixing of organic matters formed in different zones as it is suggested by the coexistence of type I, II and III organics components within a single UCAMM (Table 4-1). In such a scenario, the isotopic heterogeneities that plot along a correlation trend would result from isotopic heterogeneities within a given initial ice mixture whereas the isotopic anomalous spots (that do not lay on a correlation trend) would result in the mixing of organic matters formed from distinct ices. If the parent bodies of UCAMMs acquired their ice mantles by the aggregation of icy grains, anomalous spots could also result from the incorporation of individual grains with an isotopic and chemical composition different from the surrounding grains. A mixing (vertical and radial) of grains formed at different locations in the disk can result from turbulences (Bockelée-Morvan et al., 2002) and be grain size-dependent. Finally, the coexistence of high temperature crystalline minerals within the types I and II organic matters of UCAMMs (see section 4.2) indicate the occurrence of a radial mixing in the disk, but at larger scales than the ones between intermediate depths regions (or inner regions) and midplane regions.

4.4 General summary

This Ph.D. thesis focuses on the study of micrometeorites collected around the Concordia station (Dome C) in central Antarctica over the last twenty years. These particles are originating from solar system small bodies, asteroids and comets. The study of micrometeorites from the Concordia collection sheds light on the flux of interplanetary dust at 1 A.U. and the refractory material present at the surface of the small bodies that have kept the memory of the early stages of the solar system

The Concordia collection is described in the first chapter, introducing a comprehensive study aiming at constraining the extraterrestrial sub-millimeter particles flux falling on Earth. The size distributions and mass fluxes of unmelted micrometeorites (uMM) and cosmic spherules (CS) are reported in the 30-350 µm diameter range. The unique conditions at Dome C allow an accurate control on both the exposure parameter (the equivalent surface of accumulation) and the collection efficiency. Several independent measurements of the flux are reported on the same site, using a method allowing to infer a well constrained absolute value of both the uMMs and CSs fluxes. Thanks to its experimental protocol, the Concordia collection accurately samples, for the first time, all micrometeorites (including the most fragile) down to 30µm, showing that the maximum of the mass flux of both uMMs and CSs is carried by particles in a size range lower than that inferred from previous works. Combined with previous measurements performed at the South Pole Station, the results allow to derive the global flux of uMMs and CSs over the 12-700 µm diameter range. The global annual input of micrometeorites on Earth extrapolated from this study is 5,200 tons·yr^{-1} (3600 tons·yr^{-1} from CSs and 1,600 tons·yr^{-1} from uMMs). That value is substantially higher than the one derived from the South Pole collection but stays, about a factor of 3, below the flux expected at atmospheric entry. This study confirms that about 2/3 of the mass of the incoming flux is ablated at atmospheric entry and that the major contribution to the annual extraterrestrial input on Earth is indeed carried by particles in the size range studied in this work. Based on the carbon relative abundances in the different types of micrometeorites obtained from the Concordia collection analyses, the flux of carbon on Earth carried by micrometeorites is estimated to range from 20 to 100 tons·yr^{-1}. From the mass distributions obtained in this work, a Monte-Carlo simulation is performed to calculate the statistical uncertainties related to the variations of the exposure parameters. The results obtained allow one to infer the statistical uncertainties on similar measurements for future studies on the flux of sub-millimeter interplanetary particles.

In chapter 2, H, N and C isotopic data on ultra-carbonaceous micrometeorites (UCAMMs) are reported. UCAMMs are a rare carbon-rich micrometeorites population identified in the Concordia collection that most probably formed in outer regions of the solar system. The isotopic composition of the organic matter of UCAMMs provides clues to better understand their origin. Within the course of this thesis, 5 fragments of 3 UCAMMs were analyzed by Nanoscale Secondary Ion Mass Spectrometry (NanoSIMS) at the Earth and Planets Laboratory (Carnegie, Washington DC) in collaboration with Dr. L. Nittler. An analysis of C isotopic data previously acquired (prior to this thesis) on a UCAMM studied by NanoSIMS at MNHN and at Institut Curie is also presented. This work presents the most comprehensive study available today on D/H, $^{13}C/^{12}C$ and $^{15}N/^{14}N$ ratios on several UCAMMs. The data obtained show that UCAMMs exhibit a variety of H, N and C isotopic compositions differing from one particle to another and within a given fragment. The overall data reveals spatial correlations between H, C and N isotopic compositions that are further discussed in chapter 4.

Chapter 3 presents experiments made to reproduce the irradiation by Galactic Cosmic Ray of ice mantles representative of the surface of small bodies in cold regions of the protoplanetary disk. Nine refractory organic residues were produced during three experimental sessions in 2019, 2020 and 2021 at the Large Collider for Heavy Ions (GANIL, France). The experiments used a dedicated set-up developed at CIMAP (IGLIAS). Ice films with several initial chemical compositions were irradiated with swift heavy ions. The ice films were isotopically heterogeneous in order to study the transfer of the isotopic heterogeneities to the irradiation-induced residue. The H, N and C isotopic compositions of the organic residues were analyzed by NanoSIMS at Institut Curie (Orsay, France). This study reports, for the first time, combined analyses of D/H, $^{13}C/^{12}C$ and $^{15}N/^{14}N$ heterogeneities in irradiation-induced residues obtained from mixtures of a variety of ices with different condensation temperatures: CO, NH_3, N_2, CH_4. When formed under the same conditions, residues resulting from the irradiation of N_2-CH_4 ices display a more heterogeneous isotopic composition than residues formed from NH_3-CH_4 ices. However, the nature of the heterogeneities as well as the overall structure of the residues appear highly sensitive to the formation conditions such as the pace of the annealing. The formation of localized patches of matter with extreme isotopic anomalies are observed, may be linked to sporadic sublimation events during the annealing procedure. The results of these experiments are discussed with regard to the astrophysical conditions expected at the surface of icy bodies located in the cold regions of the protoplanetary disk, above 5 A.U.

In the last chapter, the results of chapter 2 and 3 are put into perspective with the aim to delineate contours for a formation scenario of the organic matter of UCAMMs. The diversity of the isotopic composition of UCAMMs is summarized and compared with that of other solar system objects. The striking similarities between the isotopic compositions of one UCAMM and that of CR chondrites indicates that these objects might have inherited their organic matter from a similar parent reservoir, further suggesting a continuum between the CR parent body and cometary objects. Based on theoretical simulations from the literature on the H, N and C isotopic compositions of different chemical reservoirs in the protoplanetary disk, molecular parent reservoirs are proposed from which the UCAMMs isotopic heterogeneities may have been inherited. It is possible to account for the isotopic composition of some UCAMMs by considering the irradiation of ice mantles originating from gaseous reservoirs formed in regions close to the disk midplane. Other UCAMMs may have inherited from the isotopy of molecular reservoirs originating from a less cold environment, at intermediate depths above the disk midplane. These hypotheses are discussed with regard to chemical data on UCAMMs.

4.5 Perspectives

In this section, some trails are proposed to further expand the understanding of the formation scenario of UCAMMs proposed above.

4.5.1. Coupling chemical and isotopic data at a sub-micron scale

Chemical and isotopic characterization techniques are complementary tools to investigate the origin of interplanetary materials. The identification of different types of organic matters (types I, II, III) with STXM analyses of UCAMMs' FIB sections and different isotopic compositions in UCAMMs with NanoSIMS suggests that these objects formed from, at least, two reservoirs with different properties (N-content and H, N, C isotopic composition). Coupling more detailed chemical and isotopic data on the organic matter of UCAMMs would allow a systematic determination of the chemical composition of isotopic anomalous spots and help to decipher their origins. This investigation requires a specific sample preparation to

perform analyses using additional techniques such as STXM-XANES, Nano-scale IR (AFMIR) together with NanoSIMS on the very same sample slice. NanoSIMS analyses were already performed on a UCAMMs thin-section (DC309) that was previously characterized by AFMIR, demonstrating the feasibility of such an approach.

The AFMIR technique couples an infrared laser system with an atomic force microscope (AFM) to measure the excitation of matter that absorbs photons (Dazzi et al., 2012; Mathurin et al., 2020). It allows to access the chemical composition of a sample at a sub-micron scale, below the diffraction limit of classic IR spectroscopy. Figure 4-14, middle panel, shows a map of the 1710 cm^{-1} to the 1600 cm^{-1} bands ratio acquired with AFMIR on DC309. This ratio, reflects the C=O/C=C relative abundance, revealing chemical heterogeneities at a sub-micron scale. The NanoSIMS maps were performed on that very same zone in an atempt to correlate the chemical and isotopic compositions at the sub-micron scale (see chapter 2 section 2.3.1.1). Comparison of the isotopic maps with the C=O/C=C maps (Figure 2-3, Mathurin et al. (2019)) did not reveal correlations on that specific region. However, a more systematic investigation of UCAMMs with AFMIR and NanoSIMS is of great interest.

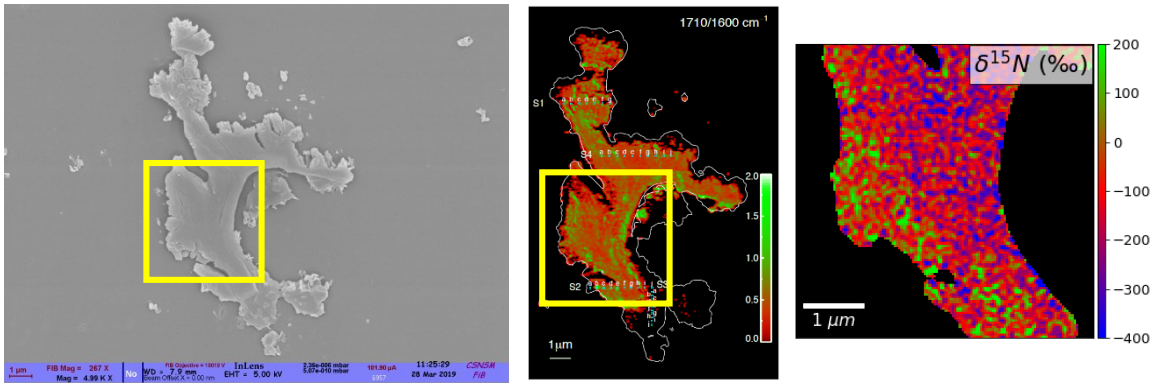

Figure 4-14. Left: SEM image of the DC309 fragment analyzed by NanoSIMS. Middle: nanoscale IR mapping of the DC309 fragment measured by AFMIR (Mathurin et al., 2019). The colarbar indicates the ratio of the 1710 cm^{-1} to the 1600 cm^{-1} bands corresponding to the C=O/C=C ratio. Right: $\delta^{15}N$ image acquired with the NanoSIMS. The raster corresponds to the yellow square in the SEM and AFMIR images.

Correlating AFMIR, STXM and NanoSIMS data on the very same regions on UCAMMs will clarify the formation scenario of the organic matter proposed in section 4.3.3. More precisely, a mapping at the same scale combining the N/C ratios, the infrared vibrational spectra, the abundance of minerals and the isotopic signatures on a sample will allow characterizing the nature of the parent reservoirs of UCAMMs as well as the possible interaction between distinct phases such as type I, II and III organic matter and minerals. An attempt has been made, however, the loss of DC18 FIB section after its transfer from a TEM grid to a NanoSIMS holder (see annex 5.1.1) recalls that the manipulation of such small samples remains highly challenging. In the framework of the recent sample-return missions on asteroids Ryugu (Hayabusa2) and Bennu (OSIRIS-REx), the development of such coupled techniques will provide a powerful tool for a future characterization of interplanetary material.

4.5.2. Abundance of pre-solar grains in UCAMMs

Pre-solar grains in meteorites and sub-millimeter dust are refractory inclusions inherited from the parent clouds of the solar system (Nittler and Ciesla, 2016; Zinner, 2014). They exhibit specific isotopic compositions that can be linked to distinct nucleosynthetic processes. Because they can be processed within the protoplanetary disk and their characteristic isotopic signatures erased at high temperature, their preservation (and therefore abundance) is expected to be higher in interplanetary samples that formed in cold regions. A comprehensive search of pre-solar grains in UCAMMs could bring important information on the heritage of pre-solar refractory materials from deep regions of the protoplanetary disk. A difference in the abundance or the types of pre-solar grains in UCAMMs formed in distinct regions could also help to constrain the amplitude of the radial and vertical mixing in the disk (Bockelée-Morvan et al., 2002).

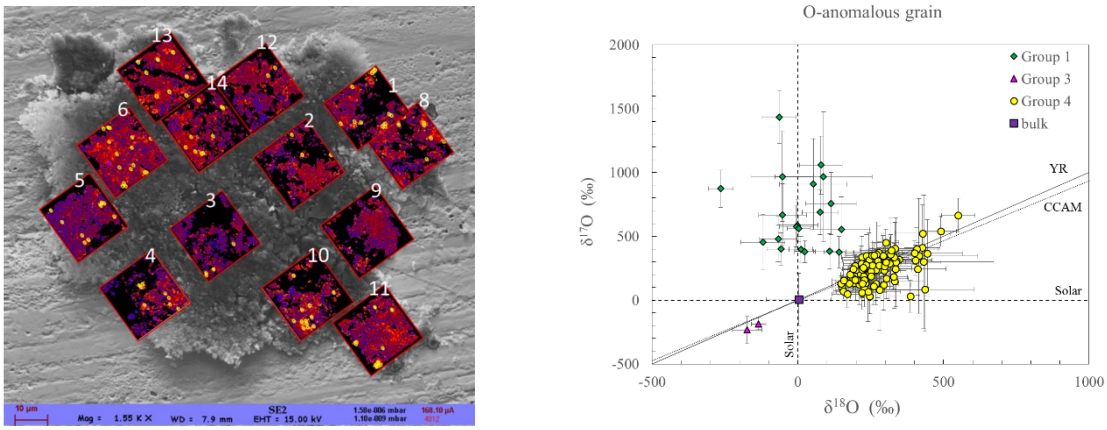

Figure 4-15: pre-solar grains identified in the UCAMM DC94 with the NanoSIMS at IMPMC-MNHN (Paris, France) (J.Duprat, C. Engrand et al., private communication).

5 Annexes

5.1 Isotopic measurements on UCAMMs

5.1.1. Preparation of the DC18 FIB section at the Naval Research Laboratory

The DC18 FIB section was a 100 nm thick slice of UCAMM DC18 prepared by Focus Ion Beam (FIB) by D. Troadec at Institut d'Electronique, de Microelectronique et de Nanotechnologie (IEMN, Lille, France). It was attached to a grid in order to perform transmission electron microscopy (Figure 5-1, top left)). Prior to the present study, the DC18 FIB section had been analyzed by scanning transmission X-ray microscopy (STXM-XANES) coupled with scanning transmission electronic microscopy (TEM/STEM) (Guérin et al., 2020). In order to perform NanoSIMS analyses on that FIB section at EPL (Washington DC, USA), the sample was detached from the TEM grid and deposited on a silicon wafer by Dr. Rhond Stroud at the Naval Research Laboratory (NRL, Washington DC, USA) as shown by the Figure 5-1. To ensure its stability, the FIB section was coated to the wafer with carbon on several spots.

Unfortunately, the FIB section detached from the wafer during the NanoSIMS analysis, possibly due to charging effects, preventing the acquisitions of isotopic data. The combination of NanoSIMS and STXM-XANES data is mandatory to deepen our understanding of the nature of the organic matter in UCAMMs. However, the sample preparation is challenging since it requires to manipulate samples with sub-micron/micron dimensions. The probability of losing a sample during its preparation remains high.

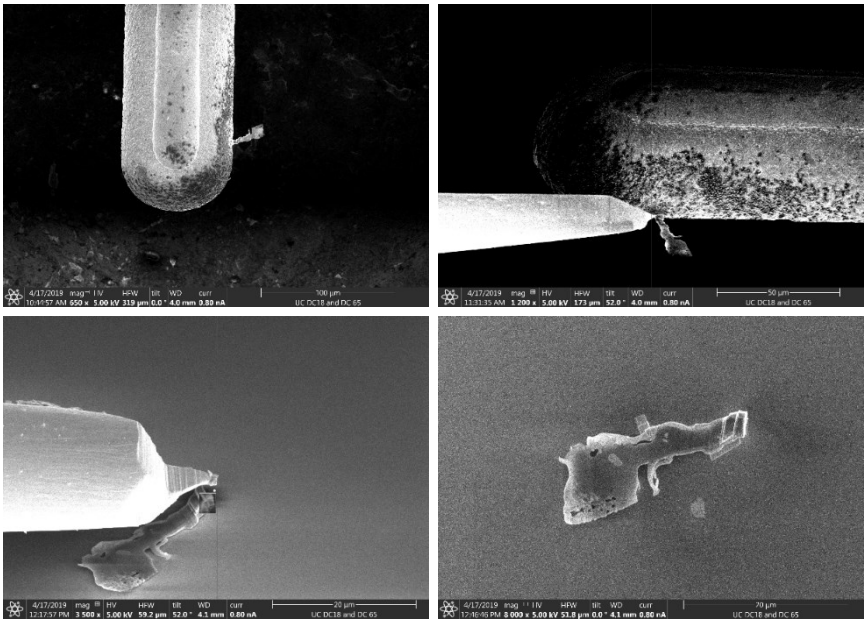

Figure 5-1: Preparation of the FIB section of DC18. DC18 FIB section was initially fixed to a STEM grid (top left). It was removed from the grid and deposited onto a silicon substarte thanks to a needle (top right and bottom left). At the end of the operation, the FIB section was stuck on the silicon substarte by a carbon coating. The handling of that transfert was done by Dr. Stroud at the Naval Research Laboratory prior the NanoSIMS analysis at EPL.

5.1.2. Control of the instrumental mass fractionation (IMF)

The instrumental mass fractionation was controlled by a set of standards during the NanoSIMS session at the Carnegie institution (Table 5-1):

- In-house standard $C_{30}H_{50}O$ with δD = -152
- SiC standard with $\delta^{13}C$ = -22‰; the IOM QUE 99177 with $\delta^{13}C$ = -20.8‰
- Si_3N_4 sample with $\delta^{15}N$ = 0‰

Table 5-1: instrumental mass fractionation measured on a set of standards during the 2019 NanoSIMS session at Carnegie Institution EPL.

			DC309	DC43	DC18 A, B, C
Standard					
Carbon	IOM QUE 99177	IMF (α)	8.92 ± 0.13	-	-
		IMF (‰)	-106 ± 13 ‰	-	-
	SiC	IMF (α)	-	8.77 ± 0.15	-
		IMF (‰)	-	-119 ± 15 ‰	-
Nitrogen	Si_3N_4	IMF (α)	10.02 ± 0.22		9.87 ± 0.16
		IMF (‰)	2 ± 22 ‰		-13 ± 16 ‰
Hydrogen	$C_3H_{50}O$	IMF (α)	9.00 ± 0.50		10.24 ± 0.38
		IMF (‰)	-85 ± 43 ‰		-20 ± 32 ‰

The instrumental mass fractionation was controlled by a set of standards during the NanoSIMS session on DC94, at the MNHN and institut Curie (Table 5-2):

- Terrestrial anthracite standard DonH8 with δD = -103 ‰; deuterated polystyrene PSD with δD = 7470 ‰ (Bardin, 2015)
- Type III kerogen with $\delta^{13}C$ = -25 ‰
- Terrestrial anthracite DonH8 with $\delta^{15}N$ = -1 ‰

Table 5-2: instrumental mass fractionation measured on a set of standards for the NanoSIMS sessions on the UCAMM DC94.

			DC94 A, B, C	DC94 D
Standard				
Carbon	Type III kerogen	IMF (α)	9.96 ± 0.09	9.55 ± 0.05
		IMF (‰)	4 ± 9 ‰	- 44 ± 5 ‰
Nitrogen	DonH8	IMF (α)	9.95 ± 0.03	
		IMF (‰)	- 5 ± 3 ‰	
Hydrogen	DonH8	IMF (α)	10.11 ± 0.11	-
		IMF (‰)	- 10 ± 10 ‰	-
	PSD	IMF (α)	-	9.1 ± 0.3
		IMF (‰)	-	760 ± 250 ‰

5.1.3. NanoSIMS images of fragments DC18A and DC18B

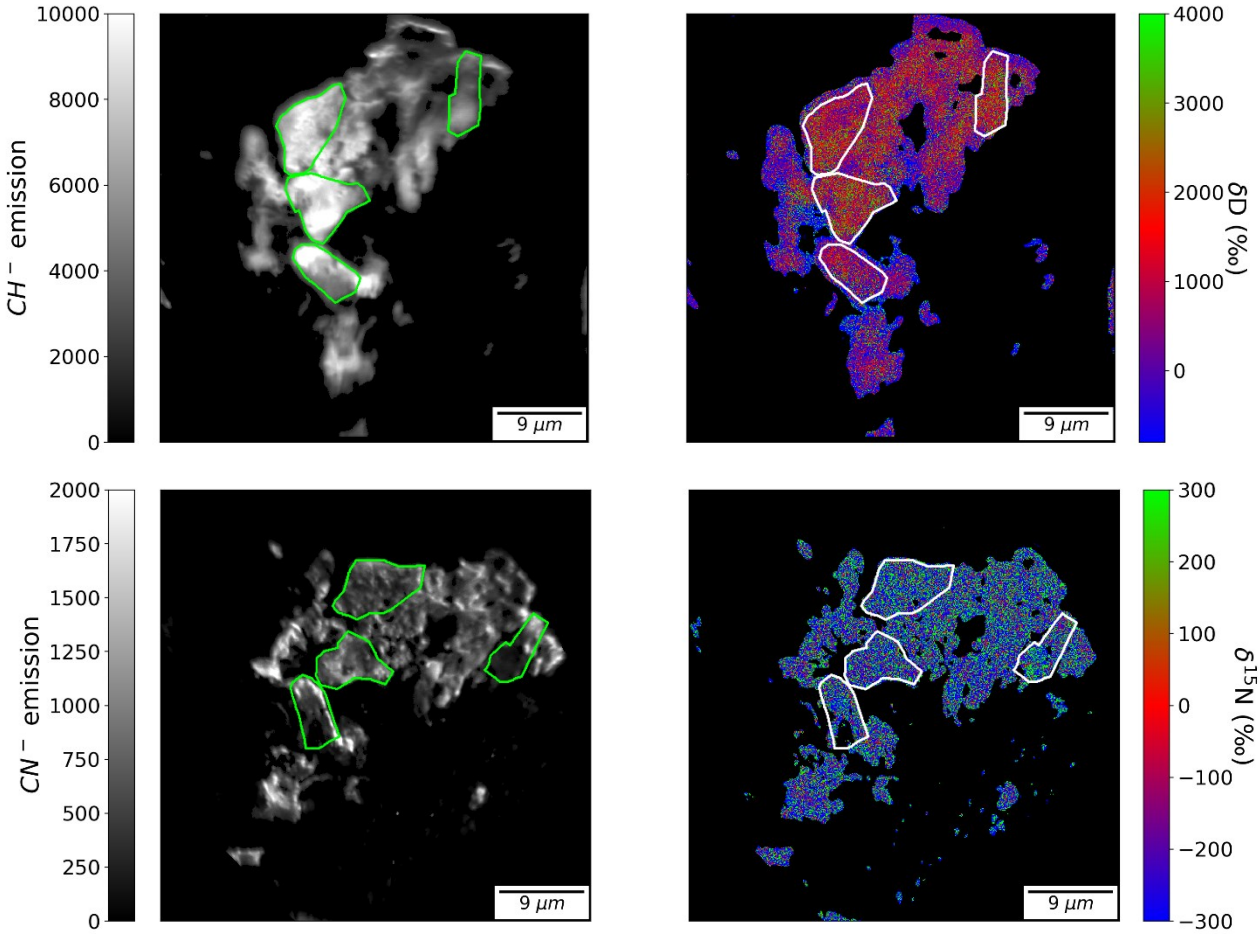

Figure 5-2: Top left: CH^- image of the DC18 A fragment analyzed by NanoSIMS. Top right: δD image of DC18 A. Bottom left: CN- image of DC18 A. Bottom right: $\delta^{15}N$ image of DC18 A. Four regions of interest are drawn in white in yellow.

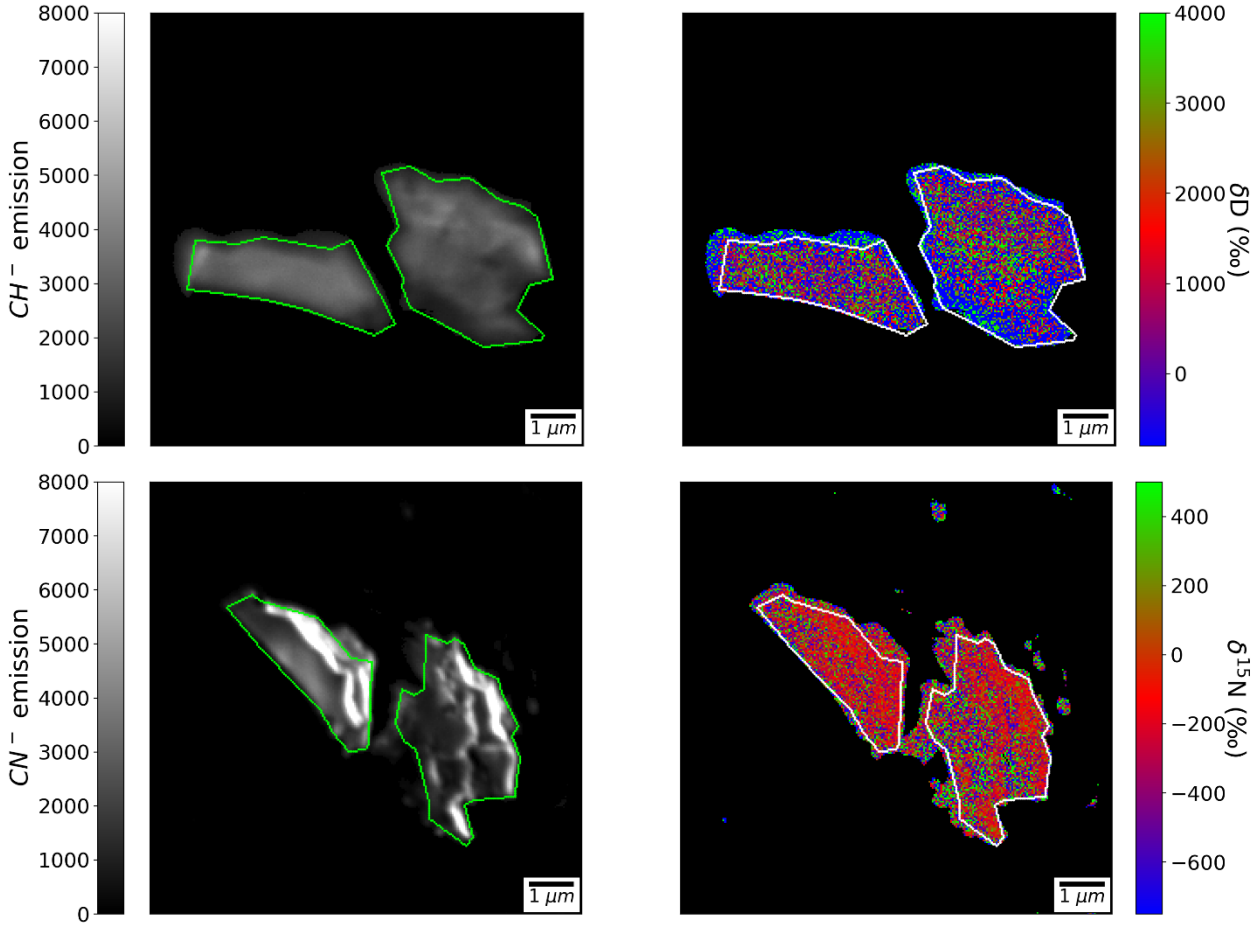

Figure 5-3: Top left: CH^- image of the DC18 C fragment analyzed by NanoSIMS. Top right: δD image of DC18 C. Bottom left: CN- image of DC18 C. Bottom right: $\delta^{15}N$ image of DC18 C. Four regions of interest are drawn in white in yellow.

5.1.4. Isotopic images on zones A, B and C on DC94 (with mesh)

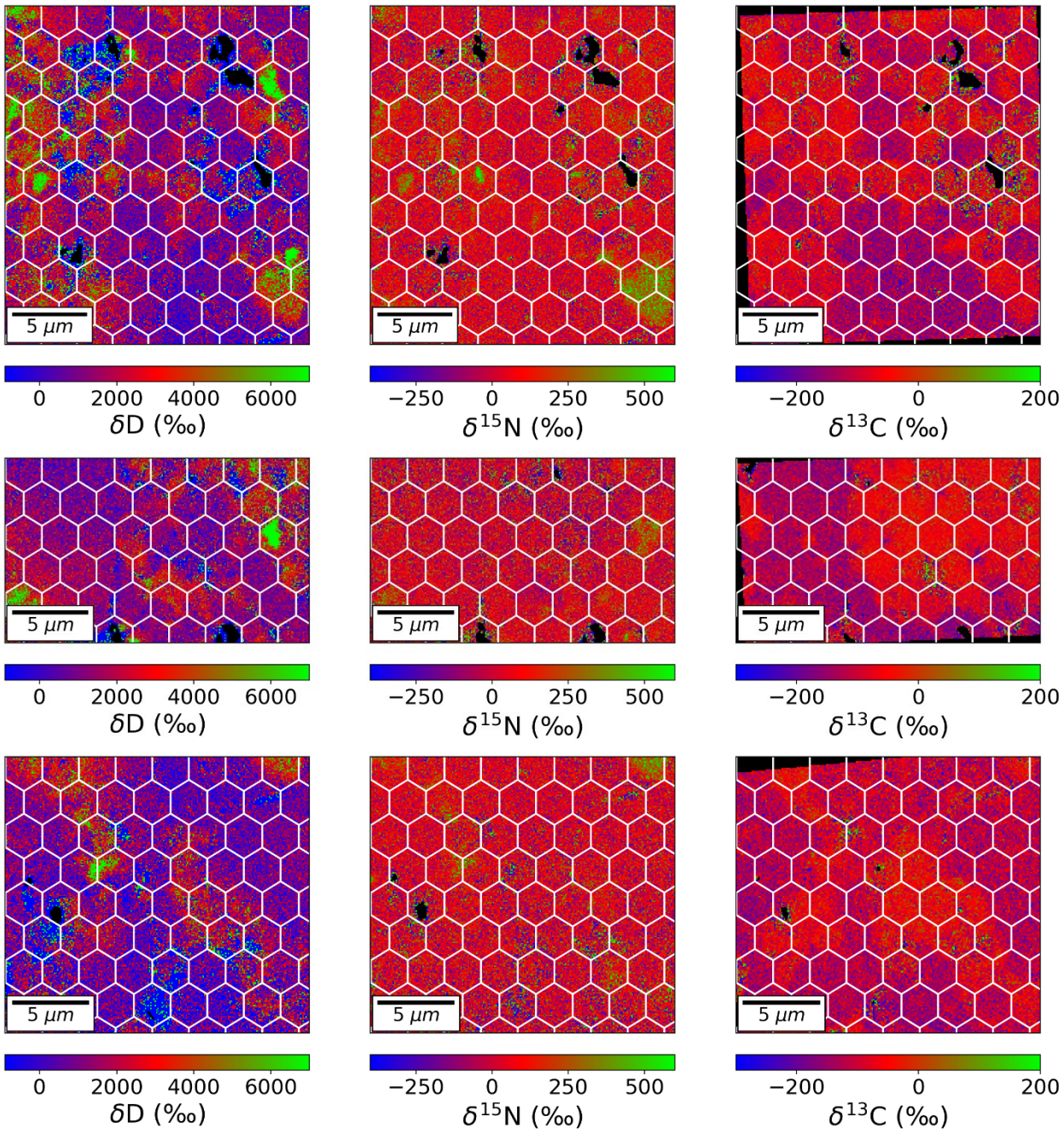

Figure 5-4: δD (left), $\delta^{15}N$ (middle) and $\delta^{13}C$ (right) images on zones A (top row), B (middle row) and C (bottom row). The hexagonal mesh is used to derive the correlations between $\delta^{13}C$, $\delta^{15}N$ and δD maps.

5.2 Ion irradiation experiments

5.2.1. NanoSIMS analyses of the residues: experimental conditions

The NanoSIMS analyses performed on the organic residues synthesized at GANIL took place during the summers 2019, 2020 and 2021. The analytical conditions of these analyses are listed in the Table 5-3.

Table 5-3 : analytical conditions of the NanoSIMS analyses performed on the organic residues formed at GANIL

Date	Ions	Sandwich	Primary current (pA)	Dwell time (ms/pix)	Area (µm²)	Definition (pixel²)	N plans
10.22.2019	$^{12}CH^-$, $^{12}CD^-$, $^{12}C^{14}N^-$, $^{12}C^{15}N^-$, $^{13}C^{14}N^-$	Sd3	8.0	0.5	20×20	256×256	150 (300)
09.07.2020	$^{12}CH^-$, $^{12}CD^-$, $^{12}C^{14}N^-$, $^{12}C^{15}N^-$, $^{13}C^{14}N^-$	Sd4	8.0	0.5	100×100	308×308	600 (1200)
09.08.2020	$^{12}CH^-$, $^{12}CD^-$, $^{12}C^{14}N^-$, $^{12}C^{15}N^-$, $^{13}C^{14}N^-$	Sd4	8.0	0.5	100×100	308×308	322 (644)
09.14.2020	$^{12}CH^-$, $^{12}CD^-$, $^{12}C^{14}N^-$, $^{12}C^{15}N^-$, $^{13}C^{14}N^-$	Sd5	8.0	0.5	100×100	308×308	757 (1514)
09.03.2020	$^{12}CH^-$, $^{12}CD^-$, $^{12}C^{14}N^-$, $^{12}C^{15}N^-$, $^{13}C^{14}N^-$	Sd6	8.0	0.5	100×100	308×308	750 (1500)
07.08.2021	$^{12}CH^-$, $^{12}CD^-$, $^{12}C^{14}N^-$, $^{12}C^{15}N^-$, $^{13}C^{14}N^-$	Sd7	3.5	0.5	30×30	256×256	300 (600)
07.09.2021	$^{12}CH^-$, $^{12}CD^-$, $^{12}C^{14}N^-$, $^{12}C^{15}N^-$, $^{13}C^{14}N^-$	Sd7	3.5	0.5	30×30	256×256	800 (1600)
07.12.2021	$^{12}CH^-$, $^{12}CD^-$, $^{12}C^{14}N^-$, $^{12}C^{15}N^-$, $^{13}C^{14}N^-$	Sd7	8.0	0.5	30×30	256×256	708 (1416)
07.13.2021	$^{12}CH^-$, $^{12}CD^-$, $^{12}C^{14}N^-$, $^{12}C^{15}N^-$, $^{13}C^{14}N^-$	Sd7	8.0	0.5	30×30	256×256	1000 (2000)
07.16.2021	$^{12}CH^-$, $^{12}CD^-$, $^{12}C^{14}N^-$, $^{12}C^{15}N^-$, $^{13}C^{14}N^-$	Sd8	8.0	0.5	30×30	256×256	681 (1362)
07.22.2021	$^{12}CH^-$, $^{12}CD^-$, $^{12}C^{14}N^-$, $^{12}C^{15}N^-$, $^{13}C^{14}N^-$	Sd8	8.0	0.5	30×30	256×256	450 (900)

5.2.2. Analytical improvements

Investigating the isotopic composition of organic residues formed with the IGLIAS setup requires to adapt the substrate windows for both IR and NanoSIMS measurements. The windows need to be transparent to IR and able to evacuate charges accumulated during the NanoSIMS analyses. For the first experimental campaign (2019), ZnSe windows, with efficient IR transmission in the wavenumber range of interest, were used. Although they enabled the acquisitions of high-quality IR spectra, charging effects occurred during the NanoSIMS analyses, prematurely ending them. In order to improve the quality of the isotopic measurements, we designed new targets made of seven 5mm large and 0.5mm thin Si windows encapsulated in 20mm large copper holders (Figure 5-5, right and middle). Si windows have good transmission in the IR working domain and have higher conductivity than ZnSe windows. The seven windows were designed with the aim to perform characterizations of the organic residues using different techniques. Unfortunately, at the end of the annealing ramp of the 2020 GANIL session, few organic residues remained on the targets (Figure 5-5, middle), with only one 5mm Si window covered in residue for Sd4 and Sd6 and two for Sd5. This can result from a loose thermal contact between the copper holder and the Si windows. Also, with such configuration, the alignment of the IR beam is critical since the copper

holder can intercept it. For the NanoSIMS analyses, the windows covered in residues were extracted from the copper holders and glued with a colloidal carbon mixture in a specially designed aluminum holder (Figure 5-5, right). No charging effects were observed during the NanoSIMS acquisitions that lasted up to 12 hours. However, due to the uncertainties on the effective thermic contact of the Si windows during the irradiation experiments and their delicate handling during the experimental preparation, we did not use this target configuration for the 2021 session and opted for the conventional 20mm large Si windows. These IR-transparent windows allow an efficient charge evacuation and an easier handling. Though, they do not allow a multi-technique approach as proposed by the seven-window holder.

Figure 5-5. Left: visual aspect of the target Sd 4 at the end of the temperature ramp. Middle: close-up on the Sd4 window at the exit of the IGLIAS chamber. The 2020 experimental targets were made of seven 5mm large Si windows to insure a good charge evacuation during NanoSIMS analyses. The organic residue is visible on the lefternmost window. Craters on the surface of the residue are certainly due to the formation of buble during the temperature ramp. Right: dedicated aluminium holder for the NanoSIMS analyses. Three 2mm large Si windows from Sd4, Sd5 and Sd6 were fixed to the holder with a conductive carbon glue.

5.3 The NS-ION-VISU labview of the NanoSIMS mass spectrometer

This section presents a labview program of the ion optics of the NanoSIMS' mass spectrometer which have been developed based on the work by Georges Slodzian on the comprehensive study on the NanoSIMS settings. It aims at helping to visualize the effective impacts of the several devices on the trajectories of ion beams.

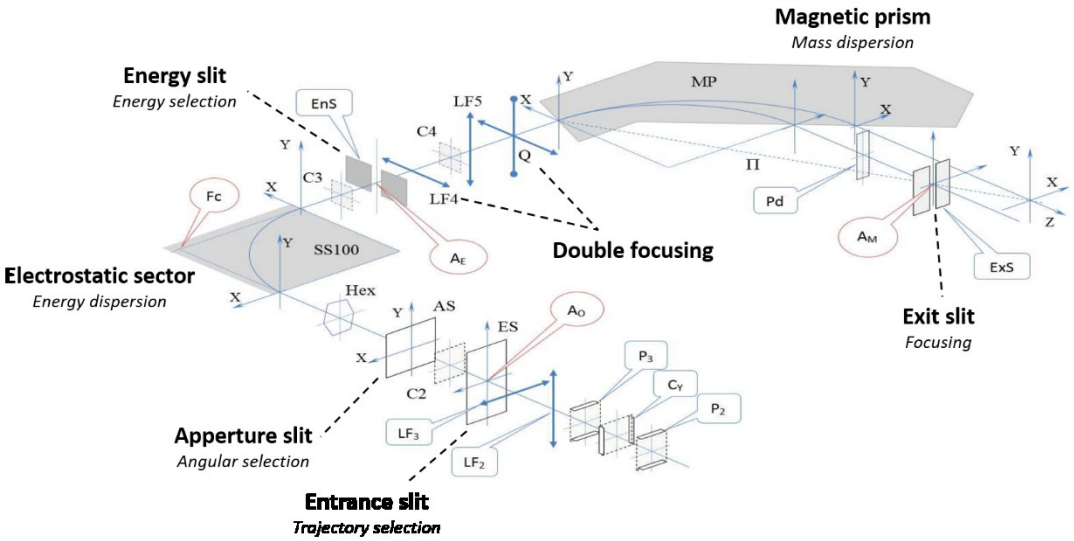

Figure 5-6: schematic view of the mass spectrometer of the Cameca NanoSIMS 50 (Georges Slodzian).

A schematic view of the NanoSIMS' mass spectrometer is given in Figure 5-6. The Z axis is the theoretical reference axis of the mass spectrometer; the X and Y axes defines the orthogonal axes in the horizontal and vertical directions, respectively. Figure 5-6 details the set of devices that guides the secondary ion beam through the mass spectrometer (i.e., deviation plate, lens, multipoles,…) and allows to perform the double focusing. The magnetic prism disperses the ions with different masses along the X axis. The fine selection of a beam of a given mass is performed by adjusting the horizontal position (along the X axis) of the exit slits (ExS), placed before the electron multipliers (EM). Because the mass resolution directly depends on the fine selection of a beam in the X direction, it is mandatory to monitor the spread of the secondary beams at the exit slits. Moreover, a too large extension of the secondary ion beam in X and Y direction along the mass spectrometer may cause instrumental mass fractionation, resulting from the interception of the beam by obstacles. Understanding the behavior of the secondary ions in the mass spectrometer and the actions of the ion optics is thus crucial to optimize the settings of the NanoSIMS.

Georges Slodzian developed a method aiming at evaluating the trajectories of narrow beams of secondary ions in the mass spectrometer (i.e. "pencils" in Slodzian et al. (2014)). Pencils of trajectories are selected by adjusting the entrance slit (ES) and the aperture slit (AS) at the entrance of the mass spectrometer. The modification of the positions of those pencils, in ExS, under the action of the ion optics settings enables to understand the individual effect of the mass spectrometer optics on the beam.

In support to this experimental work, Georges Slodzian proposed me to developed the NS-ION-VISU, a numerical code of the NanoSIMS' mass spectrometer in Labview programming language. The Labview program is a transcription of the work performed Georges Slodzian on an Excel sheet that he is currently using to follow the instrumental adjustments aiming at narrower mass lines for better mass resolving power. This program aims at providing an interactive approach of the ion optics of the mass spectrometer that allows to observe in real time the effects of settings' changes on the secondary ions' trajectories. The Labview program is more user-friendly and convenient to follow the effects of instrumental adjustments than a worksheet. The different devices constituting the MS were modeled by transformation matrices as explained in the following section.

5.3.1. The theoretical mass spectrometer

The NS-ION-VISU numerical model of the mass spectrometer relies on the transfer matrices of the NanoSIMS' components that act on the secondary ions' trajectories. An ion beam is modeled by a 5 dimensions' vector. The distance between the different components of the NanoSIMS and their dimensions are approximate. The matrix used do not take into account the possible stray fields and thus provide a semi-quantitative approach. Nevertheless, such calculations are suitable enough to represent qualitatively the main features of the CAMECA NanoSIMS-50 instrument at Institut Curie (Orsay, France).

5.3.1.1. *The trajectory vector and translation matrix*

The trajectory vector is initially determined by the positions of ES and AS, defining the initial position X_0, Y_0 and angles α_0 and β_0. The energy of the ion is given by E_0 (E_0 can be set to 0 in a first approach). The initial trajectory vector is then:

$$X_0 = \begin{pmatrix} X_0 \\ Y_0 \\ \alpha_0 \\ \beta_0 \\ E_0 \end{pmatrix}$$

More generally, trajectory vectors are written:

$$X = \begin{pmatrix} X \\ Y \\ \alpha \\ \beta \\ E \end{pmatrix}$$

The drift of the secondary ions through a distance L where no electromagnetic fields impact the ions is modeled by the translation matrix:

$$T = \begin{pmatrix} 1 & 0 & L & 0 & 0 \\ 0 & 1 & 0 & L & 0 \\ 0 & 0 & 1 & 0 & 0 \\ 0 & 0 & 0 & 1 & 0 \\ 0 & 0 & 0 & 0 & 1 \end{pmatrix}$$

such as the new coordinates X' after the translation are given by:

$$X' = \begin{pmatrix} X+\alpha L \\ Y+\beta L \\ \alpha \\ \beta \\ E \end{pmatrix} = T \cdot \begin{pmatrix} X \\ Y \\ \alpha \\ \beta \\ E \end{pmatrix} = T \cdot X$$

5.3.1.2. *The deviation plates C3 and C4*

The deviation plates C3 and C4 allow to modify the angles α and β of the ion beam. Their action is represented by the addition of the vector X_C to the trajectory vector:

$$X' = \begin{pmatrix} X \\ Y \\ \alpha+\alpha_C \\ \beta+\beta_C \\ E \end{pmatrix} = \begin{pmatrix} X \\ Y \\ \alpha \\ \beta \\ E \end{pmatrix} + \begin{pmatrix} 0 \\ 0 \\ \alpha_C \\ \beta_C \\ 0 \end{pmatrix} = X + X_C$$

Than angles α_C and β_C can be tuned on the C3 and C4 plates.

5.3.1.3. *The lenses LF4, LF5 and the quadrupole Q.*

The lenses LF4 and LF5 aim at taking back the ion trajectory to the main axis of the mass spectrometer on the X and Y direction, respectively. The quadrupole Q has the same action on both the X and Y direction simultaneously. The deviation angles induced by LF4, LF5 or Q are proportional to the distance of the beam position from the center of the lens/quadrupole in the lens/quadrupole plane. The transformation matrix of the quadrupole with a deviation factor q is:

$$Q = \begin{pmatrix} 1 & 0 & 0 & 0 & 0 \\ 0 & 1 & 0 & 0 & 0 \\ -1/q & 0 & 1 & 0 & 0 \\ 0 & -1/q & 0 & 1 & 0 \\ 0 & 0 & 0 & 0 & 1 \end{pmatrix}$$

with:

$$X' = \begin{pmatrix} X \\ Y \\ \alpha-X/q \\ \beta-Y/q \\ E \end{pmatrix} = Q \cdot \begin{pmatrix} X \\ Y \\ \alpha \\ \beta \\ E \end{pmatrix} = Q \cdot X$$

The lens LF4 has a similar action on the angle α while LF5 only acts on the angle β.

5.3.1.4. *The hexapole, electrostatic sector and the magnetic prism*

More complex ion optic devices such as the hexapole, the electrostatic sector and the magnetic prism are described by 5x25 matrixes that include second order terms coupling the X, Y, α, β and E coordinates. To compute the output trajectory vector, the input vector is extended to include second order terms (resulting in a 25 dimensions' vector). The transformation matrices associated with those objects were derived from the literature (Boerboom, 1972, 1987, 1995; Brown et al., 1964; Matsuo et al., 1982; Taya and Matsuda, 1972; Wollnik, 1965, 1967). Second order terms introduced by the action of these devices are responsible for second order aberrations that may induce undesirable cuts of the ion beam.

5.3.2. General features of the NS-ION-VISU program

5.3.2.1. *The initialization and monitoring of the ions' trajectories*

The NS-ION-VISU program is conceived to follow individual or multiple ion trajectories along the mass spectrometer. The initial ion beam(s) is defined thanks to the control panel (Figure 5-7, left). The angles α,

β of single ion beam trajectories are set by adjusting the position of AS. A square shape beam (square plus a cross), made of multiples ions, is implemented with the aim to follow the evolution of various ions' trajectories simultaneously (Figure 5-7, right). The number of ions in the square shape, its size and its main axis can be adjusted to explore various configurations.

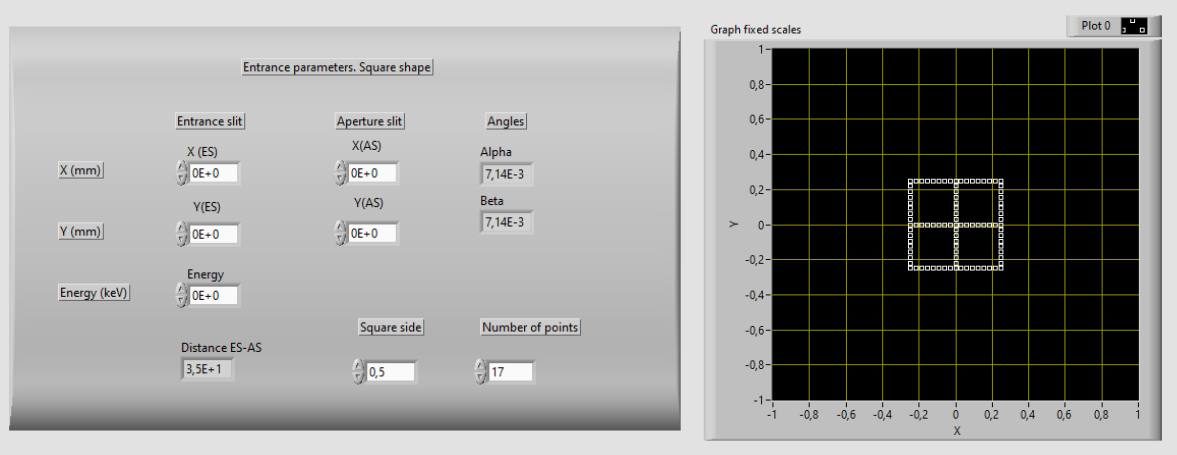

Figure 5-7: screenshots of the NS-ION-VISU initialization procedure. The initial properties of the ion beam are set in the left panel where the its position, angles and energy can be tuned. In order to investigate simultaneously several secondary ions' trajectories, a "square shape" mode has been implemented: multiple ion trajectories are implemented. The size of the square and the number of points can be adjusted in the field "square side" and "number of points". An interactive graph allows to see the resulting figure as imaged in the AS plan (right panel).

Several graphical interfaces are implemented in order to monitor the evolution of the ion beam at various stages. Figure 5-8 shows the images of the square shape ion beam set on Figure 5-7 at AS, EnS and ExS. Graphs of the components of the trajectory vectors at different locations are also available (e.g. X(AS) vs X(ExS) to visualize the second order aberration introduced by the mass spectrometer).

5.3.2.2. *The setting of the mass spectrometer components*

Each component of the MS can be tuned thanks to dedicated interfaces such as shown in Figure 5-9 in the case of the hexapole. The effect resulting for modifying a parameter is directly observable on the graphic interface. A shift of the ion optic devices on the (X,Y) plan can be introduced in order to take into account deviations of the mass spectrometer elements from the theoretical reference axis Z. Additional options were added in the program to cancel or activate second order terms. Third order terms were also implemented for the LF4, LF5 and quadrupole since experimental works on the NanoSIMS suggested that they might play an important role in the formation of aberrations, especially in the vertical direction. Their values can be adjusted empirically on the dedicated control panels.

5.3.2.3. *Use of the model*

The NS-ION-VISU labview program will be convenient for investigating the spatial extension of the ion beams. It can help to understand the occurrence of beam cuts at different locations in the NanoSIMS. Graphs on the ExS plan allow to quantify the importance of the vertical extension of the beam that may carry an important part of the ionic signals in some configurations. Comparing the prediction of the NS-

ION-VISU model with the experimental observations will be of a great help in tuning the NanoSIMS mass spectrometer.

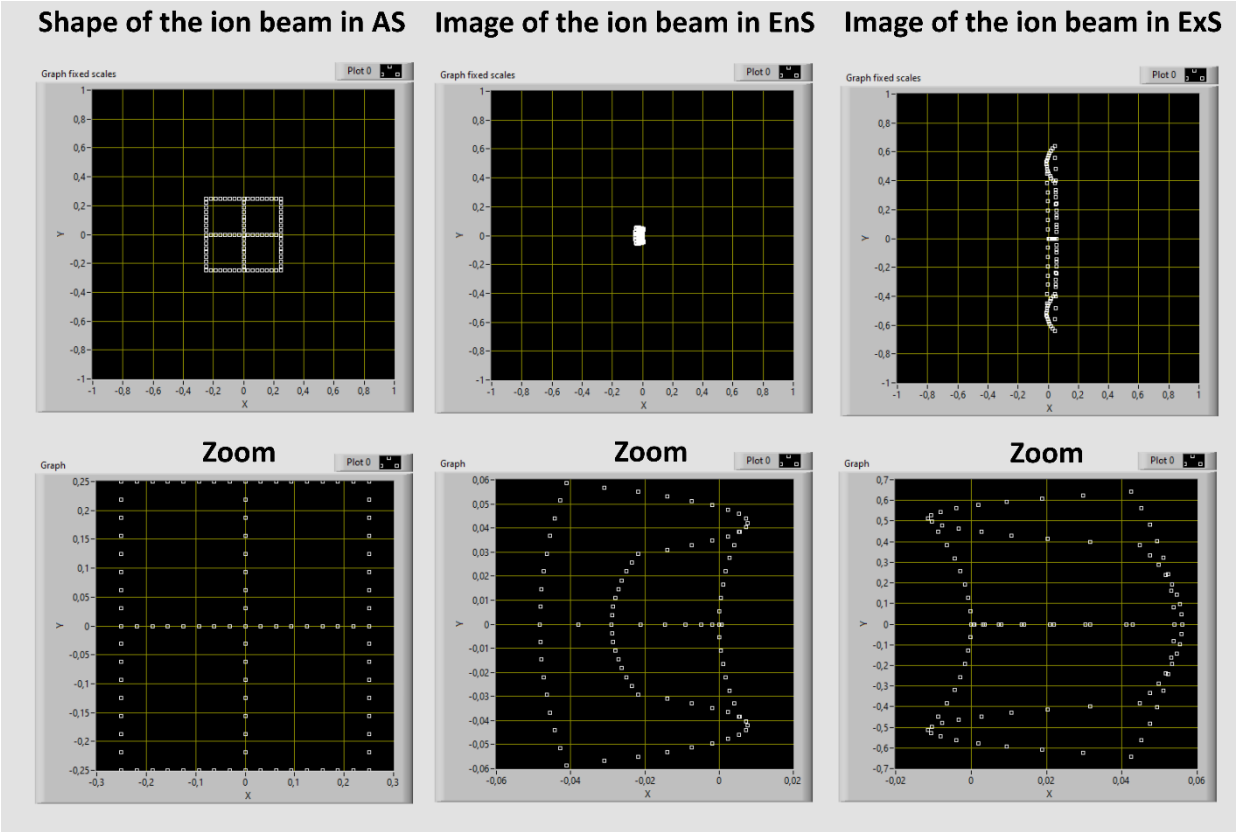

Figure 5-8: NS-ION-VISU images of the ions' trajectories in the (X,Y) plan of the aperture slit (AS, left), energy slit (EnS, center) and exit slit (ExS, right). Zoom can be made to see details of the shape of the ion beam (bottom row).

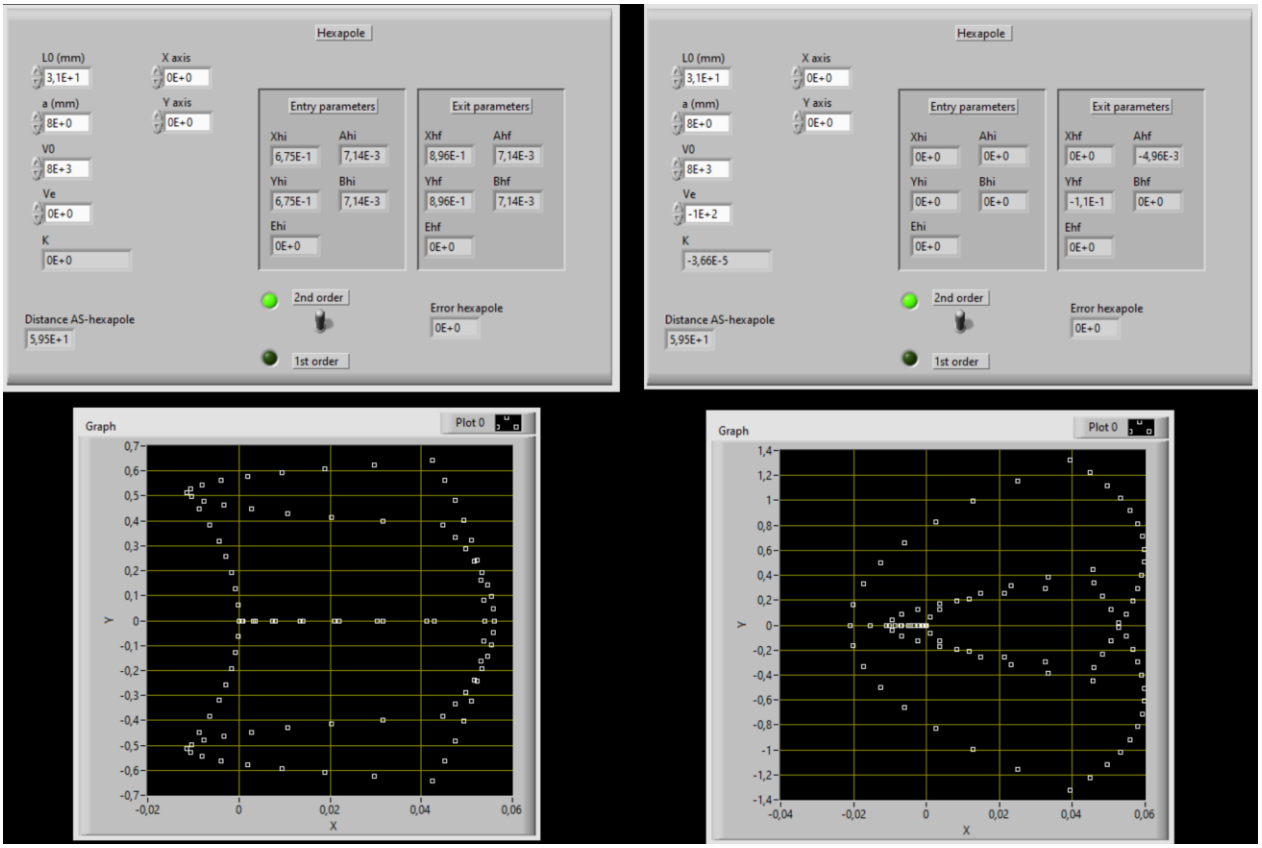

Figure 5-9: NS-ION-VISU images of the square shape ion beam initialized in Figure 5-7 visualized in ExS for two different voltages applied to the hexapole (left: Ve = 0; right Ve =-100). The action of the ion optics is observed in real time thanks to the graphs. It is worth noting that the left and right graphs are not plotted on the same scales. Modifications of the mass spectrometer settings can have large impacts on the shape and positions of the beam on the exit slit.

5.4 List of publications, oral presentations and posters

5.4.1. List of publications

- **J. Rojas**, J. Duprat, C. Engrand, E. Dartois, L. Delauche, M. Godard, M. Gounelle, J.D. Carrillo-Sánchez, P. Pokorný, J.M.C. Plane. *The micrometeorite flux at Dome C (Antarctica), monitoring the accretion of extraterrestrial dust on Earth*. Earth and Planetary Science Letters, Volume 560, 2021, 116794.

- E. Dartois, M. Chabot, T. Id Barkach, H. Rothard, P. Boduch, B. Augé, J. Duprat, **J. Rojas**. *Electronic sputtering of solid N2 by swift ions*. Nuclear Instruments and Methods in Physics Research, Section B: Beam Interactions with Materials and Atoms, Volume 485, 2020, 13-19.

5.4.2. List of oral presentations and posters

- **84th Annual Meeting of the Meteoritical Society** **August 2021**
  - Oral presentation
  - *Ion-Irradiation Induced Organic Refractory Residues from Nitrogen-rich Ices: Clues on the Isotopic Composition of the Organic Matter in UCAMMs.* J. Rojas, J. Duprat, E. Dartois, T-D. Wu, C. Engrand, B. Augé, Ph. Boduch, H. Rothard, M. Chabot, B. Guérin, J. Mathurin.

- **6th Workshop of the Scientific Committee on Antarctic Research (SCAR)** **September 2021**
  - Oral presentation
  - *The micrometeorite flux at Dome C (Antarctica) with the CONCORDIA collection.* J. Rojas, J. Duprat, C. Engrand, E. Dartois, L. Delauche, M. Godard, M. Gounelle, J.D. Carrillo-Sánchez, P. Pokorný, J.M.C. Plane.

- **51st Lunar and Planetary Science Conference** **March 2020**
  - Poster
  - *Isotopic Analyses of Ion Irradiation-Induced Organic Residues, Clues On the Formation of Organics from UCAMMs.* J. Rojas, J. Duprat, E. Dartois, T-D Wu, C. Engrand, B. Augé, J. Mathurin, B. Guerin, J-L. Guerquin-Kern, Ph. Boduch, H. Rothard.

- **51st Lunar and Planetary Science Conference** **March 2020**
  - Poster
  - *The Isotopic Diversity of UltraCarbonaceous Antarctic Micrometeorites, a Coupled NanoSIMS and AFMIR Study.* J. Rojas, J. Duprat, L. R. Nittler, J. Mathurin, E. Dartois, C. Engrand, N. Bardin, A. Dazzi, A. Deniset-Besseau, M. Godard, J-L. Guerquin-Kern, B. Guerin, S. Mostefaoui, L. Rémusat, R. M. Stroud, T-D Wu.

- **50th Lunar and Planetary Science Conference** **March 2019**
    - Poster
    - *Micrometeorite Mass Flux Measurements at Dome C, Antarctica.* J. Rojas, J. Duprat, C. Engrand, E. Dartois, L. Delauche, J.D. Carrillo-Sánchez, J.M.C. Plane.

5.4.3. Article: The micrometeorite flux at Dome C (Antarctica) (2021)

Earth and Planetary Science Letters 560 (2021) 116794

Contents lists available at ScienceDirect

Earth and Planetary Science Letters

www.elsevier.com/locate/epsl

The micrometeorite flux at Dome C (Antarctica), monitoring the accretion of extraterrestrial dust on Earth

J. Rojas [a,*], J. Duprat [b,a], C. Engrand [a], E. Dartois [c], L. Delauche [a], M. Godard [a,c], M. Gounelle [b], J.D. Carrillo-Sánchez [d,e], P. Pokorný [d,f], J.M.C. Plane [g]

[a] Université Paris-Saclay, CNRS/IN2P3, IJCLab, 91405 Orsay, France
[b] IMPMC, CNRS-MNHN-Sorbonne Universités, UMR7590, 57 rue Cuvier, 75005 Paris, France
[c] ISMO, CNRS, Univ. Paris Saclay, Bât 520, 91405 Orsay, France
[d] Department of Physics, Catholic University of America, 620 Michigan Ave., N.E., Washington, DC 20064, USA
[e] ITM Physics Laboratory, NASA Goddard Space Flight Center, Code 675, 8800 Greenbelt Rd., Greenbelt, MD 20771, USA
[f] Astrophysics Science Division, NASA Goddard Space Flight Center, Code 667, 8800 Greenbelt Rd., Greenbelt, MD, USA
[g] School of Chemistry, Univ. of Leeds, Leeds LS2 9JT, UK

ARTICLE INFO

Article history:
Received 17 September 2020
Received in revised form 21 January 2021
Accepted 29 January 2021
Available online 10 February 2021
Editor: F. Moynier

Keywords:
Antarctic micrometeorites
cosmic spherules
interplanetary dust particles
extraterrestrial flux
atmospheric entry
zodiacal cloud

ABSTRACT

The annual flux of extraterrestrial material on Earth is largely dominated by sub-millimetre particles. The mass distribution and absolute value of this cosmic dust flux at the Earth's surface is however still uncertain due to the difficulty in monitoring both the collection efficiency and the exposure parameter (i.e. the area-time product in m^2.yr). In this paper, we present results from micrometeorite collections originating from the vicinity of the CONCORDIA Station located at Dome C (Antarctica), where we performed several independent melts of large volumes of ultra-clean snow. The regular precipitation rate and the exceptional cleanliness of the snow from central Antarctica allow a unique control on both the exposure parameter and the collection efficiency. A total of 1280 unmelted micrometeorites (uMMs) and 808 cosmic spherules (CSs) with diameters ranging from 30 to 350 μm were identified. Within that size range, we measured mass fluxes of 3,0 $\mu g.m^{-2}.yr^{-1}$ for uMMs and 5,6 $\mu g.m^{-2}.yr^{-1}$ for CSs. Extrapolated to the global flux of particles in the 12-700 μm diameter range, the mass flux of dust at Earth's surface is $5,200 \pm ^{1500}_{1200}$ $tons.yr^{-1}$ ($1,600 \pm 500$ and $3,600 \pm ^{1000}_{700}$ $tons.yr^{-1}$ of uMMs and CSs, respectively). We indicate the statistical uncertainties expected for collections with exposure parameters in the range of 0.1 up to 10^5 m^2.yr. In addition, we estimated the flux of altered and unaltered carbon carried by heated and un-heated particles at Earth's surface. The mass distributions of CSs and uMMs larger than 100 μm are fairly well reproduced by the CABMOD-ZoDy model that includes melting and evaporation during atmospheric entry of the interplanetary dust flux. These numerical simulations suggest that most of the uMMs and CSs originate from Jupiter family comets and a minor part from the main asteroid belt. The total dust mass input before atmospheric entry is estimated at 15,000 $tons.yr^{-1}$. The existing discrepancy between the flux data and the model for uMMs below 100 μm suggests that small fragile uMMs may evade present day collections, and/or that the amount of small interplanetary particles at 1 AU may be smaller than expected.

Contents

* Corresponding author.
E-mail address: julien.Rojas@csnsm.in2p3.fr (J. Rojas).

https://doi.org/10.1016/j.epsl.2021.116794

1. Introduction

More than a century after the discovery of cosmic spherules in deep-sea sediments (Murray and Renard, 1891), the origin, composition and magnitude of the cosmic dust accretion on Earth is still a matter of debate. Extraterrestrial dust flux studies have been performed before atmospheric entry, while collections at the Earth's surface of both melted and unmelted micrometeorites were achieved in numerous locations such as the deep sea, deserts, sedimentary rocks and the polar ice caps (Yada et al. (2004), and reference therein). Although all these studies demonstrated that the annual extraterrestrial mass input on Earth is essentially carried by sub-millimetre particles, the precise mass distribution of particles down to a few tens of µm and its integrated value at the Earth surface remain uncertain (Plane, 2012). A first reason for these large uncertainties is the difficulty of collecting and identifying, with a well-controlled efficiency, extraterrestrial particles with diameters in the range of a few tens to hundreds of µm. A second reason is the difficulty of inferring a well-quantified exposure parameter (the area-time product, in m^2.yr). In order to provide an accurate constraint on the exposure parameter, that is the area of fall multiplied by the duration of the accumulation, it is mandatory to control both the volume of the host matrix of the particles (sediment, ice, snow, ...) from which the particles are extracted, and its local accumulation rate (in $g.m^{-2}.yr^{-1}$).

We present here results from a long-term collection of extraterrestrial particles performed during the last two decades in the vicinity of the CONCORDIA station located at Dome C, in the central regions of the Antarctic continent. The unique characteristics of Dome C and the specific collection protocol developed for this study allowed an accurate control maintained on both the collection efficiency, specifically in the lowest diameter range where the flux mass contribution was the least constrained, and on the exposure parameter. The comprehensive study presented in this work allows to perform several independent measurements of the absolute flux, and hence to obtain a better constraint on the size distribution of micrometeorites reaching the Earth's surface. We use these data to perform numerical simulations to quantify possible statistical biases impacting the flux estimation; this is done by considering a large range of exposure parameters. Finally, we compare the results obtained with this collection with data from previous studies at the Earth's surface and with observations and model predictions of the flux before atmospheric entry.

The size distribution of cosmic dust in the 10-1000 µm diameter range before atmospheric entry can be inferred using infrared observations of the Zodiacal Cloud (Ade et al., 2014; Hauser et al., 1984; Sykes, 1990), dust detectors in space (Love and Brownlee, 1993) or radar observations (Plane, 2012). During atmospheric entry, part of the flux is vaporized while another part survives as melted and unmelted particles. The complex physico-chemical processes occurring during atmospheric entry can be described using the CABMOD-ZoDy model (Carrillo-Sánchez et al., 2016; Nesvorný et al., 2011; Plane, 2012). In this study, the CABMOD-ZoDy model was updated to take into account the measured mass distribution. The comparison between the data from the CONCORDIA collection and the predictions of the updated CABMOD-ZoDy model allows light to be shed on the evolution of dust from the interplanetary reservoir, through the partially destructive processes at atmospheric entry to final deposition at the Earth's surface.

2. Materials and methods

2.1. Collection of micrometeorites at Dome C

The micrometeorites presented in this work were collected in the vicinity of the French-Italian CONCORDIA station at Dome C (hereafter DC). The station is located 1100 km inland on the high Antarctic plateau, at 75°06'S 123°20'E, 3200 m above sea level (Fig. 1). The specific location of this site offers unique preservation conditions for micrometeorites against aqueous alteration, and anthropic and terrestrial contaminations. To prevent potential anthropic contamination due to activities at the station, samples of snow were extracted in trenches with depths larger than 2 m, corresponding to years prior to 1995, which is the beginning of human presence in that area. The trenches were located several hundreds of meters to a few km upwind from the station. The snow was extracted from the trenches using saws and shovels that were previously cleaned with water and ethanol.

In this work, we derive results from particles extracted from 3 field campaigns that took place during the December-February period (austral summers) 2001-2002, 2005-2006 and 2015-2016. The average temperature in the trench was stable, ranging from −45 °C to −55 °C. The 2001-2002 collection (hereafter DC02) was performed in a 4 m deep trench located about 200 m from the station, at GPS coordinates (75°06′25.5″S 123°20′39.66″E). The snow was extracted from depths ranging from 2.0 to 3.5 m. The 2005-2006 collection (hereafter DC06) was performed in two trenches located at about 1 km from the station. The first trench was at GPS coordinates (75°06′35.46″S 123°20′39.66″E), the second trench was located 100 m from the first one in the SW direction. The extraction depths ranged from 3.3 to 4.3 m. The 2015-2016 collection (hereafter DC16) was performed in a trench located 3 km from the station at GPS coordinates (75°07′29.1″S 123°21′42.6″E), and the snow was extracted from depths ranging from 6.5 to 8.5 meters.

The snow was carried from the trench to the station in 60 litres high-density polyethylene closed barrels, with an average snow-per-barrel weight of about 15-20 kg. The snow was melted using a dedicated stainless-steel melter (Fig. 1) combined with a 35 kW propane gas boiler that gently warmed the stainless-steel tank via an external water bath. The melted snow water was sieved on a 30 µm mesh nylon filter for the DC02 and DC06 collections, and on a 20 µm mesh filter for the DC16 campaign. The filtering was made using gravity without water pumping to avoid putting mechanical stress on micrometeorites. The melter was a closed system

Fig. 1. Left: Location of the CONCORDIA station (Dome C, Antarctica). Centre: View of a trench at Dome C. Right: Monitoring the melting of the snow in the double tank melter for the extraction of micrometeorites.

Table 1
Number (a,b) and mass (c,d) of uMMs and CSs collected in each melt (before collection efficiency correction). Weight of snow in each melt (e) and corresponding exposure parameter S (f, see text). Numbers (g,h) and mass (i,j) of uMMs and CSs per kg of snow. The 4 first rows display data from the selected melts used to infer the absolute value of the flux. The additional set of particles is reported on row 7 (noted Add. Set) and the complete set on row 8 (noted All data) (see text).

	N uMM (a)	N CS (b)	Mass uMM (μg) (c)	Mass CS (μg) (d)	Snow weight (kg) (e)	S (m^2.yr) (f)	N(uMM)/kg of snow (g)	N(CS)/kg of snow (h)	M(uMM)/kg of snow (μg/kg) (i)	M(CS)/kg of snow (μg/kg) (j)
DC06-07	103	89	48	120	681	25.2	0.151	0.131	0.070	0.176
DC06-08	65	123	71	136	835	30.9	0.078	0.147	0.085	0.163
DC06-09	294	116	116	136	903	33.4	0.326	0.128	0.128	0.151
DC06-11	195	–	146	–	1142	42.3	0.171	–	0.128	–
uMMs Dataset #1	657	–	381	–	3561	131.9	0.185	–	0.107	–
CSs Dataset #1	–	328	–	392	2419	89.6	–	0.136	–	0.162
Add. set	623	480	368	647	–	–	–	–	–	–
All data	1280	808	749	1039	–	–	–	–	–	–

and the total weight of melted snow was obtained by measuring the volume of filtered water. The usual exposure of the particles to water was about 10 hours, and in rare cases longer, but always less than 3 days. Each melt was sieved on a single filter and extensive rinsing of the melter walls was performed to ensure maximum recovery of the particles. All filters were subsequently analysed in a dedicated clean room (ISO 7) under a clean hood at CSNSM (Centre de Sciences Nucléaires et de Sciences de la Matière, now IJCLab).

The most recent studies of the snow accumulation rate R_{snow} at Dome C indicate values ranging from 2.6 to 2.8 $g.cm^{-2}.yr^{-1}$ over the last century (Frezzotti et al., 2005; Le Meur et al., 2018). In the present work, we take an average value of $R_{snow} = (2.7 \pm 0.1)$ $g.cm^{-2}.yr^{-1}$. Considering an average mass density of snow of 300 $kg.m^{-3}$, the corresponding dates of fall of the particles range between 1920 and 1980.

We attributed to each melt an exposure parameter S, expressed in m^2.yr (Table 1). S is an area-time product (Peucker-Ehrenbrink et al., 2016) representing the accumulated quantity of snow trapping the particles. It is derived from the mass of snow in a melt M_{melt} (g) and the accumulation rate R_{snow} ($g.m^{-2}.yr^{-1}$) by:

$$S = \frac{M_{melt}}{R_{snow}}$$

The micrometeorite collection efficiency Q was monitored by introducing in the inner tank, before the snow-melting, a given number of coloured terrestrial sand and glass particles of two size ranges: 50-100 μm and 100-400 μm. The colours were different from one melt to another and between the two size ranges in order to identify possible size dependence in the collection efficiency as well as possible mixing between consecutive melts in the case of incomplete rinsing. These coloured particles were recovered and counted during the extraction procedure at CSNSM. The inferred average Q for these two size ranges was found to be $Q = (90 \pm 10)\%$ with no significant variations from one melt to another or between the two size ranges. This high Q was obtained by virtue of the dedicated design and polishing of the melter walls, and the extensive and careful rinsing of the overall apparatus after each melt. We systematically divided the number of micrometeorites recovered per melt by Q.

2.2. Micrometeorite identification and statistics

The filters were examined in the clean room at CSNSM under a binocular microscope and particles were manually extracted using dedicated fine brushes. The main contaminants observed in the filters were fibres from polar clothes and gloves, plastic chips from the barrels and from the tools used to extract and transport the snow. These contaminants were easily identified and removed during the filter sorting procedure.

Optical images of all extracted particles were taken and both their longest (a) and shortest (b) dimensions were documented, providing an equivalent diameter, D_{eq}, defined as:

$$D_{eq} = (a \times b \times b)^{\frac{1}{3}}$$

Although the size of the filters' mesh is 30 μm for DC02 and DC06, and 20 μm for DC16, some particles with D_{eq} slightly smaller than the mesh sizes were retrieved due to their non-spherical geometry and/or trapping within the textile fibres present in the filters. After extraction from the filters, all unmelted micrometeorites (uMMs) were fragmented. A fragment was then deposited on a carbon tape mounted on a one-inch aluminium disk for analytical scanning electron microscopy (SEM-EDX). Cosmic spherules (CSs) were mounted on carbon tape without fragmentation. All CS and uMM fragments were analysed with a SEM equipped with secondary and back-scattered electron detectors and an Energy Dispersive X-ray

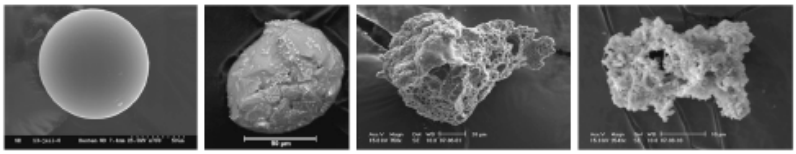

Fig. 2. Cosmic spherules and unmelted micrometeorites from CONCORDIA collection (SEM images). From left to right: glassy cosmic spherule, stony cosmic spherule, partially melted (scoriaceous) micrometeorite, unmelted fine-grained micrometeorite.

spectrometer (EDX) to determine the major elemental composition patterns. Examples of the various kinds of micrometeorites encountered are displayed in Fig. 2.

We performed a comprehensive search for CSs and uMMs contained in the filters of 3 selected melts from the DC06 fieldwork, hereafter referred as DC06-07, DC06-08, DC06-09. We performed a comprehensive search of only uMMs (not CSs) in one additional melt: DC06-11. The total numbers of uMMs and CSs in these selected melts are summarized as dataset #1, in Table 1.

Besides these selected melts in which the particle extraction was exhaustive, we recovered many CSs and uMMs from 19 other melts performed during the DC02, DC06 and DC16 campaigns. The collection protocols from these melts were identical to those of the selected melts. From these 19 additional melts, we extracted 480 CSs and 623 uMMs (see Table 1). The average number of particles per kg of snow in these additional melts was lower than that found in the selected melts mentioned above, due to incomplete scanning of the filters. However, the size distribution of particles within these additional melts was found compatible with that of the selected melts, indicating that there was no significant size bias between the two sets of data (dataset #1 and additional). We used the dataset #1 to infer the absolute value of the fluxes, and the complete set of data (dataset #1 + additional melts) to infer the global size and mass distributions. The global mass influx distributions were then normalized to the absolute values of the flux inferred from the selected melts.

The individual CS masses were estimated assuming an average density of 3.0 $g.cm^{-3}$ (Murrell et al., 1980). The density of an individual uMM depends on the composition and porosity of the particle. Different average densities have been reported for unmelted extraterrestrial particles originating from space-borne, stratospheric and Antarctic collections. In their detailed study of Antarctic micrometeorites, Yada et al. (2004) reported an average density of 1.0 $g.cm^{-3}$ for unmelted particles. The GIADA instrument onboard Rosetta measured an average mass density of 0.795 $g.cm^{-3}$ for cometary dust ejected from 67P-Churyumov-Gerasimenko (Fulle et al., 2016). Individual interplanetary dust particles collected in the stratosphere by NASA (IDPs) exhibit densities ranging from 0.6 up to 4.2 $g.cm^{-3}$ depending on their compact or fluffy nature (Joswiak et al., 2007). The range of densities reported in genuine interplanetary material provides clues for identifying their asteroidal or cometary origin (Consolmagno et al., 2008). Unmelted particles originating from the cometary reservoir most probably have higher porosity, i.e. densities around 0.8–1.0 $g.cm^{-3}$, while those originating from the asteroidal reservoir have lower porosity and an average density close to that reported for carbonaceous chondrites, i.e. 2.2 $g.cm^{-3}$ (Consolmagno et al., 2008; Flynn and Sutton, 1991; Joswiak et al., 2007; Love et al., 1994). In the following, we considered an average density of 1.5 $g.cm^{-3}$ for uMMs, that is intermediate between these two end-members. This average density is slightly higher than that used by Yada et al. (2004), but in agreement with the fact that we include partially melted grains in the set of uMMs particles. We will return to the discussion of uMM densities when comparing the measurements with the predictions from dynamical simulations (see 4.2).

Despite the high intrinsic Q, the normalized number of particles recovered per kg of snow in each filter exhibits substantial variations (see Table 1). These variations are much larger for uMMs than for CSs and are probably due to uncertainties in the handpicking extraction procedure itself, especially for particles in the lowest size range ($D_{eq} < 50$ µm) that are the most difficult to identify optically. While CSs are straightforward to identify as their spherical shape contrasts with neighbouring particles, the smallest uMMs are more difficult to identify and may escape binocular inspection.

In DC06-07, DC06-08 and DC06-09, 328 CSs were identified with D_{eq} ranging from 20 to 240 µm. The total weight of snow for these 3 melts was 2419 kg, equivalent to $S = 89.6 \pm 3.3$ m^2.yr (Table 1). The average mass of CSs per kg of snow is comparable in the 3 melts ranging from 0.151 $\mu g.kg^{-1}$ to 0.176 $\mu g.kg^{-1}$, with an average value of 0.163 $\mu g.kg^{-1}$. The average number of CSs per kg of snow for each melt ranges from 0.128 to 0.147 $CS.kg^{-1}$, with an average value of 0.135 $CS.kg^{-1}$.

In DC06-07, DC06-08, DC06-09 and DC06-11 we found 657 uMMs with D_{eq} ranging from 17 to 332 µm. The 4 melts correspond to a total of 3561 kg of snow, i.e. $S = 131.9 \pm 4.9$ m^2.yr. The average mass of uMMs per kg of snow for each melt ranges from 0.070 $\mu g.kg^{-1}$ to 0.128 $\mu g.kg^{-1}$, with an average value of 0.103 $\mu g.kg^{-1}$. The average number of uMMs recovered per kg of snow exhibits more pronounced relative variations, from 0.078 to 0.326 $uMMs.kg^{-1}$. As mentioned before, these large variations in counting are probably due to an incomplete recovery of the smallest particles within given melts. Since the smallest particles do not make a substantial contribution to the mass flux, this incomplete recovery has a limited impact on the inferred total uMMs mass flux.

The percentage of terrestrial grains extracted from the filters varied, depending on the cleanliness of each collection and on the completeness of the extraction. However, it was found to be below 50% in most cases: for melts in which a comprehensive search of all particles was performed, i.e. DC06-07, DC06-08 and DC06-09, it was respectively equal to 28%, 16% and 20%. This high extraterrestrial to terrestrial particle ratio (ET/T ratio) is due to the very low intrinsic abundance in the snow of terrestrial particles with $D_{eq} > 30$ µm; most terrestrial particles reaching the central regions of Antarctica having $D_{eq} < 5$ µm (Delmonte et al., 2004). The variation we observed in the ET/T ratio is thus directly related to contaminations occurring during the collection process itself.

In the results section, we present absolute flux values using the selected melts (dataset #1) comprising 657 uMMs and 328 CSs, and global distributions inferred from the full data set, amounting to 1280 uMMs and 808 CSs.

2.3. Dynamical and atmospheric entry simulations

Recently, Carrillo-Sánchez et al. (2020a, 2020b) combined the Chemical ABlation MODel (CABMOD, Vondrak et al. (2008)) with the Zodiacal Cloud Model (ZoDy, Nesvorný et al. (2010, 2011)) to quantify the integrated deposition rates of the main meteoritic metals in the upper atmospheres of Earth, Mars and Venus, along with the accretion rates of uMMs and CSs. The CABMOD model contains a detailed description of the physical and chemical pro-

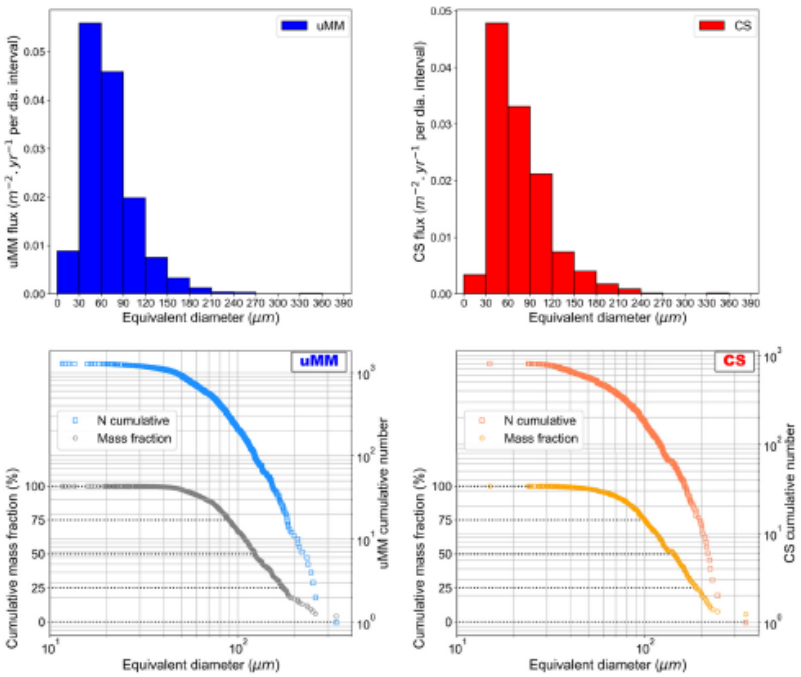

Fig. 3. (Top) Histograms of the uMM (blue) and CS (red) size distributions for the full dataset using equivalent diameter bins of 30 µm. (Bottom) Cumulative number and mass distributions of uMMs (blue and grey) and CSs (red and orange) for the full dataset. The numbers of particles are reported on the right vertical axis and mass fractions on the left vertical axis. (For interpretation of the colours in the figure(s), the reader is referred to the web version of this article.)

cesses of meteoric ablation for a particle of specified mass, velocity and zenith angle entering a planetary atmosphere. Meteoroids are assumed to be spherical with an initial bulk density of 2.2 $g.cm^{-3}$. (Consolmagno et al., 2008), whereas CSs exhibit a higher density, 3.2 $g.cm^{-3}$ (Kohout et al., 2014). The densities considered in these models are different from that used for the flux calculations from the DC data, however ablation is relatively insensitive to the choice of initial density, e.g. representative particles with a density of 2.2 $g.cm^{-3}$ ablate only 5% more efficiently than those with the same mass and a density of 1.5 $g.cm^{-3}$ (Vondrak et al., 2008). The uncertainties related to the particles density will be considered in the discussion section.

The ZoDy model describes the spatial distribution of position and velocity vectors of meteoroids in the inner solar system for masses between 10^{-3} and 5×10^{3} µg (particle diameters from 10 µm to 2 mm), and is calibrated to match various ground-based and space-borne data sets. ZoDy combines products of three major meteoroid source populations in the inner solar system: Jupiter-Family Comets (JFCs), Halley-type Comets (HTCs), and main-belt asteroids (MBAs). In this paper we updated the contributions from these populations using the new CS mass flux from DC collection. The contribution of each meteoroid population to the total mass flux at Earth in turn reflects the total budget of meteoroids in the solar system. Since the work of Nesvorný et al. (2011, 2010), JFCs have been considered the most abundant source of micrometeoroids, dominating 70-90% of Earth's mass flux. The size-frequency distribution (SFD) with which the meteoroids are produced is constrained by Planck satellite observations that only show the overall SFD of the Zodiacal Cloud (Ade et al., 2014), so this mostly provides insight into the SFD of the dominating JFC population and leaves the MBA and HTC SFDs much less constrained. This SFD predominantly influences the detected SFD at Earth. Finally, the collisional lifetime of meteoroids in the inner solar system influences the survivability of meteoroids during their pathway from their sources until they impact Earth; the lifetimes can be constrained using meteor orbit radars (Nesvorný et al., 2011; Pokorný et al., 2014).

3. Results

3.1. The size and mass distributions of cosmic spherules and unmelted micrometeorites

The size distributions of uMMs and CSs from the complete data set are reported in Fig. 3. The uMMs and CSs exhibit a maximum flux in number of particles at $D_{eq} = 50$ µm. The cumulative size distributions and mass fraction derived from the overall data set are also shown in Fig. 3. It is worth noting that a single power law cannot describe these cumulative size distributions.

In Fig. 4, we report the uMM and CS mass influx distributions from the selected melts (dataset #1) and the complete dataset using 30 µm diameter bins (in the upper panels of Fig. 4, grey and orange squares for the selected melts, and blue and red for the complete dataset) along with their fits assuming log-normal laws. The shape of the particle size distribution of the complete data set is compatible with that of the selected melts data (dataset #1), indicating that there is no size bias between the two sets of data (selected and additional).

The sum of the particles' masses relative to the exposure parameter in the selected melts is 2.7 $\mu g.m^{-2}.yr^{-1}$ for uMMs and 5.2 $\mu g.m^{-2}.yr^{-1}$ for CSs. These values, which are corrected from Q, provide the absolute mass flux within the 30 to 240 µm diameter range. The log-normal laws were normalized to fit the absolute

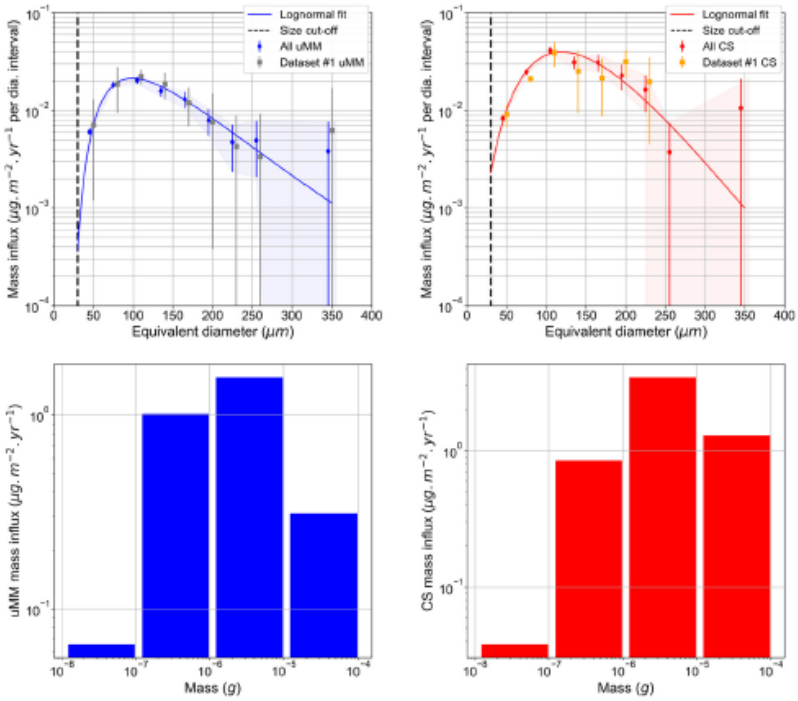

Fig. 4. (Top panels) Size distributions for uMMs (left) and CSs (right) given as mass influxes using 30 μm bins in equivalent diameter. The sizes distributions of uMMs and CSs from the selected melts (Dataset #1) are reported in grey and orange symbols, and that considering the full dataset in blue and red symbols. The uncertainties of the uMM and CS size distributions of the full dataset are outlined in the shaded areas. (bottom panels) Mass distributions for uMMs (left) and CSs (right) deduced from the full dataset, plotted with logarithmic bins in mass.

values from the selected melts (i.e. in the $D_{eq} = 30$ and 240 μm range). Data points from the selected and complete data sets are available in the supplementary table. If one restricts the analysis to melts for which both uMMs and CSs were comprehensively searched for (i.e. excluding DC06-11), as performed e.g. by (Yada et al., 2004), the total mass influx in the 30-240 μm diameter range is 7.7 $\mu g.m^{-2}.yr^{-1}$, a value consistent within uncertainties with that found above.

The total mass influx for uMMs and CS over a broader size range can then be obtained by integrating the normalized analytic log-normal fits. Considering a lower cut-off at 12 μm and an upper cut-off at 700 μm, the inferred global values for uMMs and CSs are $\Phi_{uMM} = 3.0 \pm 1.0$ $\mu g.m^{-2}.yr^{-1}$ and $\Phi_{CS} = 5.7 \pm 1.5$ $\mu g.m^{-2}.yr^{-1}$, respectively (see Table 1). The errors are derived assuming that the number of influx particles follows Poisson statistics. Extrapolating over the entire Earth's surface, the flux of uMMs is $1,600 \pm 500$ $tons.yr^{-1}$ (4.4 ± 1.4 $tons.d^{-1}$).

As detailed in the Table 2, about 75% of the uMMs and CSs in the CONCORDIA collection are within the 30-100 μm size range, but they account for less than 30% of the mass influx. uMMs and CSs with diameters ranging from 100 up to 200 μm account for 15% to 20% of the total numbers of particles, whereas they represent about half of the total mass influx. Finally, particles with $D_{eq} > 200$ μm are rare (a few % in numbers) but their contribution to the mass influx is significant, close to 20%. Due to their scarcity, the uncertainties on the contribution of these large particles to the mass influx are higher compared to the contribution in the 30-100 μm range. The extrapolation of the global CSs flux will be discussed below, taking into account the contribution of CSs with diameter greater than 200 μm (see discussion section).

The mass distributions of uMMs and CSs respectively reach their maxima at $D_{eq} = 100$ μm and $D_{eq} = 120$ μm. These sizes correspond to uMMs and CSs of masses around 0.8 μg and 2.7 μg (Fig. 4 bottom panels). For masses above 10 μg, uMMs contribute 10 times less than CSs to the mass influx. The total mass is not sensitive to the broad cut-off considered here (12 –700 μm) as long as their values are chosen sufficiently far from the mass distribution maxima. If one restricts the integration to the range in which particles are actually recovered, i.e. from 30 μm to 350 μm, the mass influxes are respectively 3.0 ± 1.0 $\mu g.m^{-2}.yr^{-1}$ and 5.6 ± 1.5 $\mu g.m^{-2}.yr^{-1}$ for uMMs and CSs, i.e. about 2% lower than the total mass flux inferred from the normalised log-normal fit over the whole size range for CSs (12-700 μm).

3.2. Statistical uncertainties related to the exposure parameter

We performed Monte-Carlo simulations to compare the dispersion of the mass influx observed in the different selected melts for both uMMs and CSs with that expected from statistical fluctuations induced by the finite number of micrometeorites collected in each melt. The procedure is detailed in the Annex. We considered a nominal flux Φ_0 given by Φ_{uMM} and Φ_{CS}, carried by particles following the total mass distributions of Fig. 4. The number of particles collected with a sufficiently large S ($S_{ref} = 10^5$ $m^2.yr$) was taken to be constant, and corresponded to the average number of uMMs and CSs per unit of surface and time within

Table 2
Numbers and mass of uMMs and CSs extracted from selected melts (Dataset#1) and from the complete data set (All) in 4 different size ranges (<30 µm, 30-100 µm, 100-200 µm, >200 µm). The 2 last rows indicate their corresponding contributions to the mass flux, taking into account the collection efficiency (see text). Particles in the 100-200 µm size range make the highest contribution to the mass flux. The uMM and CS distributions from the complete data set are normalized to the selected data set between 30 and 240 µm in diameter. The inferred total mass influx from both uMMs and CSs in the 30-240 µm range and on a global range (12-700 µm) are reported in the last columns. For CSs, we indicate their mass influx considering the Dome C data alone (noted †) and that (noted *) considering the merging of the distribution from this work with that from the SPWW collection (Taylor et al.) for diameters >200 µm (see section 4.1).

D	<30 µm		30 µm-100 µm		100 µm-200 µm		>200 µm		TOTAL	
	Dataset #1	*All*	*Dataset #1*	*All*	*Dataset #1*	*All*	*Dataset #1*	*All*	*Dataset #1*	*All*
N_{CS}	5	23	264	614	55	160	4	11	328	808
N_{uMM}	18	79	532	997	102	194	5	10	657	1280
M_{CS} (µg)	<1	1	112	292	228	624	67	224	407	1141
M_{uMM} (µg)	<1	1	126	243	144	357	65	116	335	717
Flux (with efficiency correction)									30-240 µm	12-700 µm
Φ_{CS} (µg.m^{-2}.yr^{-1}) (fit)	<0.1		1.3		3.3		1.1		5.2	5.7†/7.1*
Φ_{uMM} (µg.m^{-2}.yr^{-1}) (fit)	<0.1		0.9		1.5		0.6		2.7	3.0

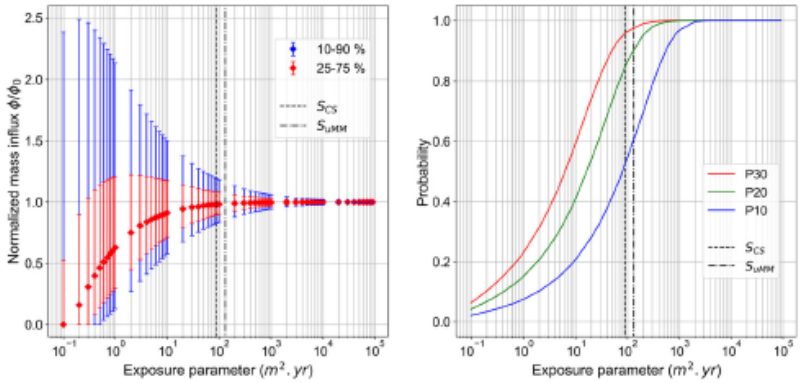

Fig. 5. (left) Variation of the ratio between the measured flux (Φ) and the nominal input flux Φ_0 for different percentile ranges and recovery probability as a function of the exposure parameter S. (right) P30, P20 and P10 are the probabilities (depending on the exposure parameter) that the nominal input flux is estimated to have with less than 30%, 20% or 10% uncertainty, respectively. The vertical dashed lines indicate the exposure parameters S_{CS} and S_{uMM} of the CS and uMM collection from this work.

the 12-700 µm diameter range: $N_{ref}(\text{uMM}) = 4.3$ m^{-2}.yr^{-1} and $N_{ref}(\text{CS}) = 3.6$ m^{-2}.yr^{-1}.

We then simulated the number N_{simu} of collected particles for a set of exposure parameter S. For each simulation, the N_{simu} value was sorted with a binomial law of parameters ($n = N_{ref}$, $p = \frac{S}{S_{ref}}$). The masses M_{simu} of the N_{simu} particles were subsequently sorted according to the global uMM and CS mass distributions reported in Fig. 4 and the numerical measured flux was computed as $\Phi = \frac{M_{simu}}{S}$. For each S, we simulated 10^5 measured fluxes Φ, to infer their median values and the 10-90% and 25-75% variations from the nominal flux Φ_0. The resulting distributions as function of S are presented in the Fig. 5 left panel, for S ranging from 10^{-1} to 10^5 m^2.yr. From these numerical simulations, we derive the probability for a collection of extraterrestrial particles in the 12-700 µm diameter range to estimate the real flux Φ_0 with a relative uncertainty $(\Phi - \Phi_0)/\Phi_0$ smaller than 10%, 20% and 30% (respectively P10, P20 and P30 on Fig. 5, right) as a function of S.

The accuracy of a flux measurement for a given S is monitored by the median Φ/Φ_0 ratio and its variations at the first and last quartile (25-75%) and decile (10-90%). For S lower than 1 m^2.yr, more than 75% of the simulated fluxes have relative uncertainties greater than 30% (Fig. 5, right), preventing reliable statistical measurements being achieved. The left panel in Fig. 5 also demonstrates that collections performed with S lower than a few m^2.yr are subjects to a systematic bias toward an underestimation of the real flux. This feature is due to the fact that, for such low S, the collection statistically misses a significant number of large size particles so that the masses collected tend to be lower than expected from the actual mass distribution. For S greater than a few tens of m^2.yr, this systematic effect becomes negligible (the median Φ/Φ_0 approaches 1), and variations on the measured flux substantially decrease.

For $S \approx 100$ m^2.yr, the probability is about 90% (about 2 σ) that the relative difference between the measured flux Φ and the real flux Φ_0 is less than 20%. We report on Fig. 5 the exposure parameter of the sum of the selected melts (dataset #1) for CSs and uMMs ($S = 89.6$ m^2.yr for CSs and $S = 131.9$ m^2.yr for uMMs). Fig. 5 is helpful for evaluating the statistical biases inherent in a collection for a given exposure parameter.

4. Discussion

Fig. 6 shows the distribution of extraterrestrial particles in near-Earth orbit, derived from hyper-velocity impacts of grains on the *Long Duration Exposure Facility satellite* (LDEF) panel (Love and Brownlee, 1993). Size measurements of the craters caused by high velocity sub-millimetre grain collisions with the panel were used to establish a size distribution of extraterrestrial particles before atmospheric entry. The integrated flux derived from this distribution is about one order of magnitude above that measured in this work. However, ground-based distributions can differ substantially from the pre-atmospheric distribution as a higher mass loss by ablation is expected for larger particles (Vondrak et al., 2008) and partial heating of grains should lead to a mass reduction, shift-

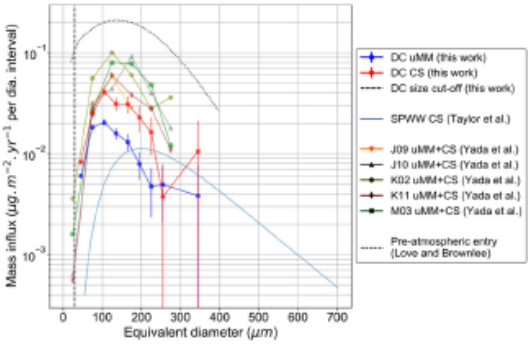

Fig. 6. Distributions of CSs and uMMs obtained from different Antarctic collections. DC uMM and CS: uMM and CS mass distributions from this study. SPWW CS: CS distribution from Taylor et al. (1998). Yada: distributions of mixed uMMs and CSs from Yada et al. (2004). Pre-atmospheric entry distribution of particles are from Love and Brownlee (1993).

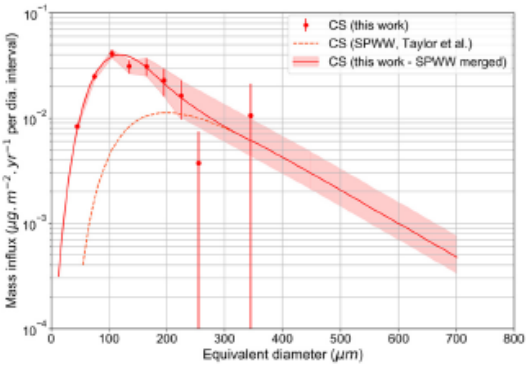

Fig. 7. Global distribution of CSs inferred from the DC data (this work) for $D <$ 200 μm and SPWW (Taylor et al., 1998) data for CS with $D >$ 200 μm. The two datasets consider fully melted particles (CSs) recovered from melted Antarctic snow. The shaded area outlines the uncertainties in the global distribution.

ing the distributions to smaller diameters. The degree of heating experienced by the particles during their atmospheric entry depends on various factors including the initial mass of the particles, their entry angle and velocity. The ablated metallic vapours oxidize and the resulting metal oxides, hydroxides and carbonates condense into nm-sized particles termed meteoric smoke (Plane et al., 2015). These particles are transported by the general atmospheric circulation until eventually deposited at the surface, where their flux can be evaluated by elemental or isotopic measurements (Gabrielli et al. (2004)).

4.1. Comparison with previous flux measurements at the Earth's surface

Several attempts have been made to determine the fluxes of uMMs and CSs in ice caps, deep-sea sediments and surface sediments (Genge et al., 2020; Murrell et al., 1980; Peucker-Ehrenbrink, 2001; Rochette et al., 2008; Suavet et al., 2009; Suttle and Folco, 2020; Taylor et al., 1998; Yada et al., 2004). Each estimation method has its own limitations. Here, we compare the results from the CONCORDIA collection to those obtained under comparable conditions, from Antarctic ice and snow (Taylor et al., 1998; Yada et al., 2004). Yada et al. (2004) performed 5 independent collections in 3 different blue ice fields around the Yamato Mountains (Antarctica). The mass distributions, including both CSs and uMMs, exhibit a maximum between 100 and 200 μm, slightly higher than that determined in the present work for uMMs (100 μm), and in relative agreement with that for CSs (120 μm). The global micrometeorite (CSs and uMMs) flux measured in this work is, within uncertainties, in broad agreement with that measured by Yada et al. (2004) in locations J09 and J01, but is lower than that in the 3 other locations. The variations between the flux measured in distinct blue ice field locations may be explained by the differences in snow accumulation rate and erosion leading to an uncertainty in the S parameter associated with each collection site, and/or by possible variations of the extraterrestrial influx over long periods of time (several 10 kyrs).

Taylor et al. (1998) performed a collection of CSs in the 50-700 μm diameter range from material recovered at the bottom of the South Pole water well (SPWW) of the South Pole Scott-Amundsen station, allowing a large number of particles with sizes mainly above a few hundred μm, up to 700 μm, to be obtained. More recently, Suttle and Folco (2020) reported a flux value and size distributions from thousands of extraterrestrial particles gathered from a collection performed in a sediment trap in the Transantarctic Mountains (TAM). The maximum in the size distributions inferred from both the SPWW and TAM collections is significantly larger ($D_{eq} = 200$-300 μm) than that reported in this work. The high statistics of both the SPWW and TAM collections for large particles allows a precise size distribution above 200 μm to be inferred. The contribution of smaller particles is more uncertain in these two collections due to lower statistics and uncertainties in the Q value. The transport and settling of the particles within the SPWW geometry and the accumulation in the TAM sediment trap are complex processes resulting in uncertainties in the S and thus on the absolute value of the CS flux. The work presented here is complementary to the SPWW and TAM measurements as it provides an accurate constraint on the absolute value of the flux and on its mass/size distribution for both uMMs and CSs in the lower size range, i.e. below 200 μm.

Only considering the DC data, we infer a total mass flux of $4,500 \pm 1,300$ tons.yr^{-1} (i.e. $1,600 \pm 500$ and $2,900 \pm 800$ tons.yr^{-1} of uMMs and CSs, respectively); however, that estimation should be considered as a lower limit of the flux value, since it does not include large CSs that make a significant contribution to the flux. In Fig. 7 we combine the DC distribution for the low size range with the SPWW distribution for the higher size range (>200 μm), in order to infer a global CS distribution in the overall diameter range (12-700 μm). The uncertainties (the envelope in red) were deduced by shifting vertically the SPWW distribution, but constraining its values to stay consistent with the DC CS experimental points at 195 μm and 225 μm. Such an error range on the absolute value of the SPWW flux is conceivable given the uncertainties on Q and S estimate for this collection. While the flux deduced only from the DC collection yielded a mass flux of $2,900 \pm 800$ tons.yr^{-1} for CSs, taking into account the SPWW data, the integration of the resulting distribution over the total range (12-700 μm) yields a total CS flux of $7.1 \pm^{2.0}_{1.4}$ μg.m^{-2}.yr^{-1} ($3600 \pm^{1000}_{700}$ tons.yr^{-1}) at the Earth's surface, which is a 25% increase of the flux derived from the DC CSs only.

Adding the total contribution of uMMs deduced above, we thus infer that the total mass flux of dust at Earth's surface is $5,200 \pm^{1500}_{1200}$ tons.yr^{-1} ($1,600 \pm 500$ and $3,600 \pm^{1000}_{700}$ tons.yr^{-1} of uMMs and CSs, respectively). This total mass flux of extraterrestrial particles at the Earth's surface is important for many astrophysical and geophysical issues (Peucker-Ehrenbrink and Schmitz, 2001), including the influx of elements on our planet. As far as the carbon (C) flux is concerned, one part reaches the Earth's surface carried by particles that did not suffer from high temperature at atmo-

spheric entry (unaltered C: C_{unalt}) while another part (altered C: C_{alt}) is carried by CSs or uMMs that suffered various degrees of heating at atmospheric entry. C_{unalt} is carried by the fine-grained uMMs (Fg-uMMs) and the Ultra-Carbonaceous Antarctic micrometeorites (UCAMMs) with extreme C concentrations (Dartois et al., 2013, 2018; Duprat et al., 2010; Yabuta et al., 2017). The Fg-uMM mass flux represents ~40% of the uMM flux and their C concentration, [C], is similar to that in carbonaceous chondritic material. Considering an average [C] = (3 ± 2) wt% (Matrajt et al., 2003), their global Carbon flux is (19 ± 13) tons.yr^{-1}. The C/Si ratio in UCAMMs varies over a wide range from 10 to 10^3 (Dartois et al., 2018) and thus an average is [C] = (60 ± 30) wt%. In the CONCORDIA collection, the mass of UCAMM is 0.7% of that of uMMs and so, their associated C flux is (7 ± 3) tons.yrs^{-1}. The resulting global flux of C_{unalt} is thus (26 ± 16) tons.yr^{-1}. Considering an average [C] of (0.6 ± 0.4) wt% for CSs and (1 ± 0.8) wt% for non-Fg uMMs (Matrajt et al., 2003), the inferred total flux of C_{alt} is (31 ± 22) tons.yr^{-1}, with ~70% carried by CSs and ~30% by partially heated uMMs. Given these uncertainties, the total C flux shows a quite large range of variation (20-100 tons.yr^{-1}), with up to half of this C flux is in form of C_{unalt}. Noticeably, the flux of C from UCAMMs represents about 25% of the C_{unalt} flux, indicating that a substantial part of the interplanetary organics reaching Earth surface can originate from the specific cometary reservoir that is the parent body of UCAMMs.

4.2. Comparison with dynamical and atmospheric entry simulations

The fluxes measured in this work together with the ZoDy and CABMOD models produce new constraints on the total dust flux encountered by Earth and the fraction that is ablated at atmospheric entry. For each dust population (JFCs, MBAs, and HTCs), particles are Monte-Carlo selected from the size and velocity distributions predicted by the ZoDy model. The CABMOD model then provides their Na and Fe ablation rates, and the size of the residual CSs (if complete ablation does not occur). To determine the mass contribution of the three cosmic dust sources, we follow the fitting procedure developed by Carrillo-Sánchez et al. (2020a, 2020b), using global mass input rates of Na and Fe in the Earth's atmosphere (above 87.5 km) of 0.3 ± 0.1 tons.d^{-1} and 2.3 ± 1.1 tons.d^{-1} (Gardner et al., 2014), respectively, and the CS flux inferred here (see Annex). Table S1 (Supporting Information) lists the partitioning of the mass influx from the three dust sources into uMMs, CSs, and the total ablated mass (the main elemental components are also shown). JFCs are the main mass contributor (>60%); the contribution from MBAs is lower (20%), about twice the previous estimate by Carrillo-Sánchez et al. (2020a, 2020b).

Fig. 8 shows that in the D_{eq} = 100-350 µm range, ZoDy dynamical simulations satisfactorily account for the proportion of CSs and uMMs determined from the CONCORDIA collection. In order to compare the measurements with the simulations, we indicate in Fig. 8 the range of variation (blue envelope) of the uMM mass distribution for density values between 0.8 g.cm^{-3} and 2.2 g.cm^{-3}, representing the cometary and asteroidal end-members discussed in Section 2.2. Considering these two end cases, the resulting average global uMM flux on Earth would be shifted by about 45%, to 800 or 2,400 tons.yr^{-1}, for average densities of 0.8 g.cm^{-3} and 2.2 g.cm^{-3}, respectively. In contrast, CABMOD-ZoDy predicts an overall uMM influx of 5,000 tons.yr^{-1} in the size range between 30 µm and 360 µm (see Table S1). As a result, the CS:uMM ratio of the CONCORDIA dataset in this size range (=2.0) is 3.4 times larger than the CABMOD-ZoDy estimate.

A marked discrepancy between the experimental and modelled distributions is observed for D_{eq} < 100 µm (Fig. 8), where the number of particles collected is much lower than that expected from the model. This difference may be explained by the occurrence of extremely fragile particles that fragment during atmospheric entry, and/or by the fact that particles in the smallest size range cannot be collected efficiently with the state-of-the-art collection techniques. An alternative explanation is that there is an underestimated process in the orbital evolution of dust, which leads to a lower number of small particles entering the Earth's atmosphere. However, meteoroids migrate toward Earth-crossing orbits via Poynting-Robertson drag (e.g., Burns et al., 1979), where the migration speed scales as $1/D_{eq}$. Since smaller meteoroids migrate faster, they are always more likely to survive the migration. Therefore, changing the collisional lifetime in the model will not diminish the number (or mass contribution) of small meteoroids but will mostly affect the relative contribution of larger meteoroids.

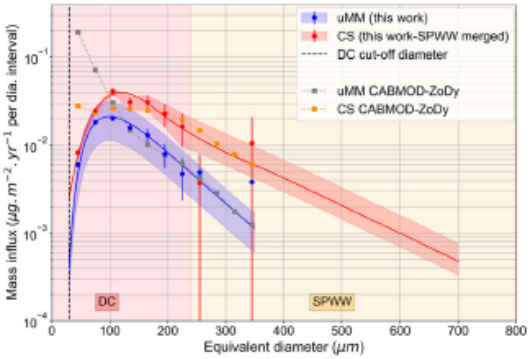

Fig. 8. Global mass influx distributions for uMMs (blue) and CSs (red) compared to the CABMOD-ZoDy estimate of uMMs (grey) and CSs (orange) at the Earth's surface. The blue envelope indicates the impact of the mass density of uMMs on the uMM mass influx distribution, the lower and upper limits of the envelope correspond to uMM average densities of 0.8 and 2.2 g.cm^{-3}.

With the hypotheses considered in this work, the inferred total dust mass before atmospheric entry deduced from the CABMOD-ZoDy modelling is ~15,000 tons.yr^{-1} (~40 tons.d^{-1}). Because of the difference between the CABMOD-ZoDy modelling and the measurements of uMMs flux below 100 µm, an uncertainty remains regarding the absolute value of this flux. Since the contribution of uMMs and CSs below 100 µm to the mass flux measured at DC is less than 30% of the total, the total dust mass before atmospheric entry should be in the range 10,000-20,000 tons.yr^{-1}, in agreement with previous studies (Plane (2012), Love and Brownlee, 1993). The flux of unaltered carbon deduced considering the progressive pyrolysis of carbon at atmospheric entry (Carrillo-Sánchez et al. (2020a, 2020b)), is ~12 tons.yr^{-1} (see Annex) that is compatible with the lower limit of that inferred from the CONCORDIA collection.

5. Conclusion

We performed several independent collections of micrometeorites from ultra-clean snow samples in the vicinity of the CONCORDIA Station at Dome C. The regular snow accumulation rate at Dome C allows to control the related exposure parameter (in m^2.yr) and the exceptional cleanliness of Dome C surface snow allows fragile particles to be recovered with high efficiency. 1280 uMMs and 808 CSs were collected from snow and subsequently characterized by conventional scanning electron microscopy techniques. This collection provides new constraints on size distributions of extraterrestrial dust reaching the Earth's surface, down to a size of 30 µm. The resulting mass distributions show well-defined maxima at D_{eq} = 100 µm for uMMs and D_{eq} = 120 µm for CSs,

slightly below estimates from previous studies. From four independents melts analyzed, we measured a total mass flux carried by particles in the 30-240 µm diameter range of 2.7 $\mu g.m^{-2}.yr^{-1}$ for uMMs and 5.2 $\mu g.m^{-2}yr^{-1}$ for CSs. The mass distributions were fitted with log-normal distributions. Comparison with previous measurements up to higher sizes (Taylor et al., 1998) enabled extrapolation to a global flux covering the 12-700 µm diameter range at Earth's surface of $(1,600 \pm 500)$ and $(3,600 \pm \frac{1000}{700})$ $tons.yr^{-1}$ for uMMs and CSs, respectively. The corresponding flux in carbon carried by these particles ranges from 20 to 100 $tons.yr^{-1}$. About 25% of the flux reaching Earth's surface as unaltered C is carried by particles with extreme carbon concentration (UCAMMs) originating from the cometary reservoir. We performed numerical simulations that can be used to evaluate the statistical uncertainties of future collections considering a wide range of exposure parameters from 0.1 to 10^5 $m^2.yr$.

New calculations were performed using the CABMOD-ZoDy model constrained by the CONCORDIA uMM and CS flux. These numerical simulations confirm that a majority of the incoming extraterrestrial flux are expected to originate from Jupiter family comets. The CABMOD-ZoDy model satisfactorily reproduces the CONCORDIA mass distribution of CSs and uMMs above 100 µm at the Earth's surface, and the total dust mass input before atmospheric entry is about 15,000 $tons.yr^{-1}$. Below 100 µm, the model calculations predict a flux of uMMs substantially greater than that measured in the CONCORDIA collection. This suggests several possibilities: the existence of highly fragile particles that would not be collected with the collection protocol in Dome C snow; fragmentation removal of a significant number of small particles before atmospheric entry; or that the actual amount of small interplanetary particles at 1 AU may be smaller than expected.

CRediT authorship contribution statement

J. Rojas: Writing – original draft, Writing – review & editing, Methodology. **J. Duprat:** Supervision, Writing – original draft, Writing – review & editing, Data curation, Field work, Funding acquisition. **C. Engrand:** Writing – review & editing, Data curation, Field work, Funding acquisition. **E. Dartois:** Writing – review & editing, Data curation, Field work. **L. Delauche:** Data curation, Field work. **M. Godard:** Writing – review & editing, Data curation, Field work. **M. Gounelle:** Writing – review & editing, Field work. **J.D. Carrillo-Sánchez:** Writing – original draft, Writing – review & editing, Data curation, Methodology. **P. Pokorný:** Writing – original draft, Writing – review & editing, Data curation, Methodology, **J.M.C. Plane:** Writing – original draft, Writing – review & editing, Data curation, Methodology.

Declaration of competing interest

The authors declare that they have no known competing financial interests or personal relationships that could have appeared to influence the work reported in this paper.

Acknowledgements

This work was performed at CONCORDIA Station (project #1120) and was supported by the French Polar Institute (IPEV). We are very grateful to IPEV for financial support and to IPEV and PNRA staff for logistical help. E. Le Meur kindly provided us helpful information on accumulation rates central Antarctic regions. We thank the anonymous referees for their thoughtful and constructive suggestions. This work was financially supported by ANR (Project COMETOR 18-CE31-0011), Region Ile de France (DIM-ACAV and ACAV+), PNP/INSU, CNES, IN2P3 and Labex P2IO. The CABMOD-ZoDy work was supported by the UK NERC (Grant Number NE/P001815/1) and NASA ISFM awards.

Appendix A. Supplementary material

Supplementary material related to this article can be found online at https://doi.org/10.1016/j.epsl.2021.116794. These data include the Google map of the most important areas described in this article.

References

Ade, P.A.R., Aghanim, N., Alves, M.I.R., Armitage-Caplan, C., Arnaud, M., Ashdown, M., Atrio-Barandela, F., Aumont, J., Aussel, H., Baccigalupi, C., Banday, A.J., Barreiro, R.B., Barrena, R., Bartelmann, M., Bartlett, J.G., Bartolo, N., Basak, S., Battaner, E., Battye, R., Benabed, K., Benoît, A., Benoit-Lévy, A., Bernard, J.-P., Bersanelli, M., Bertincourt, B., Bethermin, M., Bielewicz, P., Bikmaev, I., Blanchard, A., Bobin, J., Bock, J.J., Böhringer, H., Bonaldi, A., Bonavera, L., Bond, J.R., Borrill, J., Bouchet, F.R., Boulanger, F., Bourdin, H., Bowyer, J.W., Bridges, M., Brown, M.L., Bucher, M., Burenin, R., Burigana, C., Butler, R.C., Calabrese, E., Cappellini, B., Cardoso, J.-F., Carr, R., Carvalho, P., Casale, M., Castex, G., Catalano, A., Challinor, A., Chamballu, A., Chary, R.-R., Chen, X., Chiang, H.C., Chiang, L.-Y., Chon, G., Christensen, P.R., Churazov, E., Church, S., Clemens, M., Clements, D.L., Colombi, S., Colombo, L.P.L., Combet, C., Comis, B., Couchot, F., Coulais, A., Crill, B.P., Cruz, M., Curto, A., Cuttaia, F., Da Silva, A., Dahle, H., Danese, L., Davies, R.D., Davis, R.J., de Bernardis, P., de Rosa, A., de Zotti, G., Déchelette, T., Delabrouille, J., Delouis, J.-M., Démoclès, J., Désert, F.-X., Dick, J., Dickinson, C., Diego, J.M., Dolag, K., Dole, H., Donzelli, S., Doré, O., Douspis, M., Ducout, A., Dunkley, J., Dupac, X., Efstathiou, G., Elsner, F., Enßlin, T.A., Eriksen, H.K., Fabre, O., Falgarone, E., Falvella, M.C., Fantaye, Y., Fergusson, J., Filliard, C., Finelli, F., Flores-Cacho, I., Foley, S., Forni, O., Fosalba, P., Frailis, M., Fraisse, A.A., Franceschi, E., Freschi, M., Fromenteau, S., Frommert, M., Gaier, T.C., Galeotta, S., Gallegos, J., Galli, S., Gandolfo, B., Ganga, K., Gauthier, C., Génova-Santos, R.T., Ghosh, T., Giard, M., Giardino, G., Gilfanov, M., Girard, D., Giraud-Héraud, Y., Gjerløw, E., González-Nuevo, J., Górski, K.M., Gratton, S., Gregorio, A., Gruppuso, A., Gudmundsson, J.E., Haissinski, J., Hamann, J., Hansen, F.K., Hansen, M., Hanson, D., Harrison, D.L., Heavens, A., Helou, G., Hempel, A., Henrot-Versillé, S., Hernández-Monteagudo, C., Herranz, D., Hildebrandt, S.R., Hivon, E., Ho, S., Hobson, M., Holmes, W.A., Hornstrup, A., Hou, Z., Hovest, W., Huey, G., Huffenberger, K.M., Hurier, G., Ilić, S., Jaffe, A.H., Jaffe, T.R., Jasche, J., Jewell, J., Jones, W.C., Juvela, M., Kalberla, P., Kangaslahti, P., Keihänen, E., Kerp, J., Keskitalo, R., Khamitov, I., Kiiveri, K., Kim, J., Kisner, T.S., Kneissl, R., Knoche, J., Knox, L., Kunz, M., Kurki-Suonio, H., Lacasa, F., Lagache, G., Lähteenmäki, A., Lamarre, J.-M., Langer, M., Lasenby, A., Lattanzi, M., Laureijs, R.J., Lavabre, A., Lawrence, C.R., Le Jeune, M., Leach, S., Leahy, J.P., Leonardi, R., León-Tavares, J., Leroy, C., Lesgourgues, J., Lewis, A., Li, C., Liddle, A., Liguori, M., Lilje, P.B., Linden-Vørnle, M., Lindholm, V., López-Caniego, M., Lowe, S., Lubin, P.M., Macías-Pérez, J.F., MacTavish, C.J., Maffei, B., Maggio, G., Maino, D., Mandolesi, N., Mangilli, A., Marcos-Caballero, A., Marinucci, D., Maris, M., Marleau, F., Marshall, D.J., Martin, P.G., Martínez-González, E., Masi, S., Massardi, M., Matarrese, S., Matsumura, T., Matthai, F., Maurin, L., Mazzotta, P., McDonald, A., McBwen, J.D., McGehee, P., Mei, S., Meinhold, P.R., Melchiorri, A., Melin, J.-B., Mendes, L., Menegoni, E., Mennella, A., Migliaccio, M., Mikkelsen, K., Millea, M., Miniscalco, R., Mitra, S., Miville-Deschênes, M.-A., Molinari, D., Moneti, A., Montier, L., Morgante, G., Morisset, N., Mortlock, D., Moss, A., Munshi, D., Murphy, J.A., Naselsky, P., Nati, F., Natoli, P., Negrello, M., Nesvadba, N.P.H., Netterfield, C.B., Nørgaard-Nielsen, H.U., North, C., Noviello, F., Novikov, D., Novikov, I., O'Dwyer, I.J., Orieux, F., Osborne, S., O'Sullivan, C., Oxborrow, C.A., Paci, F., Pagano, L., Pajot, F., Paladini, R., Pandolfi, S., Paoletti, D., Partridge, B., Pasian, F., Patanchon, G., Paykari, P., Pearson, D., Pearson, T.J., Peel, M., Peiris, H.V., Perdereau, O., Perotto, L., Perrotta, F., Pettorino, V., Piacentini, F., Piat, M., Pierpaoli, E., Pietrobon, D., Plaszczynski, S., Platania, P., Pogosyan, D., Pointecouteau, E., Polenta, G., Ponthieu, N., Popa, L., Poutanen, T., Pratt, G.W., Prézeau, G., Prunet, S., Puget, J.-L., Pullen, A.R., Rachen, J.P., Racine, B., Rahlin, A., Räth, C., Reach, W.T., Rebolo, R., Reinecke, M., Remazeilles, M., Renault, C., Renzi, A., Riazuelo, A., Ricciardi, S., Riller, T., Ringeval, C., Ristorcelli, I., Robbers, G., Rocha, G., Roman, M., Rosset, C., Rossetti, M., Roudier, G., Rowan-Robinson, M., Rubiño-Martín, J.A., Ruiz-Granados, B., Rusholme, B., Salerno, E., Sandri, M., Sanselme, L., Santos, D., Savelainen, M., Savini, G., Schaefer, B.M., Schiavon, F., Scott, D., Seiffert, M.D., Serra, P., Shellard, E.P.S., Smith, K., Smoot, G.F., Souradeep, T., Spencer, L.D., Starck, J.-L., Stolyarov, V., Stompor, R., Sudiwala, R., Sunyaev, R., Sureau, F., Sutter, P., Sutton, D., Suur-Uski, A.-S., Sygnet, J.-F., Tauber, J.A., Tavagnacco, D., Taylor, D., Terenzi, L., Texier, D., Toffolatti, L., Tomasi, M., Torre, J.-P., Tristram, M., Tucci, M., Tuovinen, J., Türler, M., Tuttlebee, M., Umana, G., Valenziano, L., Valiviita, J., Van Tent, B., Varis, J., Vibert, L., Viel, M., Vielva, P., Villa, F., Vittorio, N., Wade, L.A., Wandelt, B.D., Watson, C., Watson, R., Wehus, I.K., Welikala, N., Weller, J., White, M., White, S.D.M., Wilkinson, A., Winkel, B., Xia, J.-Q., Yvon, D., Zacchei, A., Zibin, J.P., Zonca, A., 2014. Planck 2013 results. I. Overview of products and scientific results. Astron. Astrophys. 571, A1.

Burns, J.A., Lamy, P.L., Soter, S., 1979. Radiation forces on small particles in the solar system. Icarus 40, 1.

Carrillo-Sánchez, J.D., Nesvorný, D., Pokorný, P., Janches, D., Plane, J.M.C., 2016. Sources of cosmic dust in the Earth's atmosphere. Geophys. Res. Lett. 43, 11,979–11,986.
Carrillo-Sánchez, J.D., Gómez-Martín, J.C., Bones, D.L., Nesvorný, D., Pokorný, P., Benna, M., Flynn, G.J., Plane, J.M.C., 2020a. Cosmic dust fluxes in the atmospheres of Earth, Mars, and Venus. Icarus 335, 113395.
Carrillo Sánchez, J.D., Bones, D., Douglas, K.M., Flynn, G.J., Wirick, S., Fegley, B., Araki, T., Kaulich, B., Plane, J.M.C., 2020b. Injection of meteoric phosphorus into planetary atmospheres. Planet. Space Sci. 187, 104926.
Consolmagno, G.J., Britt, D.T., Macke, R.J., 2008. The significance of meteorite density and porosity. Chem. Erde 68, 1–29.
Dartois, E., Engrand, C., Brunetto, R., Duprat, J., Pino, T., Quirico, E., Remusat, L., Bardin, N., Briani, G., Mostefaoui, S., Morinaud, G., Crane, B., Szwec, N., Delauche, L., Jamme, F., Sandt, C., Dumas, P., 2013. UltraCarbonaceous Antarctic micrometeorites, probing the Solar System beyond the nitrogen snow-line. Icarus 224, 243–252.
Dartois, E., Engrand, C., Duprat, J., Godard, M., Charon, E., Delauche, L., Sandt, C., Borondics, F., 2018. Dome C ultracarbonaceous Antarctic micrometeorites. Infrared and Raman fingerprints. Astron. Astrophys. 609.
Delmonte, B., Petit, J.R., Andersen, K.K., Basile-Doelsch, I., Maggi, V., Lipenkov, V.Y., 2004. Dust size evidence for opposite regional atmospheric circulation changes over East Antarctica during the last climatic transition. Clim. Dyn. 23, 427.
Duprat, J., Dobrică, E., Engrand, C., Aléon, J., Marrocchi, Y., Mostefaoui, S., Meibom, A., Leroux, H., Rouzaud, J.-N., Gounelle, M., Robert, F., 2010. Extreme deuterium excesses in ultracarbonaceous micrometeorites from central Antarctic snow. Science 328, 742–745.
Flynn, G.J., Sutton, S.R., 1991. Cosmic dust particle densities: evidence for two populations of stony micrometeorites. Proc. Lunar Planet. Sci. Conf. 21, 541.
Frezzotti, M., Pourchet, M., Flora, O., Gandolfi, S., Gay, M., Urbini, S., Vincent, C., Becagli, S., Gragnani, R., Proposito, M., Severi, M., Traversi, R., Udisti, R., Fily, M., 2005. Spatial and temporal variability of snow accumulation in East Antarctica from traverse data. J. Glaciol. 51, 113–124.
Fulle, M., Della Corte, V., Rotundi, A., Rietmeijer, F.J.M., Green, S.F., Weissman, P., Accolla, M., Colangeli, L., Ferrari, M., Ivanovski, S., Lopez-Moreno, J.J., Epifani, E.M., Morales, R., Ortiz, J.L., Palomba, E., Palumbo, P., Rodriguez, J., Sordini, R., Zakharov, V., 2016. Comet 67P/Churyumov-Gerasimenko preserved the pebbles that formed planetesimals. Mon. Not. R. Astron. Soc. 462, S132.
Gabrielli, P., Barbante, C., Plane, J.M.C., Varga, A., Hong, S., Cozzi, G., Gaspari, V., Planchon, F.A.M., Cairns, W., Ferrari, C., Crutzen, P., Cescon, P., Boutron, C.F., 2004. Meteoric smoke fallout over the Holocene epoch revealed by iridium and platinum in Greenland ice. Nature 432, 1011–1014.
Gardner, C.S., Liu, A.Z., Marsh, D.R., Feng, W.H., Plane, J.M.C., 2014. Inferring the global cosmic dust influx to the Earth's atmosphere from lidar observations of the vertical flux of mesospheric Na. J. Geophys. Res. Space Phys. 119, 10.
Genge, M.J., Van Ginneken, M., Suttle, M.D., 2020. Micrometeorites: insights into the flux, sources and atmospheric entry of extraterrestrial dust at Earth. Planet. Space Sci. 187.
Hauser, M.G., Gillett, F.C., Low, F.J., Gautier, T.N., Beichman, C.A., Neugebauer, G., Aumann, H.H., Baud, B., Boggess, N., Emerson, J.P., Houck, J.R., Soifer, B.T., Walker, R.G., 1984. IRAS observations of the diffuse infrared background. Astrophys. J. 278, L15.
Joswiak, D.J., Brownlee, D.E., Pepin, R.O., Schlutter, D.J., 2007. Densities and mineralogy of cometary and asteroidal interplanetary dust particles collected in the stratosphere. In: Dust in Planetary Systems, p. 141.
Kohout, T., Kallonen, A., Suuronen, J.P., Rochette, P., Hutzler, A., Gattacceca, J., Badjukov, D.D., Skála, R., Böhmová, V., Čuda, J., 2014. Density, porosity, mineralogy, and internal structure of cosmic dust and alteration of its properties during high-velocity atmospheric entry. Meteorit. Planet. Sci. 49, 1157–1170.
Le Meur, E., Magand, O., Arnaud, L., Fily, M., Frezzotti, M., Cavitte, M., Mulvaney, R., Urbini, S., 2018. Spatial and temporal distributions of surface mass balance between Concordia and Vostok stations, Antarctica, from combined radar and ice core data: first results and detailed error analysis. Cryosphere 12, 1831–1850.
Love, S.G., Brownlee, D.E., 1993. A direct measurement of the terrestrial mass accretion rate of cosmic dust. Science 262, 550–553.
Love, S.G., Joswiak, D.J., Brownlee, D.E., 1994. Densities of stratospheric micrometeorites. Icarus 111, 227.
Matrajt, G., Taylor, S., Flynn, G., Brownlee, D., Joswiak, D., 2003. A nuclear microprobe study of the distribution and concentration of carbon and nitrogen in Murchison and Tagish Lake meteorites, Antarctic micrometeorites, and IDPs: implications for astrobiology. Meteorit. Planet. Sci. 38, 1585–1600.
Murray, J., Renard, A.F., 1891. Report on the Scientific Results of the Voyage of HMS Challenger during the Years 1873-76, Part 3, Deep-Sea Deposits. HMSO.
Murrell, M.T., Davis, P.A., Nishiizumi, K., Millard, H.T., 1980. Deep-sea spherules from Pacific clay: mass distribution and influx rate. Geochim. Cosmochim. Acta 44, 2067–2074.
Nesvorný, D., Janches, D., Vokrouhlický, D., Pokorný, P., Bottke, W.F., Jenniskens, P., 2011. Dynamical model for the zodiacal cloud and sporadic meteors. Astrophys. J. 743, 129.
Nesvorný, D., Jenniskens, P., Levison, H.F., Bottke, W.F., Vokrouhlický, D., Gounelle, M., 2010. Cometary origin of the zodiacal cloud and carbonaceous micrometeorites. Implications for hot debris disks. Astrophys. J. 713, 816.
Peucker-Ehrenbrink, B., 2001. Iridium and osmium as tracers of extraterrestrial matter in marine sediments. In: Accretion of Extraterrestrial Matter Throughout Earth's History. pp. 163–178.
Peucker-Ehrenbrink, B., Ravizza, G., Winckler, G., 2016. Geochemical tracers of extraterrestrial matter in sediments. Elements 12, 191–196.
Peucker-Ehrenbrink, B., Schmitz, B., 2001. Accretion of Extraterrestrial Matter Throughout Earth's History.
Plane, J.M.C., 2012. Cosmic dust in the Earth's atmosphere. Chem. Soc. Rev. 41, 6507–6518.
Plane, J.M.C., Feng, W., Dawkins, E.C.M., 2015. The mesosphere and metals: chemistry and changes. Chem. Rev. 115, 4497–4541.
Pokorný, P., Vokrouhlický, D., Nesvorný, D., Campbell-Brown, M., Brown, P., 2014. Dynamical model for the toroidal sporadic meteors. Astrophys. J. 789, 25.
Rochette, P., Folco, L., Suavet, C., van Ginneken, M., Gattacceca, J., Perchiazzi, N., Braucher, R., Harvey, R., 2008. Micrometeorites from the transantarctic mountains. Proc. Natl. Acad. Sci. USA 105, 18206–18211.
Suavet, C., Rochette, P., Kars, M., Gattacceca, J., Folco, L., Harvey, R.P., 2009. Statistical properties of the Transantarctic Mountains (TAM) micrometeorite collection. Polar Sci. 3, 100.
Suttle, M.D., Folco, L., 2020. The extraterrestrial dust flux: size distribution and mass contribution estimates inferred from the Transantarctic Mountains (TAM) micrometeorite collection. JGR Planets 125.
Sykes, M.V., 1990. Zodiacal dust bands: their relation to asteroid families. Icarus 85, 267.
Taylor, S., Lever, J.H., Harvey, R.P., 1998. Accretion rate of cosmic spherules measured at the South Pole. Nature 392, 899–903.
Vondrak, T., Plane, J.M.C., Broadley, S., Janches, D., 2008. A chemical model of meteoric ablation. Atmos. Chem. Phys. 8, 7015–7031.
Yabuta, H., Noguchi, T., Itoh, S., Nakamura, T., Miyake, A., Tsujimoto, S., Ohashi, N., Sakamoto, N., Hashiguchi, M., Abe, K.-i., Okubo, A., Kilcoyne, A.L.D., Tachibana, S., Okazaki, R., Terada, K., Ebihara, M., Nagahara, H., 2017. Formation of an ultracarbonaceous Antarctic micrometeorite through minimal aqueous alteration in a small porous icy body. Geochim. Cosmochim. Acta 214, 172–190.
Yada, T., Nakamura, T., Takaoka, N., Noguchi, T., Terada, K., Yano, H., Nakazawa, T., Kojima, H., 2004. The global accretion rate of extraterrestrial materials in the last glacial period estimated from the abundance of micrometeorites in Antarctic glacier ice. Earth Planets Space 56, 67–79.

5.4.4. News mentions

The work described in Chapiter 1 and published in EPSL was chosen for a national press communication by the CNRS. It was subsequently mentioned in various press and media in different countries.

Communiqué de press national du CNRS 8 Avril 2021.
https://www.cnrs.fr/fr/plus-de-5-000-tonnes-de-poussieres-extraterrestres-tombent-chaque-annee-sur-terre
https://www.cnrs.fr/en/more-5000-tons-extraterrestrial-dust-fall-earth-each-year

Scientific American, By Sarah Derouin, April 29, 2021
Antarctic study shows how much space dust hits Earth every year
https://www.scientificamerican.com/article/antarctic-study-shows-how-much-space-dust-hits-earth-every-year/#

Le Devoir, Canada, Pauline Gravel 24 avril 2021 Science
Ces 5200 tonnes de poussières cosmiques qui pleuvent sur la Terre chaque année
https://www.ledevoir.com/societe/science/599440/ces-poussieres-cosmiques-qui-pleuvent-sur-la-terre

United Academics Magazine, In Earth & Environment, Space & Physics ; April 16, 2021 Alexandra de Castro
Part of the dust accumulating in your house comes from outer space
https://www.ua-magazine.com/part-of-the-dust-accumulating-in-your-house-comes-from-outer-space/

Science News, by Sid Perkins April 15, 2021 at 7:00 am
Earth sweeps up 5,200 tons of extraterrestrial dust each year, Those micrometeorites come from both comets and asteroids
https://www.sciencenews.org/article/earth-extraterrestrial-space-dust-weight-meteorite

NRC (NL) Bruno van Wayenburg, 16 april 2021
Hoeveel zwaarder wordt de aarde door invallende meteorieten?
https://www.nrc.nl/nieuws/2021/04/16/hoeveel-zwaarder-wordt-de-aarde-door-invallende-meteorieten-a4040101

Popular science By Leto Sapunar April 19, 2021,
5,000 tons of ancient 'extraterrestrial dust' fall on Earth each year
https://www.popsci.com/story/space/space-dust-falls-to-earth/

Blog Astronomy Phil Plait Apr 12, 2021, 9:00 AM EDT
Is it dusty in here or is it just the 14 tons of meteorite dust that settles to Earth every day?

https://www.syfy.com/syfywire/is-it-dusty-in-here-or-is-it-just-the-14-tons-of-meteorite-dust-that-settles-to-earth-every

France Inter, Les Savanturiers, samedi 24 avril 2021 par Fabienne Chauvière
5000 tonnes de poussières extraterrestres
https://www.franceinter.fr/emissions/les-savanturiers/les-savanturiers-24-avril-2021

5.4.5. Abstract for 6th Workshop of the Scientific Committee on Antarctic Research (2021)

SCAR AAA 2021

Contribution ID: **24** Type: **not specified**

The micrometeorite flux at Dome C (Antarctica) with the CONCORDIA collection

mercredi 8 septembre 2021 13:15 (15 minutes)

The flux of extraterrestrial material on Earth is dominated by sub-millimeter particles, however the mass distribution and absolute value of this cosmic dust flux at the Earth surface is still uncertain due to the difficulty to monitor both the collection efficiency and the exposure parameter (*i.e.* the area-time product in $m^2.yr$). Thanks to the exceptional conditions encountered in central Antarctic regions, we recently succeeded to measure there the micrometeorite flux down to 30 µm (Rojas et al., 2021).

During the last 2 decades, we performed several field trips at Dome C to recover micrometeorites by melting and sieving large volume of ultra-clean snow using a dedicated protocol (IPEV program #1120, Duprat et al. (2010); Duprat et al. (2007)). The CONCORDIA station is operated by the French and Italian polar institutes (IPEV and PNRA) at Dome C (Antarctica). The regular precipitation rate and the exceptional cleanliness of the snow at Dome C allow a unique control on both the exposure parameter and the collection efficiency, mandatory to derive the micrometeorite flux.

The thorough inspection of the filters for many years allowed us to recover thousands of particles. Each one was individually imaged by Secondary Electron Microscopy and its bulk composition was determined by Energy-Dispersive X-ray spectra. Micrometeorites were classified in two main types: the unmelted micrometeorites (uMM) that went through the atmosphere without melting and the cosmic spherules (CSs) that have totally melted during the atmospheric entry. Based on the inferred size/mass distribution, we derived the statistical uncertainties expected for collections with exposure parameters ranging from 0.1 up to 10^5 $m^2.yr$. Within the 30-350 µm diameter range, we measured mass fluxes of 3.0 $\mu g.m^{-2}.yr^{-1}$ for uMMs and 5.6 $\mu g.m^{-2}.yr^{-1}$ for CSs. Extrapolated to the global flux of particles in the 12-700 µm diameter range, the corresponding annual mass flux of extraterrestrial dust at Earth surface is 5,200 $tons.yr^{-1}$ (1,600 and 3,600 $tons.yr^{-1}$ of uMMs and CSs, respectively). The flux of altered and unaltered carbon carried by heated and un-heated particles at Earth surface is estimated to range from 20 to 100 $tons.yr^{-1}$. The results obtained in this study allow to put constraints on the origin of the micrometeorite mass flux (Plane, 2012).

References:

Duprat, J., Dobrică, E., Engrand, C., Aléon, J., Marrocchi, Y., Mostefaoui, S., Meibom, A., Leroux, H., Rouzaud, J.-N., Gounelle, M., Robert, F., 2010. Extreme Deuterium Excesses in Ultracarbonaceous Micrometeorites from Central Antarctic Snow. Science 328, 742-745

Duprat, J., Engrand, C., Maurette, M., Kurat, G., Gounelle, M., Hammer, C., 2007. Micrometeorites from Central Antarctic snow: The CONCORDIA collection. Adv. Space Res. 39, 605-611.

Plane, J.M.C., 2012. Cosmic dust in the earth's atmosphere. Chemical Society Reviews 41, 6507-6518.

Rojas, J., Duprat, J., Engrand, C., Dartois, E., Delauche, L., Godard, M., Gounelle, M., Carrillo-Sánchez, J.D., Pokorný, P., Plane, J.M.C., 2021. The micrometeorite flux at Dome C (Antarctica), monitoring the accretion of extraterrestrial dust on Earth. Earth Planet. Sci. Lett. 560, 116794.

Auteurs principaux: ROJAS ARISPE, Julien (IJCLab/Université Paris-Saclay); DUPRAT, Jean (CNRS-MNHN); Dr ENGRAND, Cécile (Université Paris-Saclay, CNRS/IN2P3, IJCLab); Dr DARTOIS, Emmanuel (ISMO, CNRS, Univ. Paris Saclay); Mme DELAUCHE, Lucie (Université Paris-Saclay, CNRS/IN2P3, IJCLab); Dr GODARD, Marie (ISMO,

CNRS, Univ. Paris Saclay); Dr GOUNELLE, Matthieu (IMPMC, CNRS-MNHN-Sorbonne Universités); Dr CARRILLO-SÁNCHEZ, Juan Diego (Department of Physics, Catholic University of America); Dr POKORNÝ, Petr (Department of Physics, Catholic University of America); Prof. PLANE, John M.C. (School of Chemistry, Univ. of Leeds)

Orateur: ROJAS ARISPE, Julien (IJCLab/Université Paris-Saclay)

Session Classification: Talks 2

5.4.6. Abstract for the 50th Lunar and Planetary Sciences Conference (2019)

MICROMETEORITE MASS FLUX MEASUREMENTS AT DOME C, ANTARCTICA. J. Rojas[1] J. Duprat[1], C. Engrand[1], E. Dartois[2]. L. Delauche[1], J. D. Carillo-Sánchez[3], J. M. C. Plane[3] , [1]CSNSM, CNRS/Univ. Paris Sud, Univ. Paris-Saclay, Bat 104, 91405 Orsay, France (Julien.Rojas@csnsm.in2p3.fr), [2]ISMO, CNRS/Univ. Paris Sud, Univ. Paris-Saclay, Bat 520, 91405 Orsay, France, [3]School of Chemistry, University of Leeds, Leeds LS2 9JT, UK.

Introduction: Extraterrestrial mass input on Earth is largely dominated by particles in the 30-300 µm diameter range [1-2]. Measuring the size distribution of incoming particles in this range requires the combination of complementary techniques such as infrared observations of the Zodiacal Cloud [3], dust detectors in space [1], deep sea sediment measurements [4], and sample recovery campaigns in polar ice caps [5-8]. We present here an estimation of the extraterrestrial mass input that reaches Earth surface as particles (i.e. micrometeorites) based on the CONCORDIA collection and compare the measurements with simulations of the atmospheric entry of interplanetary dust [9]. We then used the inferred mass distributions to perform numerical simulations to evaluate the dependence of such measurements on the exposure parameter (*i.e.* the area-time product expressed in $m^2.yr$).

Samples & Methods: Micrometeorites were collected in the vicinity of the French Italian CONCORDIA station (S 75°, E 123°) located 1100 km inland on the high Antarctic plateau at Dome C (DC). Its specific location offers unique conservation conditions for micrometeorites against aqueous alteration as well as anthropic and terrestrial contaminations [10]. The set of micrometeorites presented in this work was collected during 3 field campaigns (2002, 2006, 2016). Ultra-clean snow was extracted from trenches at depths ranging from 3 m to 8 m, corresponding to times (~ 1950-60) before the establishment of the station. The snow was melted using a dedicated stainless steel double tank melter. The melter is a closed system and for each melt the volume of water was measured. The exposure parameter of a melt can be inferred from its volume of water considering the average local precipitation rate. Past studies have determined the precipitation rate to be stable over the last decades and equal to 3.5 ± 0.1 $g.cm^{-2}.yr^{-1}$ at DC [11]. The snow melt water was sieved with a 30 µm mesh filter without pumping to avoid mechanical stress on the micrometeorites. The duration of the exposure of particles to water was limited to 1 to 48h. We selected melts where the volume of water of each melt was ranging from 170 to 2100 liters. We manually handpicked under a binocular microscope the particles in each filter, setting aside only obvious terrestrial contaminations (mainly fibers and plastic chips arising from the collect means). Optical pictures of all the extracted particles were taken and their long and short axes measured. The particles were subsequently fragmented and analyzed with a Scanning Electron Microscope equipped with an Energy Dispersive X-ray Spectrometer to obtain their major element compositional pattern and assess their extraterrestrial origin. For this study, we considered two types of extraterrestrial particles: unmelted MicroMeteorites (MMs) and Cosmic Spherules (CS, spherical melted grains).

The flux values were corrected for recovery efficiency that was monitored by introducing in the melter a given number of small (*i.e.* 50-100 µm and 100-400 µm) colored particles before the melting, and counting them on the filter after sieving, during the particle extraction procedure. The inferred average recovery efficiency was close to unity (90 ± 10)% and we did not observe any significant efficiency variations from one melt to another nor between the two size ranges of the calibration particles.

A comprehensive search for all extraterrestrial particles was performed in 3 melts for both MMs and CSs plus 1 additional large melt where only MMs were fully extracted. This selected sub-set contains a total of 657 MMs with size ranging from 17 µm to 330 µm extracted from a total weight of snow of ~ 3600 kg (*i.e.* a total equivalent exposure parameter of 102 m^2.yr). The extraction of CSs leads to a total of 328 particles with size ranging from 25 µm to 230 µm, from a total weight of snow of ~ 2400 kg, corresponding to an equivalent exposure parameter of 69 m^2.yr. The recovery of particles with equivalent diameters lower than the size of the filter mesh (30 µm) is due to the irregular shape of the particles and/or trapping within the few textile fibers that accumulated in the filters. The number and inferred mass of MMs or CSs per kg of snow is similar in each melt, and this value is higher than that recorded in filters where only partial sorting was performed, confirming the comprehensive extraction of both MMs and CSs in this sub-set.

Beside these 4 selected melts, we also report here the results from additional melts in which we extracted and characterized 623 MMs and 480 CSs. The size distribution of the particles from the full data set was found to be similar to that obtained with the selected melt sub-set indicating that the extraction from the additional dataset did not favour a specific size range. We normalized the size distribution of the additional melts to that of the selected melts in order to obtain size distributions including all the particles available.

Dynamical simulations were performed to model the motion and structural evolution of extraterrestrial

particles from the interplanetary medium to the Earth surface. For this purpose, the Chemical Ablation MODel (CABMOD) was combined with the Zodiacal Cloud Model (ZoDy), which is constrained by IR observations made by the IRAS and PLANCK satellites [9].

Results & Discussion: The global DC mass flux distribution was calculated assuming an average density of 1.5 for MMs and 3 for CS (Figure 1), leading to an integrated mass influx of 3.9 ± 1.0 $\mu g.m^{-2}.yr^{-1}$ for MMs and 8.5 ± 2.0 $\mu g.m^{-2}.yr^{-1}$ for CSs. Scaled to the entire Earth's surface these fluxes represent 2,000 ± 500 $tons.yr^{-1}$ for MMs, 4,400 ± 1,000 $tons.yr^{-1}$ for CS and a total mass input of 6,400 ± 1,100 $tons.yr^{-1}$. The CS distribution peaks at a particle size around 120 µm, whereas the MM distribution peaks at slightly lower sizes (~90 µm). For large particles (above ~150 µm) the mass influx is dominated by CSs. For smaller particles (below ~ 100 µm) the contributions of MMs and CSs are comparable within uncertainties.

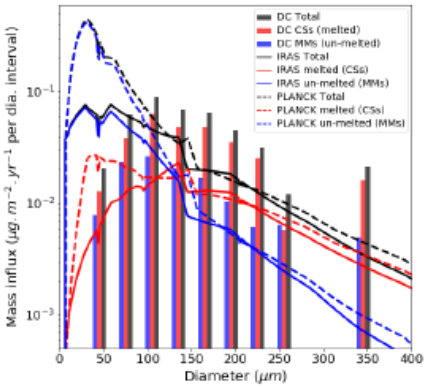

Figure 1 : Mass distribution of particles collected in Dome C (DC) snow (total, melted, and unmelted) compared to expectations inferred from IRAS and PLANCK observations. Data are plotted using 30 µm bin widths for DC and 1 µm bin widths for IRAS and PLANCK (the ordinates are normalized to the bin width).

The mass inputs deduced from IRAS are 3,500 $tons.yr^{-1}$ for unmelted particles (MMs) and ~1,900 $tons.yr^{-1}$ for melted (CSs) whereas the inputs deduced from PLANCK are 10,100 $tons.yr^{-1}$ for MMs and 2,500 $tons.yr^{-1}$ for CSs. Given the overall uncertainties, there is a reasonable match, within a factor of 2, between the integrated flux of both melted and unmelted particles measured at DC and that inferred from IRAS. By contrast, the integrated flux inferred from PLANCK data is close to that of DC only for melted particles but well above for unmelted particles, by about a factor of 5. Both dynamical simulations tends to predict a substantially greater amount of unmelted particles (mainly carried by MMs with sizes < 100 µm) than observed in DC measurements.

We used the Dome C mass distributions to model the dependency of the measured flux with the exposure parameter. The results reported in Figure 2 show that flux estimations based on exposure parameters lower than 10 $m^2.yr$ will over- or under-estimate by at least 20% the real flux input in more than 50% of the cases. Exposure parameters above 100 $m^2.yr$ are mandatory to limit the statistical errors to less than 10%.

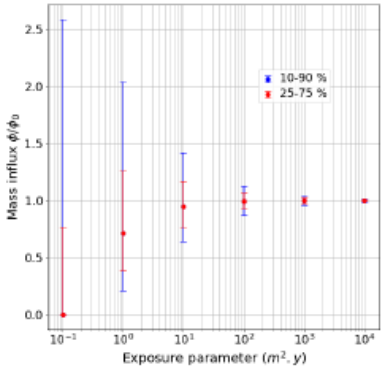

Figure 2 : Numerical simulation of the median values of the Measured/True fluxes ratio against exposure parameter. Red and blue are the 25-75% and 10-90% quantiles.

Acknowledgements: This study was funded by the ANR project OGRESSE and COMETOR, DIM-ACAV, CNRS (Defi Origines), CNES, PNP and PCMI. The collection of MMs at CONCORDIA station was supported by IPEV and PNRA.

References: [1] Love, S.G. and D.E. Brownlee, Science 1993. **262**: 550-553. [2] Plane, J.M.C., Chem. Soc. Rev. 2012. **41**: 6507-6518. [3] Nesvorny, D., *AAS/Div. Planet. Sci. Meeting #41*. 2009. [4] Peucker-Ehrenbrink, B. GCA 1996. **60**: 3187-3196. [5] Maurette, M., et al., Nature 1987. **328**: 699-702. [6] Taylor, S., et al., Nature 1998. **392**: 899-903. [7] Yada, T., et al., EPS 2004. **56**: 67-79. [8] Duprat, J., et al., Meteoritics 2006. **41**: 5239. [9] Carrillo-Sánchez, J.D., et al., GRL 2016. **43**: 11,979-11,986. [10] Duprat, J., et al., Adv. Space Res. 2007. **39**: 605-611. [11] Petit, J.R., et al., JGR 1982. **87**: 4301-4308.

5.4.7. Abstract for the 51st Lunar and Planetary Sciences Conference (2020)

ISOTOPIC ANALYSES OF ION IRRADIATION-INDUCED ORGANIC RESIDUES, CLUES ON THE FORMATION OF ORGANICS FROM UCAMMS. J. Rojas[1], J. Duprat[1], E. Dartois[2], T-D Wu[3], C. Engrand[1], B. Augé[4], J. Mathurin[1], B. Guerin[1], J-L. Guerquin-Kern[3], Ph. Boduch[5], H. Rothard[5]. [1]Univ. Paris-Saclay, CNRS, IJCLab, 91405 Orsay, France (Julien.Rojas@csnsm.in2p3.fr); [2]Univ. Paris-Saclay, CNRS, ISMO, 91405 Orsay, France, [3]Institut Curie, PSL Research University, INSERM, U1196, 91405 Orsay, France, [4]IPAG UGA/CNRS Grenoble France, [5]CIMAP (CEA/CNRS/ENSICAEN/Université de Caen-Basse Normandie), BP 5133, 14070 Caen Cedex 05, France.

Introduction: UltraCarbonaceous Antarctic MicroMeteorites (UCAMMs) are interplanetary dust particles that exhibit large concentrations of organic matter with high N concentrations and extreme D/H ratios [1-4]. The mineralogy, the elemental and isotopic composition of UCAMMs indicate that they most likely originate from the cometary reservoir [1, 2, 5]. Most UCAMMs exhibit large variations on D/H, $^{15}N/^{14}N$ and $^{13}C/^{12}C$ ratios at the micron or sub-micron scale. These isotopic fractionations are carried by the organic matter and their origin is still an open question.

We showed that the precursors of UCAMMs can be formed by irradiation with high energy ions of N-rich ice mixtures with hydrocarbons, a process likely to take place at the surface of icy bodies orbiting beyond a nitrogen snow line and irradiated by galactic cosmic rays [2, 6]. Recent experimental simulations showed that the irradiation itself does not induce large D fractionation, but that the refractory organic residue resulting from irradiation of isotopically heterogeneous ice mixtures can exhibit large D/H spatial variation at the micron scale [7]. We performed a new series of experiments on D, ^{15}N and ^{13}C labelled ices to study the transmission of the isotopic labelled ice layers to the irradiation-induced residue.

Material and method: Irradiation experiments of ices were conducted with the low-energy beam (Irrsud, 0.5-1 MeV/n) at GANIL (Caen, France). We used the IGLIAS experimental set-up [8] which allows to deposit and irradiate complex ice films mixtures on substrate windows held at temperatures ranging from 8K to 300K (Figure 1). The evolution of the ices during the irradiation was monitored *in situ* with a Brucker Vertex 70v Fourier transform infrared (FTIR) spectrometer. The gas mixtures deposited are controlled with a Quadrupole Mass Spectrometer (QMS). We followed the same protocol as described in [7]. We first irradiated a mixture of ices made of two equally thick layers of $^{14}N_2$-CH_4 (90:10) of about 5 µm each surrounding a thin layer of isotopically labeled (in D, ^{13}C and ^{15}N) ice with a thickness of about 0.2 µm. The ice films were formed by gas injections on ZnSe windows at 8K. The thickness of the central isotopically labeled ice layer was estimated from the volume of gases injected (i.e. 2% of the total thickness). The overall thickness of the ice sandwiches (11 µm) were determined from the interference fringe patterns on the IR spectra taken in situ [7, 9]. In the first experiment (hereafter referred as sandwich Sd#1) the isotopically labeled central ice layer was $^{15}N_2$-CD_4 (90:10). In the second experiment (sandwich Sd#2) the central isotopically labeled layer was $^{15}N_2$-CD_4-^{13}CO (80:10:10).

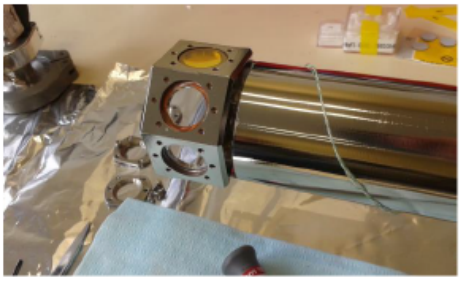

Figure 1 : Target windows holder of the IGLIAS set-up. The isotopic labeled gases are condensed at 8K on each window prior to irradiation. ZnSe IR-transparent windows (yellow window covered with a brown residue) are used, allowing IR spectroscopy monitoring during the irradiation.

The ices sandwiches were irradiated at 8K with 33 MeV Ni^{9+} ions up to a fluence of 10^{13} ions/cm². The duration of each irradiation was about 2 hours. The ion projected range estimated with the SRIM code [10] was about 23 µm, i.e. larger than the sample total thickness, allowing the high energy Ni^{9+} ions to interact with the entire ice film. At the end of the irradiation, we applied a very slow temperature ramp to the samples (0.1 K/min from 8K to 70K, 0.2 K/min from 70K to 80K, 0.3 K/min from 80K to 140K and 0.5 K/min from 140K to 300K) to allow the remaining ice to sublimate and to bring the irradiation induced residue to room temperature. IR and mass spectra were recorded by the FTIR spectrometer and the QMS prior and along each irradiation to monitor the evolution of the sample. During the warming up of the sample, a FTIR spectrum of Sd#1 sample was acquired every 15 minutes.

After irradiation and annealing to room temperature, the substrate windows were extracted from the IGLIAS chamber and mounted on a dedicated holder to perform NanoSIMS analyses on the refractory or-

ganic residue. We deposited a 40 nm thick gold coating on the windows to allow efficient charge evacuations during NanoSIMS measurements. Measurements were made with a 7 pA Cs^+ primary beam on 20×20µm² (256×256 pixels) areas in multi-frames acquisition mode with a dwell time of 33 ms per frame. For the analysis of the Sd#1 residue, the 4 detectors were set to detect simultaneously CH^-, CD^-, $^{12}C^{14}N^-$ and $^{12}C^{15}N^-$ secondary ions. For the Sd#2 residue, we used 3 detectors collecting CH^-, CD^-, $^{12}C^{14}N^-$ secondary ions and the last one, set at *m/z=27*, was set to a peak switching mode, alternatively counting $^{12}C^{15}N^-$ and $^{13}C^{14}N^-$ secondary ions. Thereby, we acquired quasi-simultaneous maps of $^{12}C^{15}N^-$ and $^{13}C^{14}N^-$ emissions, allowing a direct comparison of the hydrogen, carbon and nitrogen isotopic spatial variations. We performed additional measurements of $^{13}C/^{12}C$ ratios using both $^{13}C^{14}N^-/^{12}C^{14}N^-$ and the $^{13}C^{12}C^-/^{12}C_2^-$ secondary ions ratios to ensure that the contribution of $^{11}B^{16}O^-$ to the $^{13}C^{14}N^-$ signal at *m/z=27* was negligible. We performed 5 maps on Sd#1 and 9 maps on Sd#2. On each analysis, about 300 consecutive frames were acquired prior to the apparition of large charging effects observed due to the erosion of the residue and the insulating nature of the ZnSe windows.

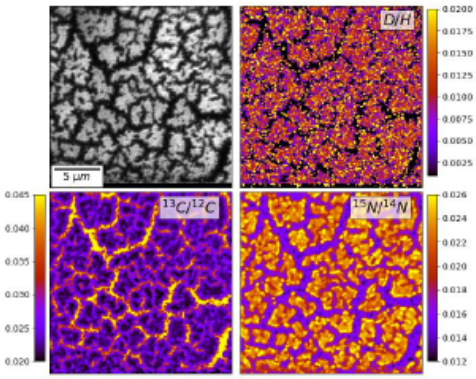

Figure 2. Isotopic ratio images on a same 20×20 µm² zone of the Sd#2 residue obtained with D, ^{15}N, and ^{13}C labeled ices. From top left to bottom right: the $^{12}C^{14}N^-$ direct image, D/H, $^{13}C/^{12}C$ and $^{15}N/^{14}N$ ratio images.

Results: The organic residues formed by the irradiation of the ices mixture tend to concentrate in micron-scale "islands" that contrast with "valleys" where the $^{12}C^{14}N^-$ ion emission is much lower (Figure 2, top-left). The low bulk abundance of D in the initial ices resulted in rather large statistical variations on the D/H images.

The behavior of the D/H and $^{15}N/^{14}N$ ratios were found similar for both Sd#1 and Sd#2 samples. D/H and $^{15}N/^{14}N$ isotopic ratios exhibit higher values on the material from the islands than in the valleys (Figure 2, top and bottom right). The matter from the islands exhibits $^{15}N/^{14}N$ spatial variations. Such variations were previously reported in D/H [7]. These experiments thus indicate that the irradiation of a D- and ^{15}N-labeled ice sandwich forms heterogeneous units in D and ^{15}N. The D-rich and ^{15}N-rich units obtained through the irradiation appear to behave similarly. The D/H and $^{15}N/^{14}N$ ratios remain stable along the 300 consecutive frames.

On the Sd#2 residue, the spatial repartition of the ^{13}C enrichments follows a pattern opposite to that of D and ^{15}N : the valleys exhibit larger $^{13}C/^{12}C$ ratios than the islands (Figure 2, bottom left). The sequential evolution of the $^{13}C/^{12}C$ ratios with the frames indicates that the ^{13}C-rich material is mostly concentrated in a layer of matter in the organic residue located below its surface, suggesting that the mixing of the carbon atoms from the ^{13}CO ice layer was not as extensive as that of hydrogen and nitrogen atoms from the $^{15}N_2$-CD_4 ices. Additional $^{16}O^-$ NanoSIMS measurements indicate that ^{13}C and ^{16}O are spatially correlated.

The marked difference between the D/H, $^{15}N/^{14}N$ and $^{13}C/^{12}C$ images suggest that, during the residue formation process, carbon atoms had a lower diffusion rate than hydrogen and nitrogen atoms, when initially present as ^{13}CO, CD_4 and $^{15}N_2$, respectively. These results confirm that the organics resulting from the irradiation of complex ice mixture can keep a memory of the isotopic heterogeneities of the initial ices. The isotopic heterogeneities observed in UCAMMs may therefore provide clues on the isotopic composition of the complex ices layers at the surface of their parent bodies and underline the diversity of the organic phases in UCAMMs.

Acknowledgements: This work is supported by ANR COMETOR, CNRS, LabEx P2IO, IN2P3, INSU, Univ. Paris-Saclay, DIM-ACAV and CNES.

References:

[1] Duprat, J., et al. (2010). *Science*, 328, 742-745 [2] Dartois, E., et al. (2013). *Icarus*, 224, 243-252. [3] Yabuta, H., et al. (2017). *GCA*, 214, 172-190. [4] Nakamura, T., et al. (2005). *MAPS*, 40 Suppl., #5046. [5] Dobrica, E., et al. (2010). *LPS XLI*, 1613. [6] Augé, B., et al. (2016). *A&A*, 592. [7] Augé, B., et al. (2019). *A&A*, 627, A122. [8] Augé, B., et al. (2018). *Rev. Sci. Instrum.*, 89, 075105. [9] Satorre, M. A., et al. (2008). *Planet. Space. Sci.*, 56, 1748-1752. [10] Ziegler, J. F. (2004). *Nucl. Instrum. Meth. B*, 219, 1027-1036.

5.4.8. Abstract for the 84th Annual Meeting of the Meteoritical Society (2021)

Ion-Irradiation Induced Organic Refractory Residues from Nitrogen-rich Ices: Clues on the Isotopic Composition of the Organic Matter in UCAMMs.

J. Rojas[1], J. Duprat[2], E. Dartois[3], T-D. Wu[4], C. Engrand[1], B. Augé[5], Ph. Boduch[6], H. Rothard[6], M. Chabot[1], B. Guérin[1], J. Mathurin[7], [1] Univ. Paris-Saclay, CNRS/IN2P3, IJCLab, 91405 Orsay, France, [2] IMPMC, CNRS-MNHN-Sorbonne Univ., 75005 Paris, France, [3] Univ. Paris-Saclay, CNRS, ISMO, 91405 Orsay, France, [4] Institut Curie, Univ. Paris-Saclay, CNRS, INSERM, 91405 Orsay, France, [5] IPAG, Univ. Grenoble Alpes, CNRS, 38000 Grenoble, France, [6] CIMAP, 14070 Caen, France, [7] Univ. Paris-Saclay, CNRS, ICP, 91405 Orsay, France

Introduction: Ultra Carbonaceous Antarctic MicroMeteorites (UCAMMs) are micrometeorites with a high carbonaceous abundance (C/Si ranging from 10 up to 10^3) [1-6]. Their organic matter is N-rich, with isotopic heterogeneities in N and C, and exibits extreme D/H ratios [2]. Despite their low abundance within the micrometeorite flux, UCAMMs represent a non-negligible source of exogenous unaltered carbon reaching Earth [7]. UCAMMs most probably originate from the surface of icy objects [2, 8] where the organic matter can be synthesized, at large heliocentric distance, by energetic processes such as Galactic Cosmic Rays (GCR) irradiation [9, 10]. In previous experiments, we showed the similarity of the IR signature and the D/H heterogenetities of UCAMMs with that observed in organic residues formed by swift ion irradiation of N-rich and D-rich ices mixed with hydrocarbons [9, 10]. We recently performed new irradiation experiments to study the transmission of light elements (H, C, N) isotopic heterogeneities from the ice to the irradiation-induced refractory residue. We also explored the impact of the ice chemical nature on the formation of the final organic residue.

Material and method: Ice irradiation experiments were performed with the ion beam (IRRSUD, 0.5-1 MeV/u) at GANIL (Caen, France). The IGLIAS experimental setup [9, 11] was used to form ice films by gas condensation on IR-transparent windows cooled down to 10K prior irradiation. A quadrupole mass spectrometer was used to monitor the gas phase during ice deposition, irradiation and subsequent sublimation. The ice evolution under irradiation was also monitored *in situ* with a Bruker Vertex 70v Fourier transform infrared (FTIR) spectrometer. Ice samples consisted in two ≈ 5 µm thick ice layers ($^{14}N_2$-$^{12}CH_4$ (90:10) or $^{14}NH_3$-$^{12}CH_4$ (90:10)) deposited around a central layer isotopically labeled with ^{13}C, ^{15}N and/or D, forming an ice-sandwich [12]. The total thickness of the ice-sandwich was estimated from the fringe pattern observed in the IR spectra [13] and the central layer accounted for 1% to 4% of its volume, depending on the sample. Nine ice-sandwiches were irradiated during three experimental sessions with $^{58}Ni^{9+}$, $^{136}Xe^{19+}$ and $^{86}Kr^{13+}$ swift ion beams. The ion fluences used to irradiate the ice-sandwiches were adapted to the ion energies in order to reach doses ranging from 8 to 25 eV/molecules corresponding to tens to hundreds million years of exposure in the outer region of the solar system. At the end of the irradiation, the ice-sandwiches were slowly warmed up from 10K to 300K with a 0.1 - 0.5 K/min temperature ramp, leading to the sublimation of the volatile ices left and to the concentration of refractory organic residues on the substrate windows. The windows were subsequently transferred from the IGLIAS chamber to a specific holder to perform isotopic mapping with the NanoSIMS instrument. Analyses were performed on areas of about 50×50 µm² with a 7 pA Cs^+ beam.

Results: Isotopic heterogeneities in D, N and C are observed at the micron scale in the organic residues, confirming the possibility to transfer isotopic heterogeneities from isotopically distinct ice layers to the irradiation-induced residue. Organic residues formed from ices with the same major composition of $^{14}N_2$-$^{12}CH_4$ (90:10) share similar IR spectra, however we observed substantial differences on the morphology of the organic residues from one sample to another. The structure of the organic residue and the repartition of the D, ^{15}N and ^{13}C within the residue seems to be sensitive to the formation mechanisms. The presence of D, ^{15}N and ^{13}C enrichements in the residue around holes associated with bubbles formed during the annealing suggests that specific components of the residue's precursors can be concentrated during the residue's formation events. Ice-sandwiches where ammonia is the major component of the ice sandwich ($^{14}NH_3$-$^{12}CH_4$ (90:10)) have led to the formation of low quantity of organic residue, resulting from the sublimation of most of the irradiated material during the annealing. These results can provide new constraints on the formation of organic matter by irradiation of icy bodies' surfaces at large heliocentric distance.

References: [1] Duprat, J., et al. (2010). *Science*, 328, 742-745, [2] Dartois, E., et al. (2018). *Astronomy and Astrophysics*, 609, [3] Noguchi, T., et al. (2017). *Geochimica et Cosmochimica Acta*, 208, 119, [4] Dartois, E., et al. (2013). *Icarus*, 224, 243-252, [5] Rojas, J., et al. (2020). *LPS LI*, 1614, [6] Yabuta, H., et al. (2017). *Geochimica et Cosmochimica Acta*, 214, 172-190, [7] Rojas, J., et al. (2021). *Earth and Planetary Science Letters*, 560, 116794, [8] Dobrica, E., et al. (2010). *LPS XLI*, 1613, [9] Augé, B., et al. (2016). *Astronomy and Astrophysics*, 592, A99, [10] Augé, B., et al. (2019). *Astronomy and Astrophysics*, 627, A122, [11] Augé, B., et al. (2018). *Review of Scientific Instruments*, 89, 075105, [12] Rojas, J., et al. (2020). *LPS LI*, 1630, [13] Satorre, M. A., et al. (2008). *Planetary and Space Science*, 56, 1748-1752.

5.4.9. Abstract for the 51th Lunar and Planetary Sciences Conference (2020)

THE ISOTOPIC DIVERSITY OF ULTRACARBONACEOUS ANTARCTIC MICROMETEORITES, A COUPLED NANOSIMS AND AFMIR STUDY. J. Rojas[1], J. Duprat[1], L. R. Nittler[2], J. Mathurin[1], E. Dartois[3], C. Engrand[1], N. Bardin[1], A. Dazzi[4], A. Deniset-Besseau[4], M. Godard[1], J-L. Guerquin-Kern[6], B. Guerin[1], S. Mostefaoui[7], L. Rémusat[7], R. M. Stroud[5], T-D Wu[6]. [1]Univ. Paris-Saclay, CNRS, IJCLab, 91405 Orsay, France (Julien.Rojas@csnsm.in2p3.fr); [2]Department of Terrestrial Magnetism, Carnegie Institution of Washington, Washington, DC 20015, USA, [3]Univ. Paris-Saclay, CNRS, ISMO, 91405 Orsay, France, [4]Univ. Paris-Saclay, CNRS, LCP, 91405 Orsay, France, [5]Naval Research Laboratory, Washington, DC 20375, USA, [6]Institut Curie, PSL Research Univ., INSERM, U1196, 91405 Orsay, France. [7]IMPMC, CNRS, MNHN, Sorbonne Univ., 75005 Paris, France.

Introduction: Antarctic MicroMeteorites (AMMs) from the Concordia collection are collected in the snow of the central regions of Antarctica within the 20 to 500 µm size range [1]. UltraCarbonaceous AMMs (UCAMMs), accounting for about 1% of the AMMs, are mainly composed of nitrogen and deuterium-rich organic matter [2-5]. The UCAMMs characteristics suggest that they originate from the outer regions of the solar system [3, 6]. UCAMMs are also identified in Japanese collections [4, 5], one UCAMM from the Dome Fuji collection do not exhibit large deuterium excesses [5].

We present here the results from NanoSIMS studies on two UCAMMs from the Concordia collection: DC16-14-309 (hereafter DC16-309) and DC06-05-94 (hereafter DC06-94). DC16-309 was also recently studied to compare its isotopic heterogeneities with the chemical composition of organic materials measured by STXM-XANES/TEM [7] and AFM-IR [8, 9].

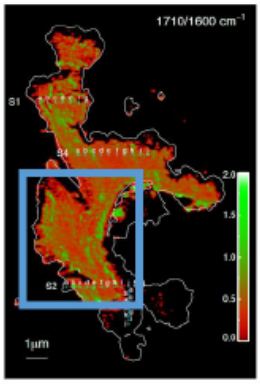

Figure 1: AFM-IR mapping of UCAMM DC16-309 showing the heterogeneity of the C=O/C=C ratios [8]. The blue zone is that analyzed by NanoSIMS.

Samples & methods: One fragment of UCAMM DC16-309 was embedded in sulfur, ultramicrotomed and the sections deposited on a diamond window. Figure 1 shows an AFM-IR image of fragment DC16-309b indicating the ratio of the 1710 cm^{-1} carbonyl (C=O) to the 1600 cm^{-1} (C=C) absorption bands [8]. The high spatial resolution of the AFM-IR technique allows identification of significant variations in this ratio at the sub-micron scale. After AFM-IR analysis, the sample was coated with 40 nm of gold for NanoSIMS analyses at the Carnegie Institution. The Cs^+ primary beam (10 pA) was rastered over 5×5 μm^2 and 128×128 pixel images were recorded with a dwell time of 2 ms/px. The hydrogen isotopic composition of DC16-309 was measured with the H^- and D^- secondary ions. A correction of the instrumental mass fractionation (IMF) was applied based on an in-house organic standard ($C_{30}H_{30}O$).

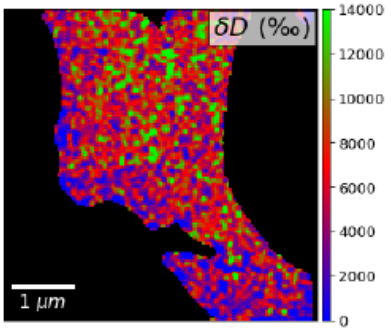

Figure 2: Hydrogen isotopic composition (expressed as δD with respect to VSMOW) mapping in a central zone of UCAMM DC16-309b (blue zone in Figure.1).

The D/H images of DC06-94 was measured on the NanoSIMS instrument at Institut Curie using the C_2D^-/C_2H^- ratio imaging, with a primary Cs^+ ion beam at 16 keV following the protocol detailed in [10]. Multiframe scanning images were acquired over a 50×50 μm^2 area (512 × 512 pixels). The probe dwell time was 0.5 ms/px and the typical counting rate for C_2H^- was 154 000 $c.s^{-1}$. The IMF calibration was carried out according to the procedure described in [11] by the use of standards with known D/H values. The carbon isotopic data were obtained on the NanoSIMS instrument at

IMPMC/MNHN. The $^{13}C/^{12}C$ map were derived from the $^{13}C^-$ and $^{12}C^-$ secondary ion emissions, using a 16 keV Cs^+ primary beam rastered over a 20×20 µm² area (256×256 pixels). Multi-frame images were acquired with a dwell time of 1 ms/pix and the average counting rate for $^{12}C^-$ was 128 400 $c.s^{-1}$. A type III kerogen was used for the IMF calibration. In order to study correlations between the $^{13}C/^{12}C$ and D/H ratio an alignment procedure was applied based on C_2^- and $^{12}C^-$ images. The $^{13}C^-$ and $^{12}C^-$ images were rotated and their size slightly rescaled to match with that of C_2H^- and C_2D^-.

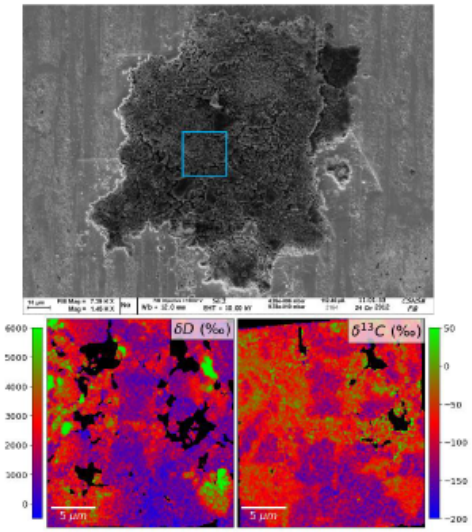

Figure 3. Top: secondary electron image of UCAMM DC06-94. Bottom: Deuterium and ^{13}C excess with respect to SMOW and PDB values measured by NanoSIMS in the blue area (top).

Results : *The DC16-309: a coupled AFMIR-NanoSIMS study.* Figure 2 shows the D anomalies in the zone reported in blue on the IR map of Figure 1. DC16-309 exhibits large D excesses with an average D/H ratio of $(1.1 \pm 0.6)\times10^{-3}$, i.e. $\delta D = 6100 \pm 3600$‰ relative to standard mean ocean water (SMOW). These large D/H ratios are comparable to that observed in previous UCAMMs from the Concordia collection [2, 3]. By contrast, there is no obvious correlation between the D-rich zones revealed by the NanoSIMS and the 1710/1600 cm^{-1} ratio from the AFM-IR image, suggesting that the D-rich component is not related to specific C=O/C=C ratios.

DC06-94 : NanoSIMS, $^{13}C/^{12}C$ – D/H correlations.

The average D/H in the image (Figure 3) is D/H = $(4.45\pm1.48)\times10^{-4}$ (i.e. $\delta D = 1860 \pm 950$ ‰) that is in agreement with $(5.4\pm0.4)\times10^{-4}$ measured in the bulk of DC06-94 in previous studies [11]. The average $^{13}C/^{12}C$ of the image is $^{13}C/^{12}C = (1.02\pm0.03)\times10^{-2}$ (i.e $\delta^{13}C = -90 \pm 28$ ‰ with respect to the Pee Dee Belemnite value, Figure 3). The comparison of hydrogen and carbon isotopic maps reveals correlations between cold and hot D/H and $^{13}C/^{12}C$ zones. First, one can distinguish a "cold" pole characterized by the lowest D/H (i.e. $\delta D <$ 1000 ‰) that is also characterized by the lowest $^{13}C/^{12}C$ ratios, with $\delta^{13}C$ lower than -100 ‰. By contrast, the "hot" endmember characterized by the highest D/H (i.e. $\delta D >$ 1000 ‰) has the highest $^{13}C/^{12}C$, with $\delta^{13}C$ greater than -100 ‰. Within this "hot" zone, some areas exhibit extreme D-rich spots (with δD ranging from 4000 up to 6000 ‰). The $\delta^{13}C$ of these D-rich spots is not significantly greater than that of other parts of the hot zone.

Conclusion: Thanks to the coupling of NanoSIMS with the novel AFM-IR technique it is possible to perform extensive characterization of the organic matter on a same sample at tens to hundreds of nm spatial resolution, giving an insight on the link between isotopic enrichment and chemical composition. Although correlations are seen between the isotopic composition of different organics components in grains (hydrogen and carbon in DC06-94), these correlations are not common to all UCAMMs. The large D excesses appear to be common in most UCAMMs confirming a formation in the outer regions of the solar system. UCAMMs organics do not exhibit the same IR signatures, nor the same isotopic variations as those seen in primitive chondrites, confirming that UCAMMs are probing a different organic reservoir than that sampled by primitive chondrites.

Acknowledgements: This work is supported by ANR COMETOR, CNRS, LabEx P2IO, IN2P3, INSU, Univ. Paris-Saclay, DIM-ACAV and CNES. The micrometeorites were collected at Concordia Station with the support of the French Polar Institute (IPEV).

References

[1] Duprat, J., et al. (2007). *Adv. Space Res.*, 39, 605-611. [2] Duprat, J., et al. (2010). *Science*, 328, 742-745. [3] Dartois, E., et al. (2013). *Icarus*, 224, 243-252. [4] Nakamura, T., et al. (2005). *MAPS*, 40 Suppl., #5046. [5] Yabuta, H., et al. (2017). *GCA*, 214, 172-190. [6] Augé, B., et al. (2016). *A&A*, 592. [7] Guérin, B., et al. (2020). *This meeting*. [8] Mathurin, J., et al. (2019). *A&A*, 622, A160. [9] Mathurin, J., et al. (2020). *This meeting*. [10] Bardin, N., et al. (2015). *Int. J. Mass Spectrom.*, 393, 17-24. [11] Bardin, N., et al. (2014). *LPS XLV*, 2647.

6 Résumé détaillé en français

Chapitre 1 : Le flux de micrométéorites mesuré avec la collection Concordia

Cette thèse de doctorat porte sur l'étude des micrométéorites collectées auprès de la station Concordia (Dôme C, Figure A) dans les régions centrales de l'Antarctique. Les micrométéorites proviennent de petits corps du système solaire, les astéroïdes et les comètes. L'étude des micrométéorites de la collection Concordia permet de mieux contraindre le flux de poussières interplanétaires à 1 U.A. et d'analyser la matière réfractaire existant à la surface des petits corps ayant gardé la mémoire des premiers stades du système solaire.

Figure A : position géographique du Dôme C en Antarctique (gauche) ; image d'une tranchée creusée pour l'extraction de micrométéorites à Dôme C (milieu) ; fondoir utilisé pour la fonte des neiges antarctiques et la collecte de micrométéorites.

La collection Concordia est décrite dans le premier chapitre, qui présente une étude sur le flux de particules submillimétriques extraterrestres tombant sur la Terre. Elle rassemble les données obtenues au cours de différentes missions de terrain effectuées au cours de vingt dernières années. Les conditions de collecte exceptionnelles à Dôme C permettent un contrôle précis du paramètre d'exposition (la surface équivalente d'accumulation) et de l'efficacité de la collecte des micrométéorites. Grâce à ce protocole expérimental, la collection Concordia échantillonne avec précision, pour la première fois, toutes les micrométéorites (y compris les plus fragiles) jusqu'à des diamètres de 30 µm. Les distributions en taille et les flux massiques de micrométéorites non-fondues (uMM) et de sphérules cosmiques (CS) sont mesurés dans la gamme de diamètres 30-350 µm. Cette étude montre que le maximum du flux en masse des uMMs et des CSs est porté par des particules dans une gamme de taille légèrement inférieure à celle déduite par les précédentes études. Plusieurs mesures indépendantes du flux sont été réalisées avec une méthodologie permettant de déduire une valeur absolue des flux de uMMs et de CSs. Les flux mesurés à Concordia combinés à une précédente mesure de flux réalisée à la station de Scott-Amundsen, au Pôle Sud (Taylor et al., 1998), permettent de déduire le flux global dans la gamme de diamètre 12-700 µm (Figure B). L'apport total annuel de micrométéorites sur Terre extrapolé à partir de cette étude est de 5200 tonnes/an (3600 tonnes/an de CS et 1600 tonnes/an de uMM).

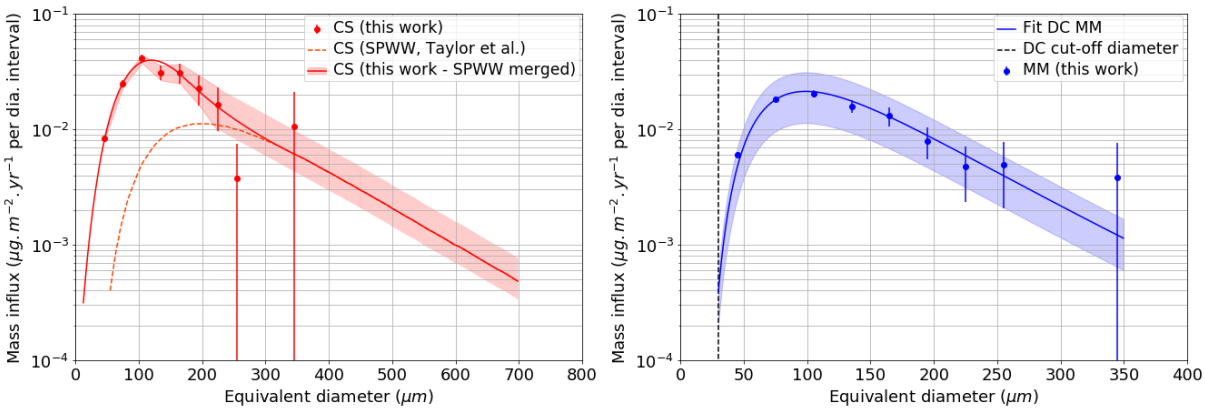

Figure B : distributions globales en taille de sphérules cosmiques (CS, gauche) et de micrométéorites non-fondues (uMM, droite). La distribution de CS est déduite de la combinaison de la distribution de la collection Concordia (DC) pour les diamètres inférieurs à 200 µm et la distribution SPWW (Taylor et al., 1998) pour les diamètres supérieurs à 200 µm. L'enveloppe rouge indique l'incertitude sur la distribution globale. L'enveloppe bleue indique l'impact de la densité sur la détermination du flux d'uMM, les limites hautes et basse de l'enveloppe correspondent à des densités de 2,2 et 0,8 $g.cm^{-3}$, respectivement.

Cette valeur comprend la contribution portée par les particules de taille inférieure à 200 µm, elle est donc plus élevée que celle déduite de la collection du Pôle Sud. Elle reste toutefois inférieure, d'un facteur 3, au flux attendu avant l'entrée atmosphérique, confirmant qu'environ 2/3 de la masse du flux entrant est volatilisée lors de l'entrée atmosphérique de ces particules. Sur la base des abondances relatives en carbone dans les différents types de micrométéorites (déduites des analyses des particules de la collection Concordia), le flux de carbone sur Terre porté par les micrométéorites est estimé entre 20 et 100 tonnes/an. A partir des distributions de masse obtenues dans cette étude, une simulation Monte-Carlo est réalisée pour calculer les incertitudes statistiques liées aux variations du paramètre d'exposition. Les résultats obtenus permettent de déduire les incertitudes statistiques typiques associées à de futures mesures de flux de particules submillimétriques sur Terre (Figure C).

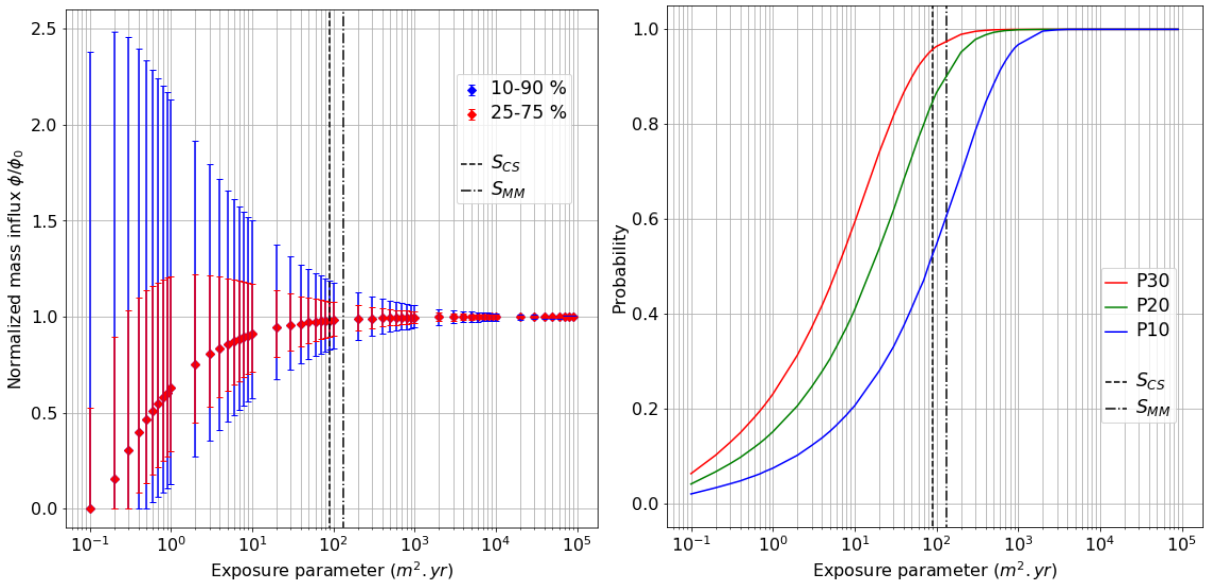

Figure C : impact du facteur d'exposition sur la mesure du flux de micrométéorites. Gauche : variations du rapport du flux mesuré (Φ) sur le flux nominal (Φ_0), indiqués par différents quantiles, en fonction du paramètre d'exposition. Droite : Probabilités d'estimer le flux avec une erreur statistique inférieure à 30% (P30), 20% (P20) et 10% (P10) en fonction du paramètre d'exposition.

Chapitre 2 : La composition isotopique en H, C et N de la matière organique des micrométéorites ultra-carbonées

Le chapitre 2 porte sur l'analyse isotopique de la matière organique de micrométéorites ultra-carbonées (UCAMM) provenant de la collection Concordia. Les UCAMMs constituent une population rare de micrométéorites riches en carbone, pauvres en minéraux. Ce carbone est sous forme de matière organique qui présente plusieurs composantes. Les caractéristiques chimiques et isotopiques de la composante riche en azote de matière organique des UCAMMs indiquent qu'elle a très probablement été formée par irradiation par les rayonnements cosmiques galactiques (GCR) de manteaux de glaces, riches en azote, dans les régions externes du système solaire. (Figure D).

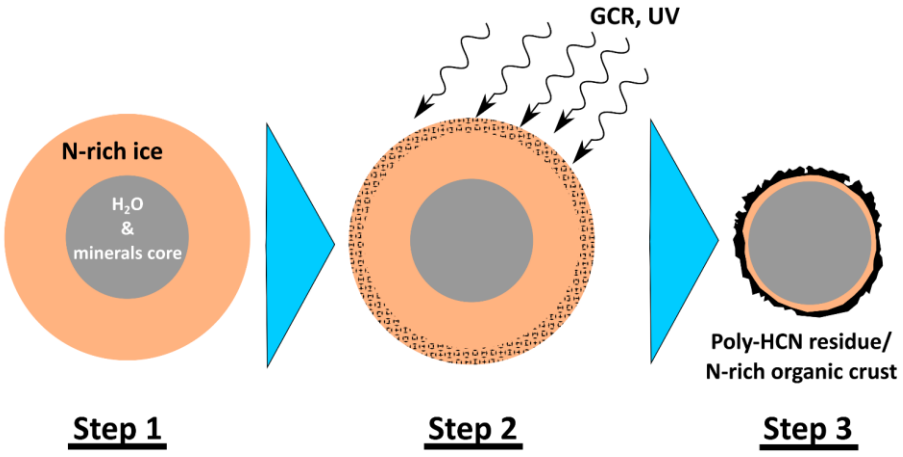

Figure D : scenario de formation de la matière organique riche en azote des UCAMMs. Gauche : étape 1, un petit corps dans les régions externes du système solaire accrète un manteau de glace volatile riche en azote. Les minéraux et la glace d'eau restent concentrés dans le noyau. Milieu : étape 2, le manteau de glace est irradié par les rayonnements cosmiques galactiques à grandes distances héliocentriques, conduisant à la transformation des molécules en surface et sub-surface. Droite : étape 3, les éléments volatiles du manteau se subliment et une croute organique réfractaire riche en azote se forme. La matière organique ainsi formée est riche en azote et pauvre en minéraux.

Dans le cadre de ce scénario de formation, la composition chimique et isotopique de la matière organique des UCAMMs permet d'étudier la nature des réservoirs gazeux condensés sur le corps parent des UCAMMs. Au cours de cette thèse, les compositions isotopiques de l'hydrogène, de l'azote et du carbone dans la matière organique de 4 UCAMMs ont été analysées. Cinq fragments de trois UCAMMs ont été analysés par spectrométrie de masse des ions secondaires à l'échelle nanométrique (NanoSIMS) au Earth and Planets Laboratory (Carnegie, Washington DC) en collaboration avec le Dr L. Nittler. Une analyse des données isotopiques acquises en carbone sur une UCAMM étudiée par NanoSIMS au MNHN et à l'Institut Curie avant cette thèse est également présentée. Ce travail présente l'étude la plus complète disponible à ce jour sur les rapports D/H, $^{13}C/^{12}C$ et $^{15}N/^{14}N$ dans les UCAMMs. Les compositions isotopiques en H, N et C des UCAMMs présentent une large gamme de variation d'une particule à l'autre, ainsi qu'au sein d'un même fragment. L'ensemble des données révèle des corrélations spatiales entre les compositions isotopiques en H, C et N qui sont discutées dans le chapitre 4.

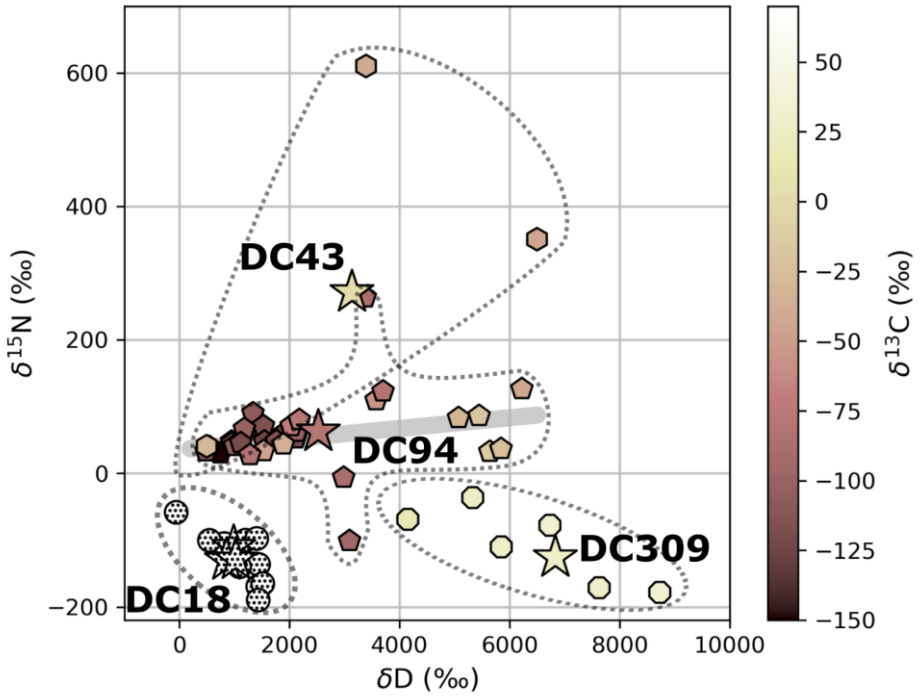

Figure E : compositions isotopiques en δD, $\delta^{15}N$, $\delta^{13}C$ des quatre UCAMMs analysées dans le chapitre 2. Les UCAMMs présentent une diversité de compositions isotopiques et des variations isotopiques à petites échelles. Les valeurs moyennes sont indiquées par des étoiles et les valeurs mesurées sur des régions d'intérêt spécifique par des pentagones (DC94), hexagones (DC43), octogones (DC309) et des cercles (DC18).

Chapitre 3 : irradiation de surfaces cométaires par les rayonnements cosmiques galactiques, une approche expérimentale

Le chapitre 3 présente un ensemble d'expériences de laboratoire simulant la synthèse de matière organique par l'irradiation de manteaux de glace de compositions isotopiques hétérogènes par des ions du GCR. Neuf résidus organiques réfractaires ont été produits au cours de trois sessions expérimentales en 2019, 2020 et 2021 au Grand Accélérateur National d'Ions Lourds (GANIL, France). Les expériences ont été réalisées avec le dispositif IGLIAS développé au CIMAP. Des films de glace avec différentes compositions chimiques et présentant des hétérogénéités isotopiques ont été irradiés avec des ions lourds d'énergie comprise entre 0,1 et 1 MeV/A (Figure F). Le but de ces expériences était d'étudier le transfert des hétérogénéités isotopiques du mélange de glace vers le résidu formé par irradiation.

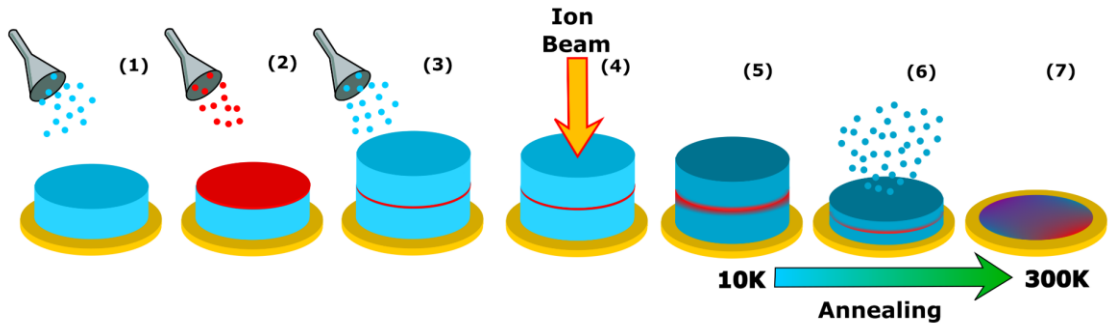

Figure F : Principe des expériences d'irradiation de glace effectuées au GANIL à l'aide du dispositif IGLIAS. (1) Une première couche (env. 5 µm) de glace non-marquée isotopiquement est déposé par condensation de gaz sur une fenêtre d'analyse à une température de 10K (bleu clair). (2) Un fin film (env. 0,1-0,4 µm) de glace marquée isotopiquement est déposé par-dessus (rouge). (3) Une seconde couche (env 5 µm) de glace non marqué isotopiquement, identique à la première, est déposée. (4) Le sandwich de glace est irradié par des ions lourds, modélisant les rayonnements cosmiques galactiques. (5-7) Le sandwich de glace irradié subit une lente remontée en température de 10K à 300K à une vitesse de 0,1 à 0,5 K/min. Les espèces volatiles se subliment et un résidu organique, réfractaire à 300K, se forme sur la fenêtre d'analyse. La répartition spatiale des hétérogénéités isotopiques du résidu organique est ensuite analysée à l'aide du NanoSIMS.

Les compositions isotopiques en éléments légers des résidus organiques ont été analysées par NanoSIMS à l'Institut Curie (Orsay, France). Cette étude rapporte, pour la première fois, des analyses combinées des hétérogénéités en D/H, $^{13}C/^{12}C$ et $^{15}N/^{14}N$ dans des résidus formés par irradiation obtenus à partir de mélanges de glaces d'intérêt astrophysique présentant différentes températures de condensation : CO, NH_3, N_2, CH_4. Cette étude montre que lorsqu'ils sont formés dans les mêmes conditions, les résidus résultant de l'irradiation de glaces N_2-CH_4 présentent une composition isotopique plus hétérogène que les résidus formés à partir de glaces NH_3-CH_4. Cependant, la nature des hétérogénéités ainsi que la structure globale des résidus sont particulièrement sensibles aux conditions de formation (par exemple la vitesse de remontée en température). Une formation d'îlots localisés de matière avec des anomalies isotopiques extrêmes est observée dans un résidu synthétisé lors de la session de 2020 (Figure G). Ce phénomène peut être liée à des événements sporadiques de sublimation pendant la procédure de remontée en température. Il indique qu'une mémoire de la composition isotopique locale de la glace peut être conservée lors de la formation du résidu organique.

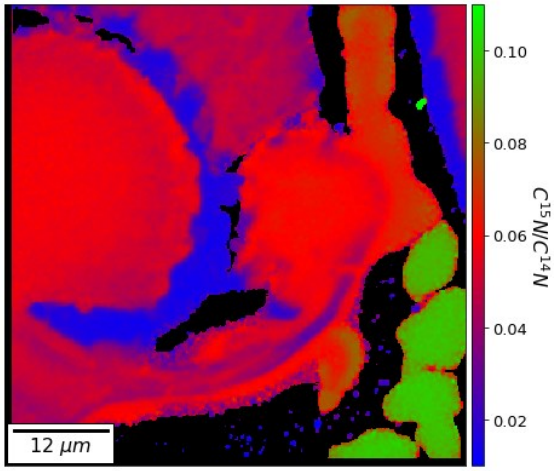

Figure G : image du rapport $^{15}N/^{14}N$ acquises par NanoSIMS sur un résidus organique formés après la remontée en température d'un sandwich de glace irradié par des ions lourds (Session expérimentale 2020). De fortes hétérogénéités isotopiques sont observées à l'échelle de quelques microns dans le résidu organique.

Les résultats de ces expériences sont discutés sur la base des conditions astrophysiques attendues à la surface des corps glacés situés dans les régions froides du disque protoplanétaire, au-delà de 5 U.A. Le phénomène d'irradiation de glaces isotopiquement hétérogènes permet d'expliquer la formation d'hétérogénéités isotopiques en H, N et C dans la matière organique des UCAMMs.

Chapitre 4 : discussion et perspectives

Dans le dernier chapitre, les résultats des chapitres 2 et 3 sont remis en perspective dans le cadre d'un scénario de formation de la matière organique des UCAMMs. La diversité de la composition isotopique des UCAMMs est résumée et comparée à celle d'autres objets du système solaire (Figure G). Les similitudes entre les compositions isotopiques de l'UCAMM DC43 et celles de la matière organique insoluble (IOM) des chondrites de type Renazzo (CR) indiquent que ces objets pourraient avoir hérité leur matière organique d'un réservoir parent similaire, ce qui suggère un continuum entre le corps parent des CR et les objets cométaires. Sur la base de modèles théoriques prédisant les compositions isotopiques en H, N et C des réservoirs gazeux primitifs du disque protoplanétaire, l'étude montre qu'il existe des réservoirs moléculaires pouvant rendre compte des compositions isotopiques observées dans la matière organique des UCAMMs. Il est ainsi possible d'expliquer les caractéristiques isotopiques de certaines UCAMMs en considérant l'irradiation de manteaux de glace hérités de réservoirs gazeux froids situés dans des régions proches du plan médian du disque à des distances héliocentriques comprises entre quelques AU et quelques dizaines d'AU. Les composantes organiques d'autres UCAMMs pourraient avoir héritées de la composition isotopiquee de réservoirs gazeux moléculaires provenant d'un environnement moins froid, à des profondeurs intermédiaires au-dessus du plan médian du disque ($z \approx 0{,}08 - 0{,}2$). Ces hypothèses sont discutées au regard des données chimiques des UCAMMs. Des recherches futures sont proposées pour caractériser l'association de minéraux et de matière organique dans les UCAMMs et approfondir notre compréhension de la composition de la surface des petits corps glacés formés au début du système solaire.

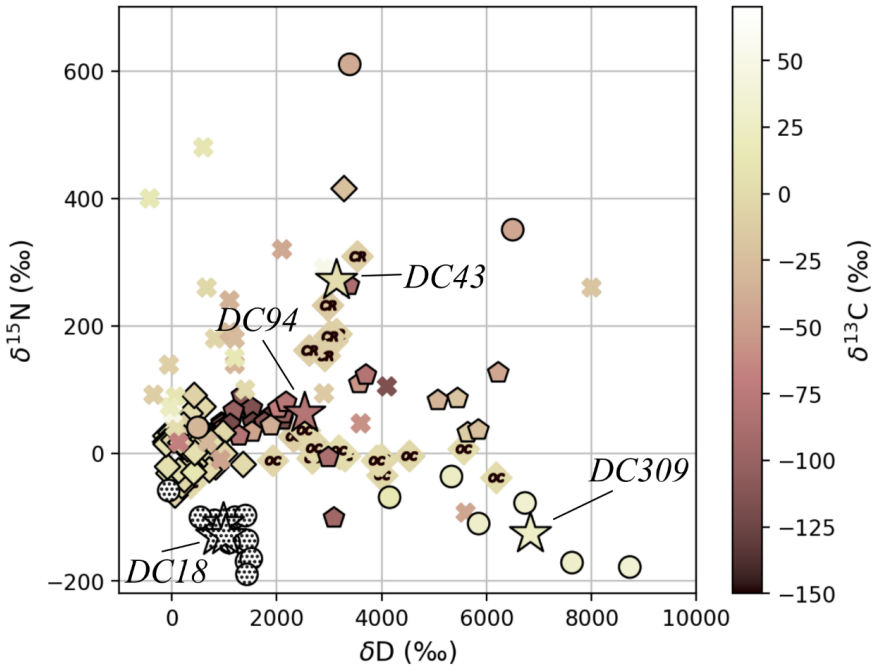

Figure H : compositions isotopiques en δD, $\delta^{15}N$, $\delta^{13}C$ des quatre UCAMMs analysées dans le chapitre 2, comparées aux compositions mesurées dans les IDPs (croix, Messenger, 2000) et dans la matière organique insoluble de chondrites (losange, OC et CR désignent les chondrites ordinaires et de type Renazzo).

7 Abbreviations

AFMIR	Atomic force microscopy-Infrared spectroscopy
AMM	Antarctic micrometeorite
BSE	Backscattered electron
CABMOD	Chemical ablation model
CIMAP	Centre de recherche sur les Ions, les MAtériaux et la Photonique, Caen, France
CP-IDP	Chondritic-porous interplanetary dust particle
CS	Cosmic spherules
CSNSM	Centre de Science Nucléaire et de Science des matériaux, Orsay, France (now IJCLAB)
CR	Rennazzo-type carbonaceous chondrite
DC	Dome C
FTIR	Fourier transform infrared
ET	Extraterrestrial
GANIL	Heavy ions accelerator, Caen, France
GCR	Galactic cosmic ray
IDP	Interplanetary dust particles
IGLIAS	Experimental chamber for the irradiation of ices of astrophysical relevance
IJCLab	Laboratoire Irène Joliot-Curie, Orsay, France
IMF	Instrumental mass fractionation
IOM	Insoluble organic matter
IR	Infrared
ISM	Interstellar medium
KBO	Kuiper belt objects
LDEF	Long duration exposure facility
MM	Micrometeorite
OC	Ordinary chondrite
OM	Organic matter
QMS	Quadrupolar mass spectrometer
ROI	Region of interest
SEM	Scanning electron microscopy
SIMS (NanoSIMS)	Secondary ions mass spectrometry
SPWW	South-Pole water well
STXM	Scanning transmission X-ray microscopy
TAM	Trans-Antarctic mountains
TEM	Transmission electron microscopy
UCAMM	Ultra-carbonaceous micrometeorite
UHV	Ultra-high vacuum
uMM	Unmelted micrometeorite
UV	Ultraviolet
Vis-UV	Visible-ultraviolet
XANES	X-Ray absorption near edge structure
ZC	Zodiacal cloud
ZoDy	Zodiacal cloud dynamical model

8 List of figures

9 Bibliography

[1] Aikawa, Y., Furuya, K., Hincelin, U., Herbst, E., 2018. Multiple Paths of Deuterium Fractionation in Protoplanetary Disks. The Astrophysical Journal 855, 119.

[2] Aikawa, Y., Wakelam, V., Hersant, F., Garrod, R.T., Herbst, E., 2012. From Prestellar to Protostellar Cores. II. Time Dependence and Deuterium Fractionation. The Astrophysical Journal 760.

[3] Aléon, J., Engrand, C., Robert, F., Chaussidon, M., 2001. Clues on the origin of interplanetary dust particles from the isotopic study of their hydrogen-bearing phases. GCA 65, 4399-4412.

[4] Aléon, J., Robert, F., Chaussidon, M., Marty, B., 2003. Nitrogen isotopic composition of macromolecular organic matter in interplanetary dust particles. GCA 67, 3773-3783.

[5] Alexander, C.M.O.D., Fogel, M., Yabuta, H., Cody, G.D., 2007. The origin and evolution of chondrites recorded in the elemental and isotopic compositions of their macromolecular organic matter. Geochimica et Cosmochimica Acta 71, 4380-4403.

[6] Altwegg, K., Balsiger, H., Bar-Nun, A., Berthelier, J.J., Bieler, A., Bochsler, P., Briois, C., Calmonte, U., Combi, M., De Keyser, J., Eberhardt, P., Fiethe, B., Fuselier, S., Gasc, S., Gombosi, T.I., Hansen, K.C., Hässig, M., Jäckel, A., Kopp, E., Korth, A., LeRoy, L., Mall, U., Marty, B., Mousis, O., Neefs, E., Owen, T., Rème, H., Rubin, M., Sémon, T., Tzou, C.-Y., Waite, H., Wurz, P., 2015. 67P/Churyumov-Gerasimenko, a Jupiter family comet with a high D/H ratio. Science 347, 1261952.

[7] Arpigny, C., Jehin, E., Manfroid, J., Hutsemékers, D., Schulz, R., Stüwe, J.A., Zucconi, J.-M., Ilyin, I., 2003. Anomalous Nitrogen Isotope Ratio in Comets. Science 301, 1522.

[8] Augé, B., 2017. Effet du rayonnement cosmique galactique sur les petits corps glacés du système solaire externe : indices pour la formation de la matière organique des micrométéorites antarctiques ultra-carbonées, in: Normandie, U.d.C. (Ed.).

[9] Augé, B., Been, T., Boduch, P., Chabot, M., Dartois, E., Madi, T., Ramillon, J.M., Ropars, F., Rothard, H., Voivenel, P., 2018. IGLIAS: A new experimental set-up for low temperature irradiation studies at large irradiation facilities. Review of Scientific Instruments 89, 075105.

[10] Augé, B., Dartois, E., Duprat, J., Engrand, C., Slodzian, G., Wu, T.D., Guerquin-Kern, J.L., Vermesse, H., Agnihotri, A.N., Boduch, P., Rothard, H., 2019. Hydrogen isotopic anomalies in extraterrestrial organic matter: role of cosmic ray irradiation and implications for UCAMMs. Astronomy and Astrophysics 627, A122.

[11] Augé, B., Dartois, E., Engrand, C., Duprat, J., Godard, M., Delauche, L., Bardin, N., Mejía, C., Martinez, R., Muniz, G., Domaracka, A., Boduch, P., Rothard, H., 2016. Irradiation of nitrogen-rich ices by swift heavy ions. Clues for the formation of ultracarbonaceous micrometeorites. Astronomy and Astrophysics 592, A99.

[12] Bacmann, A., Lefloch, B., Ceccarelli, C., Steinacker, J., Castets, A., Loinard, L., 2003. CO Depletion and Deuterium Fractionation in Prestellar Cores. The Astrophysical Journal 585, L55.

[13] Bardin, N., 2015. Composition isotopique des éléments légers dans les micrométéorites ultracarbonées par spectrométrie de masse à émission ionique secondaire à haute résolution en masse, contribution à la connaissance des surfaces cométaires Ecole Doctorale N°576, Particules, Hadrons, Energie et Noyau. Université Paris Sud.

[14] Bardin, N., Duprat, J., Slodzian, G., Wu, T.-D., Baklouti, D., Dartois, E., Brunetto, R., Engrand, C., Guerquin-Kern, J.-L., 2015. Hydrogen isotopic fractionation in secondary ion mass spectrometry using polyatomic ions. International Journal of Mass Spectrometry 393, 17-24.

[15] Bardin, N., Slodzian, G., Wu, T.-D., Baklouti, D., Dartois, E., Engrand, C., Brunetto, R., Guerquin-Kern, J.-L., Duprat, J., 2014. D/H Measurements in Ultracarbonaceous Antarctic Micrometeorites Using Polyatomic Ions with SIMS, Lunar and Planetary Science, p. 2647.

[16] Bennett, C.J., Kaiser, R.I., 2007. The Formation of Acetic Acid (CH₃COOH) in Interstellar Ice Analogs. The Astrophysical Journal 660, 1289.

[17] Biver, N., Bockelee-Morvan, D., Boissier, J., Crovisier, J., Colom, P., Lecacheux, A., Moreno, R., Paubert, G., Lis, D.C., Sumner, M., Frisk, U., Hjalmarson, A., Olberg, M., Winnberg, A., Floren, H.-G., Sandqvist, A., Kwok, S., 2007. Radio observations of Comet 9P/Tempel 1 before and after Deep Impact. Icarus 187, 253-271.

[18] Bockelée-Morvan, D., Biver, N., Jehin, E., Cochran, A.L., Wiesemeyer, H., Manfroid, J., Hutsemékers, D., Arpigny, C., Boissier, J., Cochran, W., Colom, P., Crovisier, J., Milutinovic, N., Moreno, R., Prochaska, J.X., Ramirez, I., Schulz, R., Zucconi, J.M., 2008. Large excess of heavy nitrogen in both hydrogen cyanide and cyanogen from comet 17P/Holmes. Astrophysical Journal 679, L49-L52.

[19] Bockelée-Morvan, D., Calmonte, U., Charnley, S., Duprat, J., Engrand, C., Gicquel, A., Hässig, M., Jehin, E., Kawakita, H., Marty, B., Milam, S., Morse, A., Rousselot, P., Sheridan, S., Wirström, E., 2015. Cometary Isotopic Measurements. Space Science Reviews 197, 47-83.

[20] Bockelée-Morvan, D., Gautier, D., Hersant, F., Huré, J.M., Robert, F., 2002. Turbulent radial mixing in the solar nebula as the source of crystalline silicates in comets. Astronomy and Astrophysics 384, 1107-1118.

[21] Bockelée-Morvan, D., Gautier, D., Lis, D.C., Young, K., Keene, J., Phillips, T., Owen, T., Crovisier, J., Goldsmith, P.F., Bergin, E.A., Despois, D., Wooten, A., 1997. Deuterated water in comet C/1996 B2 (Hyakutake) and its implications for the origin of comets. Icarus 133, 147-162.

[22] Boerboom, A.J.H., 1972. Ion optics of the electric hexapole. International Journal of Mass Spectrometry and Ion Processes 8, 475.

[23] Boerboom, A.J.H., 1987. Ion optics of multipoles. Nuclear Instruments and Methods in Physics Research A 258, 426.

[24] Boerboom, A.J.H., 1995. Ion optics of multipoles 2. Field calculations and contributions of higher harmonics. International Journal of Mass Spectrometry and Ion Processes 146-147, 131.

[25] Bonnet, J.-Y., Quirico, E., Buch, A., Thissen, R., Szopa, C., Carrasco, N., Cernogora, G., Fray, N., Cottin, H., Roy, L.L., Montagnac, G., Dartois, E., Brunetto, R., Engrand, C., Duprat, J., 2015. Formation of analogs of cometary nitrogen-rich refractory organics from thermal degradation of tholin and HCN polymer. Icarus 250, 53-63.

[26] Bosman, A.D., Bergin, E.A., 2021. Reimagining the Water Snowline. The Astrophysical Journal 918, L10.

[27] Bottger, G.L., Eggers, D.F., Jr., 1964. Infrared Spectra of Crystalline C₂H₂, C₂HD, and C₂D₂. Journal of Chemical Physics 40, 2010.

[28] Bouilloud, M., Fray, N., Bénilan, Y., Cottin, H., Gazeau, M.-C., Jolly, A., 2015. Bibliographic review and new measurements of the infrared band strengths of pure molecules at 25 K: H₂O, CO₂, CO, CH₄, NH₃, CH₃OH, HCOOH and H₂CO. Monthly Notices of the Royal Astronomical Society 451, 2145.

[29] Bradley, J.P., 2003. Interplanetary Dust Particles, Treatise on Geochemistry, pp. 689-711.

[30] Briani, G., Engrand, C., Duprat, J., Benoit, R., Krüger, H., Fischer, H., Hilchenbach, M., Briois, C., Thirkell, L., 2012. TOF-SIMS Analyses of an Ultracarbonaceous MicroMeteorite: Preparation of Rosetta-COSIMA Studies in 2014, Lunar and Planetary Science Conference.

[31] Bringa, E.M., 2003. Molecular dynamics simulations of Coulomb explosion. Nuclear Instruments and Methods in Physics Research B 209, 1.

[32] Brown, K.L., Belbeoch, R., Bounin, P., 1964. First- and Second-Order Magnetic Optics Matrix Equations for the Midplane of Uniform-Field Wedge Magnets. Review of Scientific Instruments 35, 481.

[33] Brown, M.E., Burgasser, A.J., Fraser, W.C., 2011a. The Surface Composition of Large Kuiper Belt Object 2007 OR10. The Astrophysical Journal 738, L26.

[34] Brown, M.E., Schaller, E.L., Fraser, W.C., 2011b. A Hypothesis for the Color Diversity of the Kuiper Belt. The Astrophysical Journal 739, L60.

[35] Bruderer, S., van der Marel, N., van Dishoeck, E.F., van Kempen, T.A., 2014. Gas structure inside dust cavities of transition disks: Ophiuchus IRS 48 observed by ALMA. Astronomy and Astrophysics 562, A26.

[36] Burgdorf, M., Cruikshank, D.P., Dalle Ore, C.M., Sekiguchi, T., Nakamura, R., Orton, G., Quirico, E., Schmitt, B., 2010. A Tentative Identification of HCN Ice on Triton. The Astrophysical Journal 718, L53.

[37] Burke, D.J., Brown, W.A., 2010. Ice in space: surface science investigations of the thermal desorption of model interstellar ices on dust grain analogue surfaces. Physical Chemistry Chemical Physics (Incorporating Faraday Transactions) 12, 5947.

[38] Busemann, H., Alexander, M.O.d., Nittler, L.R., 2007. Characterization of insoluble organic matter in primitive meteorites by microRaman spectroscopy. Meteoritics and Planetary Science 42, 1387.

[39] Calvani, P., Lupi, S., Maselli, P., 1989. The infrared spectrum of solid CD₄. Journal of Chemical Physics 91, 6737.

[40] Carrillo-Sánchez, J.D., Nesvorný, D., Pokorný, P., Janches, D., Plane, J.M.C., 2016. Sources of cosmic dust in the Earth's atmosphere. Geophysical Research Letters 43, 11,979-911,986.

[41] Carrillo-Sánchez, J.D., Plane, J.M.C., Feng, W., Nesvorný, D., Janches, D., 2015. On the size and velocity distribution of cosmic dust particles entering the atmosphere. Geophysical Research Letters 42, 6518-6525.

[42] Ceccarelli, C., Caselli, P., Bockelée-Morvan, D., Mousis, O., Pizzarello, S., Robert, F., Semenov, D., 2014. Deuterium Fractionation: The Ariadne's Thread from the Precollapse Phase to Meteorites and Comets Today, p. 859.

[43] Charnoz, S., Morbidelli, A., 2007. Coupling dynamical and collisional evolution of small bodies: II. Forming the Kuiper belt, the Scattered Disk and the Oort Cloud. Icarus 188, 468-480.

[44] Consolmagno, G.J., Britt, D.T., Macke, R.J., 2008. The significance of meteorite density and porosity. Chemie Der Erde-Geochemistry 68, 1-29.

[45] Cooper, J.F., Christian, E.R., Richardson, J.D., Wang, C., 2003. Proton Irradiation of Centaur, Kuiper Belt, and Oort Cloud Objects at Plasma to Cosmic Ray Energy. Earth Moon and Planets 92, 261-277.

[46] Crapsi, A., Caselli, P., Walmsley, C.M., Myers, P.C., Tafalla, M., Lee, C.W., Bourke, T.L., 2005. Probing the Evolutionary Status of Starless Cores through N₂H⁺ and N₂D⁺ Observations. The Astrophysical Journal 619, 379.

[47] Cremonese, G., Borin, P., Martellato, E., Marzari, F., Bruno, M., 2012. New Calibration of the Micrometeoroid Flux on Earth. The Astrophysical Journal 749, L40.

[48] Cziczo, D.J., Thomson, D.S., Murphy, D.M., 2001. Ablation, Flux, and Atmospheric Implications of Meteors Inferred from Stratospheric Aerosol. Science 291, 1772.

[49] D'Hendecourt, L.B., Allamandola, L.J., 1986. Time dependent chemistry in dense molecular clouds. III. Infrared band cross sections of molecules in the solid state at 10K. Astronomy and Astrophysics Supplement Series 64, 453.

[50] Dartois, E., Chabot, M., Bacmann, A., Boduch, P., Domaracka, A., Rothard, H., 2020. Non-thermal desorption of complex organic molecules. Cosmic-ray sputtering of CH₃OH embedded in CO₂ ice. Astronomy and Astrophysics 634, A103.

[51] Dartois, E., Engrand, C., Brunetto, R., Duprat, J., Pino, T., Quirico, E., Remusat, L., Bardin, N., Briani, G., Mostefaoui, S., Morinaud, G., Crane, B., Szwec, N., Delauche, L., Jamme, F., Sandt, C., Dumas, P., 2013. UltraCarbonaceous Antarctic micrometeorites, probing the Solar System beyond the nitrogen snow-line. Icarus 224, 243-252.

[52] Dartois, E., Engrand, C., Duprat, J., Godard, M., Charon, E., Delauche, L., Sandt, C., Borondics, F., 2018. Dome C ultracarbonaceous Antarctic micrometeorites. Infrared and Raman fingerprints. Astronomy and Astrophysics 609.

[53] Dazzi, A., Prater, C.B., Hu, Q., Chase, D.B., Rabolt, J.F., Marcott, C., 2012. AFM-IR: Combining Atomic Force Microscopy and Infrared Spectroscopy for Nanoscale Chemical Characterization. Applied Spectroscopy 66, 1365.

[54] de Barros, A.L.F., da Silveira, E.F., Bergantini, A., Rothard, H., Boduch, P., 2015. Radiolysis of Nitrogen and Water-ice Mixture by Fast Ions: Implications for Kuiper Belt Objects. The Astrophysical Journal 810, 156.

[55] Dobrică, E., Engrand, C., Quirico, E., Montagnac, G., Duprat, J., 2011. Raman characterization of carbonaceous matter in CONCORDIA Antarctic micrometeorites. Meteoritics and Planetary Science 46, 1363-1375.

[56] Domingo, M., Millán, C., Satorre, M.A., Cantó, J., 2007. Thin film thickness measurement by double laser interferometry, p. 66164A.

[57] Donn, B., 1976. The Nucleus: Panel Discussion, p. 611.

[58] Douté, S., Schmitt, B., Quirico, E., Owen, T.C., Cruikshank, D.P., de Bergh, C., Geballe, T.R., Roush, T.L., 1999. Evidence for Methane Segregation at the Surface of Pluto. Icarus 142, 421.

[59] Duprat, J., Dobrică, E., Engrand, C., Aléon, J., Marrocchi, Y., Mostefaoui, S., Meibom, A., Leroux, H., Rouzaud, J.-N., Gounelle, M., Robert, F., 2010. Extreme Deuterium Excesses in Ultracarbonaceous Micrometeorites from Central Antarctic Snow. Science 328, 742-745

[60] Duprat, J., Engrand, C., Maurette, M., Naulin, F., Kurat, G., Gounelle, M., 2006. The Micrometeorite Mass Flux as Recorded in Dome C Central Antarctic Surface Snow. Meteoritics and Planetary Science Supplement 41, 5239.

[61] Duprat, J., Maurette, M., Engrand, C., Matraj, G., Immel, G., Hammer, C., Gounelle, M., Kurat, G., 2001. An Estimation of the Contemporary Micrometeorite Flux Obtained from Surface Snow Samples Collected in Central Antarctica. Meteoritics and Planetary Science Supplement 36, A52.

[62] Engrand, C., Charon, E., Duprat, J., Dartois, E., Leroux, H., Benzerara, K., Le Guillou, C., Bernard, S., Swaraj, S., Belkhou, R., Delauche, L., Godard, M., Augé, B., 2018. Ultracarbonaceous Antarctic Micrometeorites (UCAMMs): Clues for their Origin, Lunar and Planetary Science Conference.

[63] Engrand, C., Duprat, J., Dartois, E., Godard, M., Delauche, L., 2017. Cosmic dust flux on Earth inferred from the Concordia micrometeorite collection, EGU General Assembly Conference Abstracts, p. 9979.

[64] Floss, C., Stadermann, F.J., 2009. High Abundances of Circumstellar and Interstellar C-Anomalous Phases in the Primitive CR3 Chondrites QUE 99177 and MET 00426. The Astrophysical Journal 697, 1242.

[65] Floss, C., Stadermann, F.J., Bradley, J., Dai, Z.R., Bajt, S., Graham, G., 2004. Carbon and nitrogen isotopic anomalies in an anhydrous interplanetary dust particle. Science 303, 1355-1358.

[66] Floss, C., Stadermann, F.J., Bradley, J.P., Dai, Z.R., Bajt, S., Graham, G., Lea, A.S., 2006. Identification of isotopically primitive interplanetary dust particles: A NanoSIMS isotopic imaging study. Geochimica et Cosmochimica Acta 70, 2371.

[67] Flynn, G.J., 2002. Extraterrestrial Dust in the Near-Earth Environment, p. 77.

[68] Flynn, G.J., Sutton, S.R., 1991. Cosmic dust particle densities: evidence for two populations of stony micrometeorites. Lunar and Planetary Science Conference Proceedings 21, 541.

[69] Frezzotti, M., Pourchet, M., Flora, O., Gandolfi, S., Gay, M., Urbini, S., Vincent, C., Becagli, S., Gragnani, R., Proposito, M., Severi, M., Traversi, R., Udisti, R., Fily, M., 2005. Spatial and temporal variability of snow accumulation in East Antarctica from traverse data. Journal of Glaciology 51, 113-124.

[70] Fulle, M., Della Corte, V., Rotundi, A., Rietmeijer, F.J.M., Green, S.F., Weissman, P., Accolla, M., Colangeli, L., Ferrari, M., Ivanovski, S., Lopez-Moreno, J.J., Epifani, E.M., Morales, R., Ortiz, J.L., Palomba, E., Palumbo, P., Rodriguez, J., Sordini, R., Zakharov, V., 2016. Comet 67P/Churyumov-Gerasimenko preserved the pebbles that formed planetesimals. Monthly Notices of the Royal Astronomical Society 462, S132.

[71] Füri, E., Marty, B., 2015. Nitrogen isotope variations in the Solar System. Nature Geoscience 8, 515.

[72] Furuya, K., Aikawa, Y., 2018. Depletion of Heavy Nitrogen in the Cold Gas of Star-forming Regions. The Astrophysical Journal 857, 105.

[73] Gardner, C.S., Liu, A.Z., Marsh, D.R., Feng, W.H., Plane, J.M.C., 2014. Inferring the global cosmic dust influx to the Earth's atmosphere from lidar observations of the vertical flux of mesospheric Na. Journal of Geophysical Research-Space Physics 119, 10.

[74] Genge, M.J., Larsen, J., Van Ginneken, M., Suttle, M.D., 2017. An urban collection of modern-day large micrometeorites: Evidence for variations in the extraterrestrial dust flux through the Quaternary. Geology 45, 119-122.

[75] Genge, M.J., Van Ginneken, M., Suttle, M.D., 2020. Micrometeorites: Insights into the flux, sources and atmospheric entry of extraterrestrial dust at Earth. Planetary and Space Science 187.

[76] Gerakines, P.A., Moore, M.H., Hudson, R.L., 2000. Carbonic acid production in H_2O:CO_2 ices. UV photolysis vs. proton bombardment. Astronomy and Astrophysics 357, 793.

[77] Gerakines, P.A., Moore, M.H., Hudson, R.L., 2004. Ultraviolet photolysis and proton irradiation of astrophysical ice analogs containing hydrogen cyanide. Icarus 170, 202.

[78] Gerakines, P.A., Schutte, W.A., Ehrenfreund, P., 1996. Ultraviolet processing of interstellar ice analogs. I. Pure ices. Astronomy and Astrophysics 312, 289.

[79] Gerakines, P.A., Schutte, W.A., Greenberg, J.M., van Dishoeck, E.F., 1995. The infrared band strengths of H_2_O, CO and CO_2_ in laboratory simulations of astrophysical ice mixtures. Astronomy and Astrophysics 296, 810.

[80] Goderis, S., Soens, B., Huber, M.S., McKibbin, S., van Ginneken, M., Van Maldeghem, F., Debaille, V., Greenwood, R.C., Franchi, I.A., Cnudde, V., Van Malderen, S., Vanhaecke, F., Koeberl, C., Topa, D., Claeys, P., 2020. Cosmic spherules from Widerøefjellet, Sør Rondane Mountains (East Antarctica). Geochimica et Cosmochimica Acta 270, 112.

[81] Grundy, W.M., Binzel, R.P., Buratti, B.J., Cook, J.C., Cruikshank, D.P., Dalle Ore, C.M., Earle, A.M., Ennico, K., Howett, C.J.A., Lunsford, A.W., Olkin, C.B., Parker, A.H., Philippe, S., Protopapa, S., Quirico, E., Reuter, D.C., Schmitt, B., Singer, K.N., Verbiscer, A.J., Beyer, R.A., Buie, M.W., Cheng, A.F., Jennings, D.E., Linscott, I.R., Parker, J.W., Schenk, P.M., Spencer, J.R., Stansberry, J.A., Stern, S.A., Throop, H.B., Tsang, C.C.C., Weaver, H.A., Weigle, G.E., Young, L.A., 2016. Surface compositions across Pluto and Charon. Science 351.

[82] Guerin, B., 2021. Cometary dust and origin of matter in the protoplanetary disk, Physics. Paris-Saclay University.

[83] Guérin, B., Engrand, C., Le Guillou, C., Leroux, H., Duprat, J., Dartois, E., Bernard, S., Benzerara, K., Rojas, J., Godard, M., Delauche, L., Troadec, D., 2020. STEM and STXM-XANES analysis of FIB sections of Ultracarbonaceous Antarctic Micrometeorites (UCAMMs), Lunar and Planetary Science.

[84] Hashizume, K., Chaussidon, M., Marty, B., Terada, K., 2004. Protosolar Carbon Isotopic Composition: Implications for the Origin of Meteoritic Organics. The Astrophysical Journal 600, 480.

[85] Hauri, E.H., Papineau, D., Wang, J., Hillion, F., 2016. High-precision analysis of multiple sulfur isotopes using NanoSIMS. Chemical Geology 420, 148.

[86] He, J., Gao, K., Vidali, G., Bennett, C.J., Kaiser, R.I., 2010. Formation of Molecular Hydrogen from Methane Ice. The Astrophysical Journal 721, 1656.

[87] Holt, J.S., Sadoskas, D., Pursell, C.J., 2004. Infrared spectroscopy of the solid phases of ammonia. Journal of Chemical Physics 120, 7153.

[88] Hudson, R.L., Moore, M.H., 2002. The N₃ Radical as a Discriminator between Ion-irradiated And UV-photolyzed Astronomical Ices. The Astrophysical Journal 568, 1095.

[89] Hughes, D.W., 1992. The meteorite flux. Space Science Reviews 61, 275-299.

[90] Isokoski, K., Poteet, C.A., Linnartz, H., 2013. Highly resolved infrared spectra of pure CO₂ ice (15-75 K). Astronomy and Astrophysics 555, A85.

[91] Jewitt, D.C., Matthews, H.E., Meier, R., 1997. Measurements of $^{12}C/^{13}C$, $^{14}N/^{15}N$, and $^{32}S/^{34}S$ ratios in comet Hale-Bopp (C/1995 O1). Science 278, 90.

[92] Joswiak, D.J., Brownlee, D.E., Pepin, R.O., Schlutter, D.J., 2007. Densities and Mineralogy of Cometary and Asteroidal Interplanetary Dust Particles Collected in the Stratosphere, Dust in Planetary Systems, p. 141.

[93] Kerridge, J.F., 1985. Carbon, hydrogen and nitrogen in carbonaceous chondrites: abundances and isotopic compositions in bulk samples. GCA 49, 1707-1714.

[94] Khare, B.N., Sagan, C., Thompson, W.R., Arakawa, E.T., Meisse, C., Tuminello, P.S., 1994. Optical properties of poly-HCN and their astronomical applications. Canadian Journal of Chemistry 72, 678-694.

[95] Krueger, F.R., Kissel, J., 1987. The organic component in dust from Comet Halley as measured by the PUMA mass spectrometer on board Vega 1. Nature 326, 755-760.

[96] Landsberg, H.E., 1947. A Report on Dust Collections Made at Mount Weather and Arlington, Virginia, 1 October to 20 November, 1946. Contributions of the Meteoritical Society 4, 50-52.

[97] Langer, W.D., Graedel, T.E., 1989. Ion-Molecule Chemistry of Dense Interstellar Clouds: Nitrogen-, Oxygen-, and Carbon-bearing Molecule Abundances and Isotopic Ratios. The Astrophysical Journal Supplement Series 69, 241.

[98] Langevin, Y., Hilchenbach, M., Ligier, N., Merouhane, S., Hornung, K., 2015. Typology of dust particles collected by the COSIMA mass spectrometer in the inner coma of 67P/Churyumov Gerasimenko from Rendez-Vous to perihelion, pp. EPSC2015-2591.

[99] Lasue, J., Maroger, I., Botet, R., Garnier, P., Merouane, S., Mannel, T., Levasseur-Regourd, A.C., Bentley, M.S., 2019. Flattened loose particles from numerical simulations compared to particles collected by Rosetta. Astronomy and Astrophysics 630, A28.

[100] Le Meur, E., Magand, O., Arnaud, L., Fily, M., Frezzotti, M., Cavitte, M., Mulvaney, R., Urbini, S., 2018. Spatial and temporal distributions of surface mass balance between Concordia and Vostok stations, Antarctica, from combined radar and ice core data: first results and detailed error analysis. The Cryosphere 12, 1831-1850.

[101] Lis, D.C., Keene, J., Young, K., Phillips, T.G., Bockelée-Morvan, D., Crovisier, J., Schilke, P., Goldsmith, P.F., Bergin, E.A., 1997. Spectroscopic Observations of Comet C/1996 B2 (Hyakutake) with the Caltech Submillimeter Observatory. Icarus 130, 355.

[102] Loeffler, M.J., Baragiola, R.A., 2012. Blistering and Explosive Desorption of Irradiated Ammonia-Water Mixtures. The Astrophysical Journal 744, 102.

[103] Love, S.G., Brownlee, D.E., 1993. A direct measurement of the terrestrial mass accretion rate of cosmic dust. Science 262, 550-553.

[104] Love, S.G., Joswiak, D.J., Brownlee, D.E., 1994. Densities of Stratospheric Micrometeorites. Icarus 111, 227.

[105] Lyons, J.R., Gharib-Nezhad, E., Ayres, T.R., 2018. A light carbon isotope composition for the Sun. Nature Communications 9, 908.

[106] Mahjoub, A., Brown, M.E., Poston, M.J., Hodyss, R., Ehlmann, B.L., Blacksberg, J., Choukroun, M., Eiler, J.M., Hand, K.P., 2021. Effect of H₂S on the Near-infrared Spectrum of Irradiation Residue and Applications to the Kuiper Belt Object (486958) Arrokoth. The Astrophysical Journal 914, L31.

[107] Malamud, U., Prialnik, D., 2015. Modeling Kuiper belt objects Charon, Orcus and Salacia by means of a new equation of state for porous icy bodies. Icarus 246, 21-36.

[108] Martin, E., Schmitz, B., Schönlaub, H.-P., 2018. From the mid-Ordovician into the Late Silurian: Changes in the micrometeorite flux after the L chondrite parent breakup. Meteoritics and Planetary Science 53, 2541.

[109] Marty, B., Chaussidon, M., Wiens, R.C., Jurewicz, A.J.G., Burnett, D.S., 2011. A 15N-Poor Isotopic Composition for the Solar System As Shown by Genesis Solar Wind Samples. Science 332, 1533.

[110] Mathews, J.D., Janches, D., Meisel, D.D., Zhou, Q.-H., 2001. The micrometeoroid mass flux into the upper atmosphere: Arecibo results and a comparison with prior estimates. Geophysical Research Letters 28, 1929-1932.

[111] Mathurin, J., Dartois, E., Pino, T., Engrand, C., Duprat, J., Deniset-Besseau, A., Borondics, F., Sandt, C., Dazzi, A., 2019. Nanometre-scale infrared chemical imaging of organic matter in ultra-carbonaceous Antarctic micrometeorites (UCAMMs). Astronomy and Astrophysics 622, A160.

[112] Mathurin, J., Deniset-Besseau, A., Dazzi, A., 2020. Advanced Infrared Nanospectroscopy Using Photothermal Induced Resonance Technique, AFMIR: New Approach Using Tapping Mode. Acta Physica Polonica A 137, 29.

[113] Matrajt, G., Taylor, S., Flynn, G., Brownlee, D., Joswiak, D., 2003. A nuclear microprobe study of the distribution and concentration of carbon and nitrogen in Murchison and Tagish Lake meteorites, Antarctic micrometeorites, and IDPs: Implications for astrobiology. Meteoritics & Planetary Science 38, 1585-1600.

[114] Matsuo, T., Matsuda, H., Nakabushi, H., Fujita, Y., Boerboom, A.J.H., 1982. Third-order ion optics of an electrostatic multipole lens. International Journal of Mass Spectrometry and Ion Processes 42, 217.

[115] Maurette, M., Bradley, J.P., Jouret, C., Veyssieres, P., 1989. High resolution electron microscope studies of ''Cap-Prudhomme'' unmelted micrometeorites; preliminary comparisons with stratospheric IDPs and primitive meteorites. Meteoritics 712, 152.

[116] Maurette, M., Jehanno, C., Robin, E., Hammer, C., 1987. Characteristics and mass distribution of extraterrestrial dust from the Greenland ice cap. Nature 328, 699.

[117] Maurette, M., Olinger, C., Christophe, M., Kurat, G., Pourchet, M., Brandstätter, F., Bourot-Denise, M., 1991. A collection of diverse micrometeorites recovered from 100 tons of Antarctic blue ice. Nature 351, 44-47.

[118] McKeegan, K.A., J.; Alexander, C.; Bradley, J.; Brownlee, D.; Burnard, P.; Butterworth, A.; Chaussidon, M.; Davis, A.; Floss, C.; Gilmour, J.; Guan, Y.; Hohenberg, C.; Hoppe, P.; Hutcheon, I.; Ito, M.; Jacobsen, S.; Leshin, L.; Lyon, I.; Marhas, K.; Marty, B.; Meibom, A.; Meshik, A.; Messenger, S.; Nakamura, K.; Nittler, L.; Palma, R.; Pellin, M.; Peppin, R.; Tsou, P.; Robert, F.; Schlutter, D.; Stadermann, F.; Stroud, R.; Westphal, A.; Young, E.; Ziegler, K.; Zinner, E., 2006. Isotopic compositions of cometary matter returned by the Stardust mission. MAPS 41 Suppl., A119.

[119] McKeegan, K.D., Aléon, J., Bradley, J., Brownlee, D., Busemann, H., Butterworth, A., Chaussidon, M., Fallon, S., Floss, C., Gilmour, J., Gounelle, M., Graham, G., Guan, Y., Heck, P.R., Hoppe, P., Hutcheon, I.D., Huth, J., Ishii, H., Ito, M., Jacobsen, S.B., Kearsley, A., Leshin, L.A., Liu, M.-C., Lyon, I., Marhas, K., Marty, B., Matrajt, G., Meibom, A., Messenger, S., Mostefaoui, S., Mukhopadhyay, S., Nakamura-Messenger, K., Nittler, L., Palma, R., Pepin, R.O., Papanastassiou, D.A., Robert, F., Schlutter, D., Snead, C.J., Stadermann, F.J., Stroud, R., Tsou, P., Westphal, A., Young, E.D., Ziegler, K., Zimmermann, L., Zinner, E., 2006. Isotopic compositions of cometary matter returned by Stardust. Science 314, 1724-1728.

[120] Meier, R., Owen, T.C., Matthews, H.E., Jewitts, D.C., Bockelée-Morvan, D., Biver, N., Crovisier, J., Gautier, D., 1998. A determination of the HDO/H_2O ratio in comet C/1995 O1 (Hale-Bopp). Science 279, 842-844.

[121] Messenger, S., 2000. Identification of molecular-cloud material in interplanetary dust particles. Nature 404, 968-971.

[122] Milam, S.N., Savage, C., Brewster, M.A., Ziurys, L.M., Wyckoff, S., 2005. The 12C/13C Isotope Gradient Derived from Millimeter Transitions of CN: The Case for Galactic Chemical Evolution. The Astrophysical Journal 634, 1126.

[123] Millar, T.J., 2015. Astrochemistry. Plasma Sources Science Technology 24, 043001.

[124] Miotello, A., Bruderer, S., van Dishoeck, E.F., 2014. Protoplanetary disk masses from CO isotopologue line emission. Astronomy and Astrophysics 572, A96.

[125] Moore, M.H., Donn, B., Khanna, R., A'Hearn, M.F., 1983. Studies of proton-irradiated cometary-type ice mixtures. Icarus 54, 388.

[126] Moore, M.H., Hudson, R.L., 1998. Infrared Study of Ion-Irradiated Water-Ice Mixtures with Hydrocarbons Relevant to Comets. Icarus 135, 518.

[127] Moore, M.H., Hudson, R.L., 2003. Infrared study of ion-irradiated N ₂-dominated ices relevant to Triton and Pluto: formation of HCN and HNC. Icarus 161, 486.

[128] Moore, M.H., Hudson, R.L., Gerakines, P.A., 2001. Mid- and far-infrared spectroscopic studies of the influence of temperature, ultraviolet photolysis and ion irradiation on cosmic-type ices. Spectrochimica Acta Part A: Molecular Spectroscopy 57, 843.

[129] Muñoz Caro, G.M., Schutte, W.A., 2003. UV-photoprocessing of interstellar ice analogs: New infrared spectroscopic results. Astronomy and Astrophysics 412, 121.

[130] Murad, E., Williams, I.P., 2002. Meteors in the Earth's Atmosphere.

[131] Murray, J., Renard, A.F., 1891. Report on the Scientific Results of the Voyage of HMS Challenger during the Years 1873-76, Part 3, Deep-Sea Deposits. HMSO.

[132] Murrell, M.T., Davis, P.A., Nishiizumi, K., Millard, H.T., 1980. Deep-sea spherules from Pacific clay: mass distribution and influx rate. Geochimica et Cosmochimica Acta 44, 2067-2074.

[133] Nakamura, T., Noguchi, T., Ozono, Y., Osawa, T., Nagao, K., 2005. Mineralogy of ultracarbonaceous large micrometeorites. Meteoritics 40 Suppl., #5046.

[134] Nesvorný, D., Janches, D., Vokrouhlický, D., Pokorný, P., Bottke, W.F., Jenniskens, P., 2011. Dynamical Model for the Zodiacal Cloud and Sporadic Meteors. The Astrophysical Journal 743, 129.

[135] Neveu, M., Desch, S.J., Shock, E.L., Glein, C.R., 2015. Prerequisites for explosive cryovolcanism on dwarf planet-class Kuiper belt objects. Icarus 246, 48-64.

[136] Nittler, L.R., Ciesla, F., 2016. Astrophysics with Extraterrestrial Materials. Annual Review of Astronomy and Astrophysics 54, 53.

[137] Nittler, L.R., Stroud, R.M., Trigo-Rodríguez, J.M., De Gregorio, B.T., Alexander, C.M.O.D., Davidson, J., Moyano-Cambero, C.E., Tanbakouei, S., 2019. A cometary building block in a primitive asteroidal meteorite. Nature Astronomy 3, 659.

[138] Öberg, K.I., Garrod, R.T., van Dishoeck, E.F., Linnartz, H., 2009. Formation rates of complex organics in UV irradiated CH_3OH-rich ices. I. Experiments. Astronomy and Astrophysics 504, 891.

[139] Pagani, L., Bacmann, A., Cabrit, S., Vastel, C., 2007. Depletion and low gas temperature in the L183 (=L134N) prestellar core: the N2H^+-N2D⁺ tool. Astronomy and Astrophysics 467, 179.

[140] Palumbo, M.E., Strazzulla, G., 1993. The 2140 cm-1 band of frozen CO : laboratory experiments and astrophysical applications. Astronomy and Astrophysics 269, 568.

[141] Petit, J.R., Jouzel, J., Pourchet, M., Merlivat, L., 1982. A detailed study of snow accumulation and stable isotope content in Dome C (Antarctica). Journal of Geophysical Research 87, 4301-4308.

[142] Peucker-Ehrenbrink, B., 2001. Iridium and Osmium as Tracers of Extraterrestrial Matter in Marine Sediments Accretion of Extraterrestrial Matter Throughout Earth's History, pp. 163-178.

[143] Peucker-Ehrenbrink, B., Ravizza, G., Winckler, G., 2016. Geochemical Tracers of Extraterrestrial Matter in Sediments. Elements 12, 191-196.

[144] Piani, L., Marrocchi, Y., Vacher, L.G., Yurimoto, H., Bizzarro, M., 2021. Origin of hydrogen isotopic variations in chondritic water and organics. Earth and Planetary Science Letters 567, 117008.

[145] Piani, L., Tachibana, S., Hama, T., Tanaka, H., Endo, Y., Sugawara, I., Dessimoulie, L., Kimura, Y., Miyake, A., Matsuno, J., Tsuchiyama, A., Fujita, K., Nakatsubo, S., Fukushi, H., Mori, S., Chigai, T., Yurimoto, H., Kouchi, A., 2017. Evolution of Morphological and Physical Properties of Laboratory Interstellar Organic Residues with Ultraviolet Irradiation. The Astrophysical Journal 837, 35.

[146] Plane, J.M.C., 2012. Cosmic dust in the earth's atmosphere. Chemical Society Reviews 41, 6507-6518.

[147] Prasad, M.S., Rudraswami, N.G., Panda, D.K., 2013. Micrometeorite flux on Earth during the last ~50,000 years. Journal of Geophysical Research (Planets) 118, 2381-2399.

[148] Qi, C., Öberg, K.I., Wilner, D.J., D'Alessio, P., Bergin, E., Andrews, S.M., Blake, G.A., Hogerheijde, M.R., van Dishoeck, E.F., 2013. Imaging of the CO Snow Line in a Solar Nebula Analog. Science 341, 630.

[149] Raymond, S.N., Morbidelli, A., 2020. Planet formation: key mechanisms and global models, p. arXiv:2002.05756.

[150] Reipurth, B., 2005. The Early Sun: Evolution and Dynamic Environment, p. 54.

[151] Rochette, P., Folco, L., Suavet, C., van Ginneken, M., Gattacceca, J., Perchiazzi, N., Braucher, R., Harvey, R., 2008. Micrometeorites from the Transantarctic Mountains. PNAS 105, 18206-18211.

[152] Rojas, J., Duprat, J., Engrand, C., Dartois, E., Delauche, L., Carillo-Sánchez, J.D., Plane, J.M.C., 2019. Micrometeorite mass flux measurements at Dome C, Antarctica., Lunar and Planetary Science, The Woodlands, Texas, United States.

[153] Rojas, J., Duprat, J., Engrand, C., Dartois, E., Delauche, L., Godard, M., Gounelle, M., Carrillo-Sánchez, J.D., Pokorný, P., Plane, J.M.C., 2021. The micrometeorite flux at Dome C (Antarctica), monitoring the accretion of extraterrestrial dust on Earth. Earth and Planetary Science Letters 560, 116794.

[154] Sandford, S.A., Allamandola, L.J., 1993. Condensation and Vaporization Studies of CH 3OH and NH 3 Ices: Major Implications for Astrochemistry. The Astrophysical Journal 417, 815.

[155] Sandford, S.A., Walker, R.M., 1985. Laboratory infrared transmission spectra of individual interplanetary dust particles from 2.5 to 25 microns. ApJ 291, 838-851.

[156] Sangely, L., 2004. Development of an ion microprobe technique for the in situ isotopic analysis of organic carbon : application of the origin of bitumens associated with uranium deposits in the Athabasca (Canada) and Witwatersrand (South Africa)

Développement de l'analyse in situ de la composition isotopique du carbone organique par sonde ionique : apports à l'étude de l'origine des bitumes associés aux gisements d'uranium de l'Athabasca (Canada) et du Witwatersrand (Afrique du Sud). Institut National Polytechnique de Lorraine.

[157] Satorre, M.A., Domingo, M., Millan, C., Luna, R., R. Vilaplana, R., Santonja, C., 2008. Desnity of CH4, N2 and CO2 ices at different temperatures of deposition. Planetary and Space Science 56, 1748-1752.

[158] Satorre, M.Á., Leliwa-Kopystynski, J., Santonja, C., Luna, R., 2013. Refractive index and density of ammonia ice at different temperatures of deposition. Icarus 225, 703.

[159] Schaller, E.L., Brown, M.E., 2007. Volatile Loss and Retention on Kuiper Belt Objects. The Astrophysical Journal 659, L61.

[160] Schmitz, B., Feist, R., Meier, M.M.M., Martin, E., Heck, P.R., Lenaz, D., Topa, D., Busemann, H., Maden, C., Plant, A.A., Terfelt, F., 2019. The micrometeorite flux to Earth during the Frasnian-Famennian transition reconstructed in the Coumiac GSSP section, France. Earth and Planetary Science Letters 522, 234.

[161] Schutte, W.A., 2002. Production of organic molecules in interstellar ices. Advances in Space Research 30, 1409.

[162] Schutte, W.A., Khanna, R.K., 2003. Origin of the 6.85 μm band near young stellar objects: The ammonium ion (NH₄⁺) revisited. Astronomy and Astrophysics 398, 1049.

[163] Shen, C.J., Greenberg, J.M., Schutte, W.A., van Dishoeck, E.F., 2004. Cosmic ray induced explosive chemical desorption in dense clouds. Astronomy and Astrophysics 415, 203.

[164] Shinnaka, Y., Kawakita, H., Jehin, E., Decock, A., Hutsemékers, D., Manfroid, J., Arai, A., 2016. Nitrogen isotopic ratios of NH2 in comets: implication for 15N-fractionation in cometary ammonia. Monthly Notices of the Royal Astronomical Society 462, S195.

[165] Slodzian, G., Hillion, F., Stadermann, F.J., Zinner, E., 2004. QSA influences on isotopic ratio measurements. Appl. Surf. Sci. 231-232, 874-877.

[166] Slodzian, G., Wu, T.-D., Bardin, N., Duprat, J., Engrand, C., Guerquin-Kern, J.-L., 2014. Simultaneous Hydrogen and Heavier Element Isotopic Ratio Images with a Scanning Submicron Ion Probe and Mass Resolved Polyatomic Ions. Microscopy and Microanalysis 20, 577-581.

[167] Slodzian, G., Wu, T.-D., Duprat, J., Engrand, C., Guerquin-Kern, J.-L., 2017. Dynamic transfer applied to secondary ion imaging over large scanned fields with the nanoSIMS 50 at high mass resolution. Nuclear Instruments and Methods in Physics Research B 412, 123-173.

[168] Strazzulla, G., Johnson, R.E., 1991. Irradiation Effects on Comets and Cometary Debris, p. 243.

[169] Suavet, C., Rochette, P., Kars, M., Gattacceca, J., Folco, L., Harvey, R.P., 2009. Statistical properties of the Transantarctic Mountains (TAM) micrometeorite collection. Polar Science 3, 100.

[170] Suttle, M.D., Folco, L., 2020. The Extraterrestrial Dust Flux: Size Distribution and Mass Contribution Estimates Inferred From the Transantarctic Mountains (TAM) Micrometeorite Collection. Journal of Geophysical Research (Planets) 125, e06241.

[171] Tachibana, S., Kouchi, A., Hama, T., Oba, Y., Piani, L., Sugawara, I., Endo, Y., Hidaka, H., Kimura, Y., Murata, K.-i., Yurimoto, H., Watanabe, N., 2017. Liquid-like behavior of UV-irradiated interstellar ice analog at low temperatures. Science Advances 3, eaao2538.

[172] Taya, S., Matsuda, H., 1972. A third-order transfer matrix of an electrostatic hexapole lens. International Journal of Mass Spectrometry and Ion Processes 9, 235.

[173] Taylor, S., Lever, J.H., Harvey, R.P., 1998. Accretion rate of cosmic spherules measured at the South Pole. Nature 392, 899-903.

[174] van Dishoeck, E.F., Black, J.H., 1988. The Photodissociation and Chemistry of Interstellar CO. The Astrophysical Journal 334, 771.

[175] Verstraete, L., 2011. The role of PAHs in the physics of the interstellar medium, p. 415.

[176] Visser, R., Bruderer, S., Cazzoletti, P., Facchini, S., Heays, A.N., van Dishoeck, E.F., 2018. Nitrogen isotope fractionation in protoplanetary disks. Astronomy and Astrophysics 615, A75.

[177] Visser, R., van Dishoeck, E.F., Black, J.H., 2009. The photodissociation and chemistry of CO isotopologues: applications to interstellar clouds and circumstellar disks. Astronomy and Astrophysics 503, 323.

[178] Warin, S., Benayoun, J.J., Viala, Y.P., 1996. Photodissociation and rotational excitation of interstellar CO. Astronomy and Astrophysics 308, 535.

[179] Watson, W.D., Anicich, V.G., Huntress, W.T., Jr., 1976. Measurement and significance of the reaction 13C+ +12CO = 12C+ +13CO for alteration of the 13C/12C ratio in interstellar molecules. The Astrophysical Journal 205, L165.

[180] Weaver, H.A., A'Hearn, M.F., Arpigny, C., Combi, M.R., Feldman, P.D., Tozzi, G.-P., Dello Russo, N., Feaga, L.M., Festou, M.C., 2008. Atomic deuterium emission and the D/H ration in comets, Asteroids, Comets, Meteors, Baltimore, p. #8216.

[181] Weisberg, M.K., Prinz, M., Clayton, R.N., Mayeda, T.K., 1993. The CR (Renazzo-type) carbonaceous chondrite group and its implications. GCA 57, 1567-1586.

[182] Whipple, F.L., 1950. The theory of micrometeorites, 1. In a isothermal atmosphere. Proc. Nat. Acad. Sci. 36, 687-695.

[183] Wimmer-Schweingruber, R.F., Berger, L., Köten, M., Bochsler, P., Gloeckler, G., 2014. The 13C/12C Isotopic Ratio in the Solar Wind, p. 1114.

[184] Wollnik, H., 1965. Second order approximation of the three-dimensional trajectories of charged particles in deflecting electrostatic and magnetic fields. Nuclear Instruments and Methods 34, 213.

[185] Wollnik, H., 1967. Second order transfer matrices of real magnetic and electrostatic sector fields. Nuclear Instruments and Methods 52, 250.

[186] Wright, I.P., Pillinger, C.T., 1994. On the Isotopic Chemistry of Carbon at the Martian Surface. Philosophical Transactions of the Royal Society of London Series A 349, 309.

[187] Wu, Y.-J., Chen, H.-F., Chuang, S.-J., Huang, T.-P., 2013. Ultraviolet and Infrared Spectra of Electron-Bombarded Solid Nitrogen and Methane Diluted in Solid Nitrogen. The Astrophysical Journal 768, 83.

[188] Wyckoff, S., Kleine, M., Peterson, B.A., Wehinger, P.A., Ziurys, L.M., 2000. Carbon Isotope Abundances in Comets. The Astrophysical Journal 535, 991.

[189] Yabuta, H., Noguchi, T., Itoh, S., Nakamura, T., Miyake, A., Tsujimoto, S., Ohashi, N., Sakamoto, N., Hashiguchi, M., Abe, K.-i., Okubo, A., Kilcoyne, A.L.D., Tachibana, S., Okazaki, R., Terada, K., Ebihara, M., Nagahara, H., 2017. Formation of an ultracarbonaceous Antarctic micrometeorite through minimal aqueous alteration in a small porous icy body. Geochimica et Cosmochimica Acta 214, 172-190.

[190] Yada, T., Nakamura, T., Takaoka, N., Noguchi, T., Terada, K., Yano, H., Nakazawa, T., Kojima, H., 2004. The global accretion rate of extraterrestrial materials in the last glacial period estimated from the abundance of micrometeorites in Antarctic glacier ice. Earth, Planets, and Space 56, 67-79.

[191] Ziegler, J.F., Ziegler, M.D., Biersack, J.P., 2010. SRIM - The stopping and range of ions in matter (2010). Nuclear Instruments and Methods in Physics Research B 268, 1818.

[192] Zinner, E., 2014. Presolar Grains, p. 181.

[193] Ziurys, L.M., Savage, C., Brewster, M.A., Apponi, A.J., Pesch, T.C., Wyckoff, S., 1999. Cyanide Chemistry in Comet Hale-Bopp (C/1995 O1). The Astrophysical Journal 527, L67.